TECHNISCHE
UNIVERSITÄT
WIEN
Vienna University of Technology

Doctoral Thesis

Air Entrainment in Free Falling Water Jets

submitted in satisfaction of the requirements for the degree of
Doctor of Philosophy in Civil Engineering
of the Vienna University of Technology, Faculty of Civil Engineering

---

Dissertation

Lufteintrag in vertikalen Fallstrahlen

ausgeführt zum Zwecke der Erlangung des akademischen Grades eines
Doktors der technischen Wissenschaft
eingereicht an der Technischen Universität Wien Fakultät für Bauingenieurwesen von

Freddy Alberto Flórez Otero

Gutachter : Ao.Prof. Dipl.-Ing. Dr.techn. Reinhard Prenner
Institute für Wasserbau und Ingenieurhydrologie
Technische Universität Wien

Gutachter : Univ.-Prof. Dipl.-Ing. Dr.sc.techn. Robert Boes
Versuchsanstalt für Wasserbau, Hydrologie und Glaziologie
Eidgenössische Technische Hochschule Zürich

Vienna, September 2016 _____

Of course to my lovely inspirations Benjamin and Lorena

Abstract

The determination of air entrainment in free falling water jets is still a topic subject to large uncertainties that come from the strong interaction among independent parameters including such dominant ones as the nozzle geometry and the turbulence intensity that have not been considered in many researches. Despite many findings on this topic about the determination of the water jet breakup length, a mathematical generalization has not been found yet. The complete behavior of the jet stability curve through the turbulent regime remains unknown (also hysteresis and supercavitation may take place) in hydraulic engineering and the equations proposed in the literature are valid for specific conditions and they lack universality.

Specifically, when the law of Froude similarity is adopted, commonly used for the conversion from the model to prototype for free surface flows, the results depend on the scale ratio and the amount of air entrainment is generally under-predicted. In this study, different air entrainment mechanisms (according to the modes of breakup reported in the literature) under steady flow conditions were tested in the laboratory on the basis of a model family of circular pipe nozzles at different scales. In evaluating the scale effects affecting air entrainment in a falling water jet by means of an encasing pipe, it was found that the model length scale had a strong effect. Moreover, the air entrainment coefficient scale varies linearly with the length scale. The scale effects were determined by measuring the air concentration profile at several distances from the nozzle exit with a sapphire optic probe and the similarity between the experimental curves of model and prototype were evaluated by means of Discrete Fréchet distance and Procrustes analysis based on a Standardized Dissimilarity Measure SDM.

Furthermore, two modes of disintegration of the experimental tests (spiral and spray) were used to validate the results using Computational Fluid Dynamics (CFD) by means of two different turbulent approaches: 1) Reynolds Average Navier-Stokes RANS methods, with the standard $k-\epsilon$ and the $k-\omega$-SST models, and 2) Large Eddy Simulation LES, with the Smagorinsky, the k-equation eddy-viscosity and the $k-\omega$-SST scale adaptative simulation (SAS) models. Finally, it was found that RANS turbulence models in neither case generated water separation from the water surface, it had a smooth condition and there was no breakup. However, LES models were able to reproduce the physics of the

phenomena in nature consisting of the high dynamic interaction between the air-water phases and the breakup processes but in an early stage. Finally, despite LES turbulence models requiring a computational time twice that of RANS models, it is suggested that it should be used in hydraulic engineering for studying cases in which air is of concern.

Acknowledgements

I would like to express my sincere and deepest gratitude to my supervisor Ao.Prof. Dipl.-Ing. Dr.techn. Reinhard Prenner for his continuous support, for the encouragement given, many valuable suggestions, and guidance provided throughout the course of my studies and projects.

I'm also indebted to Univ-Prof. Dipl.-Ing. Dr.sc.techn. Dipl.-Ing. Robert Boes for his valuable comments, suggestions and support in culminating this research.

I am grateful to the head of the Institute of Hydraulic Engineering and Water Resources Management Univ.Prof. Dipl.-Ing. Dr.techn. Günter Blöschl for his support and for the encouragement given to continue my research.

My thanks also go to Prof. John Fenton for his valuable comments and review of this document; to Andreas Kothmayer, Andreas Leopoldseder, Harald Kornherr, Dipl.-Ing. Hubert Honsowitz and Kornelia Selig for their continuous support at the Institute and Hydraulics laboratory; and to Dipl.-Ing. Dr.techn. Markus Hamik for his valuable suggestions and comments in the chapter concerning CFD.

My thanks also to the Austrian Agency for International Cooperation in Education and Research (OEAD, in German) which granted me funds to carry on this research during the first year of my studies.

Finally, I take the opportunity to thank my parents Luzmila Otero and Freddy Florez; my siblings Favio Florez and Luz Angela Florez, and also to Mrs Brigida Gomez for their infinite support.

I am also much indebted to my wife Lorena Nisperuza and my son Benjamin for all their love, support and patience during the years abroad. I am quite sure I could not have brought this work to this degree of completion without their sustained encouragement.

Contents

List of Figures

List of Tables

Nomenclature

Acronyms

A.R.	Aspect ratio of the nozzle
C.R.	Contraction ratio of the nozzle
CFD	Computational Fluid Dynamics
DNS	Direct Numerical Simulations
FVM	Finite Volume Method
LES	Large Eddy Simulation
RANS	Reynolds Averaged Navier-Stokes equations
S.L.	Streamlining of the nozzle
S.Q.	Surface quality (roughness) of the nozzle
SDM	Standardized Dissimilarity Measure (Procrustes analysis)
VOF	Volume of Fluid Method

Greek Symbols

α	Phase fraction	[-]
α_d	Spread angle	°
α_n	Contraction angle of the nozzle	°
β	Air entrainment coefficient	[-]
δ	Boundary layer thickness	m
δ_2	Lateral spread of the liquid jet	m
δ_c	Diameter of the solid inner of the liquid jet	m

δ_{dF}	Discrete Fréchet distance	cm
ϵ	Average rate of dissipation of turbulence kinetic energy	[-]
κ	Turbulent kinetic energy	m^2/s^2
κ_c	Mean curvature of the free surface	[-]
λ	Stability parameter according to Phinney	[-]
μ	Dynamic viscosity of the fluid	$Pa \cdot s$
ν	Cinematic viscosity of the fluid	m^2/s
$\overline{\delta_{dF}}$	Average Discrete Fréchet distance	cm
ρ	Density of the fluid	kg/m^3
ρ_a	Density of the ambient fluid	kg/m^3
σ	Surface tension between fluid and surrounding gas	N/s
ε	Lateral spread distance of turbulence jet in atmosphere	m
ε/r	Surface roughness	[-]

Roman Symbols

Fr_r	Froude number similarity scale	[-]
La	Laplace number, equal to Su	[-]
Su	Suratman number, equal to La	[-]
$\overline{L}$	Length of jet breakup	m
$\overline{L}/d$	Relative jet breakup length	[-]
$\overline{r}$	Apparent mean radius	m
$\overline{u}$	Mean velocity	m/s
ϕ	Diameter of the casing pipe	m
$\sqrt{\overline{u_i}^2}$	Mean square transverse component of the turbulence	%
A	Cross sectional area	m^2
A_g	Cross-sectional area of the air fraction	m^2
C	Air concentration, defined as $(Q_a)/(Q_a + Q_w)$	[-]
C_d	Drag coefficient	[-]
C_E	Jet turbulent parameter given by 1.14 $Tu\,Fr^2$	[-]
d	Diameter of the nozzle	m

D_0	Dispersion number	[-]
f_b	Body forces	[-]
g	Acceleration of the gravity	m/s^2
H	Depth of the water in the water tank	m
L	Length dimension	m
L_m	Length dimension in the model	m
L_n	Exit length of the nozzle	m
L_p	Length dimension in the prototype	m
L_r	Length scale ratio	[-]
L_R	Characteristic linear dimension	m
m	Mass	kg
p	Pressure	N/m^2
Q_a	Volumetric flow rate of air	m^3/s
Q_w	Volumetric flow rate of water	m^3/s
R^1	Coefficient of determination	[-]
r_0	Radius of the liquid jet at the nozzle exit, equal to the radius of the nozzle	m
r_c	Radius of the jet at the contracted section	m
r_d	Perpendicular distance to the axis of the jet	m
r_w	Water jet radius	m
T	Deviator viscous stress tensor	[-]
t	Total time of measure of the air fraction	s
t_g	Duration in the time of the air fraction	s
Tu	Turbulence intensity of jet, u'/U_0	%
U	Velocity of the fluid	m/s
u'	Root mean square of the turbulence velocity fluctuations	s
u'_x	Root mean square of the velocity turbulent fluctuation in the jet streamwise direction	s
u'_y	Root mean square velocity fluctuation in jet transverse direction y	s
u'_z	Root mean square velocity fluctuation in jet transverse direction z	s
$u*$	Shear velocity	m/s

U_0	Mean jet velocity at nozzle exit	m/s
u_a	Air velocity	m/s
u_r	Velocity at a distance r from the jet axis	m/s
U_t	Terminal velocity	m/s
U_{cp}	Mean jet velocity at nozzle exit at which atomization take place	m/s
u_{max}	Maximal velocity	m/s
V	Total volume that goes through certain section area A	m^3
V_g	Volume of gas	m^3
V_w	Volume of water	m^3
x	Distance from the nozzle exit or orifice	m
y_a	Distance from the water surface	m

Other Symbols

ℓ	Root mean square difference	[-]
∇	Del or nabla operator	
U	Velocity field	

CHAPTER

1 Introduction

The capturing of air bubbles and pockets by convection or turbulence within a water flowing flow, so called air entrainment, may take place naturally or artificially by injection. On the one hand, the most common evidence of the occurrence of this phenomenon in the environment is the whiteness of the water during breaking waves, high velocity open channel flows (rapids), waterfalls (see Figure 1.1) and even every day during our domestic activities by using a showerhead, the garden hose and turning on the tap. On the other hand, the forced aeration is used in industrial processes, in water treatment for improving its quality (drinking water and waste water) as well as in hydraulic structures like chute spillways and bottom outlets to reduce the risk of cavitation.

Figure 1.1: Cascade Seljalandsfoss (Iceland). Courtesy of R. Kratky (2015).

The types of air entrainment in hydraulic structures are distinguished as: a) *surface aeration or natural aeration*, in the case of free jets and high speed channels like spillways and chutes, and b) *local aeration* consisting of the air entrainment on flows occurring locally at a surface discontinuity like hydraulic jumps, impinging jets, transition from free surface to conduit flow and the wakes of bluff bodies.

1.1 Motivation: air entrainment in hydraulic engineering

In hydraulic engineering the movement of the water at high velocities develops an interaction with the surrounding air consisting of air bubble entrainment and by dragging them in their vicinity in the flow direction. On the one hand, certain circumstances the entrapped air may be beneficial in case of reducing the risk of cavitation, but on the other hand the excess of air can generate harmful effects, such is the case of blowback of the entrained air in sag pipes and the inability of the system to transport the air demand suitably in bottom outlets. In both cases the excess of air can trigger the generation of pulsating flows (because of hydraulic blockage of the flow) with damaging consequences for the stability of the structure itself. Consequently, for the safety of hydraulic structures the impact of the air must be evaluated and guaranteed during the design.

Falvey [16] classified the air-water flow into three basic types: air-water flows in open channels, air-water flows in closed conduits, and free-fall water flows. In general this classification is called *air-entraining* flows because the air is trapped into the water mass. In the specific case of aerated turbulent jets (type free-fall water flows) the thickness, the initial turbulence and the height play an outstanding role during the dispersion (atomization) of the jet. As is observed in Figure 1.2, the overturning surface waves, the water droplets being projected above the water surface and the incremental velocity during the falling are the major entrainment mechanisms. Furthermore, in such water jets the compactness and a delayed breakup of the water jet, is a critical condition for the tailwater of a dam because it may affect its own stability by scour if the energy is not suitably dissipated.

Figure 1.2: Tsankov Kamak (Bulgaria): spillway test. Courtesy of D. Kischlat (2010)

One of the challenges of air-water flows in hydraulic physical models deals with matching model and prototype because the latter shows basically a structure more aerated and turbulent than under-scaled models. In nature the high water velocity and the presence of irregular high energy three dimensional vortices causes the air to be trapped and released (so called *detrainment*) actively in comparison with the restricted dynamic con-

ditions in the laboratory. According to Kobus [19] the bubble size distribution depends upon the turbulent characteristic of the flow and in reduced hydraulic models it is proportionally too large. As a consequence it would hint about scale effects in the sense that detrainment is too large in the model and hence the transport too small. Additionally, the turbulence level in the models is evidently lower than in prototypes.

Consequently, to overcome the difficulties of the imperfect similarity in under-scaled models and the probability that disdained parameter may induce large scale effects, the use of two-phase Computational Fluids Dynamic(CFD) models rise up as a plausible alternative to avoid, additionally, the difficulties during the experimentation of measuring air-water mixtures with intrusive probes and the hight costs of construction and operation of hydraulic physical models.

1.2 Aim of investigation and hypothesis

Experimental investigations have demonstrated the complexity of the air-water interaction process under turbulence effects. In spite of the significant findings of mathematical theories and models concerning gas-liquid (two-phase) flow interaction in hydraulic engineering, there is a lack of information in research on scale effects, limited records of experimental measurements of the amount of air in water (because the limited access to specialized instrumentation by hydraulic laboratories) and a lack of evidence and success in the validation of using Computational Fluid Dynamics (CFD) for simulating dynamic and high turbulent air entrainment process in water resources engineering.

In order to analyse the complexity and improve understanding of scale effects of air-water mixtures, a model family of circular nozzles ejecting vertically downwards into quiescent air, so called free falling water jets, has been selected to be tested because the laboratory facility is easily adaptable to these experiments, and due to the adjustability and ease construction of the nozzles, and the lack of a solid boundary during its fall which may produce a strong influence in the flow behavior for the different models. In spite of the broad research on the topic of liquid jets issuing from circular nozzles, the impact of various parameters has not been investigated and scientific understanding about length breakup is still incomplete because of the variability of formulae.

Furthermore, based in measurement of air entrainment in laboratory, it is necessary to be able to simulate them by means of two-phase Computational Fluid Dynamics (CFD) techniques and to use these methods as a tool for predicting the behaviour of flow mixtures into systems (quantify the air entrainment with certain accuracy) for a more appropriate design of hydraulic structures. By using these numerical methods it may be helpful to solve problems involving air-water high turbulent flows which could lead us to overcome the uncertainty originated by scale effects of reduced models in Laboratory.

The following goals were aimed at:

- To evaluate and analyse the existing formulae concerning to breakup length in vertical free falling water jets.

- To determinate scale effects in a model family of free falling water jets. Likewise, to evaluate and analyze the range of validity and universality.
- To simulate the behavior of free falling water jets by using Computational Fluid Dynamics methods. Furthermore, to analyse and validate their results with the air concentration profiles obtained experimentally.

1.3 Methodology

The following research strategy will be executed in order to succeed in verifying the hypotheses mentioned above:

- Review the state of the art concerning free falling water jets, establishment of the underlying physical behaviour of air entrainment and computational fluid dynamics applied to air-water mixtures.
- Calculation of scale effects in a small range (due to restriction in the laboratory) by using a model family of nozzles by quantifying the air entrainment and the air concentration.
- Simulation of free falling water jets according to the laboratory experiments by using Computational Fluid Dynamics (CFD) techniques.

CHAPTER

2 Basics and existing literature

A *free falling water jet* is a fluid spread from a nozzle or an orifice into a surrounding medium (e.g. air) which is substantially less denser that the jet itself on which the direction of the fluid is led mainly downwards. When the liquid emerges from a nozzle its constitution is like an unbroken column with the presence of ruffled (rippled) forms on the surface and, later on due to turbulence effects overcoming the surface tension it turns into unstable forms leading to the formation of discrete masses of fluid and consequently into small droplets.

In the following chapter the relevant investigations concerning jet instability, jet formation, break up length, water break up process, and air entrainment mechanisms are described. Furthermore some additional studies concerning horizontal and inclined water jets are presented, whose researches have been mainly led to analyze its behavior under high flow velocities, the break-up process and dispersion.

In conclusion, the state of the art in Computational Fluid Dynamics (CFD) applied to free surface flows is expounded, as well as the relevance of the differential equations and mathematical models used for describing an incompressible, isothermal and immiscible fluid.

2.1 Nomenclature and basic concepts of air entrainment

A two-phase flow is a particular case of multiphase flow where the continuum contains gas and liquid fractions interacting. The process of air entrainment is quantifiable in terms of the *void fraction* ϵ_k which designates the fraction of a phase k over the total mixture. Depending on the type of measure, the *time averaged local void fraction* $\overline{\epsilon_{gi}}$ and the *time averaged cross-sectional void fraction* $\langle\overline{\epsilon_g}\rangle$ can be determined as follows [20]:

- **Time averaged local void fraction** is the duration in time of the air fraction t_g over the total time of measure t at a certain point (x, y, z).

$$\overline{\epsilon_{gi}} = \frac{t_g}{t} \tag{2.1}$$

- **Time averaged cross-sectional void fraction** is a two-dimensional measure which is defined as the local area (cross-sectional area) of the gas (index g) fraction A_g over the total cross sectional area A. Likewise it can be defined in terms of the volume of gas V_g and the total volume V that goes through a cross sectional area, A.

$$\langle\overline{\epsilon_g}\rangle = \frac{A_g}{A} = \frac{V_g}{V} \tag{2.2}$$

The concentration is defined as a quantity, usually measured by volume, of a material A either dissolved or suspended in another material B. Thus, if the material A is air (index a) and the material B is water (index w), the air concentration would be the volume of air V_a in a given volume of water V_w [16]. However, when the dissolved material becomes large, the reference volume is the sum of the volume of air and water, or even it could be expressed in terms of volumetric flow rate of water Q_w and air Q_a. As a consequence, the average air concentration C is defined as:

$$C = \frac{V_a}{V_a + V_w} = \frac{Q_a}{Q_a + Q_w} = \frac{\beta}{\beta + 1} \tag{2.3}$$

where $\beta = Q_a/Q_w$ is the air entrainment coefficient.

2.2 Types of jet disintegration

The break up phenomenon is the last stage when a fluid is discharged from a nozzle with an outlet velocity, U_0. As soon as a certain critical velocity U_{cp} is exceeded then the whole fluid has a compactness which becomes broken because the increasing of the speed of the flow as well as the internal turbulence of the fluid breaks the surface tension of the fluid walls. At this stage small globules of air (so called bubbles) entrain into the water, are transported by convection downwards, inside the flow, until the massive entrainment effect along the falling fluid affects the stability of the fluid and suddenly the entire liquid collapses, consisting initially in the presence of independent and detached masses of fluid and finally into small rounded shapes, called droplets.

The investigations concerning falling water jets have been conducted over the years in terms of the compactness and the breakup lengths, the last being the main concern of research in the fields of irrigation systems, fire nozzles, energy dissipation in hydraulic structures, and industrial processes.

Rayleigh [21], based on the studies of Plateau [22], established the criteria of stability of a cylindrical jet and affirmed that the cause of instability of jets of fluid, excluding the gravity forces, is caused by: a) *capillary forces* whose effect is to render the infinite cylinder an unstable form of equilibrium, and b) a *dynamical character*, which is depending on the fluid surrounding the jet, mostly air. His mathematical formulation considered a frictionless, potential flow and strong capillarity effects. The stability is acquired if the

wavelength fluctuation of the transverse fluctuation is less than $2\pi r$, where r is the radius of the jet. Afterwards a refining of the theory concerning the jet disintegration by taking into account the viscosity and the surface tension was proposed by Weber [23].

Haenlein [24] conducted experiments with several fluids (water, fuel oil, glycerine, and ricinus oil) with the purpose of determining the liquid velocity and to characterize its breakup disintegration when they are jetted from nozzles of various diameters under the influence of the air. Furthermore, he aimed at a classification of the disintegration mechanism of water jets (see Figure 2.1-a) by defining the following German words: 1) *Zertropfen*, breaking into drops due to surface tension with or without the effect of air; 2) *Zerwellen*, breaking up through wave formation and; 3) *Zerschmettern*, disruption of jet.

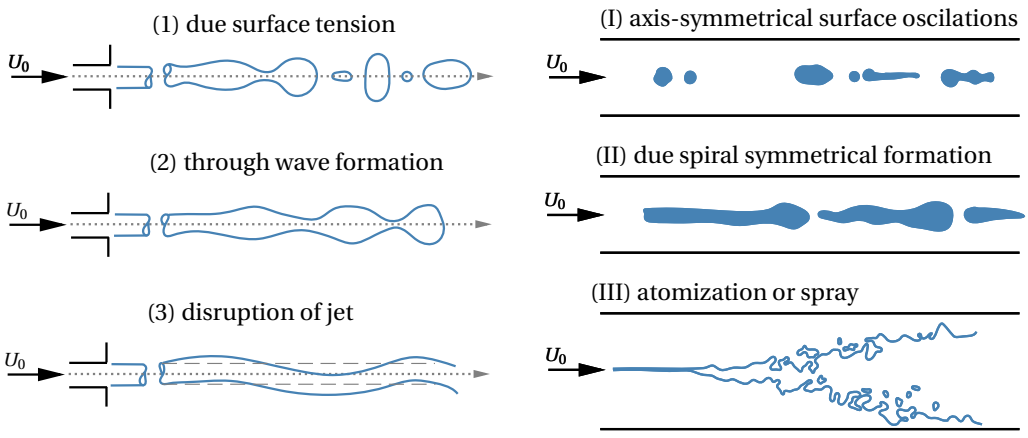

a) Haenlein (1931) b) Ohnesorge (1937)

Figure 2.1: Types of jet disintegration according to: a) Haenlein, and b) Ohnesorge.

By using a novel high speed photography technique, Ohnesorge [1] documented the dripping and jetting phenomena of several liquids into air: water, aniline, glycerine and two hydrocarbon oils. Based on dimensional analysis, combining the Reynolds number *Re*, generally accepted as the most important parameter in fluid mechanics, and Weber numbers *We*, he defined a new dimensionless group Z nowadays known as the Ohnesorge number *Oh* that relates the viscous forces to the inertial and surface tension forces. The Reynolds number *Re* and the Weber number *We* may be written as:

$$Re = \frac{U\, L_R}{\nu}, \tag{2.4}$$

$$We = \frac{\rho\, U^2\, L_R}{\sigma}, \tag{2.5}$$

where U is the characteristic velocity, L_R is the characteristic linear dimension, ν is the kinematic viscosity of the fluid defined as $\nu = \mu/\rho$, μ is the dynamic viscosity of the fluid, ρ is the density of the fluid and σ is the surface tension between fluid and surrounding gas. Typically, for water jets discharging from nozzles, the nozzle diameter d is taken as

characteristic linear dimension. Therefore, the Ohnesorge number may be written as:

$$Oh = \frac{\sqrt{We}}{Re} = \frac{\mu}{\sqrt{\sigma \rho L_R}} = \frac{1}{La^2} = \frac{1}{Su^2}, \tag{2.6}$$

where La is the dimensionless Laplace number, also know as the Suratman number Su which is defined as:

$$La = Su = \frac{\sigma \rho \, L_R}{\mu^2}. \tag{2.7}$$

Ohnesorge related his dimensionless number to the Reynolds number Re in a graphical form $Oh = f\,(Re)$, (see Figure 2.2), and let it distinguish different modes of jet disintegration exiting from a nozzle (see Figure 2.1-b), separated by straight lines, so called regimes, which were labeled from 0 to III and described as follows:

- (0) or Rayleigh breakup regime: slow dripping from the nozzle under gravity effects without jet formation (*Abtropfen*, in German). In this regime the jet has low velocities and there are small disturbances on the water surface due the surface tension which dominate the breakup process.

- Region (I) or first wind-induced breakup regime or sinuous regime: disintegration of the cylindrical jet by means of axis-symmetrical surface oscillations at higher velocities that are associated with the Rayleigh breakup.

- Region (II) or second wind-induced breakup regime: disintegration by means of spiral formation (screw-like perturbations) of the jet according to Weber-Hänlein (*Zerwellen* in German). Additionally the atmospheric effects become important and the surface irregularities because of the aerodynamics effects disrupt the jet more notably than that in the previous region [10].

- Region (III): drop or atomization of the jet (*Zerstäubung* in German) in the vicinity of the nozzle exit due to very high velocities. Under high speeds of the fluid atomization might take place. At this stage, the cavitation may arise as has been reported by Tamaki et al. [25] and Tamaki et al. [26].

In the static case 0, the ratio r_0/a is relevant, where r_0 is the radius of the orifice and a is the *Laplace constant* defined as

$$a = \sqrt{\frac{\sigma}{\rho g}}, \tag{2.8}$$

where g is the acceleration of gravity. The meridian curve of the axis-symmetric jet which is nothing else that a plane section of a surface of revolution containing the axis of revolution, can be calculated by using numerical integration and thus the weight of the falling jet with good accuracy in the range $0.01 < r_0/a < 1.0$ can be determined.

For the successive regions the jet will break up insofar as the velocities increase, and as a consequence, the effect of the inertial and the frictional forces will be higher and meanwhile the gravitational effects begin to reduce. Ohnesorge remarks the irrelevance of using the Froude number Fr for describing the jet disintegration phenomena (region

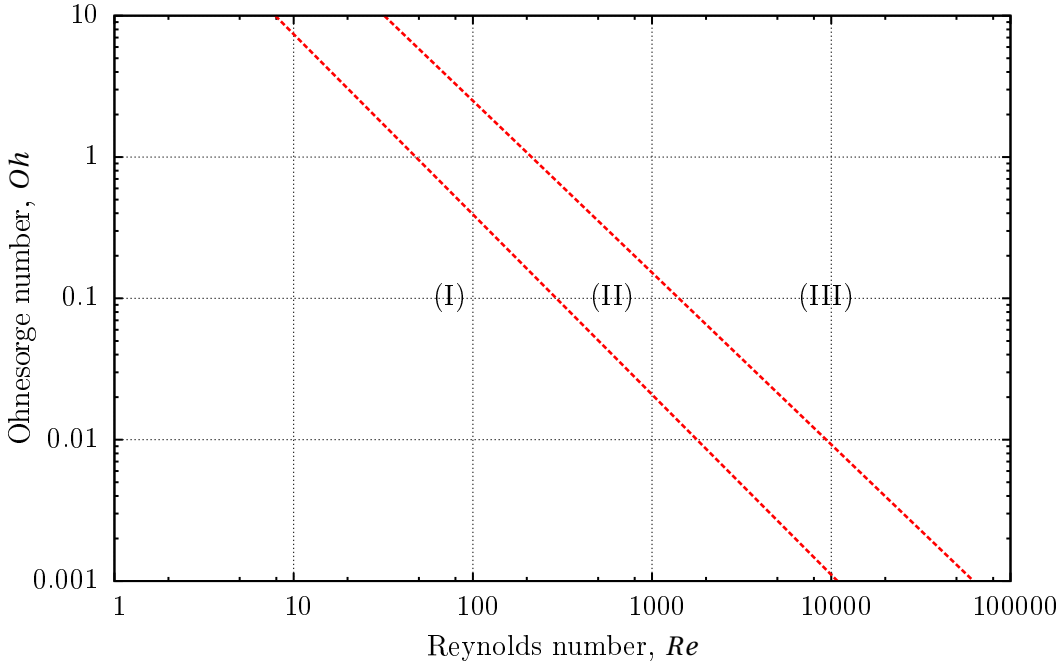

Figure 2.2: Drop formation and jet disintegration (adap. from Ohnesorge [1]).

III) instead of using the Weber number for capillarity and the Reynolds number for viscosity. The Froude number is defined as:

$$Fr = \frac{U}{\sqrt{gL_R}} \tag{2.9}$$

Although Ohnesorge mentioned the character of a power law relationship for classifying the regimes, an equation was not proposed by him. McKinley & Renardy [27] suggested the following expression for the transition from region I (Rayleigh breakup) to region II (screw-symmetric break up),

$$Oh \sim 125\, Re^{-5/4}. \tag{2.10}$$

Building upon the ideas of Ohnesorge, Miesse [28] erroneously stated that experimental jet disintegration data is more suitable if the boundary line between regions II and III is translated to the right. The new boundary line proposed by Miesse is nothing else than the same line proposed initially by Ohnesorge.

2.3 Jet stability curve and stability parameter λ

Based on the dimensionless Reynolds number *Re*, the breakup mechanism for laminar ($Re < 2100$) and turbulent ($Re > 4000$) liquid jets have many similarities, but the most obvious difference lies in the disturbance level at the jet nozzle exit, the so-called initial turbulent intensity *Tu* [2].

As soon as the whole liquid jet disrupts and the separation into droplets starts, the phenomenon is known as the *primary breakup of a liquid* and essentially at this stage, due to the high density differences, $\Delta\rho$, the jet does not have a significant resistance by the medium. Later as the jet moves forward, there is a massive breakup into finer droplets (called *secondary breakup*) which consists of the formation of a scattered flow where the velocity and the dynamic pressure progressively decrease and the fluid is influenced by the aerodynamics forces and the fluid properties.

The direct mechanism of breakup of a liquid is by means of discharging it from a nozzle or an orifice with a suitable outlet velocity. As a consequence, the disintegration of the jet can be characterized by the breakup length, $\overline{L}$, which is the measured distance from the edge of the nozzle or exit until the breakup point. The function $\overline{L} = f(U_0)$, known as the *jet stability curve* (first proposed by Smith & Moos [29]), is the general description of the behavior of a liquid ejected into air. In general, parameters as the density of the ambient fluid (in general, air ρ_a), the geometry of the nozzle and the inlet conditions in the nozzle are not considered (Grant & Middleman [6], Phinney [2], Giffen & Muraszew [30], Skripalle [31]).

If the experimentally-determined breakup length of a jet $\overline{L}$ is plotted against the averaged nozzle exit velocity U_0, a curve similar to that shown in Figure 2.3 is obtained. The *jet stability curve* is composed of the following regions which are described below:

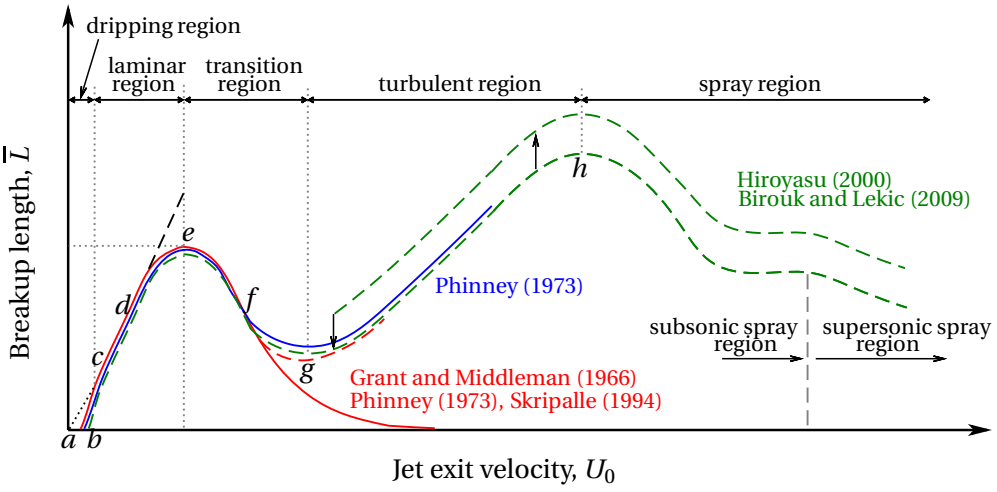

Figure 2.3: Jet stability curve

ac, bc For small velocities a critical initial velocity (at *b*) must be accomplished with the

purpose of filling the cross section of the nozzle with the fluid. At this stage, simply, the fluid drips out from the nozzle and as consequence a definable jet length is not possible.

cd Belongs to the laminar region. Here the jet breakup is strongly dependent on the surface tension σ and the jet breakup will be induced by undulations and variations in the surface of the jet. The interaction with the surrounding air is not relevant and there is no influence in the drop formation. This laminar linear portion is well described by Weber's theory [23] which considered as remarkable parameters the diameter d, the surface tension σ, the jet viscosity μ, and the density ρ; however, the ambient density ρ_a was ignored [2].

de By increasing the outlet velocity U_0 the fictitious forces of the surrounding air should not be neglected. However if the density of the surrounding media ρ_a is low enough there is no influence on the jet breakup. As soon as the inlet velocity is increased, the breakup distance $\overline{L}$ does not increase proportionally until the maximal velocity u_c is reached at e. In this region Weber's linear theory [23] does not match at all because the additional factors that contribute to the jet breakup were not considered. Weber and numerous other authors attempted to properly account for the atmospheric effects. However, none of the improved theories successfully predicts the local maximum and the laminar to semi-turbulent transition of the stability curve [10]. The laminar region ends with the peaking in the breakup curve because of: the initial turbulence level [32] and, of the ambient atmosphere.

A generalized function based on experimental data for determining the location of the transition from laminar to turbulent flows (to get the peak) has been attempted by McCarthy & Molloy [33]; however, their results are only usable for a particular case under certain boundary conditions.

eg From here the transition region starts and the aerodynamic forces become more prominent. After getting the maximal breakup length, $\overline{L}$, the relationship $\overline{L} = f(U_0)$ decreases almost linearly through the curve *ef*. Additionally, in this region the drop formation is influenced by the air. According to Phinney [2], in addition to achieving a critical Reynolds number *Re* the aerodynamical forces and the turbulence of the jet will generate and increase the oscillations in the surface of the cylindrical jet.

According to Schweitzer [34] this region is characterized by a turbulent core wrapped in a laminar envelope. In principle the outer layer (laminar envelope) hinders turbulent particles from reaching the jet surface and disrupting the flow. In the end downstream from the nozzle exit, the momentum is redistributed between the two layers, the velocity profile is flattened, and the radial velocity components disrupt the jet, resulting in its breakup. With increasing Reynolds number *Re*, the thickness of the laminar envelope reduces until it disappears completely in the turbulent region.

gh In the case of turbulent flow regimes the impact of the high momentum convection results in dominating inertial forces, which are considerably higher than the viscous forces in the jet flow. It is well known that this a rather simplistic definition of

the physics of the Reynolds number, but the consequences lies in the increase of the hydrodynamic forces by means of shear stress at the liquid surface.

$\geq h$ The spray region is clearly governed by high speed velocities and the nature of the flow has been an object of controversy due to recent new findings through observations. Early studies reported that as the jet velocity increases, the breakup length decreases and eventually becomes zero. However, McCarthy & Molloy [33] found experimentally that a small continuous portion of the jet remains after the nozzle exit, regardless of the jet velocity. The previous results were confirmed by Hiroyasu et al. [35] [36], Hiroyasu [37], and Arai et al. [38] [39] [40]. Those authors reported that there always appears to be a finite breakup length and the jet does not appear to ever break up at the actual nozzle exit.

The phenomenon of hysteresis is also observed in figure 2.3, represented by arrows which indicate that for the same Reynolds number there are two different jet breakup lengths. The higher and lower breakup length values are obtained when decreasing and increasing the exit jet Reynolds number respectively, caused by the occurrence of hydraulic flip. Similar to the maximum breakup length, the point at which hysteresis is encountered also appears to shift to a lower jet velocity with increasing nozzle exit diameter as has been reported by Arai et al [38].

Phinney [2] defined the *stability parameter* λ used to characterize the breakup which can be considered as the reciprocal of the amplification rate for disturbances or as the logarithm of the initial disturbance level:

$$\lambda = \frac{\overline{L}/d}{\left[We\left(1+3\,Oh\right)\right]^{1/2}}. \tag{2.11}$$

According to Phinney the factor (1+3 *Oh*), contains the effect of the viscosity and accounts for the stabilizing influence of viscosity. When curves λ vs *Re* are plotted (see Figure 2.4) for various nozzle-fluid combinations and considering absence of effects of the surrounding media, there is a critical Reynolds number $\hat{Re}$ above which λ starts to decrease rapidly, associated with an increase in the initial disturbance level.

The laminar plateau region shown in Figure 2.4 is characterized by a constant *amplification rate* (from laminar theory) and *disturbance level*. The dotted line corresponds to the condition in which the ambient density is high. In the range $500 < Re < 3000$ there occurs a marked decrease in the λ parameter which is associated with an increase in the disturbance level. Phinney suggested that a second plateau may exist in the fully turbulent regime where the influence of the *amplification rate* and the *disturbance level* over the breakup length $\overline{L}$ are combined.

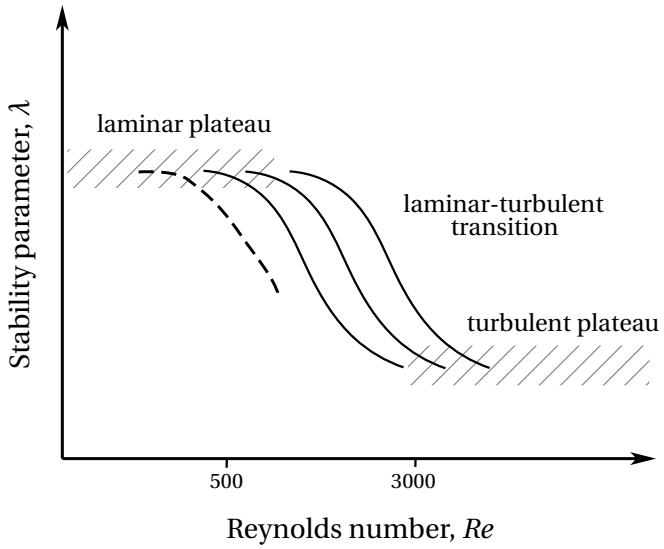

Figure 2.4: Variation of λ vs *Re* (adap. from Phinney [2]).

2.4 Dispersion and disintegration of liquid jets

Immiscibility occurs as a result of the cohesion forces between fluid molecules. How easily liquid jets can be mixed or not depends on the surface tension σ and the degree of turbulence intensity applied to one or both phases. The larger is the surface tension difference between a fluid *A* from *B*, e.g. $\sigma_A \gg \sigma_B$, the stronger the required mixing process [41].

In hydraulic engineering, high turbulence in the water because of high velocities (U > 20 m/s) of the flow plays a main role in the entrainment and detrainment of the air fraction. As a consequence, the bulk of the mixed flows increases, and depending on the level of air in the mixture and the geometry of the structures lead to unpredictable behavior of the flow results, requiring resizing the hydraulic structures for working under safe conditions.

In general, water jets can be classified mainly depending on the nature of the fluids that form and following their geometrical characteristics:

- Concerning the nature of the fluid a jet can be formed by a fluid that penetrates another fluid, with a density less, equal or higher than the jet expelled itself. Different cases can be present in nature: a water jet that penetrates into the air, like in the case of a waterfall; and a compact water jet that penetrates into a reservoir of water.
- In the case of the geometrical characteristics the main features are related to the symmetries of revolution and the symmetry of the plane. The geometrical parameters of the nozzle are crucial because their angles, curves and internal geometries impact the form of the jet, and as a consequence, it leads to a variability in the

forms of the ejected fluid and how it spreads. Additional effects arise when wall roughness is induced, as it has been studied by Heraud [42].

The dispersion is a phenomenon associated with the instability of the jet that can occur in the following ways [43]:

- Instability due the internal turbulence of the fluid associated with the kinetic energy κ of the particles that has a radial component of the fluctuations directed from the axis of the jet to the outside of the jet.
- Instability due the exchange of momentum between the liquid and the gas. However the inertia of the air is relatively so small and the action of the gas in relatively reduced.

The actions of instability previously mentioned are opposed by the stabilizing effect of the viscosity of the fluid which determines the turbulence of the fluid by dissipating the transverse kinematic energy of the jet. Furthermore, the surface tension damps the amplitude of the displacements of the particles in the surface interaction leading as a consequence to a mitigation of the dispersion of the fluid.

Oguey & Mamin [44] grounded on theoretical and experimental tests of the dispersion of high speed water jets in Pelton turbines found that jet dispersion essentially depends on the turbulence, *Re*, being the decisive similitude parameter. Moreover they found that the dispersion increases as the speed and the diameter of the jet increase and additionally confirmed that the effect of the air resistance is negligible [44]. Later Oguey et al. [45] confirmed the presence of a convergent water core region in the axis of the jet which is surrounded by a divergent air-water mixture.

Kozeny [46], based on experimental tests done by Farmer [47], established a relationship between discharge coefficients and static pressure in circular, quadratic and rectangular forms of an orifice or ejector of equal cross sectional area. Furthermore he noted the influence of the inlet conditions on the jet formation.

In the case of rectangular water jets in air, Horeni [48] found that the breakup length ($\overline{L}$) is a function of the Reynolds number:

$$\overline{L} = 7.8\ Re^{0.319} \tag{2.12}$$

Dodu [49] [43] developed experimental studies to analyse the dispersion of water jets at high velocities into air. For carrying out his studies, circular and convergent nozzles (with diameters up to 41 mm) were tested and the fluctuations of the dispersion were plotted in the form of normalized apparent mean radius versus the normalized streamwise coordinate ($\overline{r}/r_c$ vs x/r_c). Here $\overline{r}$ is the apparent mean radius, r_c is the radius of the jet at the contracted section, and x is the streamwise coordinate (in the measurement section).

Chen & Davis [50] performed investigations concerning the mechanism of disintegration of turbulent water jets in straight pipes and sharp-edged orifices. Based on considering the independent variables that influence the breakup of jets, such as the properties of the liquid, the mean characteristics of the water jet, the initial drop size, some

expressions were obtained by applying dimensional analysis and expressed in terms of the Weber number *We* and the Reynolds number *Re* which grounded the basis for the experimental investigations.

According to them, the resilience of the jet surface and the inertia forces of the internal turbulence are the two predominant forces in the moving jet, which are described by the Weber number *We*. The influence of the Reynolds number is noticed only in its connection with the change of flow. As a consequence they concluded that the Weber number alone should describe the phenomenon of jet disruption.

In Figure 2.5-a the experimental results for different liquids discharging vertically in still air from smooth pipe nozzles with an aspect ratio L_n/d = 100 are presented. $\overline{L}$ is the breakup length, L_n is the length of the nozzle, d is the diameter of the pipe, $\overline{L}/d$ is the relative breakup length and *We* (see eq. 2.5) is the Weber number.

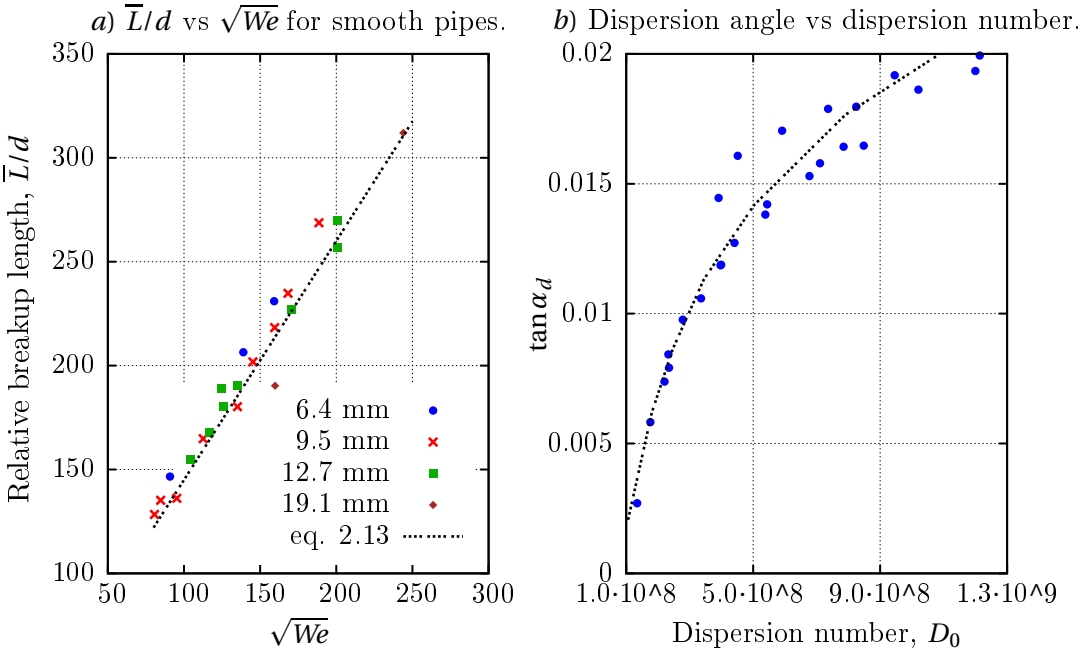

Figure 2.5: Experimental results of jet disintegration: a) adap. from Chen & Davis [50], and b) adap. from Hager [51].

Based on these experimental tests, Chen & Davis determined an explicit function for determining the length breakup and they suggested that the breakup distance ejected from pipes is independent of the viscosity, and the influence of the Reynolds number is negligible:

$$\frac{\overline{L}}{d} = 1.15 \cdot \frac{U_0}{\sqrt{\sigma/(\rho\, d)}} + 30 = 1.15\sqrt{We} + 30 \tag{2.13}$$

The constant value of 30, called *critical Weber number*, defines the lower limit of applicability of equation 2.13 for a turbulent jet. "*Physically, the critical Weber number is related to* $\overline{L}/D$ *in the same manner as the critical Reynolds number is related to the*

friction factor in pipes". In orifices, the Reynolds number suggests a great impact on the initial breakup distance, however in nozzle pipes it does not happen. It is worth mentioning that the term $U_0/\sqrt{\sigma/(\rho d)}$ in equation 2.13 is nothing else that $\sqrt{We}$. Chen & Davis mistakenly called this term the Weber number, and committing the same error on their diagram 2.5-a (here corrected) and the analysis throughout their paper.

By reanalysing Dodu's data, Hager [51] found for horizontal jets that the dispersion angle (or so-called spread angle) α_d=dr /dx thus depends on *Re, We* and the nozzle characteristics, as well as, for any given liquid, the dispersion angle α_d varies proportionally with the dispersion number $D_0 = Re^2/We$. However, it is worth mentioning that the last affirmation of proportionality is not valid at all because the dispersion number D_0 in his original plot is presented in a logarithmic scale on the x-axis and also the experiments are limited to a small range. In Figure 2.5-b the relationship between D_0 vs α_d is shown in an arithmetic scale.

Kraatz [3] developed equations and diagrams to determine the velocity distribution for vertical and throwing ranges of free circular water jets in still air at high velocities. Based on experimental he concluded that free circular jets are characterized through a flow core, which has the form of a slender paraboloid. Moreover, he found that the length of the flow core is difficult to establish because of the instability process at the end of the core zone. A schematic representation of the parameter involved in his analysis is shown in Figure 2.6.

According to Kraatz, the velocity distribution in the core region follows:

$$\frac{u_r}{U_0} = \exp\left[-\frac{1}{2C^2}\left(C + \frac{r - d/2}{x}\right)^2\right] \quad \text{for} \quad 0 < x < \overline{L}, \tag{2.14}$$

where u_r is the velocity at a distance r from the axis, U_0 is the velocity in the orifice, d is the diameter of the orifice, $C = 0.01$ is a constant obtained experimentally, x is the streamwise coordinate and r is the radial coordinate. The velocity distribution beyond the core is:

$$\frac{u_x}{U_0} = \frac{d}{2xC^2}\exp\left[-\frac{1}{2C^2}\left(\frac{r}{x}\right)^2\right] \quad \text{for} \quad \overline{L} \leq x \tag{2.15}$$

Nevertheless, equations 2.14 and 2.15 are only valid when the flow conditions fall into the region III of Figure 2.2. Likewise, the relative core zone length (nowadays called the breakup length $\overline{L}$) is given by

$$\frac{\overline{L}}{d} = \frac{5}{\left[\dfrac{\rho_a}{\rho}\right]^{0.345}} \tag{2.16}$$

where ρ is the density of the liquid jet and ρ_a is the density of the surrounding gas phase.

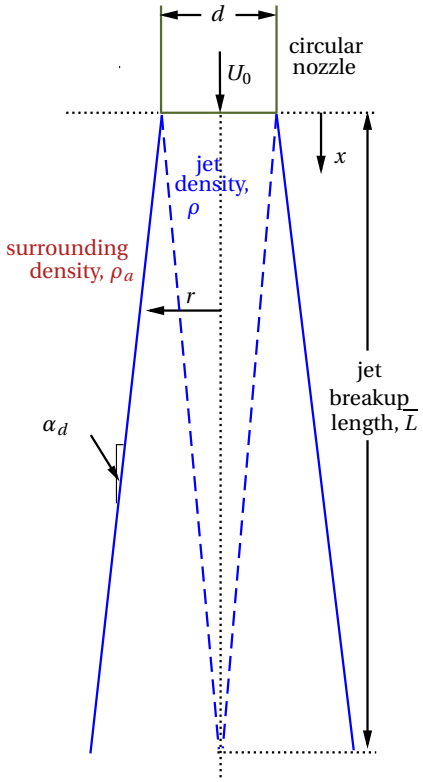

Figure 2.6: Schematic of a circular jet (adap. from Kraatz [3]).

In case of water and air at 20°C, $\rho = 998$ kg/m^3 and $\rho_a = 1.20$ kg/m^3 equation 2.16 reduces to $\overline{L}/d = 50.8$, but Kraatz [3] suggested that due to the turbulence of the emerging jet, values of $40 < \overline{L}/d < 60$ can be obtained. Furthermore Kraatz found that the practical achievable throwing range is greatest (called *maximal trajectory length*) by an inclination (or take-off angle) of $\alpha_n = 30°$ under a relative value $x/d = 3600$ which corresponds to a relative pressure head of $H/d = 7000$.

Di Silvio [4] compared geometrically similar water jets using Froude similarity laws in at a scale of 1:3, and documented the characteristic of the jets and the breakup phenomena by means of photography under low exposures times (1/50000 s). He remarked that the turbulent characteristics of the flow at the outlet depend on the geometry of the feeding conduit, as well as the inertial forces and the viscosity which are represented through the Reynolds number. However, if the Reynolds number is substantially increased, the turbulence will be independent of these parameters and the ratio of the mean square transverse component of the turbulence $\sqrt{\overline{u_i}^2}$ and the mean velocity u (known as the relative intensity of the turbulence in the three components) will depend on the form of the pipe at the outlet. The parameters previously described are shown in Figure 2.7.

Based on experimental tests of water jets discharging into still air Isachenko & Chanishvili [52] determined that the ratio of the cross sectional jet area $\alpha_j = A/A_0$ and the density ratio ρ/ρ_o vary as a function of the relative distance L_j/h_o according to the fol-

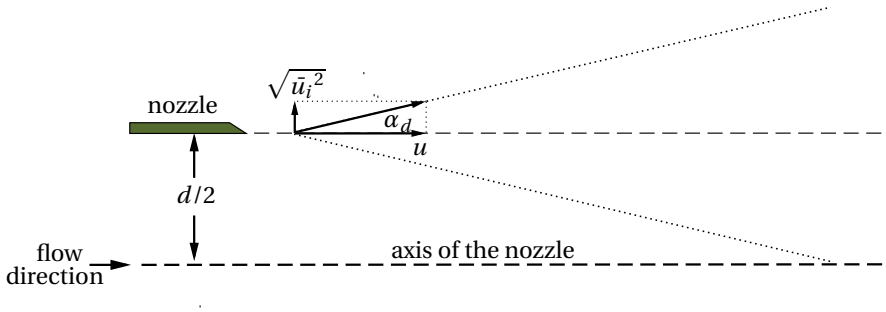

Figure 2.7: Dispersion angle of a jet (adap. from Di Silvio [4]).

lowing equation:

$$\alpha_j = \frac{A}{A_0} = 2.5\left(\frac{L_j}{h_0}\right), \tag{2.17}$$

where L_j is the distance of from the take-off and h_0 is the flow depth at the take-off section.

Heraud [42] experimentally investigated the influence of the wall roughness of nozzles in the dispersion of liquid jets. To carry out his experiments, smooth and rough nozzles of diameter d = 33 mm ejecting into still air were tested. The wall roughness in the nozzles was simulated by fitting regular serrated shapes of different heights (up to 0.3 mm) and lengths at the wall close to the outlet of the nozzle. Finally the statistical results demonstrated that far from the nozzle the free surface of the jet is influenced by the initial turbulence of the flow and does not depend on the modifications generated by the additional roughness in the ejectors. However, close to the nozzle, the roughnesses modify the jet free surface in terms of distance and amplitude that grows as a function of the flow velocity, the roughness height and the roughness length.

Baron (cited by Ervine et al. [11]) by using dimensional analysis found that the non-dimensional breakup length in the case of air and water is:

$$\frac{\overline{L}}{d} = 1.7\frac{We}{\left(10^{-4}Re\right)^{5/8}}. \tag{2.18}$$

In the particular case of inclined jets the large *throw distance* d_j is achieved with a *take-off angle* at a nozzle of 30° instead of 45°, and it can be significantly reduced by using a swirl nozzle, increasing the initial turbulence and the initial concentration of air. Likewise, jets of elliptical or other cross-sections have much smaller trajectory lengths than circular jets [51].

2.5 Description of the turbulent free falling water jet zones

In general a liquid jet is a column of liquid emerging from a nozzle into a quiescent gaseous atmosphere which breaks up in one or two stages: 1) *primary breakup* occurs when the jett's surface is torn into ligaments which, once peeled from the jet surface, transform or breakup into drops, and 2) secondary breakup takes place if these drops further break into smaller drops [10].

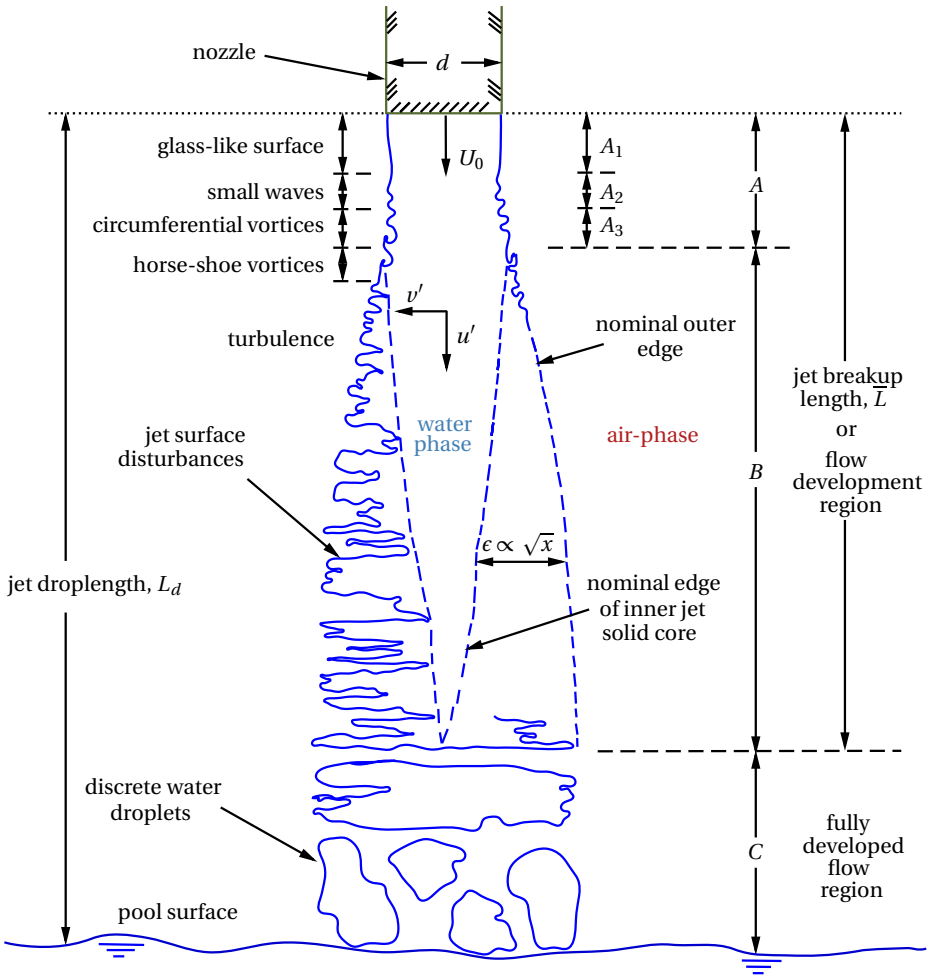

Figure 2.8: Schematic of plunging jet instability (adap. from Ervine et al. [5]).

According to Ervine et al. [5] a vertical plunging jet is characterized mainly by three zones which are shown schematically in Figure 2.8 and can be described as follow:

Zone A As soon as the liquid jet is expelled into the air the water has a glassy smooth surface where small waves start to appear because of the influence of the internal turbulence in the liquid. Along this zone the surface tension on the disrupted surface tries to return the water into the column of water and there is a constant

growing of instabilities on the water surface (zone A2). Afterwards, in the zone A3 there is a transition from surface waves into circumferential vortex elements.

Zone B This is a turbulent and chaotic zone which starts with the breakdown of the circumferential vortices and ends with the breakup of the jet. Along this region there is a dynamic interchange of air with the surrounding media. The air is entrained into a boundary layer surrounding the jet passing over the protuberance of the jet.

Zone C There is a massive formation of discrete water droplets or satellite droplets which trend to break up into smaller ones. At this stage the turbulence fluctuations have penetrated the core of the jet and the flow is not a continuous mass of fluid anymore. This has the consequence that the water is accelerated due to the gravitational force giving rise to a change of momentum within the jet by decreasing the effective jet diameter as it falls.

2.6 Influencing factors on the water jet breakup

Most of the parameters involved in the breakup process are related to each other but some factors may have a dominant influence and overshadow others. However, in the last decades it has been concluded that the main independent variables that modify the jet characteristics are the inlet conditions and the nozzle geometry. Recent studies of Birouk & Lekic [10] have confirmed this hypothesis and also that the nozzle geometry and the internal flow have a profound impact on the jet characteristics and its breakup.

Based on observations Grant & Middleman [6] suggested that there is not correspondence between the regime of a flow (laminar-transitional or turbulent) and the stability of the jet under similar conditions as it can be observed in Figure 2.9. In part [a] of that figure a laminar jet presents a bursting breakup and a less stable disintegration than a turbulent jet under similar conditions as can be seen in Figure 2.9-b. In spite of the instinctive suggestion that the turbulent jet will be more unstable than laminar jets, the experiments of Grant & Middleman confirmed that this is not entirely accurate and the turbulence has a stabilizing effect on the flow.

2.6.1 Surrounding media

Based on the experiments of Weisbach [53] [54] and Freeman [55], Neményi [51] [56] concluded that "(...) *the deviation between a water jet in air and the parabolic trajectory of a material point in a vacuum is insignificant for a compact jet. However, if the water disintegrates in the air, the length of trajectory is much less than the conventional calculation*". In the case of jets discharging into vacuum, Schuster [57] found the same jet texture and breakup characteristics as observed by Dodu [43] in jets discharging into air.

Rouse [58] emphasizes that the breakup is caused primarily by the internal turbulence of the jet and only secondarily by the action of the air. However, Falvey [16] remarks that any turbulent flow always disintegrates somewhere along its length if it is allowed to travel far enough, and the effect of the air becomes significant only after the jet atomizes

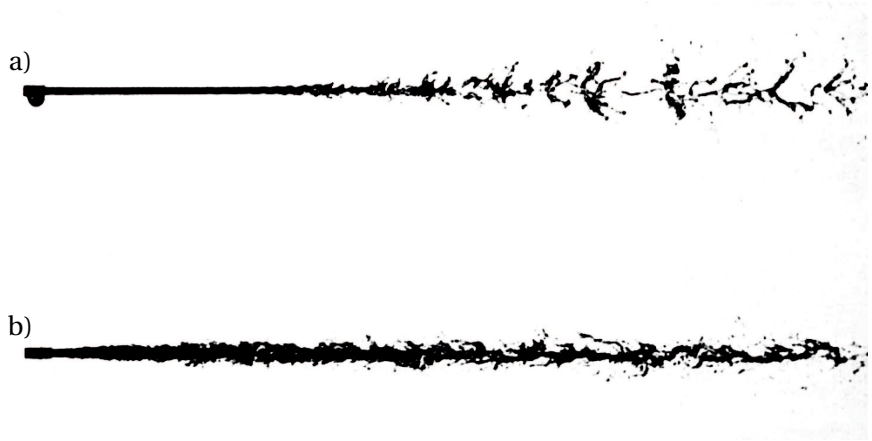

Figure 2.9: Jet breakup: a) laminar and, b) turbulent. From Grant & Middleman [6].

into individual drops (region C of Figure 2.8).

The surrounding medium has a deep effect on the atomization regime because if the gas inertia force is high, the liquid jet may break up into droplets, and at elevated pressures it will increase the unstable jet surfaces, as was observed by Hiroyasu et al. [35].

Fenn & Middleman [59] observed the stability of high speed laminar Newtonian jets under ambient air pressure. They found that for $We < 5.3$ the air pressure has no effect on the stability but for larger Weber numbers the aerodynamic forces become important and lead to a reduced stability of the jet.

It is important to remark that, over time, any jet will break up by the action of air friction alone and even the smallest surface disturbances will expose the jet to the aerodynamic effects and cause its eventual disintegration.

2.6.2 Water jet velocity

As has been previously described in Figure 2.3, when a liquid jet leaves the nozzle exit into the atmosphere, any of three flow regimes can occur, depending on the Reynolds numbers associated with the flow velocity: laminar, transitional and turbulent. The atomization, a dynamical consequence of the high velocity of the fluid is considered as the upper state of a fluid in the turbulent regime.

Based on experiments and literature review Schweitzer [34] and McCarthy & Molloy [33] considered that the jet velocity and the level of turbulence are the main factors that affect the disintegration of a liquid jet.

For a laminar flow regime the velocity distribution at the nozzle exit adopts a parabolic profile (because of the no-slip condition inside the nozzle) with a maximal velocity located at the center or axis of the nozzle. In accordance, as the flow velocity is increased and the turbulent regime is reached, the velocity profile will tend to be flattened along

the cross section [7] [60] as shown in Figure 2.10.

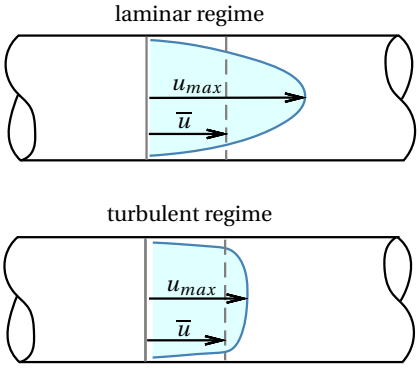

Figure 2.10: Comparison of laminar and turbulent velocity profiles (adap. from White [7]).

The influence of the liquid jet velocity on the jet breakup becomes more clear in the jet instability curve shown in Figure 2.3. Here the continuous increase on jet velocity implies changes in the flow regime (from laminar to turbulent) and different values of the breakup length $\overline{L}$.

2.6.3 Level of turbulence at the nozzle exit

For turbulent flow, because of the fluctuations, the velocity u is a rapidly varying random function of time and space [7]. Due to instantaneous fluctuating variables cannot provide a mathematical solution to problems, a statistical approach leads to the concept of average or mean values of the velocity u in the components x, y and z such as u_x, u_y and u_z respectively.

The time mean $\overline{u}$ of a turbulent function $u(x,\ y,\ z,\ t)$ is defined by

$$\overline{u} = \frac{1}{T}\int_0^T u\ dt \tag{2.19}$$

where T is an averaging period taken to be longer than any period of the fluctuations themselves. Likewise, the fluctuation u' is defined as the deviation of the velocity from its average value U.

$$u' = u - U \tag{2.20}$$

In each direction x, y and z the corresponding fluctuations u'_x, u'_y and u'_z can be computed as well. Likewise, the turbulent fluctuation of the flow velocity u' is defined as,

$$u' = \sqrt{u'^2_x + u'^2_y + u'^2_z}. \tag{2.21}$$

As consequence, the root mean square value (index *rms*) of the velocity fluctuations u_{rms} is defined as:

$$u_{rms} = \sqrt{(u')^2}, \tag{2.22}$$

The *turbulence intensity* or turbulence level Tu is defined as the Root-Mean-Square of the turbulent velocity fluctuations (or turbulence strength) at a particular location over the average of the velocity u in a specified period of time:

$$Tu = \frac{u_{rms}}{U} = \frac{\sqrt{(u')^2}}{U}, \tag{2.23}$$

The turbulent kinetic energy is defined as:

$$\kappa = \frac{1}{2}\rho u'^2, \tag{2.24}$$

where ρ is the density of the water.

Ervine & Falvey [8], based on studies over jets issued into air, measured the longitudinal turbulence intensity Tu by means of a laser doppler velocimeter, and concluded that the turbulence is the most important air-entrainment mechanism because it determines the degree of lateral spread and the rate of inner core decay of the jet. Furthermore they suggested that the surface undulations of the jet exhibit a fine-grained turbulent structure superimposed on larger underlying eddies.

Based on experiments on orifices ejecting into still air, Ervine & Falvey [8] found experimentally that the rate of jet spray obeys the following relationship with the parameter involved in the spreading of a turbulent jet schematized in Figure 2.11:

$$\frac{\delta_2}{x} = 0.38\frac{u'_x}{U_0}, \tag{2.25}$$

where δ_2 is the lateral spread of the jet, x is the distance from the orifice, and U_0 is the average velocity at the nozzle exit. Likewise, based on analysis of the *jet core decay* they defined the parameters δ_1 and δ_c shown in Figure 2.11.

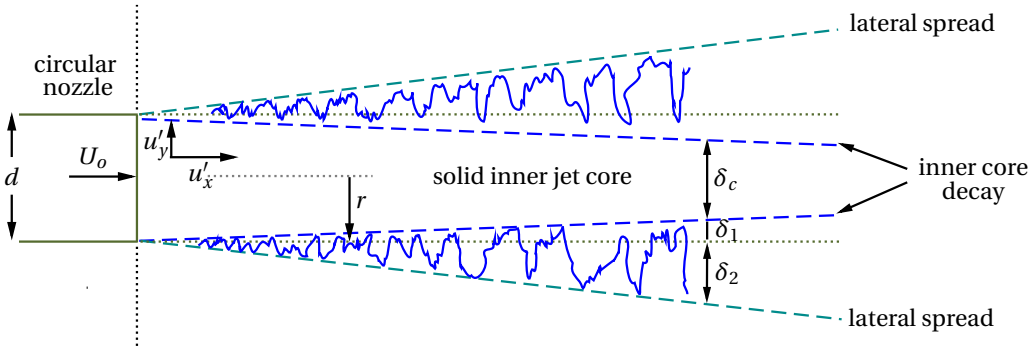

Figure 2.11: Spreading turbulent jet discharging horizontally (adap. from Ervine et al. [8])

Experimental test and mathematical analysis demonstrated that jet breakup length is given when the *inner core* (δ_1/x) decays completely, taking into account that it can be

as small as 0.5 to 1%,

$$\frac{\delta_1}{x} \sim \frac{1}{2} \div 1\% = \frac{d/2}{\overline{L}}. \tag{2.26}$$

As a consequence, the relative jet breakup length is given by:

$$\frac{\overline{L}}{d} \sim 50 - 100. \tag{2.27}$$

As can be observed in Figure 2.12 for a plunging jet with $d = 25$ mm and a variation of the turbulence intensity between 3% and 8%, the relative jet breakup length roughly varies between 50 and 100.

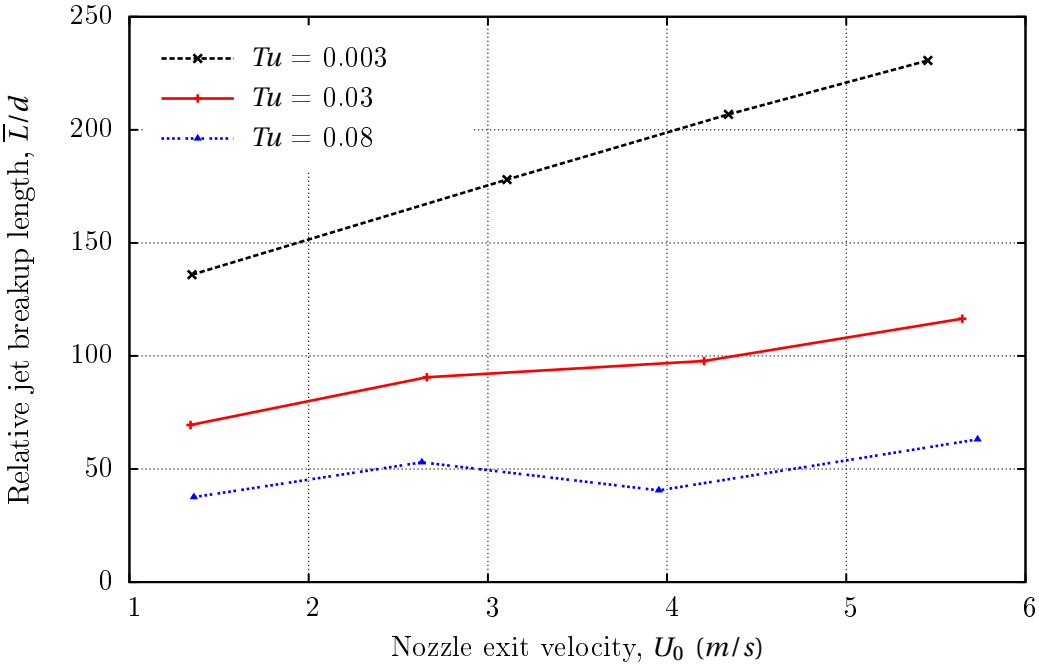

Figure 2.12: Variation of jet breakup length with turbulence intensity for a nozzle diameter $d = 25$ mm discharging horizontally (adap. from Ervine & Falvey [8])

In essence, Ervine & Falvey proposed a criterion for estimating the onset of free surface aeration expressed in the form of jet velocity, which could be applied to other situations involving free surface aeration:

$$U = \frac{0.275}{\frac{u'}{\overline{U}}} = \frac{0.275}{Tu} \tag{2.28}$$

Lately, Ervine et al. [11] by measuring the length breakup and the turbulence intensity of four nozzles discharging into quiescent air found that in very turbulent jets the breakup length is almost independent of the velocity. Likewise, the velocity has an increasing effect, for less turbulent jets. As a consequence they concluded the following:

- The spread angle is dependent on the initial turbulence for a particle of fluid at the edge of the jet:

$$\frac{u'_y}{U_o} \sim (0.4 \div 0.5\%) \frac{u'_x}{U_o} \tag{2.29}$$

- The inner decay angle can be determined once the angle of spread is known.

Ervine et al. [5] proposed a turbulence parameter which is defined as $C_E = 1.14\ Tu\ Fr^2$. After some mathematical considerations they proposed an equation to estimate the jet breakup length $\overline{L}$,

$$C_E^2 = \frac{1}{\left(\frac{2\overline{L}}{d \cdot Fr^2} + 1\right)\left(\sqrt{\frac{2\overline{L}}{d \cdot Fr^2} + 1} - 1\right)^2}, \tag{2.30}$$

shown in Figure 2.13, which additionally is compared with experimental results of Baron [61], McKeogh [62] and Whiters [63] at various turbulence levels. The best fit based on the experimental test is also observable in Figure 2.13.

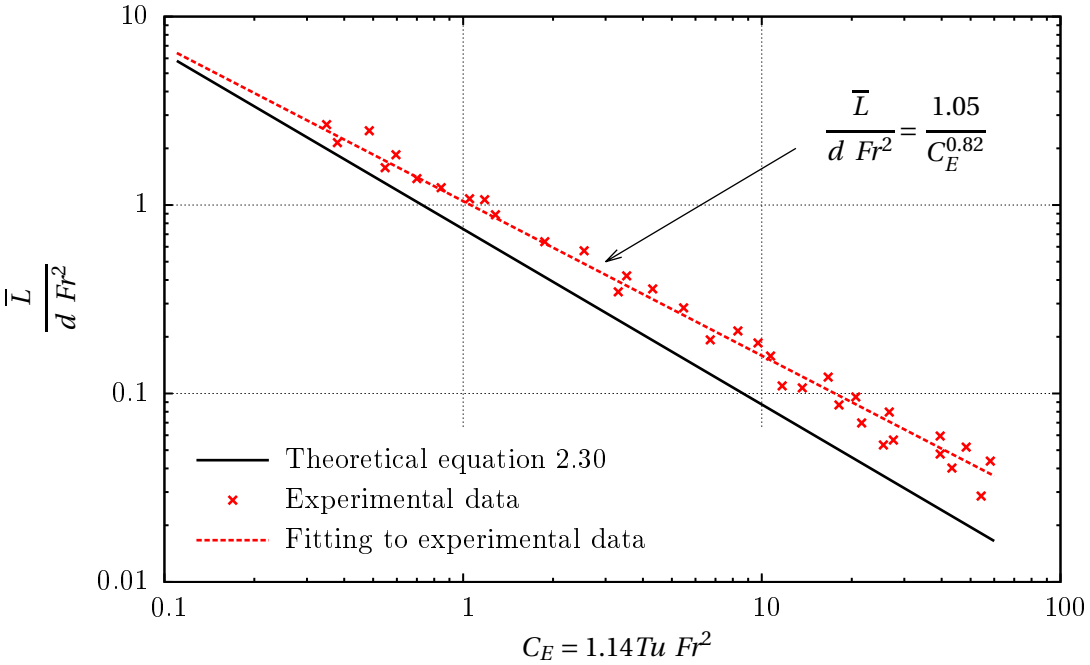

Figure 2.13: Comparison of theoretical and experimental tests for determining the jet breakup length $\overline{L}$ on circular nozzles (adap. from Ervine et al. [5])

According to Chanson [9] the onset condition of air bubble entrainment occurs when the turbulence shear stress is greater than the capillary force per unit area resisting the surface breakup. Considering an elongated spheroid, a criterion for the onset of free-surface aeration in terms of the magnitude of the instantaneous tangential Reynolds

stress, the air/water physical properties and free-surface deformation properties yield,

$$|\rho_w v_i v_j| > \sigma \frac{\pi\left(r_1 + r_2\right)}{A}, \tag{2.31}$$

where ρ_w is the water density, v is the instantaneous turbulent velocity fluctuation, (i, j) is the directional tensor (x, y), $\pi(r_1 + r_2)$ is the perimeter along which surface tension acts, r_1 and r_2 are the two principal radii of curvature of the free surface deformation, and A is surface deformation area. For a three-dimensional flow with quasi-isotropic turbulence, the smallest interfacial area per unit volume of air is the sphere (radius r). As a consequence the onset of spherical bubble entrainment yields from equation 2.31:

$$|\rho_w v_i v_j| > \frac{\sigma}{2\pi r} \tag{2.32}$$

Along an air-water interface the air-bubble entrainment process takes place usually parallel to the flow direction and the entrained air bubbles are advected in the shear flow. In Figure 2.14 the primary breakup and the spray ejection of a jet has been photographed by Hoyt & Taylor [64], and the schematic representation of the air concentration C, velocity distribution U and the bubble count rate F of Chanson [9] is presented in Figure 2.15. Where the bubble count rate F is defined as the number of bubbles crossing certain point during a lapse of time.

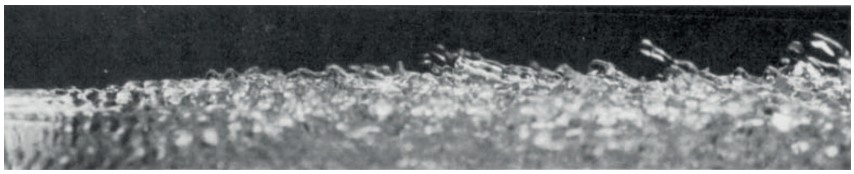

Figure 2.14: Amplified wave break and spray ejection at zero air velocity for $d = 6.35 \times 10^{-3}$ m and jet velocity of 25.3 m/s (from Hoyt & Taylor [64]).

2.6.4 Nozzle geometry

A nozzle is an attachable element designed in order to achieve particular characteristics of a fluid and to control the direction of a fluid flow as it exits an enclosed chamber or pipe. In general when a nozzle is narrowing down from a wide diameter to a smaller diameter in the direction of the flow it is called *convergent*, otherwise in the case of an expansion from a smaller cross section to a larger one are referred as *divergent*. In some cases the nozzle is the pipe itself, being called a *pipe nozzle*.

Birouk & Lekic [10] proposed a unified criterion concerning the technical and specialized terms employed for describing converging (or so called cone-up) nozzle features and its nomenclature with the purpose of clarifying and unifying the difference of concepts and the inconsistency of definitions throughout the scientific literature generated in the past decades. In Figure 2.16 the features and nomenclature concerning converging nozzles, extended to sudden contraction nozzles is shown.

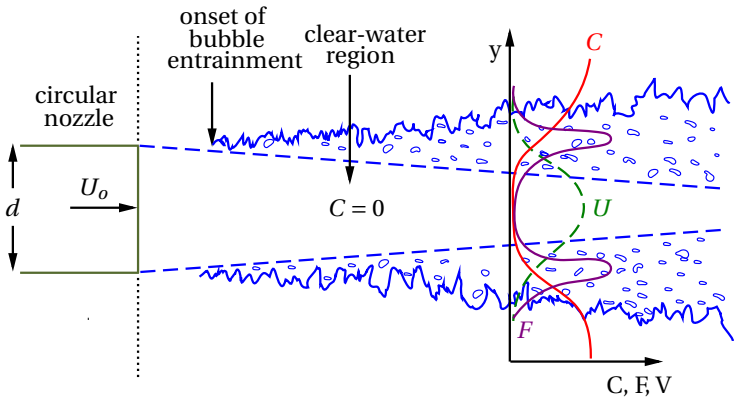

Figure 2.15: Interfacial aeration in a water jet discharging into air (adap. from Chanson [9])

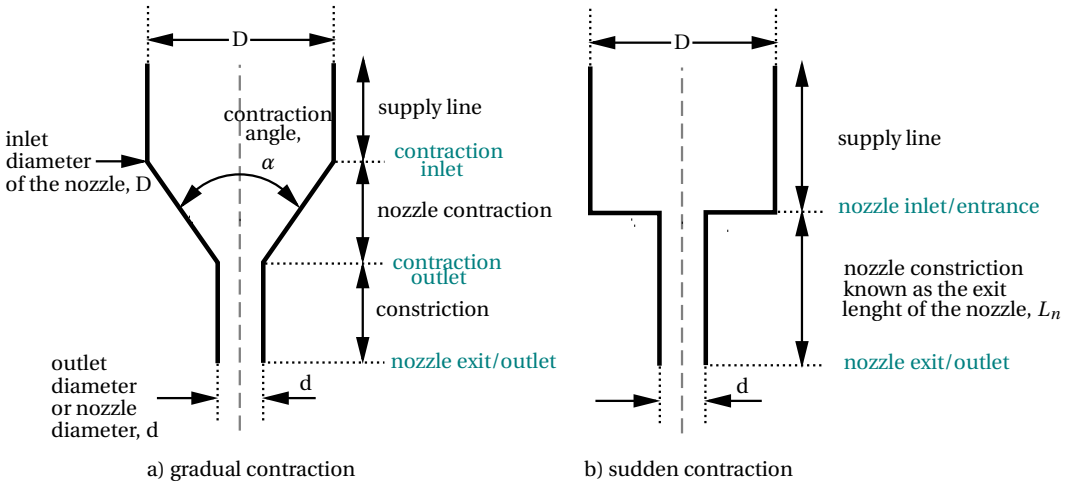

Figure 2.16: Nozzle features (adap. from Birouk & Lekic [10]).

In Table 2.1 the description and nomenclature of the nozzle geometry parameters as the contraction ratio, aspect ratio, contraction angle, streamlining and the surface roughness are summarized. *Streamlining of the nozzle interior* refers to the degree of rounding present at the nozzle inlet having a pronounced effect on jet exit conditions and on jet breakup. Moreover, the streamlining has a remarkable effect on the cavitation potential when high velocities occur. Concerning the surface roughness or surface quality, $S.Q.$, of the nozzle it refers to the largest microscopic disturbance of the nozzle walls, $S.R.$ divided by the outlet diameter d [10].

In Table 2.2 some relevant studies concerning geometrical parameters affecting the compactness of a liquid jet are compiled.

nozzle geometry parameters	symbol	equation
contraction ratio	C.R.	$\frac{d}{D}$
aspect ratio	A.R.	$\frac{L_n}{d}$
contraction angle	α_n	
streamlining	S.L.	
surface quality (roughness)	S.Q.	$\frac{S.R.}{d}$

Table 2.1: Nozzle geometry parameters.

2.6.5 Cavitation and supercavitation

Cavitation is defined as the breakdown of a liquid medium under very low pressures [66]. At high velocities, when the flow nears the *nozzle contraction*, the static pressure reduces in the *contraction outlet* triggering the occurrence of the phenomena of cavitation if certain conditions are given: critical restriction of the cross sectional area (narrow passages) or due to curvatures imposed on the flow streamlines by the local geometry (bends and sharp edges in the *contraction outlet*). If a high *contraction angle* and high velocities are present, the liquid will detach from the nozzle wall at the *nozzle constriction* and a *vena contracta* will be present in the axis of the constriction nozzle. As a consequence a cavity in the detached region will arise, because of the low pressure of the liquid, which will be composed mainly of *cavitating bubbles*. If the flow separation extends beyond the nozzle exit it will be called fully detached (separated) flow. Otherwise if the constriction is long enough the cavitating flow can re-attach in the constriction. Depending of its use in industry, a *fully detached flow* or a *cavitating flow* will be favored.

As has been previously mentioned, the nozzle geometry has a predominant impact on the water jet disintegration and the cavitation plays a strong influence on it by reducing the breakup length $\overline{L}$, increasing the spray angle and increasing the potential for damage of the *nozzle constriction*. Hiroyasu [36] compiled the effect of the nozzle streamlining over the jet breakup length, finding that round-edge nozzles (referred to the internal corner in the nozzle inlet in Figure 2.16) after the breakup length of a cavitating jet discontinuously elongate beyond the breakup length of a noncavitating jet. This sudden change in a jet's breakup behavior is called *hydraulic flip* or *supercavitation*.

A review of numerical calculations on cavitation flows in nozzles' orifices has been done by Dabiri et al. [67].

Parameter	Author	Year	Findings
C_r	R. Grant & S. Middleman [6]	1966	Reported hysteresis process when Re is increased and decreased because of hydraulic flip. For the same Re there are two different $\overline{L}$.
	M. Arai, M. Shimizu & H. Hiroyasu [38]	1985	Generally C_r does not affect the trend of the jet stability curve. Increasing $d \longrightarrow$ decreases $\overline{L}$
	M. McCarthey & N. Molloy [33]	1974	Decreasing $C_r \longrightarrow$ decreases the level of turbulence.
	S. Spangelo, N. Lekic, S. Fabro & M. Birouk [65]	1991	Decreasing $C_r \longrightarrow$ increase the level of turbulent.
A.R.	H. Hiroyasu, M. Arai & M. Shimizu [37]	1991	Increasing A.R. $\longrightarrow$ shorter $\overline{L}$. This is explained because of flow reattachment and wall friction.
	T. Karasawa, M. Tanaka, K. Abe, S. Shiga & T. Kurabayashi	1992	Longer nozzles generate more friction, more turbulence and thereby shorter $\overline{L}$. However when A.R. ≈ 50 the flow is fully developed and more stable. When A.R. ≈ 5 the best atomization can be achieved.
	S. Spangelo, N. Lekic, S. Fabro & M. Birouk [65]	1991	Decreasing A.R. $\longrightarrow$ flattens the velocity profile, thus generating a less turbulent jet.
α	T. Karasawa, M. Tanaka, K. Abe, S. Shiga & T. Kurabayashi	1992	$\alpha_n = 180^\circ$ is more suitable for atomization.
S.L.	H. Rouse, J. Howe & D. Metzler [58]	1952	The transition between the nozzle contraction (converging) and the constriction should be rounded for the elimination of eddies.
	M. McCarthy & N. Molloy [33]	1974	Smoothing the internal edges reduce flow separation and turbulent eddies of the flow.
	R. Reitz & F. Braco	1982	Rounding the inlet of short nozzles has a stabilizing effect on the jet
$S.R.$	K. Ramamurthi, K. Nandakumar, S. Shankar & R. Patnaik	2001	Remark that nozzle fabrication techniques could affect the experimental results.
	J. Chang, S. Huang, & C. Lin	2006	Found that the surface roughness, texture and material do not have an effect on cavitation. Internal flows within smaller-diameter nozzles are more susceptible to a variation in surface.

Table 2.2: Review by different authors of the parameters affecting the compactness of a liquid jet.

2.7 Air velocity distribution

The velocity measurements of air which moves in the direction of the jet and which lies near the nozzle at the periphery of the jet has been studied by Dodu [43]. He concluded that the air flow around the jet can be represented as a logarithmic distribution and it depends on the velocity of the liquid jet and the surface roughness. Falvey [16] suggest that the air distribution should follow the equation 2.33:

$$\frac{U_o - u_a}{u*} = f\left(\frac{y_a - r}{\delta}\right) \tag{2.33}$$

where u_a is the air velocity at a distance from the water surface y_a, $u*$ is the shear velocity, r is the water jet radius and δ is the boundary layer thickness. Although this equation has been proposed, it lacks experimental validation.

According to Ervine et al. [11] the rate of air entrainment Q_a in a circular jet depends on the jet velocity U_0, the diameter of the jet d, the grade of turbulence Tu, the growth of the jet roughness ε/r as it falls and the breakup length of the jet $\overline{L}$. The previous variables are shown in Figure 2.17, where r is the effective radius at any point along the jet radius and ε is the horizontal distance between the edge of the nozzle exit and the undulations of the jet. The ratio ε/r is known as *surface roughness*.

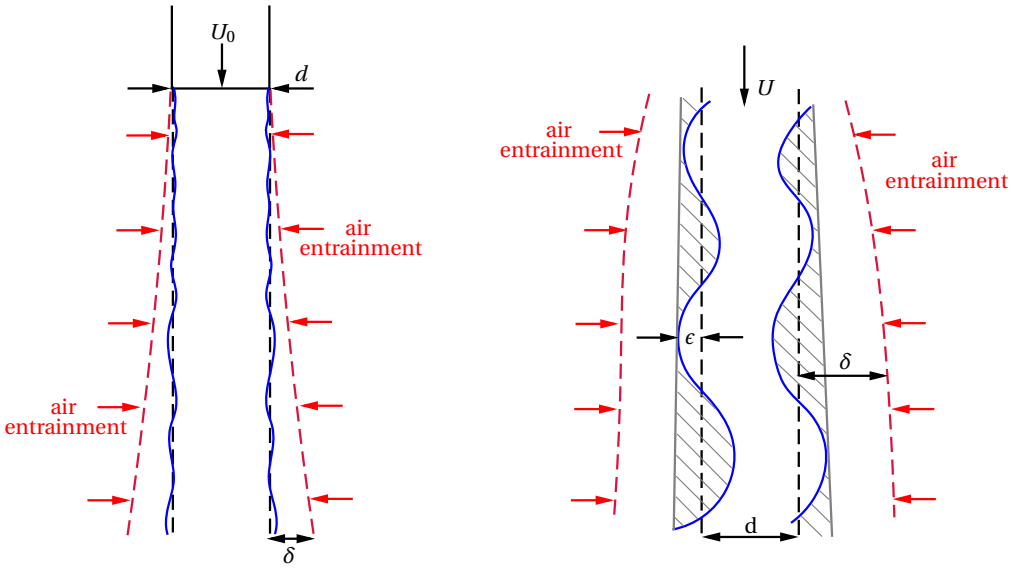

Figure 2.17: Air entrainment within surface ondulations (adap. from Ervine et al. [11]).

Likewise after a mathematical analysis they concluded that the the rate of air entrainment Q_a is proportional to the jet velocity at impact V and the degree of surface roughness ε/r. Moreover the ratio Q_a/Q_w, where Q_w is the water discharge, follows the

equation:

$$\frac{Q_a}{Q_w} = 1.4 \left[\left(\frac{\varepsilon}{r} \right)^2 + 2 \left(\frac{\varepsilon}{r} \right) - 0.1 \right]^{0.6} \tag{2.34}$$

2.8 Theoretical approximations of the jet breakup

The first attempt to describe the jet breakup consisted in approximating the surface of the jet by a sinusoidal wave, so-called surface wave instability theory. However such a theoretical description has been invalidated by experimental observations of irregular surface waves by Chigier and Reitz [10] [68].

Birouk & Lekic [10] stated that the aerodynamic theories, based on the aforementioned early theories, predict that short waves appear as the liquid leaves the nozzle, and subsequently the gaseous ambient amplifies the growth of waves. Despite experiments supporting these concepts, they have not yet been included or incorporated into any successful theory [10].

Many studies have considered that the level of turbulence, the velocity profile, the nozzle geometry, the aerodynamics effects, the liquid and gas properties, nozzle cavitation and supply line are the main variables affecting the jet breakup, however, they have been partially mentioned or ignored in the literature and mathematical formulations. As has been already mentioned, the failure of any theory owes much to the large number of variables that influence jet behavior, and also due to the complex interaction between them.

2.9 Hydraulic physical models: air-water mixture issues

Hydraulic physical modeling, or simply a *model*, is a representation (generally scaled) of the real world (herein *prototype or full-scale installation*) used as a tool for investigating, design and finding an optimal solution, offering many advantages concerned with replicating many features of a complex situation in hydraulic engineering [69] [70] [71].

Proudovsky [72] stated that the models represent the phenomena of the material world having the characteristics similar to those of the prototype and they also may correspond to its prototype in different ways, so called *similarity* [72]. Furthermore the rules for selection or building models are derived from the third theorem of the similarity theory, which states that the phenomena are similar if:

- Model and prototype are described by the same system of normalized equations
- The conditions of the equations unambiguity for the model and the prototype are similar, and
- The dimensionless groups for model and prototype are equal.

The similitude principles that form the basis for hydraulic modeling are fairly straightforward and the shortcomings in models are termed as *scale effects* or *laboratory effects* [70], which concern the impossibility of fulfilling all the similitude criteria (Kobus

[73]). An appropriate selection of the size of the model is an economical and technical optimization, where scale effects cannot fully be neglected. To fulfill the model-prototype similitude it must satisfy the following conditions: geometric similitude, kinematic similitude and dynamic similitude [70]. In order to satisfy geometric similitude, all length scales L_r must be equal, where the dimension of length is represented as L and the subscripts r, p and m represents ratio scale, dimension in the prototype and dimension in the model. As follows, the following convention for geometric similitude will be adopted:

$$L_r \equiv \frac{L_p}{L_m} \tag{2.35}$$

where L_r is the length scale ratio, L_p is the length dimension in the prototype (full-scaled) and L_m is the length dimension in the model-scale value.

Heller [69] remarks that considerable differences between up-scaled model and prototype parameters may result, due to: a) *model effects*, originating from the incorrect reproduction of prototype features such as geometry (2D modeling or reflections), flow or wave generation techniques or fluid properties; b) *scale effects*, arising due to the inability to keep each relevant force ratio constant between the scale model and its real-world prototype, and c) *measurement effects*, including non-identical measurement techniques used for data sampling in the model and prototype.

The complexity of modelling air-water mixtures lies in the dynamic interchange of gas volume, the mass interchange in the case of expansion and contraction, and the difference of velocity of each phase during the convection processes. Ettema [70] remarks that the hydraulic modelling of air-water flows is fraught with more problems than the modeling of free-surface flow, for which explicit satisfaction of Froude and Reynolds number similitude is not possible, and modeling primarily relies on Froude number similitude. The Froude number similarity criterion prescribes:

$$Fr_r = \frac{Fr_p}{Fr_m} = c\frac{U_r}{\sqrt{L_r}} = 1 \tag{2.36}$$

As follows, the main concerns about hydraulic modelling of air-water mixtures are:

1. Water and air are the fluids used in the prototype as well as in the the model. Kobus [19] added that as a consequence of using the same fluid a perfect dynamic similarity cannot be achieved since the modelling parameters derived from dimensional analysis cannot be satisfied simultaneously in a small scale model.

2. Ettema [70] remarks that considerable uncertainty arises in the interpretation of model results.

3. The impossibility of satisfying simultaneously two or more similarity laws between model and prototype.

4. The velocity of the liquid for initiating air entrainment in models is in general below the critical velocity required to entrain the air bubbles into the liquid.

5. The bubble diameter is the same in prototype as well as in the model.

In the case of water jets discharging into still air, the independent variables can be neglected, because they will be invariable and unchanged. Furthermore the initial conditions of the jet at discharge can be reduced to pipe diameter and mean discharge velocity. For highly turbulent jets, the disintegration process is completed before the jet is affected appreciably by gravity.

A number of dependent variables can be considered in describing the disintegration of a water jet:

- length,
- amplitude,
- wavelength of the surface disturbances on the continuous stream of the jet, or
- length of the continuous jet.

The kinetic energy of turbulence κ is a dominant factor in causing the instability of the jet and as a consequence the initial breakup point should have the same basic physical characteristics of turbulence.

In agreement with Ettema [70], it is necessary to recognize the possible effects of incomplete similitude, to choose the model scale with discernment, and then to interpret and scale up the final results with caution. In essence, the air bubbles formed from orifices (as well as from free-surface breakup) will often be of comparable size in model and prototype, and clearly not be equal to the scaling ratio.

The surface tension is also another relevant parameter in scaled models and its dominant action in the model may cause larger relative air bubble sizes and faster air detrainment, resulting in smaller volume fractions of air [74]. An essential, frequently mentioned point is that air bubbles formed from orifices (as well as from free-surface breakup) will often be of comparable size in model and prototype, and clearly not be equal to the scaling ratio.

As stated by Chanson [9] as the air bubble size is not correctly scalable, the phenomena including air flow have to be modelled at a relatively large scale to avoid significant scale effects. Heller [69] remarks that the air entrainment may also be a function of the atmospheric pressure (in dimensionless form an Euler number), which would have to be scaled to the miniature universe to achieve an exact model.

Wisner [75] investigated the role of using the Froude similarity law after the divergence of results of models and prototype for determining the air entrainment in hydraulic structures by means of using models at different scales, and based on a supposed analogy between the transport of solids in suspensions and air bubbles. Afterwards he found the incompatibility of these criterion.

As has already been described before, the deformations and the collapse of the liquid surface will put up resistance by the viscous forces and the surface tension. Therefore,

it would be expected that in the case of comparing two jets related by a Froude similarity law, the under-scaled one will be relatively less disrupted and disintegrated than the biggest one [4]. Di Silvio [4] at comparing model and prototypes of bottom outlets with different scales L_r suggested that the Froude similarity law $Fr_r = 1$ seems to provide a satisfactory reproduction of the global aeration in the flow, but however in general aspects it varies as well as the scale change, producing in big models more aerated flows (bulked flows) than in smaller models. Based on his experiments he concluded that the scale effects in under-scale models can be attenuated by introducing further turbulence in the model and the Froude similarity law does not represent completely the disintegration phenomena of water jets.

Heller [69] illustrated this phenomenon in Figure 2.18 where a parallelism is shown between a prototype corresponding to an overflow spillway and its corresponding physical under scaled model (scale 1:30).

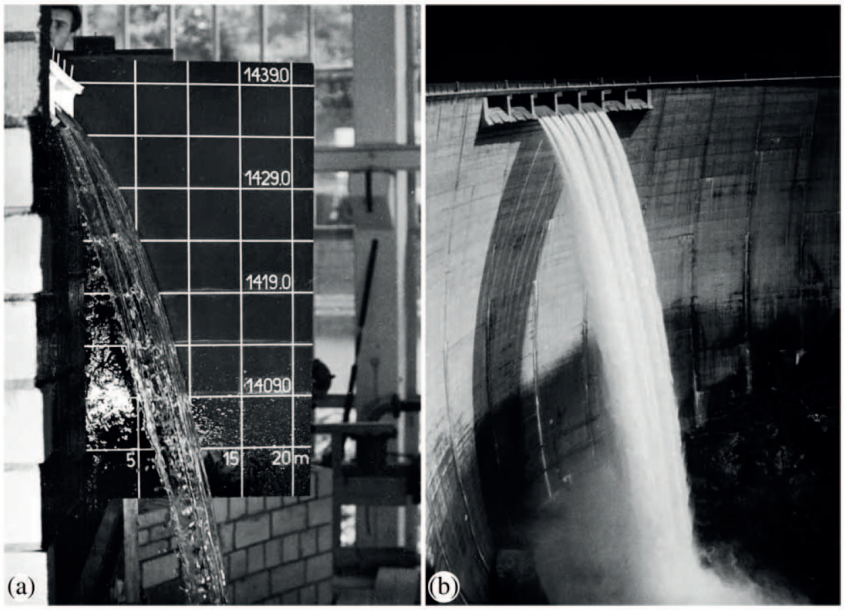

Figure 2.18: Overflow spillway of Gebidem dam, Switzerland: (a) physical hydraulic model at scale 1 : 30 (VAWFoto 03-21-20), (b) real-world prototype in 1967 (VAWDia 8870). Source: Heller [69].

Falvey [16] also mentioned that when model and prototype test are compared, the prototype jet apparently is surrounded by much more spray than the model. He justified this difference by the fact of using *time scale* relations between the two jets.

Ervine et al. [11] remark that the phenomenon of breakup of liquid jets is a "(...) *complex non-linear hydrodynamic and aerodynamic situation which is difficult to express in mathematical terms*". However they suggested that the major relations impacting the

disintegration of jets after using dimensional analysis are:

$$\frac{\overline{L}}{d} = f\left[\frac{\sqrt{\overline{u'^2}}}{U},\ Re,\ We,\ Fr,\ \frac{\varepsilon}{d},\ Re_L\right] \tag{2.37}$$

where ε/d is the surface disturbance and Re_L is a measure of air resistance when the jet surface is very smooth.

Ervine & Falvey [8] highlighted the great difficulty in modelling turbulent jets discharging into the atmosphere because in Froude models of free jets there are missing processes which are dependent on Weber *We* and Reynolds numbers *Re* and they cannot be simulated simultaneously.

Kobus [19] emphasizes that the complete similarity requirements for hydraulic models in the case of modelling free surface flow with air entrainment increase the restrictions to a under-scaled model of geometric similarity and then it reduces to equation 2.38. Then the scale effects are embedded in the fact that the Froude number is kept in the model and the Reynolds number is not modelled correctly, and hence neither are the turbulence characteristics: turbulence intensity and turbulent energy spectrum of the flow.

$$\beta = f\left(Fr,\ Re,\ Tu\right) \tag{2.38}$$

2.10 Computational Fluid Dynamics (CFD) of free surface flows

The numerical calculation of multi-phase flows is concerned with the capabilities of the methods to predict the topology and the effects of the fluid-fluid interface in an *Eulerian method of description* of the flow pattern: for certain variable ξ its field $\xi(x, y, z, t)$ is depicted and not the changes of a variable $\xi(t)$ which a particle experiences as it moves through the field.

The Eulerian-Eulerian model is appropriate for modeling multiphase flows involving gas-liquid or liquid-liquid flows, for example, droplets or bubbles of the secondary phase dispersed in the primary or continuous phase. The phases mix or separate and the secondary phase volume fraction can vary anywhere between 0 to 100%. Practical application of the Eulerian-Eulerian model would be to evaporation, boiling, separators and aeration. The Eulerian multiphase model is inappropriate for modeling situations where an accurate description of the interface boundary is important, in the case of stratified flows and free surface flows.

Actually the modelling of segregated type flow of the air-water interfaces has become a challenge because of the difficulties of tracking the movable boundary during the simulations. In Figure 2.19 the classification of immiscible fluids according to the interfacial structures is shown. Here, a liquid contained in a tank is shaken and, as well the frequency f (s^{-1}) increases, three types of fluids are obtained: static condition, segregated flow, transitional or mixed flow and disperse flow. To overcome these difficulties, several methodologies for predicting the free surface have been implemented by using static and

dynamic meshes. In the case of static meshes, the initial grid does not change during the simulations and the free surface is followed or captured. Otherwise, the dynamic mesh involved the adaptability of the mesh during the simulation with the purpose of refining it on the interface and its surrounding and as a consequence capture the details of the phenomena.

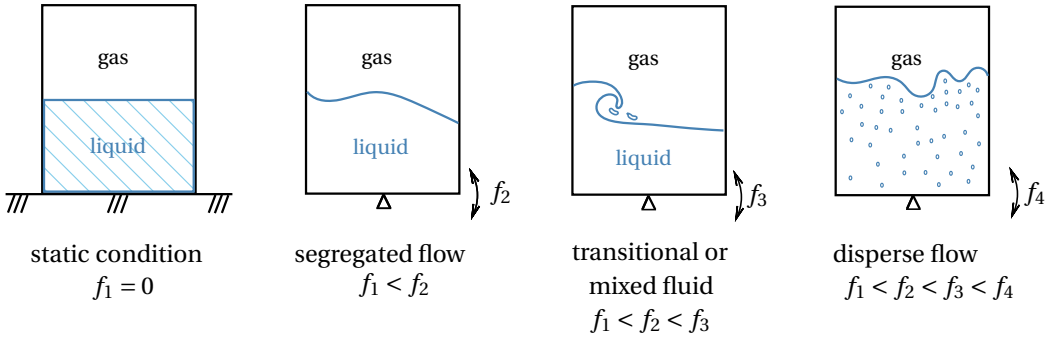

Figure 2.19: Classification of immiscible fluids according to the interfacial structures.

Many methods have been used to find the shape of free surface and they can be classified into the following major groups (Ferziger & Peric [76], Rusche [12]):

- *Interface-tracking methods*, the free surface is treated as a sharp interface whose motion is followed. Here boundary-fitted grids are used and advanced each time the free surface is moved.
- *Interface capturing methods*, the free surface is not defined as a sharp boundary and its shape is obtained by computing the fraction of each near-interface cell that is partially filled. The *Marker-And-Cell* or *MAC* scheme, proposed by Harlow & Welch (1965), falls into this group and it consists in defining massless particles at the free surface from the beginning of the simulation ($t = 0$) and following their motion. Another method which fall into this group is the *Volume-of-Fluid* or VOF scheme (Hirt & Nichols, [77]) where the transport equation for the fraction of the cell occupied by the liquid phase is solved.

In Figure 2.20 the different methods of representing the interface are shown.

2.10.1 Volume of Fluid Method

The Volume-of-Fluid (VOF) method marked a new trend in the simulation of multiphase flow by implementing an indicator function F whose value represents the fractional volume of a cell occupied by a fluid. In the particular case of a cell filled by a fluid a unit value of F will be obtained, otherwise it will get a value of zero. For values in between, a free surface will appear, and a line cutting the cell can be constructed which approximates the interface thereby knowing the normal direction and the value of F in the boundary cell. Accordingly, gradients of the phase fraction are encountered only in the region of the interface [78].

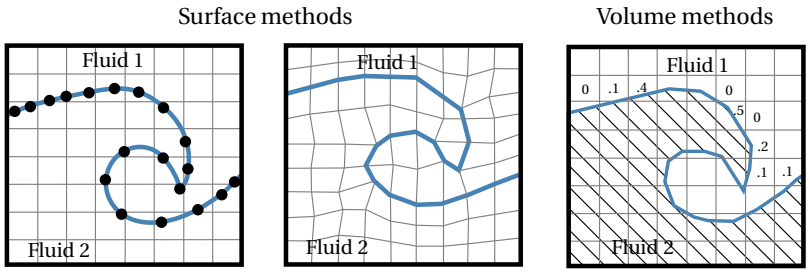

Figure 2.20: Fluid interface classification (adap. from Rusche [12])

In the VOF method the transport equation for the indicator function F (equation 2.39) is solved simultaneously with the continuity (equation 2.40) and momentum equation (equation 2.41):

$$\frac{\partial \alpha}{\partial t} + \nabla \cdot (U\alpha) = 0 \tag{2.39}$$

$$\nabla \cdot U = 0 \tag{2.40}$$

$$\frac{\partial \rho U}{\partial t} + \nabla \cdot (\rho UU) = -\nabla P + \nabla \cdot T + \rho f_b \tag{2.41}$$

where α is the phase fraction which can take values within the range $0 \leq \alpha \leq 1$, U is the velocity field shared by the two fluids through the flow domain, ρ is the density, p is the pressure, f_b are the body forces per unit of mass and T is the deviator viscous stress tensor which is defined as:

$$T = 2\mu S - \frac{2}{3}\mu(\nabla \cdot U)I \tag{2.42}$$

where μ is the dynamic viscosity. Likewise, S and I are defined as:

$$S = 0.5\left[\nabla U + (\nabla U)^T\right] \tag{2.43}$$

$$I = \delta_{ij} \tag{2.44}$$

Generally the VOF method is based on the interface capturing method which considers the surface tension between both fluids but neglects heat (in case of being implemented) and mass transfer.

2.10.2 Computational tool: OpenFOAM

OpenFOAM (Open Field Operation And Manipulation) is a free C++ toolbox developed by OpenCFD Ltd. which contents pre-written solvers applicable to a wide range of problems in continuum mechanics, complex fluid flows, turbulence, heat transfer, among others. Due to its hierarchical architecture OpenFOAM is suitable for customization and to extend its existing functionality, allowing in this way in a wide range of solutions across most areas of engineering and science [79].

2.10.2.1 Multiphase flows

The Reynolds Averaged Navier-Stokes (RANS) equations are used to simulate the 3D flow motion of incompressible turbulent flows. In the case of two incompressible and isothermal immiscible fluids, the transport equation was reformulated in OpenFOAM, based on the studies of Rusche [12], by including an additional convection term (see equation 2.45), called the *compression term*, which appears as an artificial contribution to the convection of the phase fraction in the equation 2.39. The main idea of this additional term is to *compress* the free surface towards a sharper one, contributing therefore to a higher interface resolution in comparison to the classical VOF approach.

In equation 2.45, W is an artificial velocity indicating the degree of compression which is directed normal and towards the interface. The case of $W = 0$ indicates no compression and $W = 1$ indicates conservative compression. For $W > 1$ enhanced compression is obtained, however a value of 1 is recommended by OpenFOAM.

$$\frac{\partial \alpha}{\partial t} + \nabla \cdot (\alpha U) - \underbrace{\alpha(\nabla \cdot WU)}_{\text{compression}} = 0 \tag{2.45}$$

The original momentum equation of the VOF method (equation 2.41) was refined by adding a term which accounts for the effects of surface tension at the liquid-gas interface which generates an additional pressure gradient which is assessed by using the Continuum-Surface-Force (*CSF*) model of Brackbill,

$$f_b = \sigma_{ik} \kappa_{ik} (\nabla \alpha)_{ik} \tag{2.46}$$

where $(\nabla \alpha)_{ik}$ is calculated as

$$(\nabla \alpha)_{ik} = \alpha_k \nabla \alpha_i - \alpha_i \nabla \alpha_k \tag{2.47}$$

here κ_c is the mean curvature of the free surface, determined from the expression

$$\kappa_c = -\nabla \cdot \left(\frac{\nabla \alpha}{|\nabla \alpha|} \right) \tag{2.48}$$

As both fluids are considered to be Newtonian and incompressible ($\nabla \cdot U = 0$), the rate of strain tensor is linearly related to the stress tensor, which is decomposed into a more convenient form for discretisation [78],

$$\nabla \cdot T = \mu \left[\nabla U + (\nabla U)^T \right] = \nabla \cdot (\mu \nabla U) + (\nabla U) \cdot \nabla \mu \tag{2.49}$$

Furthermore, the normal component of the pressure gradient at a stationary non-vertical solid wall, with a no-slip condition on velocity, is different for each phase due to the hydrostatic component ρg when the phases are separated at the wall [78]. As a consequence the modified pressure is defined as

$$p_d = p - \rho g \cdot x, \tag{2.50}$$

where x is the position vector. Finally, the momentum equation (2.41), based on the adjustments (2.46) (2.49) and (2.50) is rearranged to read:

$$\frac{\partial(\rho U)}{\partial t} + \nabla \cdot (\rho UU) - \nabla \cdot (\mu \nabla U) - (\nabla U) \cdot \nabla \mu = -\nabla P_d - g \cdot x \nabla \rho + \sigma \kappa \nabla \alpha \tag{2.51}$$

The density ρ and the viscosity μ are treated as volumetric mixture values calculated as:

$$\rho = \sum_{i=1}^{N} (\alpha_i \rho_i) \tag{2.52}$$

and

$$\mu = \sum_{i=1}^{N} (\alpha_i \mu_i) \tag{2.53}$$

2.10.3 Discretisation of the transport equation and Finite Volume Method

Jasak [80] cited that the purpose of any discretisation practice is to form one or more partial differential equations into a corresponding system of algebraic equations, whose system produces values at certain locations in space and time. The discretisation process consists of two steps: 1) the discretisation of the solution domain, which divides space and time into a finite number of discrete regions, so-called control volumes or cells, and time steps; and 2) the equation discretisation, which gives an appropriate transformation of terms of governing equations into algebraic expressions [81].

The transport equation for a scalar property ϕ is:

$$\frac{\partial \rho \phi}{\partial t} + \nabla \cdot (\rho UU) - \nabla \cdot \left(\rho \Gamma_\phi \nabla \phi \right) = S_\phi(\phi) \tag{2.54}$$

The Finite Volume Method (FVM) is also a technique for representing and evaluating partial differential equations in the form of algebraic equations. The conservative equations are applied over small volumes and the volume integrals in a partial differential equation that contains a divergence term ($\nabla \cdot$) are converted to surface integrals using the divergence theorem. Accordingly, the FVM requires that equation 2.54 must satisfy each *control volume* in the integral form,

$$\int_t^{t+\Delta t} \left[\frac{\partial}{\partial t} \int_{V_p} \rho \phi dV + \int_{V_p} \nabla \cdot (\rho U \phi) dV - \int_{V_p} \nabla \cdot \left(\rho \Gamma_\phi \nabla \phi \right) dV \right] dt = \int_t^{t+\Delta t} \left[\int_{V_p} S_\phi(\phi) dV \right] dt \tag{2.55}$$

2.10.4 Simulation of liquid jet disintegration

To analysis and predict the interface motion the most common numerical strategies are:

- Front tracking methods (Unverdi & Tryggvason, 1992).
- Volume of Fluid Methods (Gueyffier et al., 1999).
- Level set methods (Sussman et al., 1994).

In Figure 2.21 the results of a 3D simulation of the primary break-up of a thin turbulent liquid jet (d = 0.1 mm, Tu = 0.05, Re = 5800) by using the Level-Set/VOF/Ghost-Fluid method developed by Ménard et al. [13] is presented. The authors claimed that these results should be taken to illustrate the potentialities rather than as a reference result because it is not compared to experimental data. Likewise they stated that the Direct Numerical Simulations DNS provide a promising tool for obtaining information in the dense zone of the spray, where almost no experimental data are available.

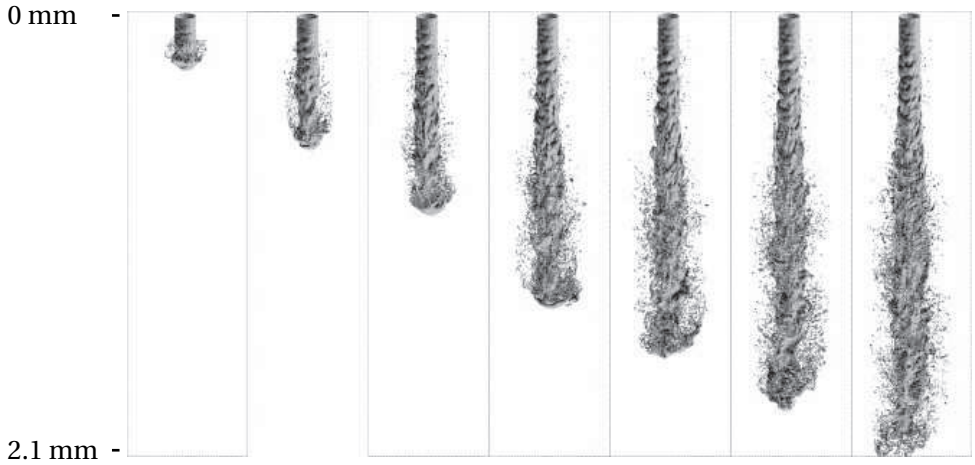

Figure 2.21: Numerical simulation of a turbulent liquid jet (ρ = 696 kg/m^3, μ = 0.0012 kg/(m · s)) with d = 0.1 mm entering a gas (ρ = 25 kg/m^3, μ = 0.00001 kg/(m · s)) with a velocity of 100 m/s. Grid spacing 2.36 μm and uniform grid size 128 x 128 x 896. From Ménard et al. [13].

Shinjo & Umemura [14] performed Direct Numerical Simulations (DNS) mainly on the physical mechanisms from liquid jet injection to droplet formation. To carry out the simulations a nozzle with a diameter d = 1 mm was tested in three different scenarios: a) U_0 = 100 m/s, Δx = 0.35 μm, grid points = 6 billion; b) U_0 = 50 m/s, Δx = 0.75 μm, grid points = 1.16 billion, and; c) U_0 = 30 m/s, Δx = 0.1.5 μm, grid points = 400 million. The authors concluded that if the resolution is not sufficient, physically wrong results will be obtained. Additionally they remarked that due to the lack of primary atomization knowledge, existing numerical spray models for Reynolds Averaged Navier Stokes simulations (RANS) or Large Eddy Simulations (LES) are done with drastic simplifications.

In Table 2.3 the main studies concerning the simulation of jets are presented and in Table 2.4 some numerical simulations by using OpenFOAM concerning air-water flows are compiled.

Author	Year	Description
Yeh, C.L.	2002	Impact of nozzle geometry on the discharge coefficient (C_D) for liquid jets emanating from a plain-orifice atomizer.
Tafreschi & B. Pourdeyhimi [82]	2003	Simulation of cone-down nozzle by using VOF method (Fluent) and the turbulence model realizable k-ϵ. No breakup is visualized or reported.
H. Tafreshi & B. Pourdeyhimi	2003	Prediction of flow behavior in various nozzles used for hydro-entangling
S. Yoon & S. Heister	2004	Demonstrated numerically that the boundary layer at the nozzle exit orifice may drastically affect jet atomization
N. Anantharamaiah, V. Tafreshi & B. Pourdeyhimi.	2006	Formation of constricted water jets in hydro-entangling nozzles
S. Dabiri, W. Sirigano & D. Joseph [67]	2007	Review of published numerical studies on cavitating flows in a nozzle's orifice
Shinjo & Umemura [14]	2010	Primary atomization of liquids injected at high speed (with sufficient grid resolution) was done. The dynamics of ligaments and droplet formation were analysed
V. Srinivasan, A. Salazar & K. Saito [83]	2011	Modelling the disintegration of modulated liquid jets by varying the simulation parameters, comprising the mean liquid jet velocity, modulation amplitude and frequency grouped together using a set of non-dimensional parameters

Table 2.3: Numerical simulation of jets.

Author	Year	Description
Liu & Garcia	2008	Compared the velocity profiles for a flow around a partially submerged cylinder with the experimental data
Berberovic et al.	2009	Compared the process of droplet impact and crater formation with their experiments
Saha & Mitra	2009	Compared microfluidic capillary flows with their experiments, with respect to dynamic and static contact angles
Saha et al.	2009	Compared microfluidic flow in rectangular channels with an analytical solution
Ishimoto et al.	2010	Simulated the cavitation assisted atomization in the gasoline injection system. The interFoam solver was modified
Roisman et al.	2010	Simulated the droplet impact on a porous surface and qualitatively compared droplet spreading with their experiments
Maiwald & Schwarze	2011	Simulated plane plunging jets and compared the results for critical conditions for air entrainment with the experiments
Saito et al.	2011	Simulated the modulated jets and compared the atomization characteristics with the experiments
Raach et al.	2011	Implemented an energy equation in the solver interFoam. Simulated heat transfer in a film falling over turbulence wires.
Gopala et al.	2011	Implemented a model for Bingham plastics. Verified their model against analytical solutions for velocity profiles in channel flow
Trujillo et al.	2011	Implemented an energy equation in interFoam for computing droplet impact heat transfer
Deshpande et al.	2012	Compared the velocity and liquid fraction profiles in a plunging jet flow with their experiments
Deshpande et al.	2012	Incorporated an interfacial compression flux on a modified VOF approach. The solver interFoam was evaluated

Table 2.4: Recent studies using OpenFOAM

a) U_0=100 m/s Δx=0.35 μm b) U_0=50 m/s Δx=0.75 μm c) U_0=30 m/s Δx=1.5 μm

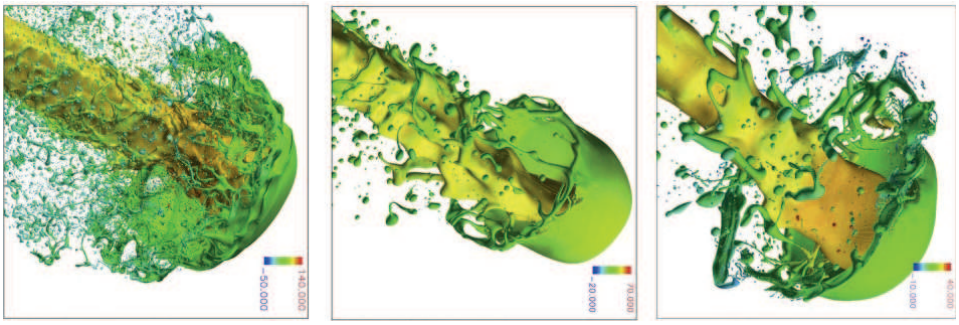

Figure 2.22: Numerical simulation of a turbulent liquid jet (ρ = 843 kg/m^3, μ = 0.000287 kg/(m · s)) for d = 1 mm entering a gas (ρ = 34.5 kg/m^3, μ = 0.0000197 kg/(m · s)) Time step is 2.5 . From Shinjo & Umemura [14].

CHAPTER

3 Experimental rig: description of the facilities

The experimental tests were carried out in the Hydraulics Laboratory of the Institute of Hydraulic Engineering and Water Resources Management of the Vienna University of Technology. The model rig facility consisted of a 5.0 m high steel trestle which had been designed to lead investigations on air entrainment on drop shaft (Velkova [84], Reis [85]) and lately adapted by the current author to do studies of free falling water jets (Nagy [86], Tabova [87]).

Two configurations of water supply were set up at the top of a 5 m high steel trestle in order to generate liquid discharges into the atmosphere through: a) a nozzle attached to the bottom of a water tank and, b) a nozzle directly attached to the pump line of the laboratory. The advantage of using both configuration led to distinguishing the influence of the inlet conditions on the flow and to widen the range of analysis of the scale effects based on increasing the capacity of the system by a pressurized flow.

3.1 Experimental setup 1: nozzle connected to the water tank

A model family of four sizes of smooth and sharp-edge circular nozzles were built and tested. Each nozzle was attachable to the bottom of a water tank (2.97 m x 0.59 m x 0.70 m) built in wood and PMMA (Methyl Methacrylate, or commercially known as Plexiglas®) which was supported over a 5 m height steel trestle as shown in Figure 3.1.

The pump system of the laboratory fed the water tank through a vertical steel pipe (DN150) erected from the ground, and then it was connected to one side of the water tank by its side with a 90° elbow. The flow discharged into the upper reservoir regulated manually by a globe valve and measured by a inductive flow meter (Proline Promag Endress + Hauser®) located on the laboratory floor.

Once the water supply pipe discharged into the water tank, a flow straightener (0.15 m x 0.59 m x 0.60 m) which was composed of an arrangement of octagonal cylinders fixed together with a diameter of $d_i \sim 3$ mm and a length of 0.15 m was located in the vicinity

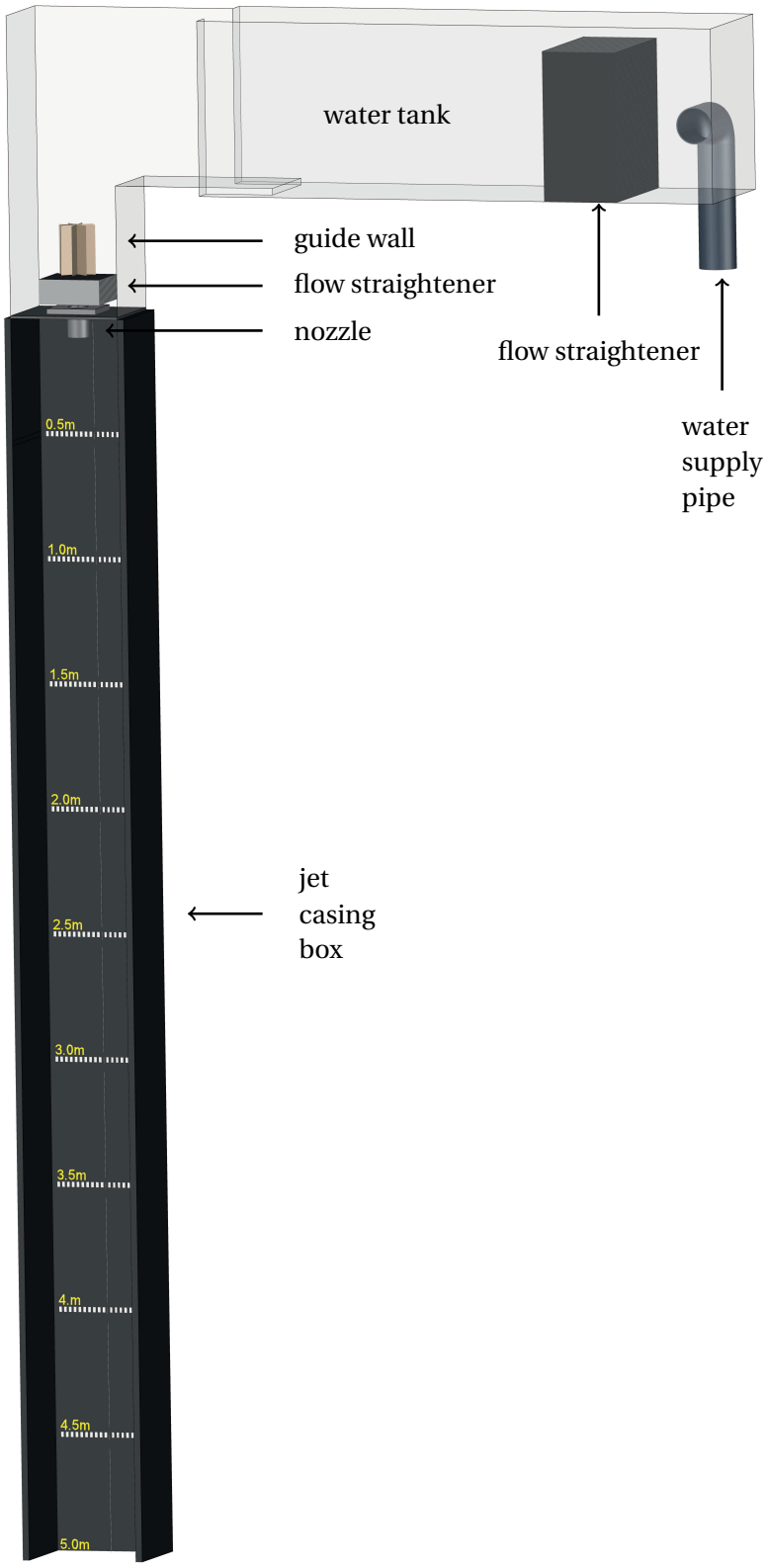

Figure 3.1: Experimental rig 1: nozzle attached to the bottom of the water tank.

of the inlet with the purpose of avoiding sending vortices and secondary currents downstream into the tank.

Before the flow neared the nozzle, it entered a lower chamber (0.444 m x 0.40 m x 0.50 m) which was designed to increase the available hydrostatic pressure by changing the water depth from ~0.6 m to ~ 1.1 m. Once the flow went into the chamber, it encountered a guide wall which had been set up in the upper part which was composed of eight steel sheets with the following measurements: angle between sheets 45°, high 0.30 m and diameter 0.25 m. Afterwards, a flow straightener was set up before the flow reached the nozzle. It is worth mentioning that without using the guide wall and the flow straightener it would not have been possible to guarantee uniform flow inlet conditions for the experiments because the vortices and the secondary flows have a noticeable effect on the jet behavior and the disintegration mechanisms.

Figure 3.2: Nozzle and jet casing box.

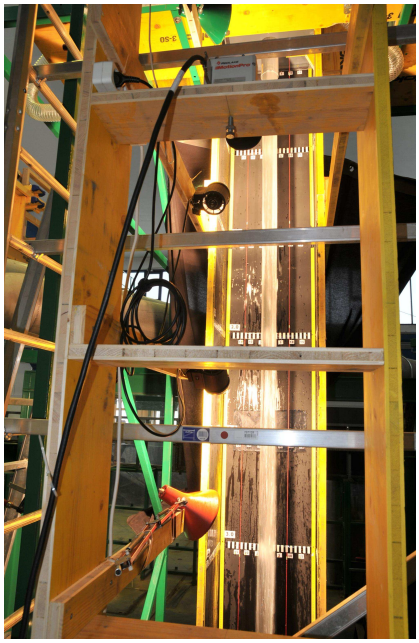

Figure 3.3: Shelf construction.

Once the water jet left the nozzle it fell vertically into the jet casing box (0.43 m x 0.40 m x 4.965 m) which had been built in wood and painted in black in order to make the flow visualizations stand out and, subsequently to do image measurement by means of attaching tape measures along the entire vertical distance each 0.50 m in the vertical direction, as shown in Figure 3.2. Furthermore two auxiliary red vertical wires, in the same plane as the nozzle axis and orthogonal to the open face of the jet casing box, were attached closely to the nozzle to improve the image analysis (see Figure 3.4). Once the liquid crossed the jet casing box, it fell into a directional manifold which conducted the water to the underground water tank storage of the Laboratory.

A shelf construction was built (see Figure 3.3) to position the photo camera devices (Nikon D300s® and Nikon D7000®) and a high speed camera MotionPro from RedLake

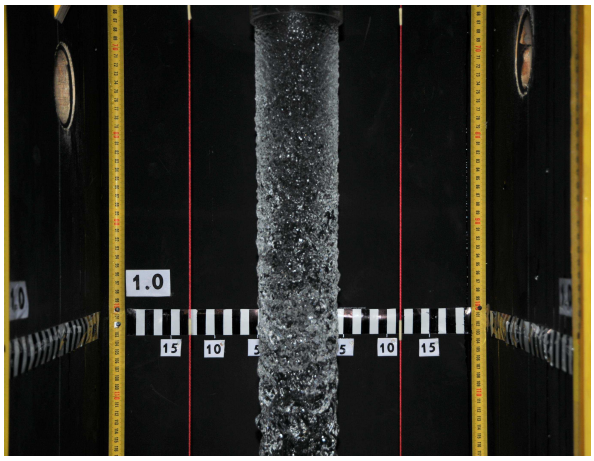

Figure 3.4: Freely falling water jet for d = 80 mm.

(see Figure 3.3) in order to compare later results of the jet behavior under different flow conditions at the same stage. The location of each shelf was designed in order to guarantee that the axis of the lens of the Nikon® cameras projected on the jet casing box was located exactly at the positions 1.25 m, 1.75 m, 2.25 m, 2.75 m, 3.25 m, 3.75 m and 4.25 m of the jet casing box.

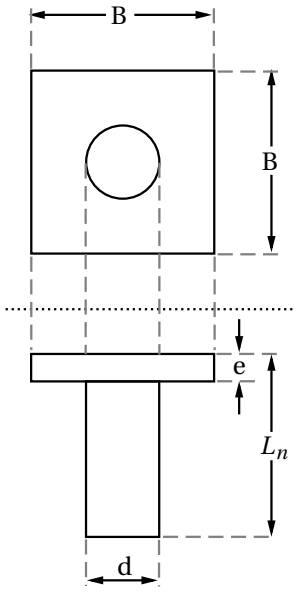

Figure 3.5: Nozzle features.

As has been mentioned before, a model family of circular nozzles were tested. The geometrical parameters of the nozzles are schematized in Figure 3.5 and detailed in Table 3.1. Each nozzle was attachable to the bottom of the water tank which consisted of a concentric holed plate where the nozzle rested and it could be screwed through a quadratic

flange located in the upper part of the nozzle (B = 0.20 m and e = 0.03 m), allowing in this way the easy mounting or demounting of the nozzles from the water tank.

In Table 3.1 the identifier, diameter of the nozzle, length of the nozzle, aspect ratio and scale corresponding to the circular nozzles (see Figure 3.5) are shown.

Experiment	d (mm)	L_n (m)	A.R.	L_r
Model 1	40	0.12	3	2
Model 2	20	0.06	3	4
Prototype	80	0.24	3	-

Table 3.1: Circular nozzle geometry.

All the nozzles were fabricated in PMMA including the upper quadratic plate which is fitted monolithically to it. The advantage of using this material concerned its thickness and translucent, allowing in this way the visualization of the flow in case it was necessary.

The sharp edge (90°) of the circular nozzle inlet was smoothed into circular arcs of diameter 2 mm, 4 mm and 8 mm for the model 1, model 2, model 3 and prototype, respectively. A detailed information concerning the geometry of the model rig was presented by Nagy [86].

3.2 Experimental setup 2: nozzle connected to the water supply pipe

The inlet condition was modified by attaching directly the nozzles to the water supply pipe to get higher water pressure than by using a water tank. As a consequence, a model family of circular nozzles with a larger exit length were tested in the rig described in the previous section. In essence it was necessary to shift the position of the water supply pipe (DN 150 mm) in order to be co-aligned with the jet casing box and through a flange the water supply pipe was guided to the nozzle (see Figure 3.6).

The intention of connecting the nozzle directly to the water supply pipe was to increase the available pressure, to generate a quasi-fully developed turbulence flow into the nozzle, to increase the initial turbulence level in the inlet and to enlarge the experimental capacity of the water discharge in a circular prototype (up to 25%).

The water supply pipe was a steel pipe which was erected vertically from the floor up to 5.7 m height. Once the pipe reached the maximal elevation it was coupled with two 90° elbows and two short pipes until reaching the correct position consisting of guaranteeing verticality and symmetry through the longitudinal axis of the jet casing box.

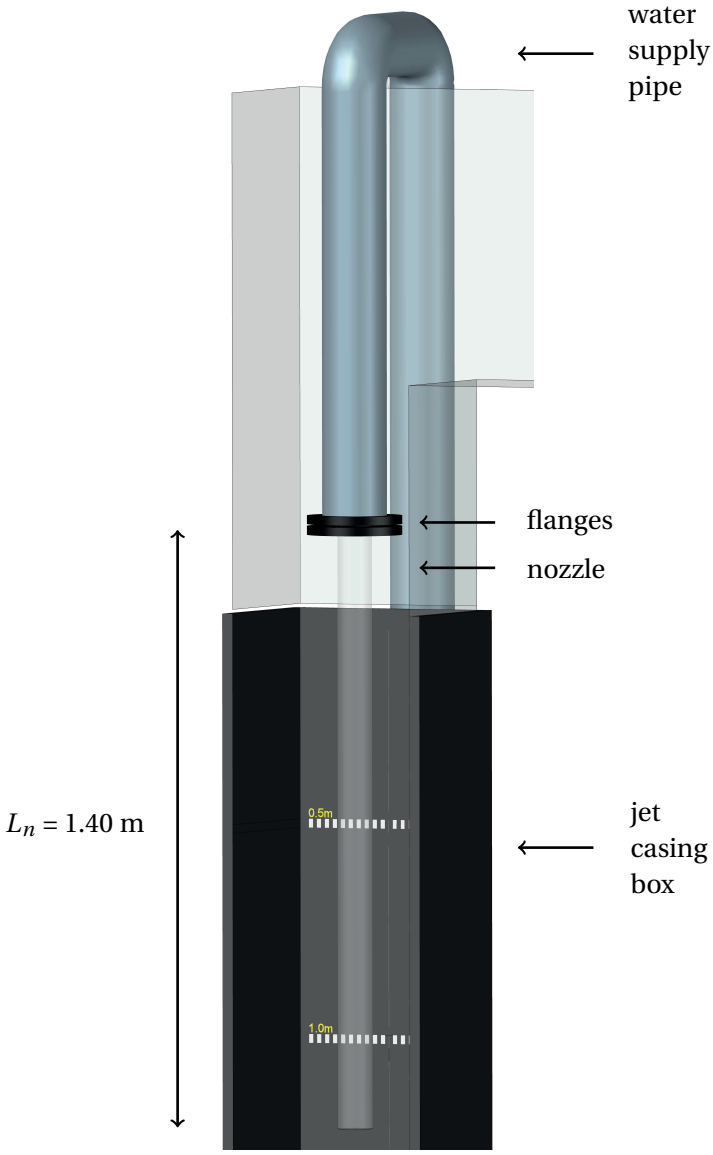

Figure 3.6: Experimental rig 2: nozzle d = 80 mm connected to the water supply pipe.

Similar to that described in section *Experimental Setup 1: nozzle connected to the water tank*, the pump system of the Hydraulics Laboratory supplied the experimental rig with water and the discharge Q_w was controlled manually by a globe valve located on the ground. Additionally, by using a magnetic flowmeter Proline Promag Endress+Hauser the water discharge was monitored in real time with a data acquisition system from HBM®.

In Table 3.2 the identifier of the experiment, diameter of the nozzle, length of the nozzle, contraction ratio $C.R.$, aspect ratio $A.R.$ (which was constant for all the experiments), and scale are shown. Unlike in experiments model 1, model 2 and prototype, the nozzle of the experiment corresponding to *model 1* was connected to a flexible hose (d_h = 0.03 m) oriented vertically.

Exp.	d (mm)	L_n (m)	$C.R.$	$A.R.$
Model 1	40	0.70	0.266	17.5
Model 2	20	0.35	0.133	17.5
Model 3	10	0.175	0.33	17.5
Prototype	80	1.40	0.53	17.5

Table 3.2: Circular nozzle geometry.

The nozzle was composed of a circular cylinder of PMMA and a flange of PVC located in one side in order to attach it to the water supply pipe. The flange had a diameter of 0.22 m, a thickness of 0.02 m and it was screwed to the steel flange of the water supply pipe. In order to damp the vibrations of the steel pipe, along the lining of the water supply pipe, several stiffeners and rubber insulated metal clamps were fixed.

The shelf construction remained from the original setup and it was used to record the experiments during the free falling of the water at several stages by using a photo camera.

3.3 Instrumentation

This section consist of describing the measuring instruments used to monitor physical variables during the performance of the experiments on the rig setups 1 and 2 at the Hydraulics Laboratory. It consisted mainly of using electronic devices which offer the advantage of recording permanently a physical variable in a personal computer and to control it during the experimentation. Likewise, the use of classical rulers and tape measures were essential for doing measurements of images and measures of water depth.

The variables measured during the experiments depended basically on the experimental setup: 1) *The experimental setup 1: nozzle attached to water tank* was built to investigate scale effects of the total air transport and air velocity in the surroundings of

the liquid jet of a model family of circular nozzles under low turbulence intensity, and 2) *The experimental setup 2: nozzle connected to the water supply pipe* was arranged to increase the turbulence intensity and to investigate scale effects of the air concentration in a model family of circular nozzles.

3.3.1 High-speed video camera

The experiments of free falling water jets were captured by using a high-speed camera MotionPro from Redlake® which was mounted in the shelf construction as can be seen in Figures 3.3 and 3.7 observed. The results of the images give a fundamental insight into how a freely jet behaves in air and to see the characteristic shapes of the falling liquid.

Figure 3.7: High-speed camera.

Obtaining a high quality shot at high frame rates depended on sensitivity, quality of the image sensor, as well as the lighting environment. Each time the camera speed increased, the amount of necessary light increased and thus a set of bright lights was put in the vicinity of each shot in order to increase the image quality.

The high-speed camera system has the following components:

High-speed camera head was compact, monochrome, equipped with a 1.280 x 1.024 pixels resolution CMOS sensor and provided with an interchangeable lens mount. The video could be set up to go from a record rate of 500 fps at full resolution (1.280 x 1.024 pixels) to over 10.000 fps at reduced resolution (256 x 48 pixels).

Controller board was fitted onto the motherboard of a PC in order to provide the communications between the PC and the high-speed camera head (peripheral component). By attaching a camera cable it was possible to transfer the signals between the camera and the software.

RedLake MiDAS Software allowed controlling the camera head according to the requirements of the experiments in terms of preprocessing (record), capture of the video (play) and postprocessing (analysis).

Parameters such as the record rate, the frame rate, the shutter speed and the exposure time were quite sensitive during the recording because depending on their setup and the experimental requirements there might have been a lack of light or not during the shot. It is known that a shorter exposure time reduces blur within each frame, otherwise additional light would be necessary to improve the capture. Another aspect to

consider during the taking of high speed videos is the size of the file generated which is dependent of the parameter previously mentioned. As well as the quality of the image being improved, the larger will be the file size generated, leading as a consequence to restrictions on the storage capacity of the computer and the handling of the information generated.

In general, after some pretesting the following setup was adopted for all the experiments: 1) frame rate: 250 fps, 2) resolution: 1280 x 960 pixels, 3) shutter speed: 1/4000 s, and 4) desired file size: < 85 Mb.

3.3.2 Air velocity and air demand

The air velocity and air entrainment in free falling water jet were measured with a portable plastic hand-held vane anemometer *micro MiniAir20*® from Schiltknecht Messtechnik AG (see Figure 3.8). The principle of this device consisted of a propeller and a tail on the same axis with a revolution counter that converted the frequency of rotation by means of an electronic chip into air speed. The device consisted basically of a propeller located in a cylindrical head (ϕ 11 mm x 15 mm for the sensor Micro) with an internal diameter of 10 mm and a length of 15 mm which related linearly the rotation and the air-flow velocity. For higher air velocities a sensor Macro ϕ 85 mm x 80 mm was used. The head rested on a support beam which was connected through a cable to a display control where the information was displayed. Hence, the volumetric flow rate could be calculated because the cross-sectional area of the propeller was known and the air velocity was measured by it.

Figure 3.8: Vane anemometer.

Additionally, to be able to measure the air velocity, the vane anemometer provided, during the data acquisition time, measurements of the averaged air temperature, minimum, maximum, and average velocity of the air. The range of measures of the air velocity was up to 40 m/s and the operating temperature was from 0°C to 50°C.

3.3.3 Air concentration

A sapphire fibre-optical double probe manufactured by RBI-Instrumentation® in 2013 was used to measure the local air concentration C at several lengths from the nozzle exit. Unlike the studies and the wide validations developed by Boes & Hager [88], Boes [89], Boes [90], Kramer [91] and Pfister [92] in chutes and stepped spillways, the current ge-

neration of sapphire-based optic fiber has allowed improvement of its performance by mitigating the light transmission losses when they are used in harsh environments of temperature, pressure or high dynamics of the flow.

The two-phase flow device developed by RBI comprised the following elements [15]: a probe with a double sapphire tip, an opto-electronic amplification module, a data acquisition board, a PC and the software ISO-Lite provided by the manufacturer. The use of dual-tips probes allowed determining not only the air concentration and the bubble-count rate but with the second tip it was possible to estimate additionally the granulometry distribution (chord length), the velocity of the air-water mixture and the specific interface area.

The measuring principle was based on the different refraction indices of air (dry air 0%) and water (clear water 100%). Initially the optoelectronic module transmitted light through an optic fiber to an optic prism shaped sapphire probe tip through which the ray of light E, once in contact with the media, is either partially reflected or diffracted. This is schematized in Figure 3.9, where a sapphire fibre-optic double probe is immersed in an air-water mixture which moves in the right direction, the first tip of the probe is surrounded by a single bubble of air (ray of light is reflected) and the second one is in water (ray of light is diffracted). Subsequently the optic signal in terms of the quantity of light reflected is converted into an electrical signal by a photo-sensitive element located in the opto-electronic unit.

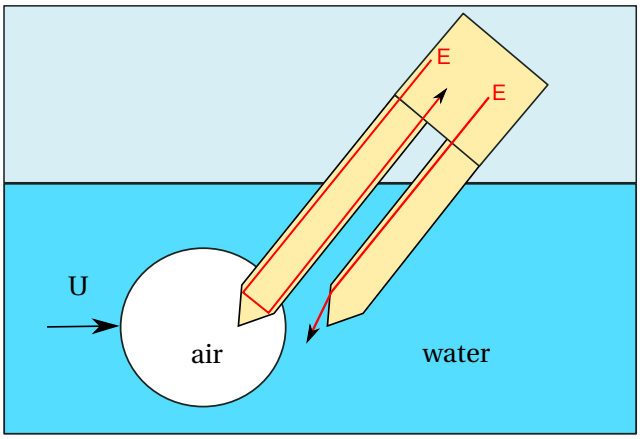

Figure 3.9: Sapphire optic double probe (adap. from User's Guide Manual RBI [15]).

Once a bubble travelled through the optic probe, a variable level analog signal was produced by the optical probe and consequently the captured rough signal was shaped (as is in Figure 3.10) shown) by the opto-electronic unit into a TTL signal by an automatic thresholding method operation.

For the velocity measurements a double probe with streamwise alignment was required. The principle consisted of recognizing of the coincidence of the probe signals. With the actual tip distance, the local velocity of air bubbles could be calculated with the

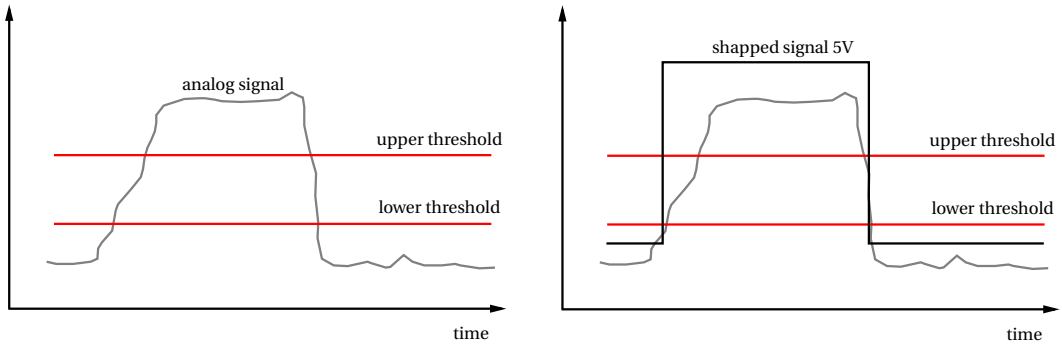

Figure 3.10: Signal shapping (adap. from User's Guide Manual RBI [15]).

time shift between the occurrences of a pair of events corresponding to the same bubble passing both probe tips.

As can be observed in Figure 3.11, the sapphire optic double probe must be positioned transversely to the flow direction by guaranteeing that the two tips are co-aligned vertically with it. The optoelectronic amplifier (unit) emits the light signal (E) through the optic fiber, once it arrives at the sensitive cone shaped tip it is returned back (R) and then the signal can be processed by a photo-sensitive element which converts the optic signal into an electrical signal. Consequently the signal is shaped (into a squared signal), being acquired by an interface board and finally transferred to a personal computer where the data could be analysed and processed by means of the software provided by RBI.

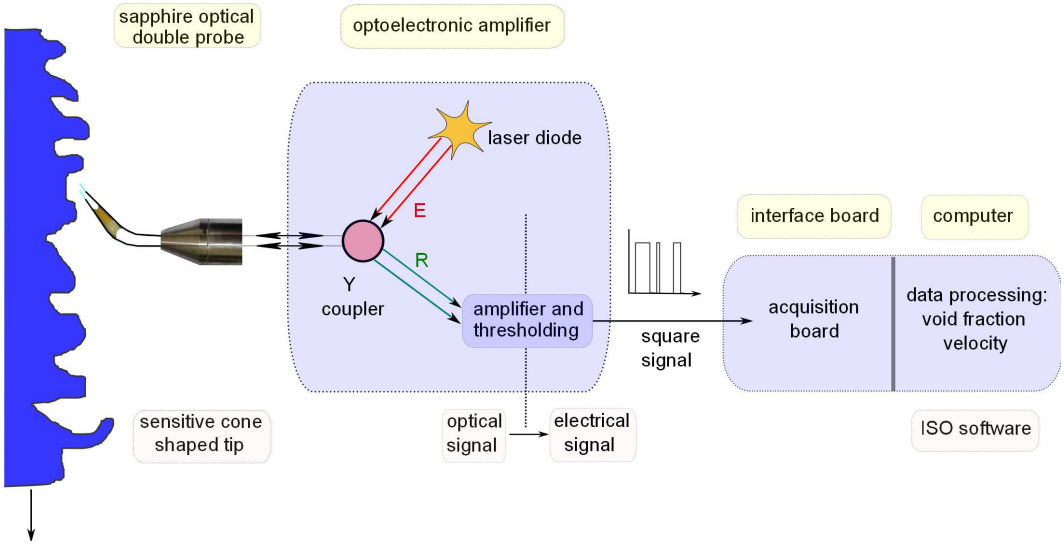

Figure 3.11: Sapphire fibre optic double probe working scheme (adap. from User's Guide Manual RBI [15] [93]).

Among the parameters that could be obtained from the data processing, mention should be made of the following:

- With a single tip the acquisition time, number of bubbles, average phase time and phase-time histograms could be captured and visualized.
- The void fraction was calculated as is described in equation 2.1. Only the first tip is able to establish the void fraction of the fluid because the second tip might be affected by the disruption of the flow and flow separation caused by the first tip. The time required to estimate the void fraction was analysed statistically (time convergence) considering the temporal influence over the results.
- By using a double probe the mixture velocity could be estimated. This could be done in two ways: cross-correlation and time of flight [93].
- The size distribution analysis was based on information from the two sensors, which, knowing the chord length, enabled determination of the bubble size distribution.

The measuring time in the tests was 200 s and the minimum acquisition time to obtain reliable results for the void fraction was about 150 s. The methodology consisted of building a converge curve based on the grouping of successive data n of air concentration into intervals in order to evaluate the variation of the air concentration on the width of the time interval. Accordingly, plots of the temporal convergence of air convergence were built and the measuring acquisition time was established [94].

The advantages of using a sapphire fibre-optic probe are as follow:

- The response time is faster than using electrical probes. The response time of a sapphire fibre-optic probe is in the order of 1µs to 6µs instead of 10µs when electrical probes are used [88].
- As an intrusive device for void fraction detection in air-water mixtures, the tiny head size of the optic probe (~ 0.5 mm) plays an appropriate role during the measure.

3.3.4 Water discharge

The water discharge Q_w was supplied by the hydraulic pump system of the Laboratory. The discharge into the experimental setups was regulated manually by a valve located at the pipe inlet of the rig and the flow was recorded by a magnetic flow meter Proline Promag Endress + Hauser® located at a certain distance behind the valve.

CHAPTER

4 Experimental results: water velocity, air entrainment and breakup length

In this chapter the results of measuring the water velocity, the air entrainment and the air velocity profile in the surrounding of free falling water jets will be presented.

The particular case of air entrainment in a model family of circular nozzles whose liquid jet falls through a casing pipe will be analyzed and discussed in terms of scale effects arising from using under-scaled models.

As a consequence, the experimental program involved calculation of the following variables:

- Calculation of the liquid velocity along the jet length. By using a high speed camera it could be obtained for different liquid discharges at several distances from the nozzle exit by using techniques of image processing.
- Determination of the jet breakup length $\overline{L}$. The measurements obtained will be discussed, analyzed and compared with other experimental test and formulas in the literature.
- Determination of the amount of air entrainment Q_a and the air velocity u_a in the surrounding of the jet by means of a portable hand-held vane anemometer micro MiniAir20® from Schiltknecht Messtechnik AG.
- Determination of the air and water temperatures.

Finally, the establishment of relationships between the air entrainment and the length scale L_r will be analysed as well as the scale effects will be discussed.

4.1 Experimental program

Some pre-tests were developed to improve the performance of the nozzles (see Figure 3.1) due to the sudden change in flow direction in the lower chamber of the water tank. A consequence of this was the presence of air in the jet due to a vortex sucking air and

causing the premature breakup of the flow once it was ejected from the nozzle. Furthermore a guide wall was set up to prevent vortices in the inlet conditions, and also a flow straightener which stabilised the flow and reduced greatly the turbulence of the flow due to the abrupt inlet conditions (90° bend).

The experimental procedure for the characterisation of the free falling water jets is detailed below:

- The range of operation (i.e. flow discharge) for the circular nozzles was determined experimentally based on the maximum and the minimum operating water elevation (without suction of air) in the water tank.
- The circular nozzles model 1, model 2 and prototype with the geometric characteristics shown in Table 3.1 were tested. The flow discharges listed in Table 4.1 were used:

d (mm)	Q_w (L/s)	U_o (m/s)	Code	Exp.	Re ($\times 10^5$)	We ($\times 10^3$)	Oh ($\times 10^{-4}$)	Fr
80	16.2	3.22	V-PR-1	558	2.57	11.4	4.17	3.6
	16.9	3.36	V-PR-2	248	2.68	12.6	4.17	3.8
	18.9	3.76	V-PR-3	238	3.00	15.6	4.17	4.2
	20.5	4.08	V-PR-4	577	3.26	18.4	4.17	4.6
40	2.56	2.04	V-M1-1	298	0.813	2.30	5.9	3.3
	2.82	2.24	V-M1-2	428	0.896	2.78	5.9	3.6
	3.09	2.46	V-M1-3	409	0.982	3.35	5.9	3.9
	3.35	2.67	V-M1-4	496	1.06	3.95	5.9	4.3
	3.62	2.88	V-M1-5	429	1.15	4.59	5.9	4.6
	4.00	3.18	V-M1-6	415	1.27	5.60	5.9	5.1
20	0.52	1.66	V-M2-1	380	0.330	0.773	8.34	3.7
	0.62	1.97	V-M2-2	250	0.394	1.10	8.34	4.5
	1.06	3.37	V-M2-3	323	0.673	3.14	8.34	7.6

Table 4.1: Experimental program for determining the water jet velocity.

- Once the discharge Q_w was setup (see Table 4.1), the high speed camera system (camera and lights) was situated at several stages of the shelf construction (see Figure 3.3) with the intention of capturing the breakup process along the water jet during its fall.

Torricelli's law (1643), which is a particular case of Bernoulli's principle, established a relation between the nozzle discharge velocity U_0 and the tank free-surface height H. It states that the discharge velocity equals the speed which a frictionless particle would attain if it fell freely from point 1 (water surface) to point 2 (nozzle exit), independent of the fluid density which is a characteristic of gravity-driven flows [7]. This approximation to the nozzle exit velocity is:

$$U_0 = \left(2\ g\ H\right)^{1/2} \tag{4.1}$$

However, by considering losses, nonuniform flow conditions and nozzle geometry, the equation 4.1 must be adjusted by including a dimensionless discharge coefficient, C_D:

$$U_0 = C_D \left(2\ g\ H\right)^{1/2} \tag{4.2}$$

4.2 Calculating the water velocity by using high speed photography

The use of image processing techniques is an outstanding tool which allows the determination of parameters related to series of images. In the particular case of turbulent water jets ejected into the air, the use of high speed videos has contributed to characterize the breakup phenomena as well as to determine the water velocity (u) along its fall.

4.2.1 Description of the experimental program

Images of the same scene can only be compared directly if they are in the same position or coordinate system. Furthermore each image captured from a camera is warped, distorted and not uniformly scaled because of the effect of the lens or the camera perspective. In order to get an undistorted image, it is necessary to correct (align) it by using techniques of reconstruction of the image, a so-called *image registration* or *image alignment algorithms* procedure.

Despite the photography with the high speed camera being positioned orthogonal and equidistant to four control points in the vicinity of the water jet (red wires besides the water jet in Figure 3.4), some distortion can arise due to the camera angle and therefore have to be corrected. As a consequence, by ignoring water surface relief, image registration can correct the camera perspective distortion by using a 2D-Projective transformation or so called Projective Mapping which requires 4 collinear points (or so called quadrilateral) which convert and brings an input image $f(x,\ y)$ into alignment with the coordinate system underlying a fixed digital orthophoto image (200 mm x 500 mm) in a new image $g(x',\ y')$ by modifying the coordinates of the image pixels [95] [96] [97]:

$$f(x,\ y) \rightarrow g(x',\ y') \tag{4.3}$$

to model this process, a mapping function T_m is needed (in x and y axes) for each pixel in the input image:

$$f(x',\ y') = T_m(x,\ y) \tag{4.4}$$

The tracking of particles of fluid was done by means of the following procedure implemented in Matlab® 8.3 for recording the images:

1. Each frame was extracted from the high speed video and saved as an individual image file.

2. Previously a rectangular scaled *base image* has been drawn with the size corresponding to the referenced red strings and the marks as they are partially shown in Figure 3.4. This procedure is done once for each single video because during the

shot the high speed video camera was positioned at certain elevations on the shelf construction.

3. Development of the inter-spatial transformation from control point pairs. This procedure consisted of matching four fixed points between a single frame and the *base image*. In order to correct the images the transformation model 2D-*projective geometric transformation* was used which will find the parameter of the projective distortion that best fits the fixed points selected.

4. Once the transformation matrix is obtained, it proceeds with the transformation of the remaining frames which are part of the high speed video.

5. Once the series of frames are recorded, the analysis followed by identifying a visible wave or protuberance in the water surface flow, to mark its position x_1 in the frame (n) and then to capture the next position x_2 of the same particle in the immediate consecutive frame $(n+1)$. As the frame rate of the high speed camera is established at the beginning of the shoot, the time between frames Δt can be calculated and, as a consequence, the instantaneous flow velocity can be computed:

$$u = \frac{\mathrm{d}x}{\mathrm{d}t} = \frac{x_2 - x_1}{\Delta t} \tag{4.5}$$

It is worth mentioning that the implementation of *computer vision*, specifically *video tracking* techniques, was not successful during the current research due to the difficulties of tracking a particle of fluid during its fall. By implementing the Lucas-Kanade method, which is an algorithm highly efficient for video tracking, it was not possible to follow a particle of fluid initially selected because the challenge was how to handle the changes in the light, the reflection of waves in the water surface, and even the frequency of emission of the light used to light up the experiment during the shoot. Nevertheless the use of a high speed camera constituted an advance in the use of non-intrusive tools to measure parameters typical in hydraulic engineering such as the water velocity.

In Figure 4.1 the flow velocities calculated for the experiment V-PR-3 are shown. The water tank height H was measured vertically from the water tank surface until the nozzle exit and it is shown as a vertical dashed line in Figure 4.1. Likewise Torricelli's equation (equation 4.1) and the equation of uniform acceleration (equation 4.6) are shown.

$$|U|^2 = |U_0|^2 + 2g(x) \tag{4.6}$$

with $x = x_i - x_0$. Where x is the vertical distance from the nozzle exit, $x_0 = H$ is the distance from the water tank free-surface height until the nozzle exit and, x_i is the vertical distance from the tank free-surface height until the reference point.

4.2.2 Water velocity in the development region

It was observed, for all the tests, that the water jet falls as a massive core and the experiments, therefore, were limited to the analysis of the velocity in the development region (zone A and B described by Ervine et al. [5]) due to the restriction in the height of the rig and the maximum velocity reachable in the nozzle that make it impossible to achieve

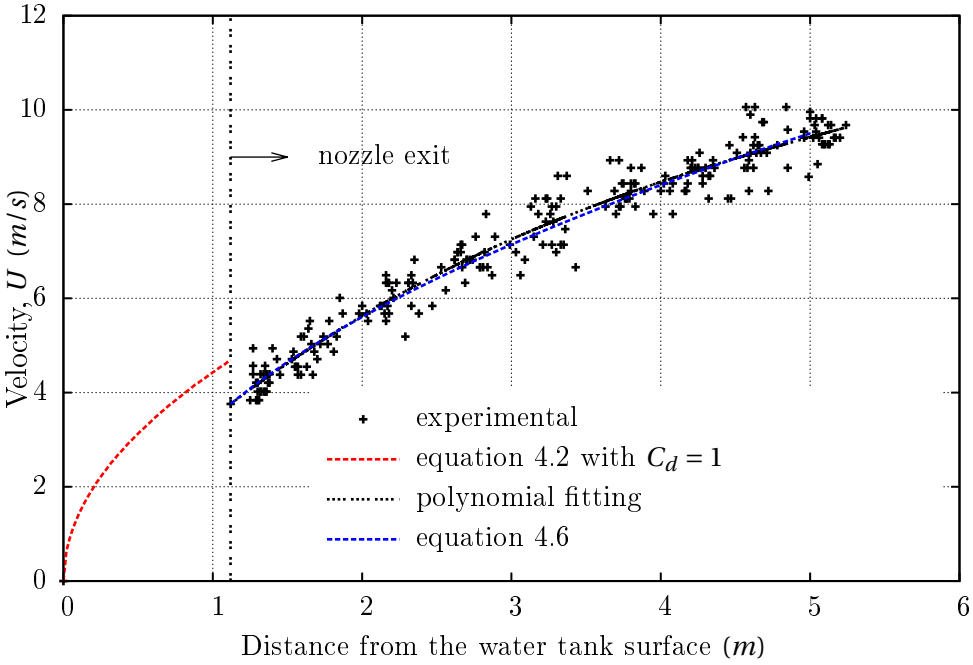

Figure 4.1: Water velocity for d = 80 mm and Q_w = 18.9 L/s.

the fully developed flow region. Additionally, the experimental water jet described in Figure 2.8 did not match the predicted velocity. On the contrary, the water surface for the lowest diameters was smooth and the water had a wavy behavior during its fall as a consequence of the controls imposed on the water at the inlet conditions.

Once the velocity was calculated for each experiment associated with Table 4.1 (in a similar way as it is shown in Figure 4.1) the theoretical equation 4.6 was compared with a polynomial curve fitted to the experiments. Furthermore, in order to represent the physics of the experiments, at the boundary condition $(h, U) \rightarrow (0, U_0)$, the fitted curve was constrained by using an optimization technique of *linear equality constraints* to force the curve to agree with the initial boundary condition (fixed point). In Figure 4.2 the fitted curves to the experiments described in Table 4.1 are shown.

The terminal velocity U_t without considering buoyancy forces is given by:

$$U_t = \sqrt{\frac{2\ m\ g}{\rho_a\ A\ C_d}} \tag{4.7}$$

where m is the mass of the falling object, g is the acceleration due to gravity, ρ_a is the density of the air, A is the projected area of the objet and C_D is the drag coefficient. If a drop of a diameter of 2 mm is falling through air, $A = 0.013$ mm^2, $C_D = 0.5$, then the terminal velocity is 9.0 m/s. Experimentally at a distance of 4.0 m from the nozzle exit the maximum velocity achieved values between 8.7 m/s and 9.7 m/s but, due the limitation in height of the facility and the controlled inlet conditions, there was no atomization of the liquid jet and as a consequence the terminal velocity was not reachable. Furthermore

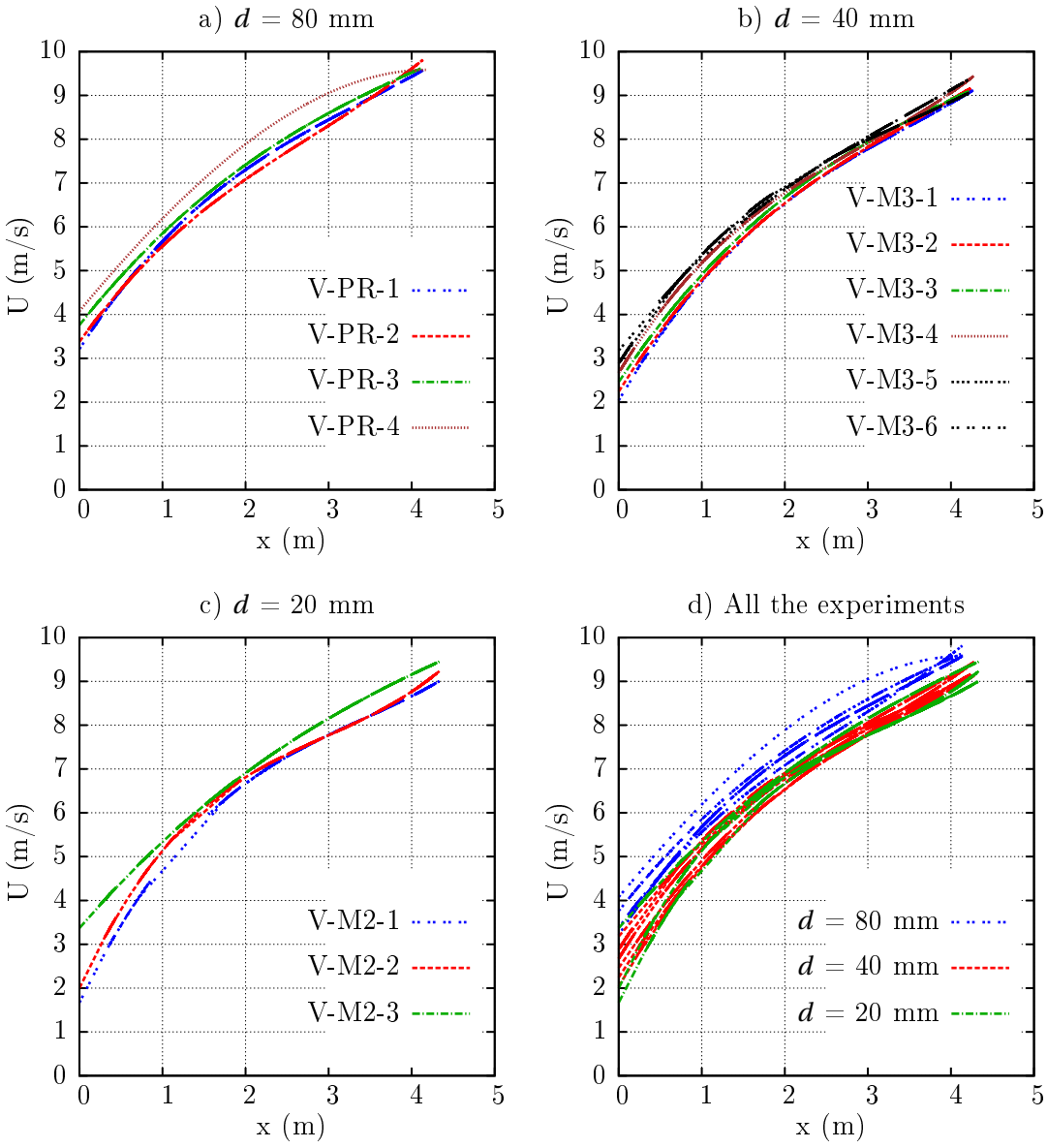

Figure 4.2: Water velocity U at several distances from the nozzle exit x discharging into the atmosphere.

it should be mentioned that for the experiments with $d = 40$ mm and $d = 80$ mm, the jet fell into the flow development region as is shown in Figure 2.8.

The outer velocity of the water jet obtained along its fall (whose fitted curves are displayed in Figure 4.2-d) were compared with equation 4.6 to analyse the accuracy of the results and to determine reductions of the velocity in the outer side of the water jet. To validate this, the Root-Mean-Square Difference (RMSD) was used to check the reliability of the experiments and, the average change from one set of data with respect to other ones was compared. The RMSD is defined as:

$$\ell(O,S) = \sqrt{\sum_{i=1}^{n} (O(x_i) - S(x_i))^2} \tag{4.8}$$

where ℓ is the root-mean-square difference; $O(x)$ and $S(x)$ are functions that denote *observation* and *simulation*, and n is the number of pairs of data. The results of evaluating the *RMSD* is presented in terms of boxplots in Figure 4.3 where the error determined for the diameters d = 20 mm, d = 40 mm and d = 80 mm is presented. Furthermore the following can be concluded:

- The smaller the diameter the lower the variability. Despite of the capability of identifying control points in the jet which are more visible and recognizable for jets with bigger diameters, in the case of the diameter d = 20 mm difficulties arose because of the glass-like condition during its fall and the limited resolution of the high speed camera. In spite of these difficulties, the variability of the results was lower for this diameter than for the other ones as can be appreciated in Figure 4.3.
- In spite of intuition, which would suggest a reduction of the error and a premature hypothesis would be the bigger the diameter the lower the error in terms of the median, the standard deviation σ indicated that the variability of the results is larger for the biggest diameter. The standard deviation for the diameters of 20 mm, 40 mm and 80 mm are 0.18, 0.91 and 2.18 respectively. It is worth mentioning that the experiments are independent and the dashed line connecting the medians shown in Figure 4.3 is just an indication of how the data varied.

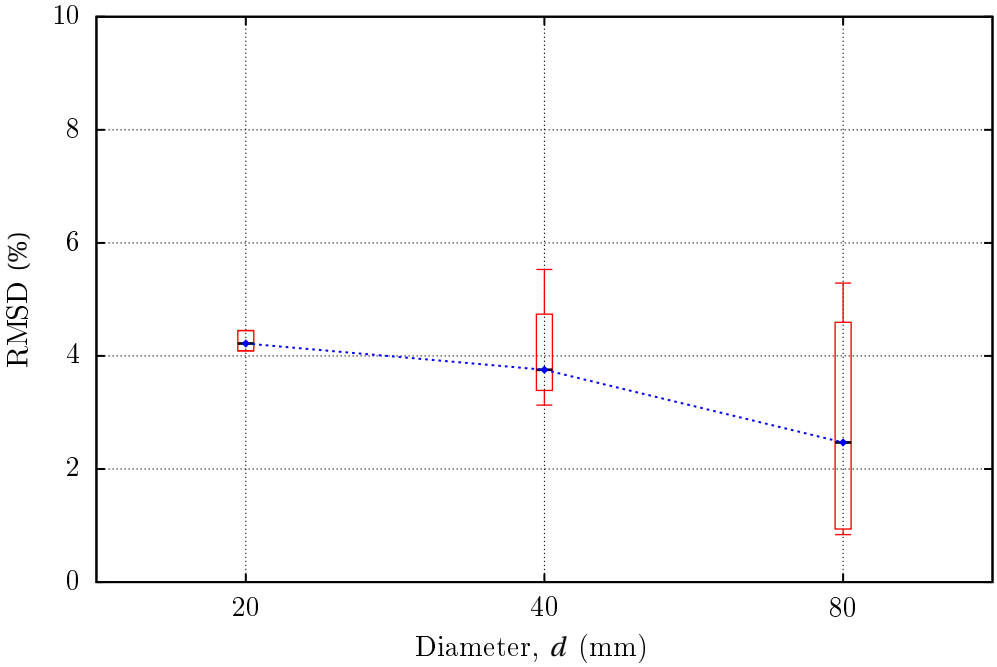

Figure 4.3: Boxplot of errors: observations by using high speed camera vs equation 4.6.

4.2.3 Comparison of the model family according to Fr_r

The consideration of air-water mixtures and the effects of the surface tension increases the difficulty of overcoming the problems in hydraulic modelling because it should always be considered even though the scaling problem is nearly insurmountable. As has been mentioned by Ettema [70], the scaling issues and the model-prototype conformity should be noted, also, that the scale ratio itself is not all-revealing, because the real issue becomes the absolute values of the dimensionless numbers. Moreover, in order to ascertain the scale effects, the influence of scale ratio for the same geometry should be analysed and furthermore the modeller should instead strive to investigate the effect of scale by employing different scale ratios.

If the Froude number similitude (Fr_r=1) with $\rho_r = 1$ is considered, the derived scale of the velocity U_r and water discharge Qw_r can be calculated by using equations 4.9 and 4.10, where L_r is the length scale ratio as is defined in equation 2.35.

$$U_r = L_r^{1/2} \tag{4.9}$$

$$Qw_r = L_r^{5/2} \tag{4.10}$$

Indeed, based on the experimental results shown in table 4.1 a model family of tests can be built in terms of the Froude number similitude consisting of the groups in Table 4.2.

#	Description	Prototype	model 1 d = 40 mm L_r=2	model 2 d = 20 mm L_r=4
1	Q_w (L/s) code	16.2 V-PR-1	2.82 (R. 2.86) V-M1-2	
2	Q_w (L/s) code	16.9 V-PR-2	3.09 (R. 2.98) V-M1-3	0.52 V-M2-1
3	Q_w (L/s) code	18.9 V-PR-3	3.35 V-M1-4	
4	Q_w (L/s) code	20.5 V-PR-4	3.62 V-M1-5	0.62 (R. 0.64) V-M2-2

Table 4.2: Model family of water jets according to Fr_r and ρ_r=1.

The required discharges in models 1 and 2 were obtained by using equation 4.10 which is based on the discharges in the prototype. In three cases there were negligible discrepancies between the required flows' discharges (indicated between parentheses with the letter R for required), however these slight values do not represent alterations in the physics of the fluid and with the purpose of comparison they will be analysed.

A first attempt to determine the type of jet disintegration for the current experimental tests was based on the studies of Ohnesorge [1] by means of his well-known diagram where the mode of breakup is associated with a region where the Ohnesorge number *Oh* (see equation 2.6) and the Reynolds number *Re* falls. In consequence the experiments compiled in Table 4.1 were plotted on Ohnesorge's diagram as can be observed in Figure 4.4, to which the following comments can be added:

- The original Ohnesorge's diagram is contained for the y-axis in the interval $0.001 < Oh < 10$. The current experiments are not specified on it but intuitively it would seem that the experiments for d = 20 mm are located in the region II (spiral formation), for d = 40 mm they fall in a transitional region between II and III (atomization), and for d = 80 mm they are located mainly in region III.
- It is worth mentioning that Ohnesorge's diagram does not consider the influence of nozzle geometry or the turbulence level *Tu* in the inlet.

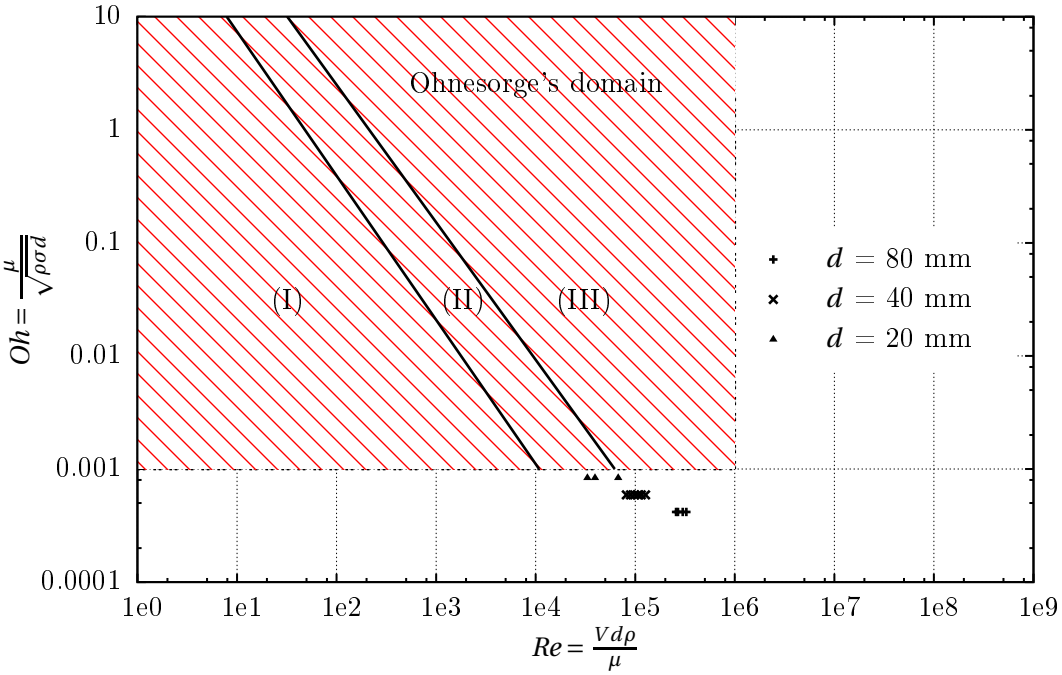

Figure 4.4: Classification of the current experiments in the Ohnesorge diagram.

Once the experiments were done, the photographic records of the water jet falling through the jet casing box (see Figure 3.1) were recorded and assembled by using Gimp 2.8® which is a free and open-source raster graphics editor. Consequently, consecutive and not simultaneous pictures were merged in order to visualize the dynamics of the jet, its topology and the process occurring during the falling as well as the liquid velocity increasing. The size of each photograph was limited to cover a range of 0.5 m of the length of the jet in order to capture more detailed information of each image and reduce the error in case of using image processing techniques as has been previously described and implemented.

The results of capturing the model family of experiments scaled according to the Froude number similitude are shown in Figures 4.5, 4.6, 4.7 and 4.8, which basically display and compare the complete fall of the water jet for the prototype and its corresponding models 1 and 2, if both experiments in the model are available, and keeping the original size between them. Additionally in order to visualize and to capture the process along the length, to each image was incorporated a real metric scale each 0.5 m on the left side. Moreover, in the case of models 1 and 2 on the right side an up-scaled length was added according to the length scale L_r of the experiment, L_r=2 and L_r=4 for the model 1 (d = 40 mm) and the model 2 (d = 20 mm).

The following observations can be made:

- In the case of the liquid discharges for d = 80 mm, immediately after the nozzle exit the jet did not display a glass-like condition. On the contrary the water surface was wrinkled, with the presence of small protuberances distributed not uniformly corresponding to the effects of the internal turbulence of the liquid jet trying to eject out or break up the water surface but being fully controlled by the surface tension of the liquid. Due to the limitations of the rig, the experiments done in the prototype were limited by the minimum and maximum reachable discharges (16.2 L/s and 20.5 L/s), which allowed only the testing of variations of 26% from the Reynolds number in the turbulent regime.

- Against expectations according to the suggested by the Ohnesorge diagram, a spray configuration for the experimented water jets d = 40 mm and d = 80 mm (Figures 4.5 to 4.8) was not found. Furthermore, it has been demonstrated an ambiguity on the original diagram if the straight lines defined for clustering the type of flows are just extended. Obviously, as can be observed, mostly of type of flows falls into region II and, in order to fall into the spray region an increase in the nozzle velocity (U_0) must be applied.

- An initial overview of the potential scale effects can be inferred initially from the Ohnesorge diagram if the Froude number is adopted as the similitude law. As the ratio of the length scale (L_r) increases, the lower the required Reynolds number in the model. This means that if a prototype has a mode of disintegration of drop formation or spray type (region III), the expected type of flow for his corresponding model family will move from the right to the left in the Ohnesorge diagram, as well as the scale is increased. As a consequence, it would expect that if the length scale (L_r) is increasing, the type of flow of any model will move from the region III, then the region II (disintegration by spiral formation) and finally the region I (disintegration by axis-symmetrical surfaces oscillations).

- The complexity of the scale effects in water jets mentioned previously can be visualized and verified in figures 4.5 to 4.8. The discussion concerning scales effects will be expounded in Section 4.4.4.

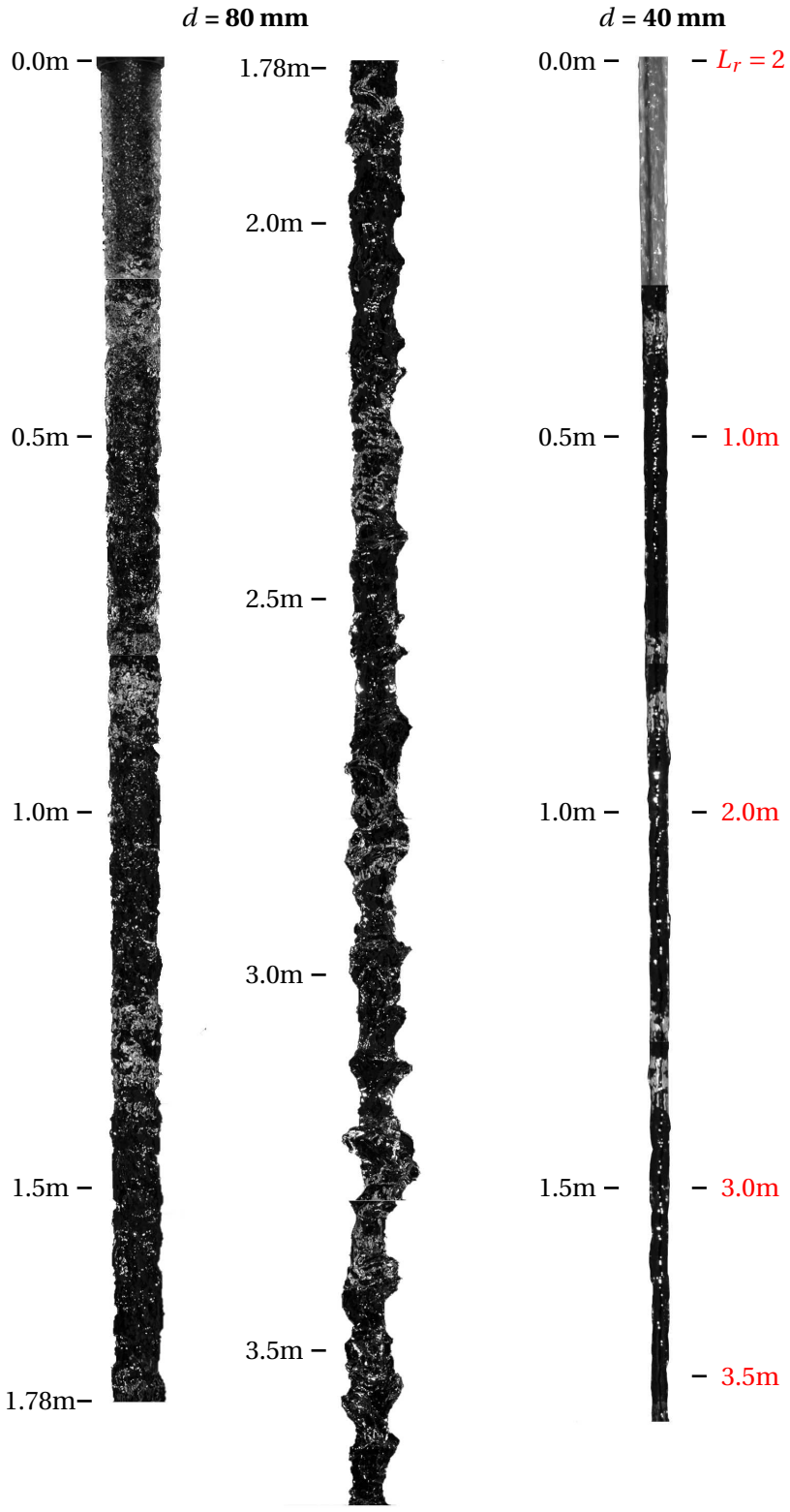

Figure 4.5: Model family 1 - Experiments: V-PR-1 and V-M1-2.

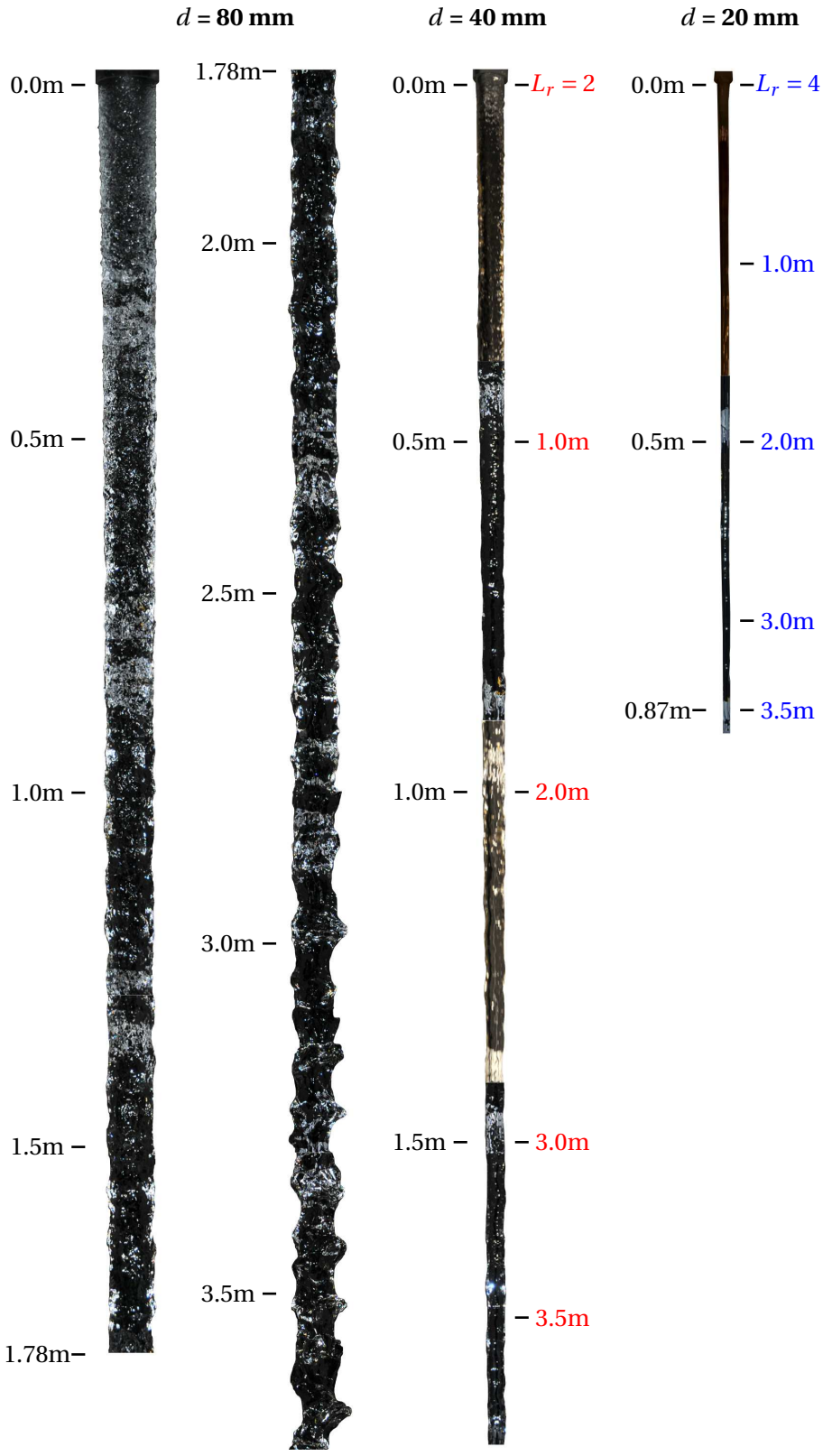

Figure 4.6: Model family 2 - Experiments: V-PR-2, V-M1-3 and V-M2-1.

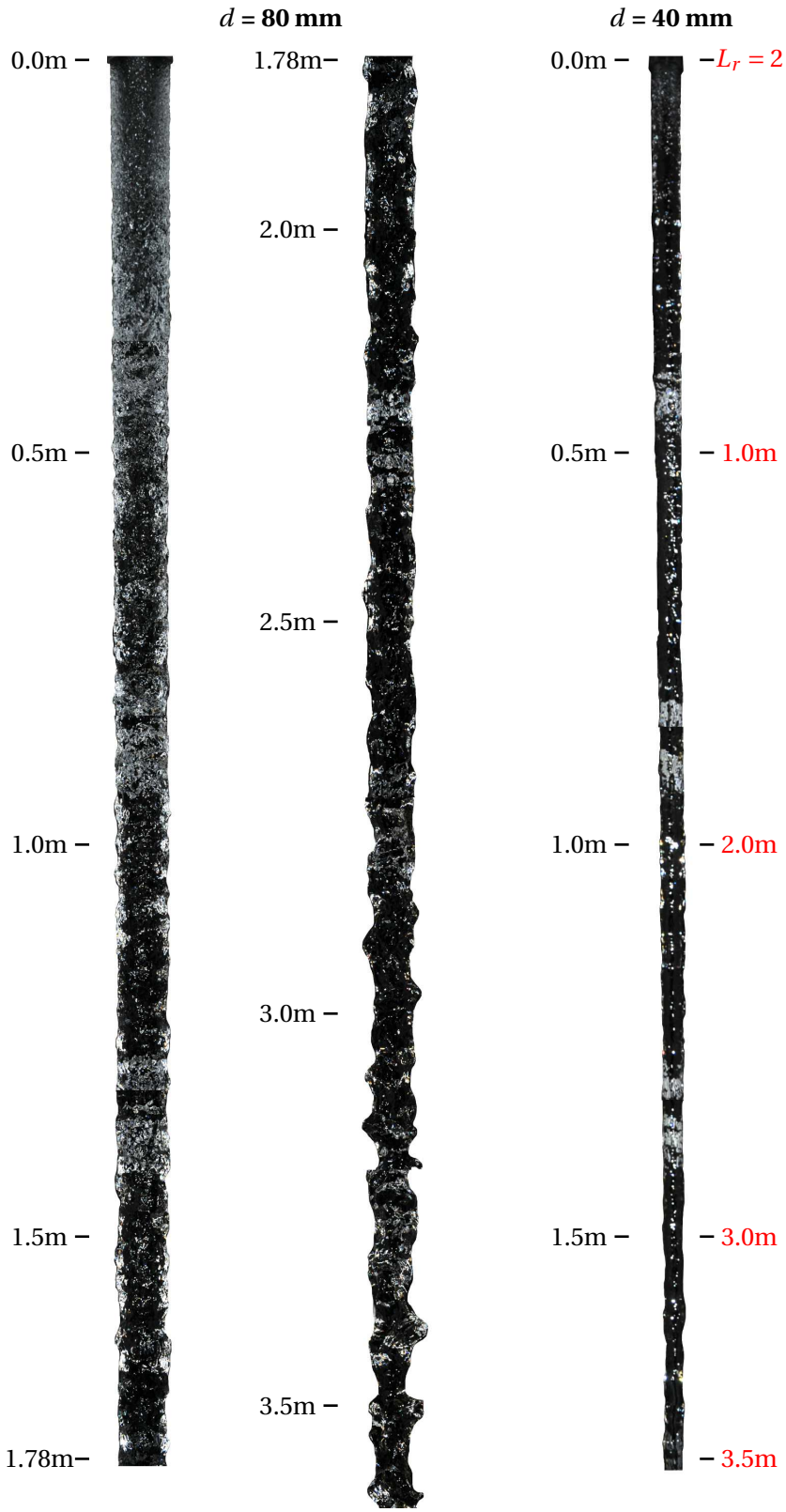

Figure 4.7: Model family 3 - Experiments: V-PR-3 and V-M1-4.

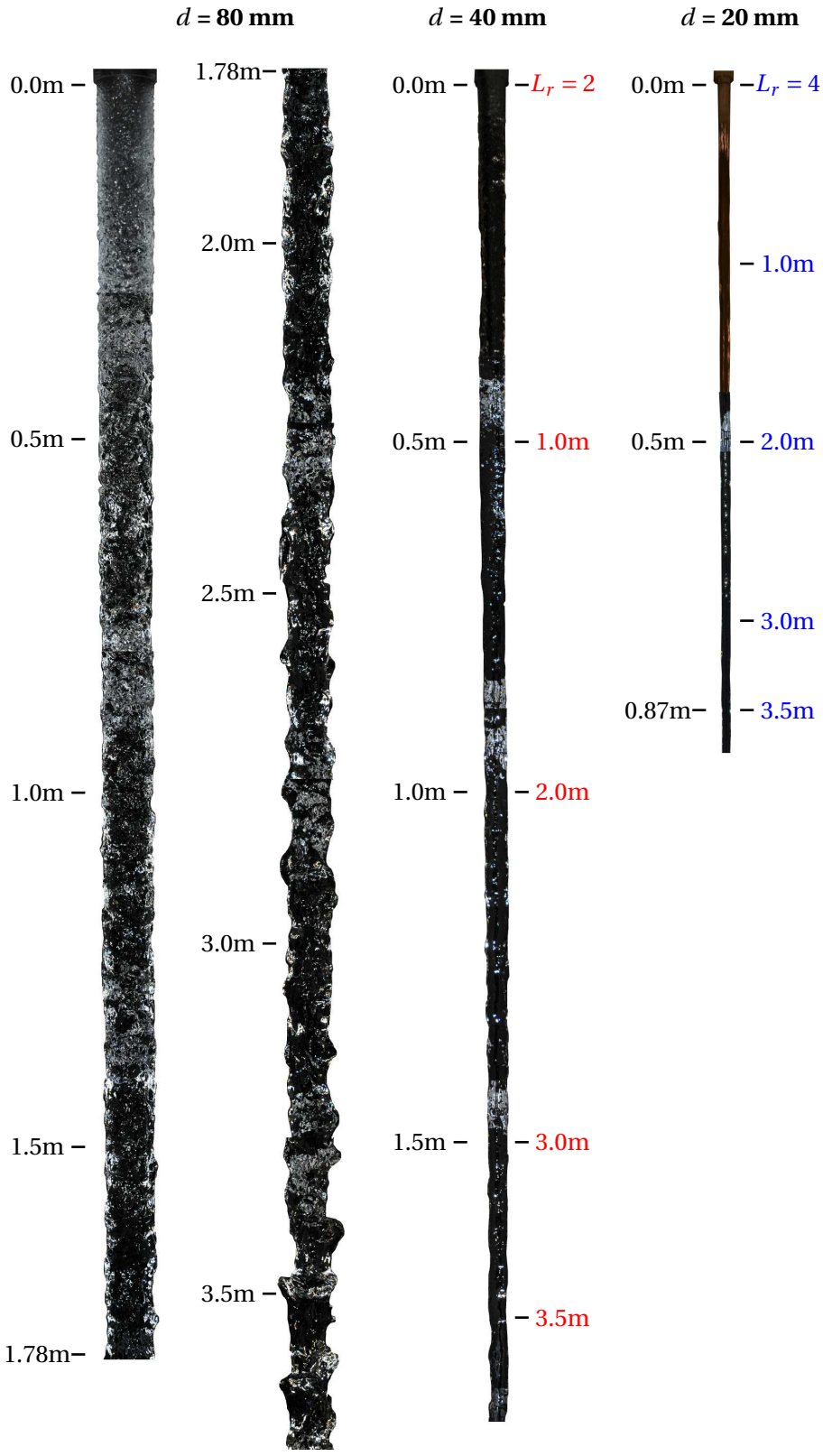

Figure 4.8: Model family 4 - Experiments: V-PR-4, V-M1-5 and V-M2-2.

4.3 Discussion: is there an unique equation for describing the breakup length $\overline{L}$ of water jets in circular nozzles into quiescent air?

Despite all that has appeared in the literature on the subject of ambient pressure effects and water jets, it is a fact that not much breakup length data is to be found. Although Weber developed a theory that takes into account ambient pressure effects, to the authors's knowledge no one has ever explored its validity by comparison with experimental data. Also, particularly in the case of atomization, it is difficult to separate ambient effects from those of turbulence. In hydraulic engineering the ambient pressure in air-water mixtures is relevant during the atomization but, in general, the experimental tests will be done under atmospheric pressure conditions.

4.3.1 Without considering turbulence level effects

By considering dimensional analysis it has been found for liquid jets that the ratio $\overline{L}/d$ is dependent on the Reynolds number *Re* and the Weber number *We*, as it has been previously reported by Chen & Davis [50].

$$\frac{\overline{L}}{d} = \left(We,\ Fr\right) \tag{4.11}$$

where *We* is defined as:

$$We = \frac{\rho U_o^2 d}{\sigma} \tag{4.12}$$

where ρ is the water density, U_o is the nozzle outlet velocity, d is the nozzle diameter and σ is the surface tension between air and water.

Chen & Davis [50] found, based on studies on circular straight nozzles with an aspect ration *A.R.* = 100 (see Table 2.1) and water with different viscosities, that the breakup length $\overline{L}$ is independent of the Reynolds number. Furthermore, it is obvious that the Weber number is the most representative dimensionless parameter that better describe the phenomena. However, in his original paper the results were expressed in terms of the square root of the Weber number, which is inconvenient even more if the fitting can be expressed explicitly in terms of the Weber number by a linear function. Herein based on Chen & Davis's data (see Figure 4.10) an equation of the type $\overline{L}/d = f(We)$ is proposed:

$$\frac{\overline{L}}{d} = 0.0037\ We + 118.17 \tag{4.13}$$

Furthermore, based on the records of the high speed camera in the current research it has been determined that the length breakup follows the procedure described in section 4.2.1, items 1, 2, 3 and 4, which explain the development of the inter-spatial transformation from control points and the recording of the images. In general, the following steps were done in order to measure the breakup distance:

1. Based on the sequence of images (frames) extracted from the videos captured with the high speed camera, several breakup positions were pre-identified on the frames were they took place.

2. By means of a routine implemented in Matlab® 8.3, the position of the length breakup $\overline{L}$ was measured directly on the frames and the position was recorded.

3. Once the position for a single experiment was stored, the averaged breakup length $\overline{L}$ was calculated based on the obtained values.

In Figures 4.9-a and 4.9-b the location of the breakup length $\overline{L}$ for liquid discharges (Q_w) of 0.45 L/s and 1.0 L/s are shown. The left image shown below, which is extracted from the high speed camera (resolution 1280 x 960 pixels and frame rate 250 fps), was used to determine the length breakups $\overline{L}$. The right one, which is obtained from a continuous shooting mode from a Nikon® camera D7000, in spite of offering better resolution (4920 x 3262 pixels), to capture in rapid succession the falling of the water has the disadvantage of offering a lower frame rate (just 6 fps) than that obtained with the high speed camera (250 fps). As a consequence, the error by using the high speed camera can be estimated as ± 15.3 mm, instead of ± 704 mm obtained with the photo camera. However, in order to illustrate the phenomena and the mode of breakup of a water jet ejected from a nozzle of diameter d = 20 mm, by using a camera, in Figure 4.9 the region where the jets breaks is presented.

Based on the current research, in Figure 4.10 an equation to determine the jet breakup length of water jets into quiescent air is presented, as follows:

$$\frac{\overline{L}}{d} = 0.00259\ We + 149.25 \tag{4.14}$$

It is worth mentioning that for the experiments of Chen & David the properties of the water such as the viscosity (maximum ratio 1:1.72) and the surface tension (maximum ratio 1:52) were modified by changing the temperature and the surface tension. In spite of the changes in the properties of the liquid jet, the trend observed is linear for the range of analyses. If the the current experiments are included, equation 4.15 is obtained (R^2 = 0.911), which can be observed in Figure 4.10.

$$\frac{\overline{L}}{d} = 0.00331\ We + 129.87 \tag{4.15}$$

4.3.2 Considering the effect of turbulence intensity in the nozzle

Doubts concerning the validity of establishing a universal equation 4.15 exist because Kraatz [3] suggested that the ratio $\overline{L}/d$ is independent of any dimensionless number, is only related to the properties of the fluids, and should take any value between 40 and 60 ($40 < \overline{L}/d < 60$). As a consequence, after an exhaustive literature review, in order to find experimental data of breakup of free falling water jets, consideration will be given to the studies developed by Chen & Davis [50], Grand & Middleman [6], Takahashi & Kitamura [98], and Ervine et al. [11]. It should be mentioned that the last one is the only research developed until now that has measured the relative turbulence intensity *Tu* of the water jet in the nozzle exit.

The experiments reported by the authors mentioned before are detailed in Table 4.3, where *Name* is the names of the researchers, *Year* is the year of the publication, d is the

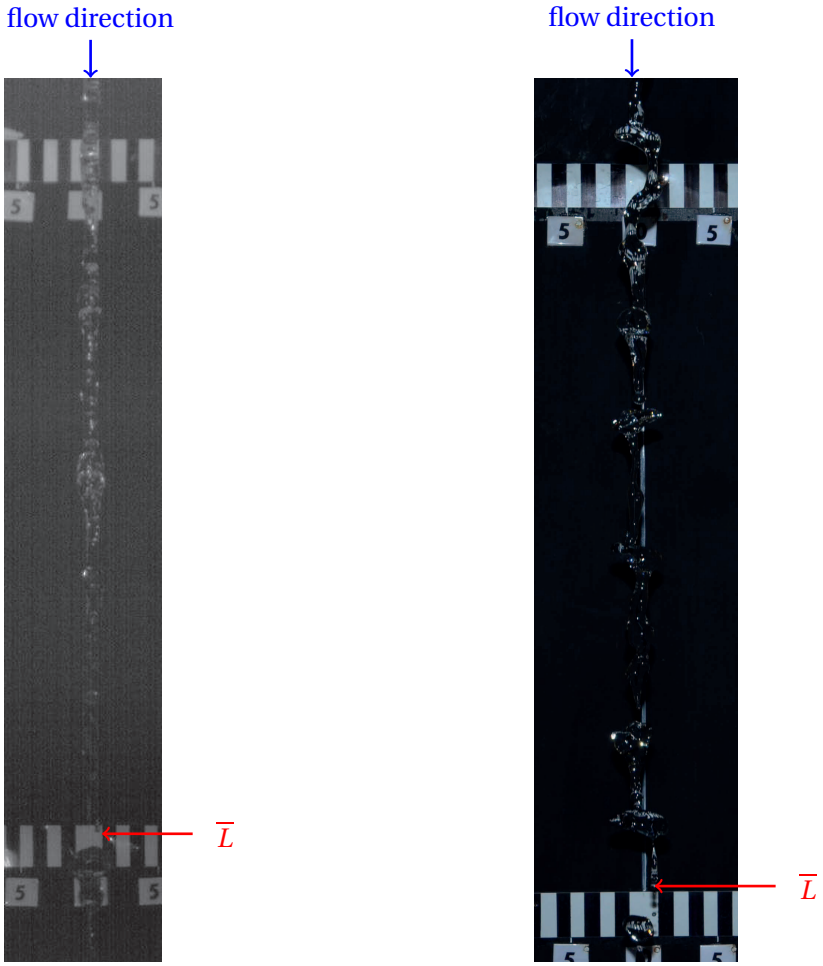

Figure 4.9: $\overline{L}$ obtained with: a) high speed camera for d = 20 mm and Q_w = 0.62 L/s, and b) photo camera for d = 20 mm and Q_w = 1.06 L/s.

diameter of the jet, *Tu* is the relative turbulence intensity, *A.R.* is the aspect ratio of the nozzle and *Code* is an identifier of the experiment. Certain fields concerning *Tu* or *A.R.* are empty because the variable was not measured or provided.

By considering the experiments mentioned in Table 4.3, in general the following observation are listed before the preparation of the plot $\overline{L}/d$ vs *We*:

- In case of the experiments of Grant & Middleman [6], identified as gm and coloured in a green dashed line, the Weber number was obtained based on the physical properties of distilled water provided by the authors: viscosity μ = 0.0091 poise, density ρ = 997 kg/m^3 and surface tension $\sigma = 7.28 \times 10^{-2}$ N/m. The velocity and the breakup ratio were provided in the paper.
- For the experiments of Chen & Davis [50], the data $\overline{L}/d$ vs *We* were obtained directly from a plot of their paper and, in Figure 4.11 they were identified with the

Name	*Year*	*d* (mm)	*Tu*	*A.R.*	*Code*
Chen & Davis	1964	6.4		100	cd1
		9.5		100	cd2
		11.7		100	cd3
		19.1		100	cd4
Grant & Middleman	1966	0.62		95	gm
Takahashi & Kitamura	1969	2.03		0.35	5-1
		2.04		0.95	5-2
		2.17		1.80	5-4
		2.1		7.15	5-6
		2.15		14.4	5-8
		2.15		17.2	5-10
Ervine, Mackeogh & Elsawy	1980	6	0.003		em 1
		9	0.003		em2
		14	0.003		em3
		25	0.003		em4
		6	0.03		em5
		9	0.03		em6
		14	0.03		em7
		25	0.03		em8
		6	0.08		em9
		9	0.08		em10
		14	0.08		em11
		25	0.08		em12
Florez	2015	20		3	fl

Table 4.3: Fluid properties and nozzle characteristics of water jets. Data set from: Chen & Davis [50], Grant & Middleman [6], Takahashi & Kitamura [98], Ervine et al. [11] and Florez (current research).

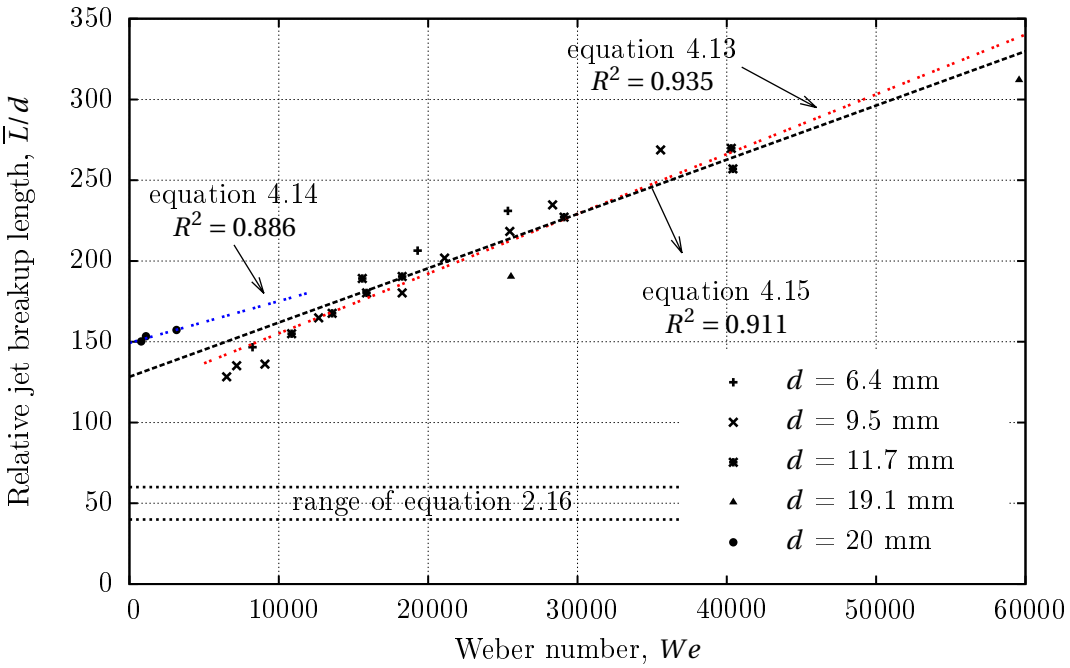

Figure 4.10: Length breakup of water jets into air with experimental data of Chen & Davis [50] ($6.4 \leq d \leq 19.1$) and own data with $d = 20$ mm.

code cd1, cd2, cd3 and cd4 and colored in yellow as is shown. Unfortunately for those data the authors did not provide information concerning the velocity and the physical properties of the fluids tested. As a consequence, due to this lack of information it was not possible to estimate kinematic variables and dimensionless numbers.

- Although the paper of Ervine et al. [11] did not provide physical properties of the water, in order to get a magnitude of the regime of the fluid, it was assumed that the water jet was under a standard pressure and a temperature of 20°C. As a consequence the properties of the water such as the density, the surface tension and the viscosity were possible to infer from tables of properties of the water under certain temperatures available in the literature.

- In Figure 4.11 the experiments of Ervine et al. [11] were grouped by colors according to the level of turbulence for the diameters of d = 6 mm, 9 mm, 14 mm and 25 mm as follows: with a red color a turbulence level Tu = 0.003 corresponding to the experiments em1, em2, em3 and em4, the blue ones corresponding to the experiments em5, em6, em7 and em8 for Tu = 0.03 and the dark violet ones corresponding to the experiments em9, em10, em11 and em11 for Tu = 0.08. In Table 4.3 the properties and general experimental conditions are listed.

- The turbulence intensity Tu, also referred to as the turbulence level, is defined as:

$$Tu \frac{\sqrt{(u')^2}}{U} \tag{4.16}$$

where $\overline{u'}$ is the instantaneous velocity fluctuation and U is the mean velocity.

- By using dimensional analysis, the variables that affect a free falling water jet have been analysed:

$$f(A.R.,\ d,\ g,\ U,\ \sqrt{(u')^2},\overline{L},\ \varepsilon,\ \sigma,\ \rho,\ \mu) = 0 \tag{4.17}$$

giving:

$$\overline{L}/d = f\left[\sqrt{(u')^2}/U,\ Re,\ We,\ Fr,\ \varepsilon/d\right] \tag{4.18}$$

- The breakup length ratios of the current research are identified with the code fl and they concern the physical conditions identified with the codes V-M2-1, V-M2-2 and V-M2-3 included in Table 4.1.

- The experiments of Takahashi & Kitamura [98], which mainly consist of studies of water jets for circular nozzles with nominal diameter of 2 mm, are identified with the legend 5-1, 5-2, 5-4, 5-6, 5-8 and 5-10 according to those shown in Table 4.3. In Figure 4.11 they were coloured in gray as can be observed.

As a consequence, the relation between the breakup length ratio vs the Weber number provided a suitable function which describes the behavior of water jet breakup, as Chen & Davis [50] have already done for their own experiments. Moreover, based on the experiments listed in Table 4.3, a semi-log plot can be observed in Figure 4.11.

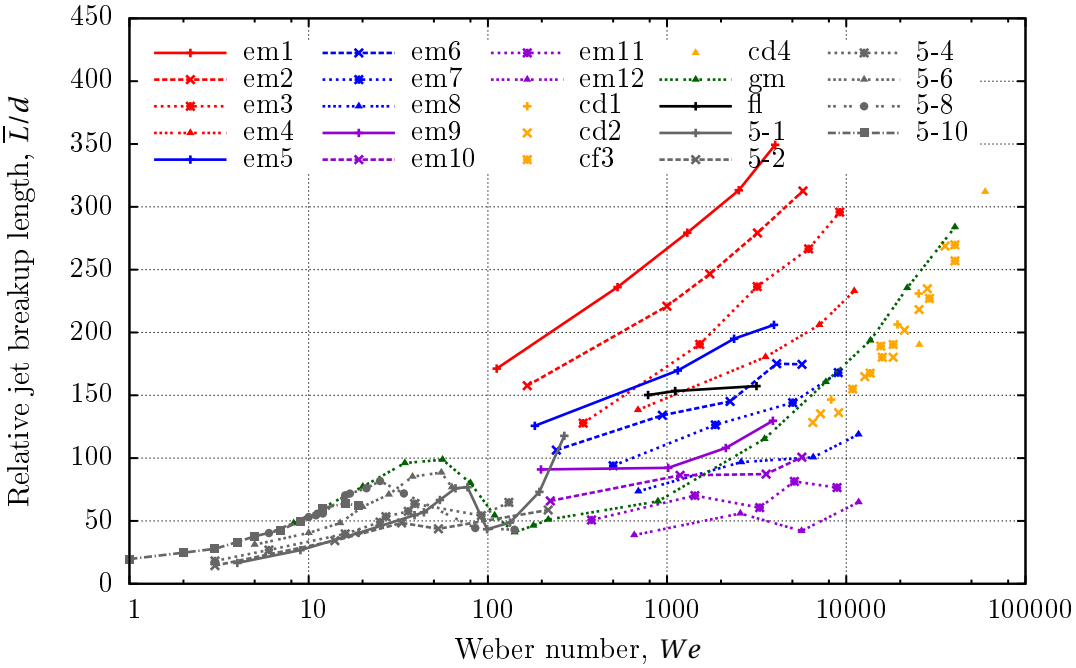

Figure 4.11: Length breakup ratio vs Weber number for water jets in air.

From Figure 4.11 the following can be concluded:

- The breakup curve obtained by Grant & Middleman [6] (here modified in terms of the Weber number) and Takahashi & Kitamura [98] remind us that all the experiments concerning liquid jets into quiescent air will behave as the jet stability curve shown in Figure 2.3 and all the equations proposed in the literature (mostly fitted curves obtained from experimental data) are just describing partially the turbulent region of the jet stability curve and any future proposed equation must emphasize at least its range of applicability, the initial turbulence level in the nozzle, and last but not least, the geometrical parameters of the nozzles listed in Table 2.1.

  The occurrence that the same breakup ratio takes place at three different Weber numbers can be observed in the curves gm, 5-1, 5-2, 5-4, 5-6, 5-8 and 5-10 of Figure 4.11 where a single experiment is covering the laminar, transitional and turbulent regimes.

- Although initially a curve was fitted satisfactorily (equation 4.15) to the experiments of Chen & Davis [50] and the current research, once the effects of the initial turbulence level are considered and compared with the experiments of Ervine et al. [11], it is concluded that to set out a unique equation is unsuitable by just considering the function $\overline{L}/d$ vs We because the effects of the turbulence level, which obviously affect the condition of the water jet once it is ejected from the nozzle, have not been considered.

- According to Ervine et al. [11], as the diameter of the nozzle is reduced and the turbulence intensity is kept constant, the lower the breakup ratio $\overline{L}/d$ for the same Weber number. However it was expected that with the variations of the turbulence intensity there would be a clear separation between the curves em4-em5 and em8-em9, relating to the changes in the turbulence level from 0.003 to 0.03 and from 0.03 and 0.008, but this was not observed.

  Moreover, for the higher diameters and a lower turbulence level the behavior was similar as with a lower diameter and a higher turbulence level.

- First at all, Kraatz [3] proposed that the breakup length ratio is dependent on the densities of the liquid jet and the surrounding fluid where it is ejected. As a consequence he defined his breakup length ratio just as a function of a constant value which is also dependent of the inlet conditions of the nozzle (not quantified in his research). In order to compare his results, although Kraatz did not consider the Weber number in his analysis, it is shown in Figure 4.11. Indeed Kraatz considered that the core zone length, apart from the density difference, is also affected by the turbulence level of the emerging jet which is essentially dependent upon the Reynolds number and the geometry of the nozzle.

  As result, after analysing Figures 4.11 and 4.12 it seems that the experimental tests of Kraatz were suited just to certain intervals (let's call it the Weber number or discharge) on which the turbulence level (not measured) was approximately in the order of 0.08. Therefore his conclusions were biased just to certain intervals of the turbulent regime where the liquid jet in the nozzle was subject to a high turbulence intensity.

- Although hysteresis may take place during the experimental tests, here it is assumed that this is not the case, but it should be taken into account for future re-

searches in the turbulent regime because the data analysis could be strongly affected by the path selected during the experiments: increasing velocity and decreasing velocity of the water jets in the nozzle.

- The turbulence intensity is in general an important parameter which leads to the classification of a water jet. Facing the lack of information concerning the geometry of the nozzle, the turbulent intensity arises as a key parameter that helps to ensure the lack of information about the inlet conditions of experimental tests in laboratories.

- The water jet is a complex non-linear phenomenon which until now has not been possible to be expressed mathematically because the variables that hold sway over the phenomenon have been neglected. Even in the scientific literature, not all the predominant variables are mentioned in the reports (geometry of the nozzle, inlet conditions and property of the fluids) or measured (as turbulence intensity) due the difficulties of set-up of specialized equipment on the rig.

- A dimensionless relationship suitable for all free water jet conditions was not reachable due to the lack of experiments.

Ervine et al. [11] found that the turbulence intensity, independent of the diameter of the circular nozzle, follows the same trend when the experiments are expressed just in terms of $\overline{L}$ vs Q, as can be observed in Figure 4.12. Moreover they proposed the following equations based in their own experiments which are valid only for the interval shown in Figure 4.12.

$$\overline{L} = 60\, Q_w^{0.39} \qquad Tu = 0.003 \tag{4.19}$$

$$\overline{L} = 17.4\, Q_w^{0.31} \qquad Tu = 0.03 \tag{4.20}$$

$$\overline{L} = 4.1\, Q_w^{0.20} \qquad Tu = 0.08 \tag{4.21}$$

The breakup length vs discharge of water jets is presented in Figure 4.13 in a semi-log plot in order to visualize the concave curve associated with the laminar-transitional regime (for the lowest water discharges) obtained by Grant & Middleman (gm) and Takahashi & Kitamura (5-1 to 5-10). Hence the experiments of Ervine et al. [11], Grant & Middlemann [6] and the current research are represented in the form of Bézier curves. In order to visualize more clearly the experiments of Takahashi & Kitamura [98] due to the closeness of the curves, colored dashed lines are plotted in Figure 4.13.

As a consequence the following can be concluded:

- The experiments of Grant & Middleman (identified with the code gm) would suggest that the water jet was subjected to high turbulence in the nozzle. Once the curve is extrapolated (not shown in the plots) beyond their experimental threshold ($Q_w < 2.0 \times 10^{-5}$ m^3/s), it seems that the curve may be positioned below the curve corresponding to the grouped data associated to a turbulence level of *Tu*= 0.08. As a consequence, it could be assumed that the turbulence intensity is higher than 0.08 for the experiments of Grant & Middleman.

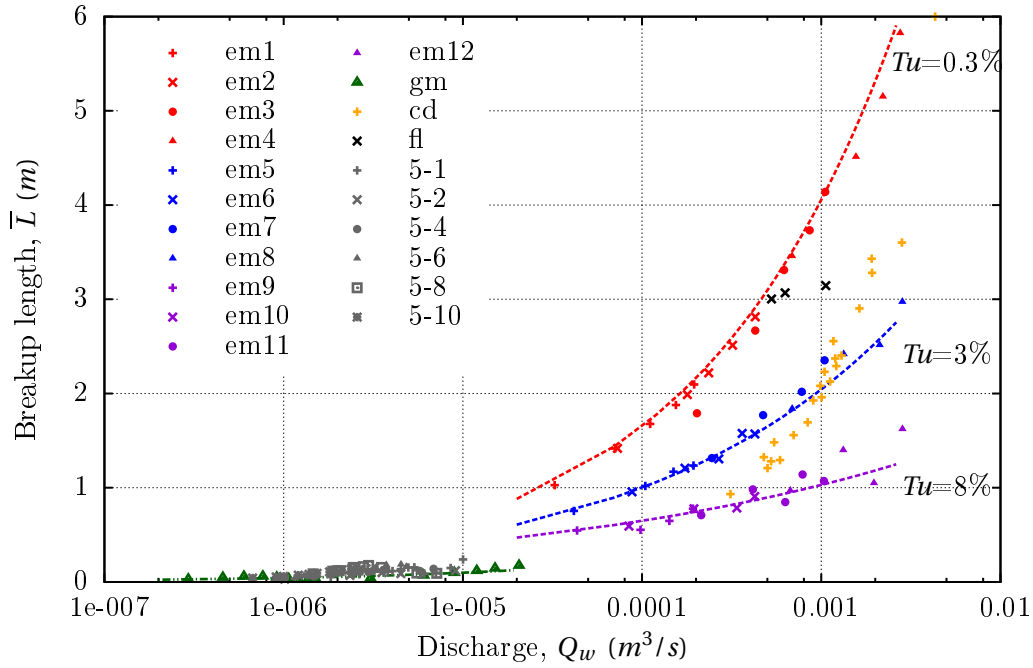

Figure 4.12: Curve length breakup vs water discharge under different levels of turbulence.

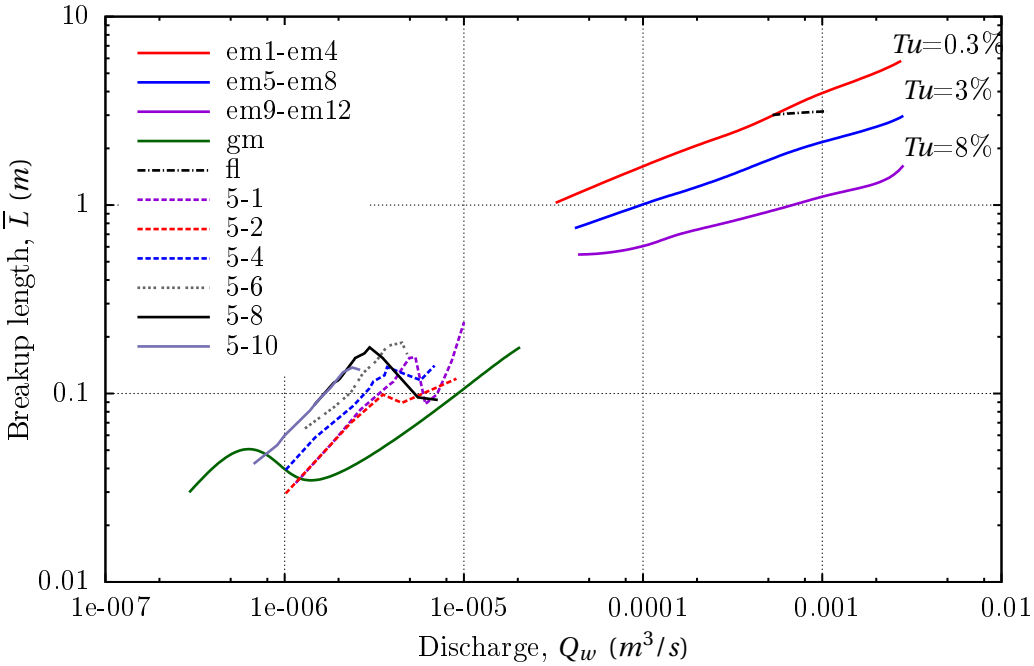

Figure 4.13: Curve Length breakup vs water discharge for water jets.

- The experiments of the current research suggest that the turbulence levels are in the range of Tu = 0.003, because the data agree with the fitting curve proposed by Ervine et al. [11] for a turbulence intensity of Tu = 0.003.

- The physical properties of the water jets experimented by Chen & Davis (identified with the label cd in Figure 4.12) were not provided by the authors and as a consequence it was not possible to estimate with certain reliability the values of the initial jet velocity U_0. However, a sector where the experimental tests are valid is shown, which is constructed based on the maximum and minimum probable values that a single test can take. As a consequence a range of variability of the data is presented which demonstrate that their experiments are, as well, in the same region as the experiments of Ervine et al. [11] and the current research.

- Due to the lack of information concerning the turbulence level in the nozzle, a general equation was not possible to be established and more experimental data about the water jet, including geometrical parameters of the nozzles, are necessary to report in future researches.

- Establishing an equation for describing the breakup of the jet should include the turbulence as a dominant parameter. However in practical terms, the turbulence level cannot be defined and its value is just pre-obtained after the setup of a system.

Ervine et al. [11] suggested the comparison of their experiments (water as main fluid) with other liquids. As a consequence, in order to analyse a dimensionless relationship which could be applicable to all the jet conditions, the experiments consigned in Table 4.4 by Phinney [2] (subjected to ambient density of 101.325 kPa = 1 atm), Takahashi & Kitamura [98] and, Fenn & Middleman [59] were considered in the analysis.

The stability parameter λ and the Reynolds number Re can be observed in Figure 4.14. Hence the liquid jets were clustered into water and other liquids jets. The first ones were drawn in blue and the second ones in red. Into the group of water jets the experiments of Grant & Middleman (gm), Takahashi & Kitamura (5-1 to 5-10), Ervine et al. (em1 to em12) and Florez (fl) described in Table 4.3 are shown in Figure 4.14. Specifically the values for the experiments of Ervine et al. with the same turbulence intensity value were grouped and fitted with a Bézier curve: a) em1 to em4, for Tu = 0.003, b) em5 to em8, for Tu = 0.03, and c) em9 to em12, for Tu = 0.08. Likewise, in order to keep in mind the turbulence level of the water jets measured by Ervine et al., their values are indicated in the graph.

Within the group of *other liquids* (see Table 4.4), particularly the experiments of Takahashi & Kitamura (5-2 to 5-8), Fenn & Middleman (s1 to s5) and Phinney (AI to DII) were considered in the analysis and included in the plot λ vs Re (see Figure 4.14).

In general the following discussion, according to information obtained from Figure 4.14 is presented:

- A common trend for distinct liquids, including water jets, was not observed. Moreover a suitable analysis by doing clustering from geometrical or dimensionless pa-

Name	*Year*	d (mm)	*A.R.*	ρ (kg/m^3)	μ 10^{-3} (Pa/s)	σ (N/m)	*Code*
Takahashi & Kitamura	1969	2.03	0.95	1110	3.68	0.0679	G5-2
		2.08	0.95	1110	3.68	0.0679	G5-3
		2.17	1.8	1110	3.68	0.0679	G5-4
		2.17	3.69	1110	3.68	0.0679	G5-5
		2.1	9.93	1110	3.68	0.0679	G5-7
		2.15	14.4	1110	3.68	0.0679	G5-8
Fenn & Midlemann	1969	0.833	51.9	960	0.49	0.0208	s1
		0.866	90.0	950	0.34	0.0205	s2
		0.866	480.19	950	0.20	0.0203	s3
		0.833	480.19	920	0.047	0.0193	s4
		0.833	480.19	850	0.013	0.0182	s5
Phinney	1973	0.493	1.035	1106	1.34	0.0775	AI
		0.206	1.031	1106	1.34	0.0775	BI
		0.125	1.027	1106	1.34	0.0775	CI
		0.0504	1.035	1106	1.34	0.0775	DI
		0.493	1.035	1116	1.41	0.0374	AII
		0.206	1.031	1116	1.41	0.0374	BII
		0.125	1.027	1116	1.41	0.0374	CII
		0.0504	1.035	1116	1.41	0.0374	DII

Table 4.4: Fluid properties and nozzle characteristics of several liquid jets. Data set from experiments of Phinney [2], Takahashi & Kitamura [98] and Fenn & Midleman [59].

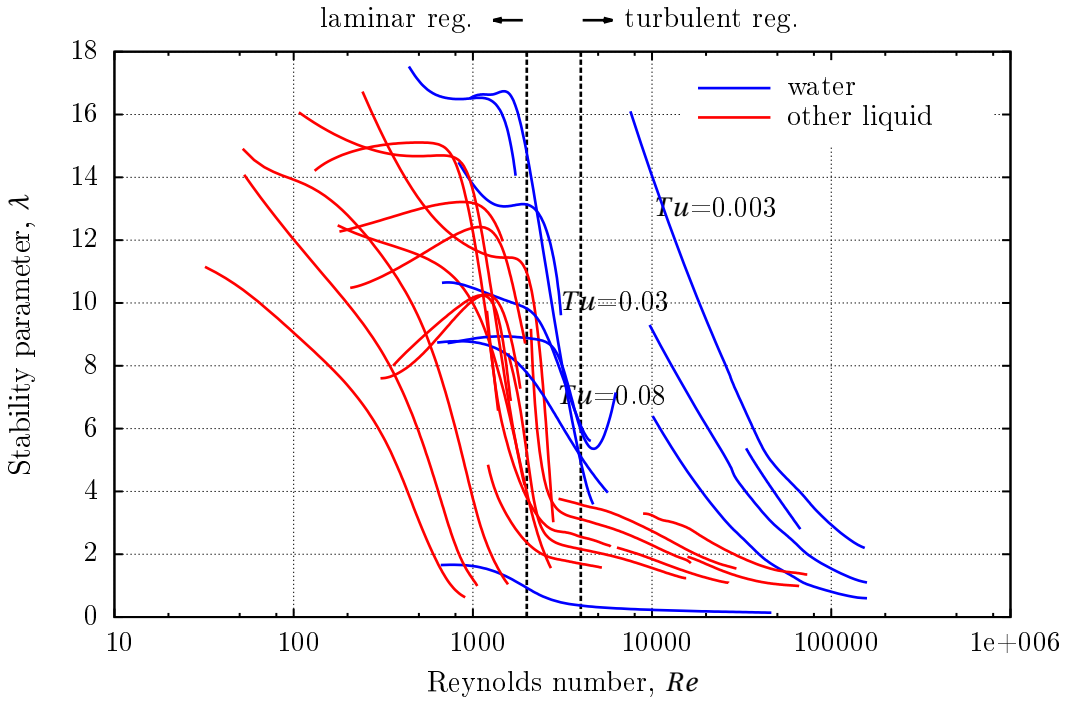

Figure 4.14: λ vs Re for water and other liquid jets at 1 atm.

rameters could not attained. Likewise it seems that other parameters, not included in the analysis, are affecting the breakup length description, or even it may suggest that the stability parameter is not an appropriate variable that expresses the variability of liquid jets.

The concept of the stability parameter λ, which has two interpretations as the reciprocal of the amplification rate for disturbances and the logarithm of the initial disturbance level, could be considered, as related to the turbulence intensity at the nozzle. However, once the experiments of Ervine at al. [11] are plotted, they suggest that the value of the turbulent intensity is dependent on the stability parameter, λ, but is common to all the values of the turbulence intensity as expected.

- The curve λ vs Re (see equation 2.11) proposed by Phinney [2] did not offer any additional advantage compared with the simplicity of the curve $\overline{L}$ vs Q_w (see Figure 4.12) in order to find a predictable function to estimate the breakup length of water and liquid jets.

- It is worth mentioning that the turbulence intensity in the nozzle exit has a strong effect on the dynamics of the jet, and until more data are available, a reasonably good relationship in order to understand the behavior and the physics of the breakup of liquid jets might not be attainable.

- If other liquids are intended to be analyzed and compared with the behavior of water jets, the experimental tests should be done under the same conservative conditions: level of turbulence, nozzle geometry, inlet conditions, among others.

In order to visualize and compare the behavior of water and other liquid jets, the curves $\overline{L}$ vs Q_w, similar to in Figure 4.13 were plotted by considering the following:

- A log-log plot is presented in order to capture the physics of the fluid for the smallest breakup length $\overline{L}$ and the lowest liquid discharges Q_w.
- All the experiments were executed under quiescent air and standard ambient pressure.
- The water jet experiments are colored with blue lines or blue dashed-lines as in Figure 4.13 observed for the experiments of Ervine et al. [11], Grant & Middleman [6], Takahashi & Kitamura [98] and the current research.
- The experiments of other liquid jets (except water) are colored in red or yellow. This are the experiments of Takahashi & Kitamura [98], Fenn & Middleman's [59] and Phinney [2].
- With the intention of not overcrowding the plot, only the representative experiments are presented individually or grouped. In the case of water jets the experiments with the same level of turbulence are grouped: em1 to em4 for $Tu = 0.003$, em5 to em8 for $Tu = 0.03$ and, em9 to em12 for $Tu = 0.08$. The experiments of Grant & Middleman [6] are identified with the legend gm, the current research with the legend fl, and the experiments of Takahashi & Kitamura [98] (5-1, 5-2, 5-4, 5-6, 5-8 and 5-10 of Table 4.3) are grouped together with the legend TKw.
- In the case of the experiments named *other liquids* (see Table 4.4), those of Takahashi & Kitamura [98] were grouped under the legend TKo.

  The experiments of Fenn & Middleman [59] were presented individually because they offer and cover a wider range of interest, with $0.013 < \mu < 0.49$ and $0.98 <$ ambient pressure < 1. These experiments are identified with the legends S1, S2, S3, S4 and S5. For this series of experiments the diameter was kept practically constant as well as the surface tension σ, five types of liquids were considered, consisting in varying the density of the liquid by 12%, and different viscosities were tested.

  Moreover the experiments of Phinney [2] are grouped with the legend Ph.

The curve breakup length vs discharge for water and other liquids is presented in Figure 4.15. As a consequence the following results were obtained:

- Once several liquid jets are plotted in diagram $\overline{L}$ vs Q_w, a consistent path attracts attention because it is common for all liquids in the lower part of the diagram. Although the turbulence intensity was not measured (except for the experiments of Ervine et al. [11]) in most of the experiments (see Tables 4.3 and 4.4), the trend of the different jets is to follow or to touch the herein called *lower envelope* of the breakup length curve. Obviously, the mechanisms of breakup are different because additional parameters are added by modifying the surface tension or the density, which cause the laminar-transitional region to be more or less flattened.

  However, after the water jet ends, the laminar regime (here referring to the peak on the stability curve), it reaches the lower envelope curve which is more or less

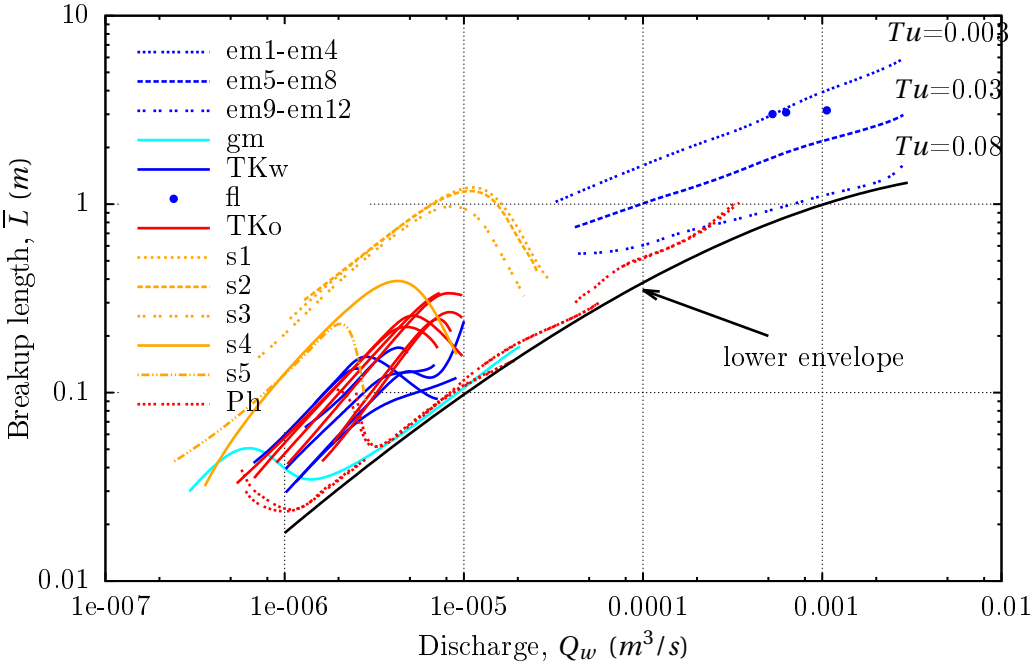

Figure 4.15: Curve breakup length vs discharge for different liquids jets.

coincident with the inflexion curve present between the transitional and turbulent regimes. But from here it can be coincident or not with the lower envelope curve. Unfortunately, these transitions have not been tested experimentally yet, but it would help to elucidate the mechanism of breakup and the impact of the turbulence intensity on it.

- The experiments 5-1 on water jets by Takahashi & Kitamura (see in detail in Figure 4.13), here grouped under the legend TKw, show partially the ascent in the turbulent regime. It seems that the turbulent intensity plays an important role because for this experiment the curve becomes suddenly steeper. Unfortunately this test was not performed beyond Q_w = 0.01 L/s but it may suggest that it was carried out under a low turbulence level ~ $Tu < 0.03$. For the rest of the experiments the trends suggest that they are reaching the lower envelope curve later on.

- The experiments on water jets by Grant & Middleman (gm) are located along the lower envelope curve, suggesting a higher turbulence level. By inference from the experiments of Ervine et al. [11] the turbulent intensity would be ~ $Tu > 0.08$.

- When the experiments of Takahashi & Kitamura in water (TKw) and other liquids (TKo) are compared, the positioning of the curves suggested that the set of experiments were done under the same turbulence level because the curves overlap. The only differences between both liquids are in the values of the viscosity which in the case of other liquid jets implies a delay in the breakup because the opposition of the viscous forces to the internal turbulence are lower than in water jets.

- A rough estimation of the turbulence level for the current experiments (fl), it would suggests that would be ~ $Tu < 0.01$.

- Fenn & Middleman's [59] experiments, identified with the legends s1, s2, s3, s4 and s5, show a wider range in the laminar and transitional regime than the water jets. In principle, as has been mentioned before, a general theory will not be available until more systematic experiments are done and a single parameter analyzed alone and its effect on the total behavior of the jet.
- Lower turbulence leads to longer break up, while higher turbulence will have a shorter breakup length.
- The lower envelope is not presented in terms of an equation because certainly it will move down as well as the turbulence intensity would be increased.
- Is there a maximal turbulence intensity attainable in circular nozzles?

The proposed equation by Ervine et al. [5], in spite of being the first approximation (and the only one until now) for determining the breakup length by including the turbulence intensity in the analysis, presents uncertainties which led to reject equation 2.30, which is based on the the following considerations:

- The experimental tests from [8] used to determine the linear function between the ratio lateral spread δ at a certain distance x versus the ratio of the streamwise turbulent component u' over the average velocity at the nozzle exit U_o , here represented by $\delta_2/x = 0.38 \;\; u'_x/U_o$ (equation 2.25), was limited to just six pairs of data. Furthermore there was not enough information provided concerning experimental conditions: how they were obtained, diameter of the pipe nozzle, initial velocity and, if δ obeys a statistical value from an experiment or from a point obtained from a single camera. According to their experiments it was assumed that the diameter is an independent variable.
- In spite of Ervine et al. [11] writing a paper in 1980 in which important experiments were done by measuring the turbulence intensity of water jets, it should be noted that none of their own data were included in the analysis, even though there was no mention at all of their previous research. On the contrary they just used limited data from other authors and skipped their previous research.

  However, in order to clarify, in Figure 4.16 the experiments of Baron (1949), McKeogh (1978), Ervine et al. (1980) for several levels of turbulence (omitted by Ervine et al. [5]), Whiter (1991) and the current research are presented.
- Once Ervine et al.'s [11] own data are included in Figure 4.16 it is clear that the hypothesis proposed in [5] is not correct at all and a new parallel line must be added.
- In Figure 4.16 the original linear fit obtained by Ervine et al. [5] is shown. Their originally proposed hypothesis (H1) considered that for all the water jets under different levels of turbulence the trend would be collinear. However, if the experiments of Baron (1949) were rejected, a second hypothesis (H2) would lead to establish that, once the turbulence level is increased, the higher the number of linear trends. It can be observed that for the experiments of Ervine et al. under a $Tu \geq 3\%$, the data are above the line labelled *Trend. H2: High Tu.* However the problem is still open and it should be verified by experimentation by testing the impact of varying the turbulence level and measuring the breakup length for pipe nozzles.

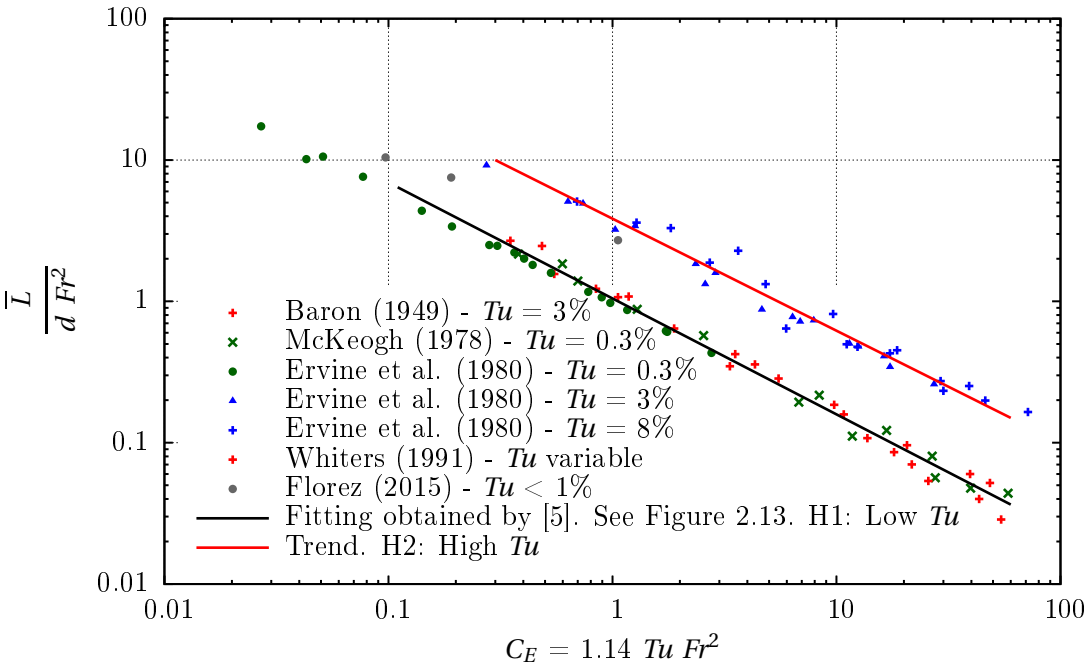

Figure 4.16: Breakup length in circular nozzles as function of the turbulent parameter C, according to [5].

4.3.3 Summary and future research

The formulae available in the literature for determining the breakup length of liquid jets emerging from circular nozzles have been discussed. Based on the analysis done in section 4.3 the following is concluded:

- All the formulae proposed in the literature for determining the breakup length $\overline{L}$ of water jets are valid only for the specific experimental conditions under which they were tested. Unfortunately many parameters such as the geometrical inlet conditions, nozzle geometry and level of turbulence of the flow have not been measured in detail or provided in the scientific literature, and as a consequence the wide variety of equations has generated confusion, with their discrepancies in the results.

- The equations presented in the Literature Review of the current research for calculating the breakup length of water jets are valid for just a certain domain of the turbulent regime of the flow, unless otherwise specified. Usually this is not mentioned in the papers or it is given as obvious. The explanation of the type of linear form (usually they relate the breakup length $\overline{L}$ or the breakup length ratio of $\overline{L}/d$ with other parameters) of such equations proposed in the literature is due to the fact that they just describe the linear trend in the turbulent section of the stability curve (see Figure 2.3) when the breakup length $\overline{L}$ is related to the exit velocity U_0. However it must be remembered that at high water velocities supercavitation may take place in the nozzle and an hysteresis behavior of the curve $\overline{L} = f(U_0)$ in the turbulent region can occur and as a consequence a unique equation is not valid even for the same nozzle and fluid conditions.

- Including the turbulence level Tu as a parameter for determining the breakup length $\overline{L}$ of water jets is necessary. Furthermore, for future analysis of the water breakup length the parameters shown in equation 4.18, such as: Tu, Re, We, ε/d and possibly Fr, should be considered.

- The only equation available in the literature based on measurements of the turbulence level Tu in jet nozzles (which is shown in Figure 2.13) has been proposed by Ervine et al. (1997) [5]. However, inexplicably, as mentioned above, these authors avoided and even did not mention their own studies from 1980 [11] where a wide range of experiments were done and the turbulence intensity was measured. If these experimental results were included in those of Ervine et al. (1997) (see Figure 4.16) it could be concluded that the relationship is not correct at all and two distinct groups can be identified: Tu below 1% and Tu greater than 3%. A transition between the different levels of turbulence was not observed and as a consequence more experimental tests are required in order to find a generalization to the behavior of the jet concerning the computation of the breakup length $\overline{L}$ from pipe nozzles.

4.4 Air entrainment mechanism in free falling water jets

When the water is moving in open channels, closed conduits or in free-fall, an interaction with the surrounding air is generated, whether by the moving of the air in its vicinity (because of friction with the undulations), by entraining into the liquid mass as bubbles, or by filling the spaces of the detached mass of liquid.

4.4.1 Conceptual frame

A fixed Control Volume CV is defined. It covers a flow pattern consisting of a water jet and a mass of air passing through a control surface as schematized in Figure 4.17. Hence, laterally the surface control is treated as a fixed boundary where there is no interchange of mass flow with the surroundings. Furthermore, the flow within the control volume is steady because the mass flow entering $\dot{m}_{in}$ and leaving $\dot{m}_{out}$ the control volume is balanced exactly.

The mass of flow ($\dot{m}$) at any cross section of a free falling water jet is composed of the falling liquid mass of water $\dot{m}_w$ and the mass flow of air $\dot{m}_a$:

$$\dot{m} = \dot{m}_w + \dot{m}_a \tag{4.22}$$

When a water jet falls the following physics dynamics occurs, accordingly to Figure 4.17:

- Once the water jet leaves the nozzle an interaction with the air take places because the jet surface roughness δ_2 increases as the liquid jet falls. This can be explained in terms of undulations on the water jet, from the effects of the turbulence level, which propagate towards the water surface (in the flow development region) and induces an increasing interaction with the adjacent air. Two masses of air flow can be distinguished during the interaction with the water jet: the air contained within

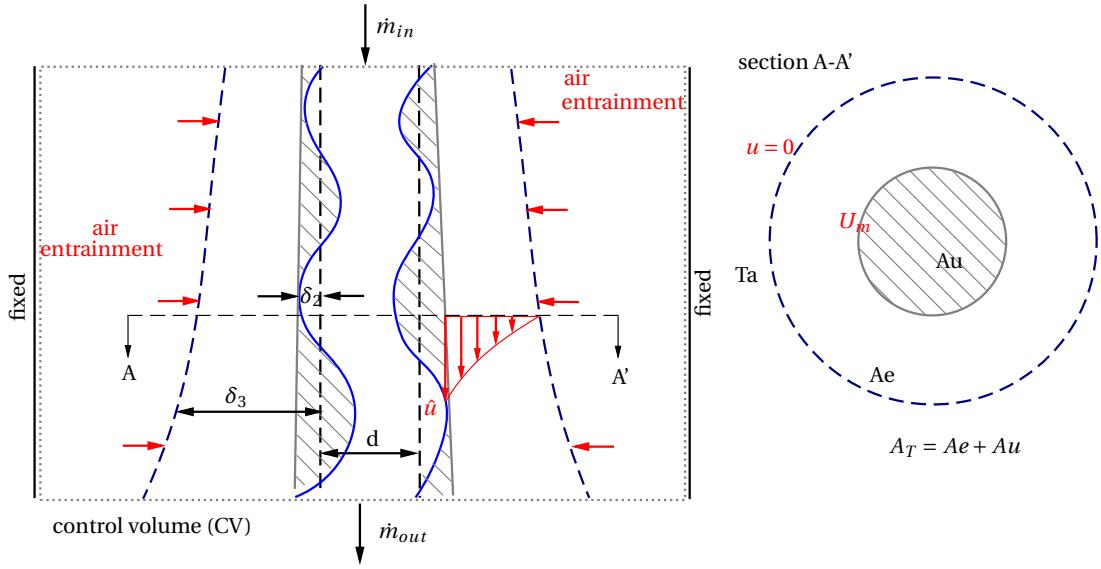

Figure 4.17: Air entrainment in a free falling water jet

the undulations of the surface roughness (here called *internal occupied air*) and the air which is moving in the vicinity named *enveloping air layer* until a certain limit where the air is in a quiescent state again.

- The *enveloping air layer* consists of a cylindrical ring layer of air enclosing the liquid jet. Likewise, the air is moving down because of the friction and the transfer of momentum by the surface undulations of the water jet. The topology of this layer is continually changing along the falling of the liquid jet and it is strongly influenced by the internal dynamics of the water and the turbulence. The width of the ring is defined as:

$$W = |\delta_2 - \delta_3| \tag{4.23}$$

  Moreover, the air velocity profile can be determined directly by anemometry up to a distance of ~ 2 mm from the *internal occupied layer*. The maximum air velocity u_m can be measured in the proximity of the falling water.

- If a cross section A-A' is defined, the schematized hatched area Au represents the cross sectional area where the water waves are moving in the development region while the water flow is not detached yet. The *internal occupied air* passing through the region Au cannot be determined easily because of the fast and sudden changes in the dynamics of the flow. In principle, the determination of the air velocity profile is based on assuming an *apparent air velocity in the surface roughness* $\hat{u}$ which is assumed to be the velocity in the air-water interface.

4.4.2 Setup of the model rig and experimental test procedure

A model family of circular nozzles have been tested with the geometric characteristics shown in Table 4.5. In the case of the circular nozzles an additional model has been tested (d = 10 mm) to widen the range of analysis of the scale effects. In Table 4.5 the

experiments assumed as prototype (d = 80 mm) and models (d = 40, 20 and 10 mm) have been defined, as well as the nozzle length L_n, the aspect ration of the nozzle $A.R.$, the length scale L_r, and the diameter ϕ of the casing pipe of length X_c (see Figure 4.18).

Experiment	d (mm)	L_n (mm)	$A.R.$	L_r	X_c (m)	ϕ (mm)
Prototype	80	240	3	1	5.00	400
Model 1	40	120	3	2	2.50	200
Model 2	20	60	3	4	1.25	100
Model 3	10	30	3	8	0.625	50

Table 4.5: Geometric characteristics of the circular nozzles.

The range of operation of the water discharge Q_w for the circular (see Table 3.1) prototype nozzles was determined experimentally based on the maximum water elevation and the minimum operating water elevation (without generating suction of air) in the water tank. Based on this, by using the Froude similarity law the required flow discharges were calculated to define the operating rules in models and prototypes as presented in Table 4.5. Accordingly, for each nozzle the following experimental procedure was carried out in order to determine the total air entrainment conveyed with a water jet:

- Each nozzle was mounted on the bottom hole of the water tank as is shown in Figure 3.1.
- For each casing pipe length X_c a series of discharges Q_w were run, corresponding to the highest and lowest water elevations in the tank. In the case of the prototype (diameter d = 80 mm) the casing pipe lengths X_c which corresponds to a length of 5.00 m was tested.

  The configuration of the casing pipe length (X_c = 2.50 m and ϕ = 200 mm) for the model 1 (diameter d = 40 mm) in the rig is presented in Figure 4.18. The air entrainment into the water jet was quantified for each casing pipe length by positioning a vane anemometer on the top of it.
- At 50 mm from the upper part of the casing pipe, in the vicinity of the nozzle, an adapter was built in order to mount a vane anemometer.
- The volumetric flow rate of air Q_a was computed by using the continuity equation:

$$Q_a = Av\, u_a \tag{4.24}$$

  where Av is the cross sectional area of the vane anemometer and u_a is the average air velocity measured with the vane anemometer during a time t = 60 s.
- The water discharge Q_w was determined by means of the magnetic flow meter located in the bottom of the rig.

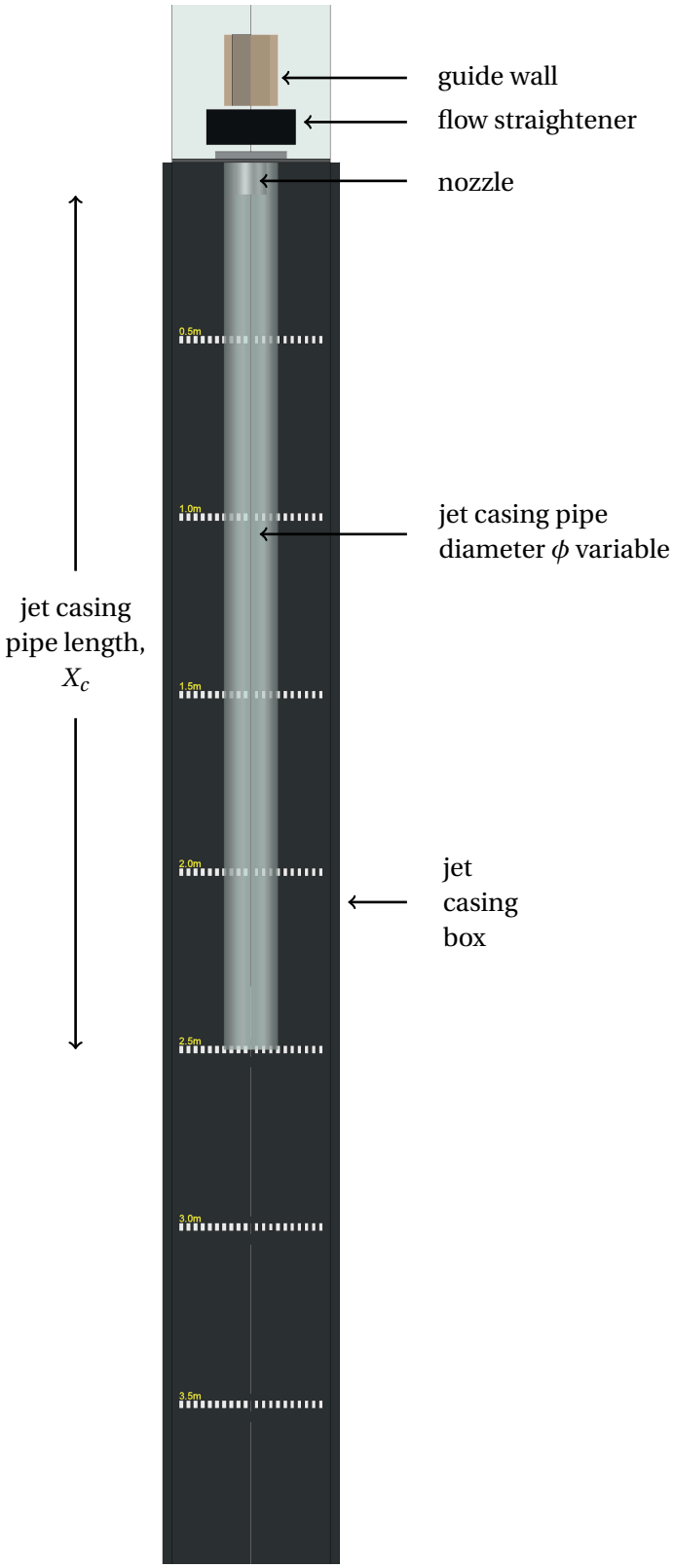

Figure 4.18: Model rig with a casing pipe for the measuring of the air entrainment.

- The time average air concentration C (defined in equation 2.3) was calculated as:

$$C = \frac{Q_a}{Q_a + Q_w}$$

- Likewise, the air entrainment ratio, the so called β-parameter, was calculated as:

$$\beta = \frac{Q_a}{Q_w} \tag{4.25}$$

- By using the Froude similitude law $Fr_r = 1$ the model family of nozzles can be compared and analyzed (based on equation 2.9, where the subscript r means scale. As the acceleration of gravity g is the same ($g_r = 1$) for model (m subscript) as well as prototype (p-subscript), then the liquid discharge required for the under scaled model Qw_m can be calculated as:

$$1 = \frac{U_r}{\sqrt{L_r}} \tag{4.26}$$

$$U_r = L_r^{1/2} \tag{4.27}$$

$$\frac{U_p}{U_m} = L_r^{1/2} \tag{4.28}$$

$$U_m = \frac{U_p}{L_r^{1/2}}, \tag{4.29}$$

then, as $Qw_r = U_r \ L_r^2$ and Qw_r=Qw_p / Qm_m,

$$Qw_m = \frac{L_r^{5/2}}{Qw_p}. \tag{4.30}$$

- For the calculation of dimensionless quantities such as the Weber (*We*), Reynolds (*Re*), Froude (*Fr*) and Ohnesorge (*Oh*) numbers,the following values of the physical properties of the water were considered: density ρ_w = 1000 kg/m^3, surface tension air-water σ = 0.07275 N/m and dynamic viscosity μ = 0.001 kg/(m s).

4.4.3 Results

In Figure 4.19 the results of the experimental tests of the volumetric flow rate of air Q_a obtained for several water discharges Q_w are presented. They correspond to the experimental tests of Q_a obtained for the length X_c shown in Table 4.5 for the prototype (d = 80 mm) and their respective models (model 1 - d = 40 mm, model 2 - d = 20 mm and model 3 - d = 10 mm).

4.4.4 Scale effects

Falvey [16] remarked that physical models should accurately predict the spread and energy content of prototype jets if the turbulent intensity in the model is similar to that in the prototype. As a consequence, by considering the analysis described in section 4.3, it

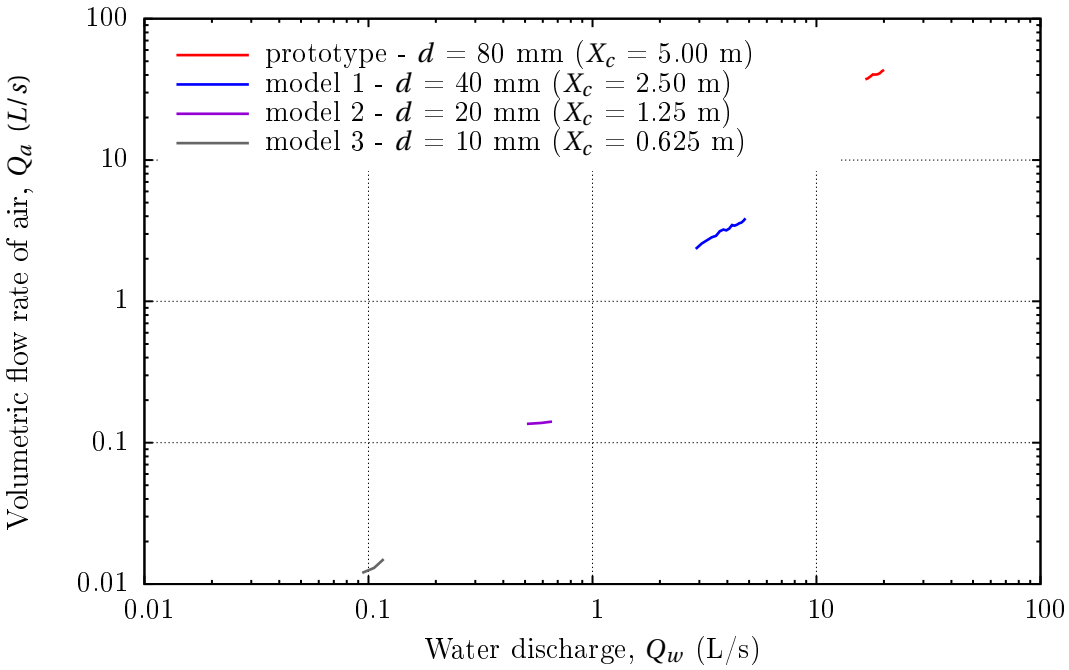

Figure 4.19: Volumetric flow rate of air (Q_a) vs water discharge (Q_w) obtained for circular nozzles.

is understood that the experiments would be subject to the same level of turbulence (or similar) in the nozzle inlet as has been already explained.

The value of the length scale ratio L_r is based on equation 2.35, L_r=L_p/L_m, where L_p is the length in the prototype and L_m is the length of the model. Likewise, the air entrainment coefficient scale β_r can be calculated as,

$$\beta_r = \frac{\beta_p}{\beta_m}, \tag{4.31}$$

where, β_p and β_m are the air entrainment coefficients obtained in the prototype and model.

In order to analyse the scale effects, the Froude similarity law $Fr_r = 1$ was used. This means that, by using equation 4.30, the discharges in the models Qw_m could be computed. In Table 4.6, the values of the water discharge and the air entrainment for the prototype (Qw_p and Qa_p), as well as the values of the water discharge and the air entrainment for the models (Qw_m and Qa_m) are presented.

Based on the experimental tests compiled in Table 4.6, in Figure 4.20 the variation of the air entrainment coefficient β with respect to the length scale L_r in the range $3.7 \leq Fr \leq 4.5$ for circular nozzles is presented. Likewise, the average air entrainment coefficient $\overline{\beta}_{L_r=1}$, $\overline{\beta}_{L_r=2}$, $\overline{\beta}_{L_r=4}$ and $\overline{\beta}_{L_r=8}$ were computed for the experiments with corresponding length scales 1, 2, 4 and 8, respectively.

Table 4.6: Water discharge, air entrainment and air entrainment coefficient for the prototype and models.

Fr	Prototype - d = 80 mm			Model 1 - d = 40 mm			Model 2 - d = 20 mm			Model 3 - d = 10 mm		
	Qw_p (L/s)	Qa_p (L/s)	β	Qw_m (L/s)	Qa_m (L/s)	β	Qw_m (L/s)	Qa_m (L/s)	β	Qw_m (L/s)	Qa_m (L/s)	β
4.50	20.03	43.44	2.2	3.54	2.93	0.83	0.626	0.140	0.22	0.111	0.0140	0.13
4.40	19.59	42.50	2.2	3.46	2.866	0.83	0.612	0.139	0.23	0.108	0.0136	0.13
4.30	19.16	41.16	2.1	3.39	2.8	0.83	0.599	0.139	0.23	0.106	0.0133	0.13
4.20	18.72	40.39	2.2	3.31	2.73	0.82	0.585	0.138	0.24	0.103	0.0130	0.13
4.11	18.29	40.20	2.2	3.23	2.67	0.83	0.571	0.138	0.24	0.101	0.0127	0.13
4.01	17.85	40.30	2.3	3.16	2.6	0.82	0.558	0.137	0.25	0.099	0.0124	0.13
3.91	17.41	38.99	2.2	3.08	2.54	0.83	0.544	0.137	0.25	0.096	0.0121	0.13
3.81	16.98	37.90	2.2	3.00	2.47	0.82	0.531	0.137	0.26	0.094	0.0118	0.13
3.71	16.54	37.20	2.2	2.92	2.41	0.82	0.517	0.136	0.26	0.091	0.0115	0.13

Furthermore, in order to analyse the variation of the air entrainment scale as the length scale is increased, in Figure 4.21 the air entrainment coefficient ratio β_r is plotted against the length scale L_r for different Froude numbers ($3.5 \leq Fr \leq 4.5$).

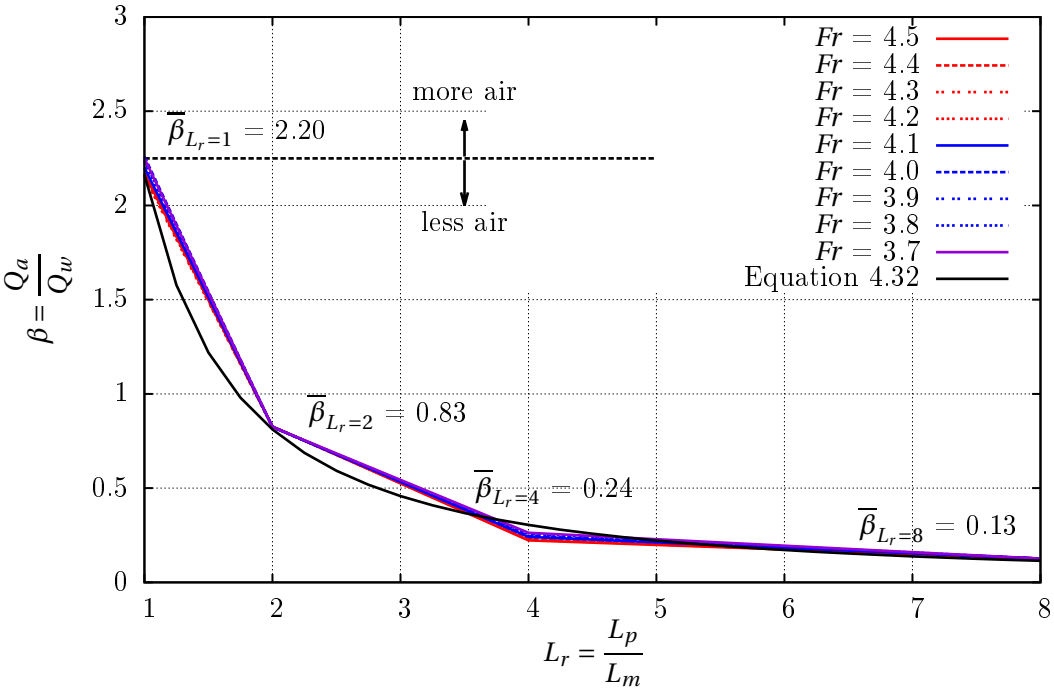

Figure 4.20: Variation of the air entrainment coefficient β with respect to the length scale L_r for circular nozzles.

Figures 4.20 and 4.21 thus reveal the following about the air entrainment:

- As the length scale increases, the air entrainment coefficient (β-parameter ratio) decreases. The trend obtained experimentally agrees with the results found in other applications in hydraulic engineering regarding the reduction of the air interaction with the water as the model size reduces, which is equivalent to an increase of the length scale L_r. In the first interval from $L_r = 1$ to $L_r = 2$ the function is rapidly decreasing in comparison with the other intervals. If the length scale $L_r = 1$ is reduced to a half $L_r = 2$, the average air entrainment coefficient reduces from $\overline{\beta}_{L_r=1} = 2.20$ to $\overline{\beta}_{L_r=2} = 0.83$. This means that the air entrainment ratio β reduces by 60%.

  In the same way, for the second interval ($2 < L_r \leq 4$), when $L_r = 4$, $\overline{\beta}_{L_r=4} \simeq 0.24$, the air entrainment coefficient reduces by 70%.

- Afterwards, when $L_r > 4$, the rate of change of the function reduces further. It is worth mentioning that for this third interval ($4 < L_r < 8$) the air entrainment coefficient varies less, just changing from $\overline{\beta}_{L_r=4} \simeq 0.24$ to $\overline{\beta}_{L_r=8} \simeq 0.13$ when the length scale increases from $L_r = 4$ to $L_r = 8$. As a consequence, the air entrainment coefficient reduces by 45%.

- Although for this third interval ($4 < L_r < 8$) the reduction of the air entrainment coefficient is lower, the percentage of reduction of the air entrainment coefficient is still high (45%). It should be kept in mind that each interval is evaluated by considering that the length scale L_r is reduced by a half.

- In order to describe the relation between the air entrainment coefficient β and the length scale L_r for the four diameters tested in the range $3.5 \leq Fr \leq 4.5$ an equation with a coefficient of determination $R^2 = 0.98$ was computed and plotted in Figure 4.20:

$$\beta = 2.16 L_r^{-1.41} \tag{4.32}$$

- In Figure 4.21 it can be seen that the relation of the air entrainment coefficient scale β_r and the length scale L_r of a model family of nozzles under the Froude similarity criteria can be described by a linear function. By using the Least Square Fitting of lines method with a constraint at $(L_r, \beta) = (1,1)$, the following equation is obtained:

$$\beta_r = 2.4 L_r - 1.4. \tag{4.33}$$

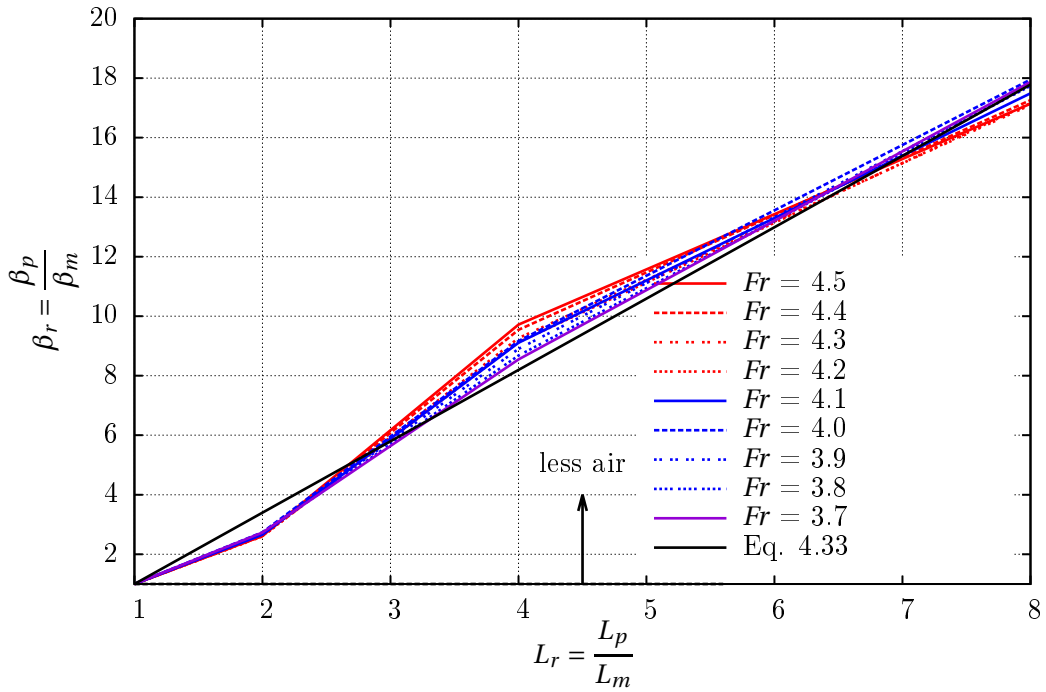

Figure 4.21: Variation of the air entrainment coefficient scale β_r with respect to the length scale L_r for circular nozzles.

- According to the discussion above, based on Figure 4.20, if the scale effects were low or negligible it would be expected that the reduction of the air entrainment coefficient between consecutive length scales be low. However that was not the case obtained here.

  Although it was expected that the curve would start horizontally from the left side $L_r = 1$ before turning downwards and subsequently flattening out after $L_r \approx 2$, the

curve continued to decrease such that scale effects were still dominant in the range $L_r = 4$ to $L_r = 8$.

Additionally due to restrictions on the model rig, the range of experimentation is limited. Ideally larger diameters could have been used, as well as higher water velocities in the nozzle exit. In that case there would have been an increase in the air-water interaction (to generate disintegration and breakup), greater capabilities for the instrumentation, and better approximation of the scales and sizes present in nature.

- In general it should be outlined that, independent of the model analyzed, any study or research for describing the interaction of the air with the water in under-scaled models should not be extrapolated or generalized to other applications in hydraulic engineering in terms of the length scale L_r because each model has its own restrictions, boundaries and dynamics. However, in the particular case of free falling water jets, the results obtained here confirm the findings by other authors in which they summarized that the smaller the model, the smaller the air entrainment.

The length scale L_r may not represent or explain adequately the scale effects in a model family of water jets, and an analysis is required in order to analyze the experimental tests in terms of dimensionless numbers, which could contribute to exploring possible generalizations, independent of the length scales chosen. If the length scale L_r is considered to be the only independent parameter of reference for predicting scale effects, this could contribute to errors in the assumptions. For example, in terms of the Ohnesorge diagram, a model family of free falling water jets will not reproduce the same results if the model family of experiments are located in region I or region III of Figure 2.2, because the dynamic of break up and mode of disintegration are distinct and their mechanisms are associated with a certain Reynolds number *Re*.

As a consequence, based on experimental tests compiled in Table 4.6 and in order to obtain a generalization of the scale effects, independent of the length scale L_r used, in Figure 4.22 the variation of the air entrainment coefficient β with respect to the Reynolds number *Re* in the range $3.7 \leq Fr \leq 4.5$ for circular nozzles is presented.

Furthermore, to compare the results and detect differences between scales, in Figure 4.23 the boxplot of air entrainment coefficient ratio β_r is plotted against Froude number ($3.5 \leq Fr \leq 4.5$) for the model family of nozzle pipes. For the specific experiment named prototype ($d = 80$), the air entrainment ratio is defined as $\beta_r = 1$ from equation 2.35.

Concerning Figures 4.22 and 4.23, the following can be concluded about the scales effects in a model family of free falling water jets in the range of $3.7 \leq Fr \leq 4.5$:

- Based on Figure 4.22, *Re* vs β, the left side of the curve fitted ($Re < 40000$) shows that the air entrainment coefficient β has a decreasing rate of change, and also it is trying to reach a horizontal plateau as the Reynolds number reduces. Although for this region the scale effects are still high, the results for this lower interval would suggest that more experiments with lower Reynolds numbers would be required in order to be able to obtain a generalization of the phenomenon consisting in minimizing the impact of the scale effects with a reasonable tolerance.

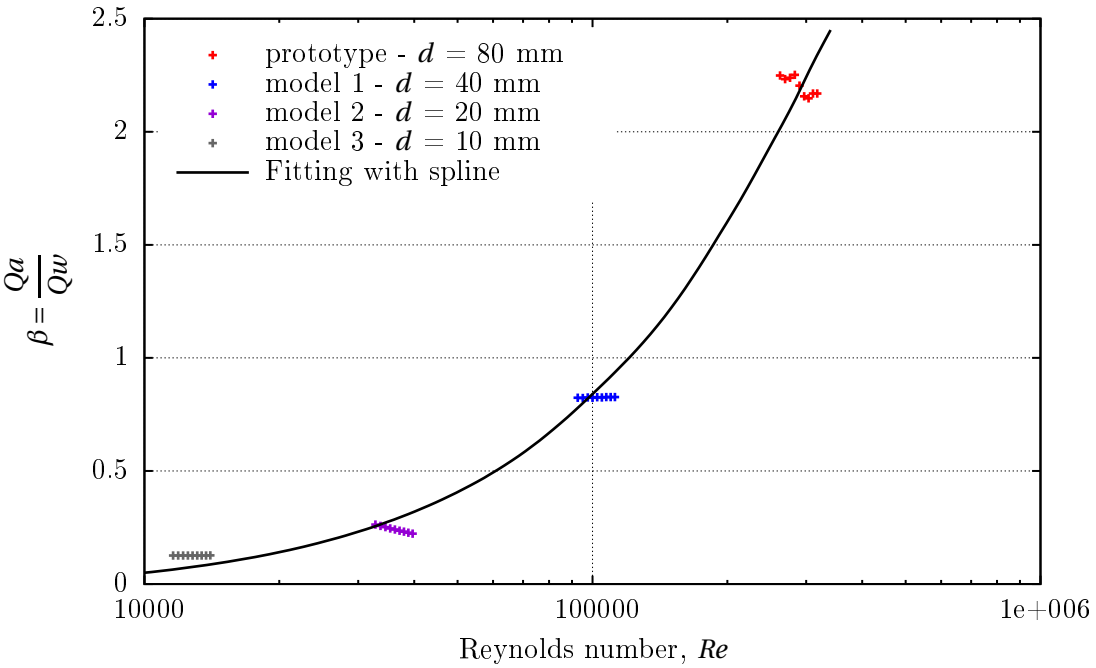

Figure 4.22: Reynolds number (*Re*) vs air entrainment coefficient (β) obtained for circular nozzles in the range of $3.7 \leq Fr \leq 4.5$.

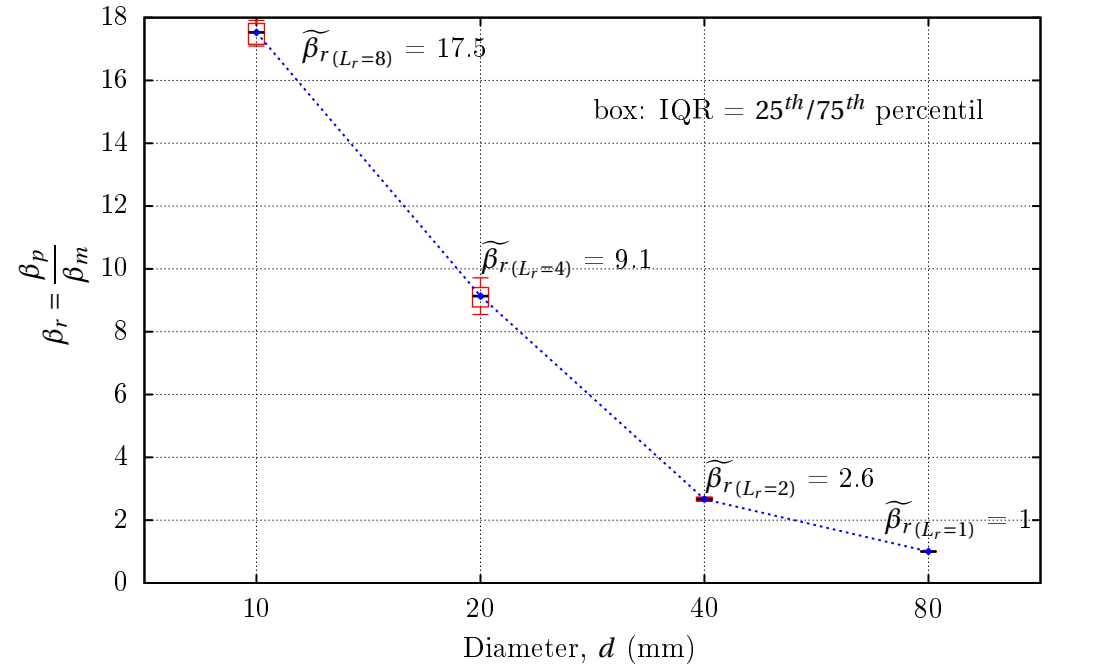

Figure 4.23: Boxplot of air entrainment ratio β_r for a model family of four nozzle pipes in diameters d of 10 mm (model 3 - $L_r = 8$), 20 mm (model 2 - $L_r = 4$), 40 mm (model 1 - $L_r = 2$) and 80 mm (prototype - $L_r = 1$) in the range $3.5 \leq Fr \leq 4.5$.

- However, as the precept of hydraulic modelling is to approximate results in nature, the interest of the research is in terms of increasing the range of experimentation for higher Reynolds numbers (*Re*).

- Once the Reynolds number is increased (according to Figure 4.22) until the maximal experimented ($Re \approx 2.9 \times 10^5$), it was found that the steepness of the fitting curve between model 1 and prototype is still high, the differences of the averaged values of the air concentration coefficient are also high and an inflection point is not seen at all. As a consequence, the aim of reaching an upper plateau was not achieved and it would suggest that additional experiments should be done with higher Reynolds numbers. However, this was not possible for the current research due to actual limitations of size and height of the Laboratory facilities.

- Concerning Figure 4.23, the air entrainment coefficient ratio β_r was grouped for each diameter and the range of flow conditions experimented $3.7 \leq Fr \leq 4.5$. By convention in such boxplots, used in descriptive statistics, it displays above and below the range of variation (the maximum and minimum value of the data set), the interquartile range (IQR) in the central rectangle, the first quartile (or 75^{th} percentile) in the lower part of the box, the third quartile (or 25^{th} percentile) in the upper part of the box and the typical value or median (50th percentile) represented by a horizontal bold line inside the rectangle.

  The median value obtained for the air concentration scale β_r for a certain length scale $L_r = j$ is

  $$\widetilde{\beta_r}_{(L_r=j)} \tag{4.34}$$

  where j is the length scale 1, 2, 4 or 8 for the diameters 80 mm, 40 mm, 20 mm and 10 mm, respectively.

  The median value of the air concentration scale β_r for d = 10 mm is $\widetilde{\beta_r}_{(L_r=8)} \approx 17.5$. This means that the averaged air entrainment coefficient $\overline{\beta}_{L_r=8}$ for model 3 (d = 10 mm) is approximately 17.5 times smaller than obtained for prototype (d = 80 mm). Likewise, for model 2 with d = 20 mm, $\widetilde{\beta_r}_{(L_r=4)} \approx 9$. Which implies that $\overline{\beta}_{L_r=4} \approx 9$ times smaller than the prototype. In the same way, for model 1 with d = 40 mm, $\widetilde{\beta_r}_{(L_r=2)} \approx 2.6$ which implies that $\overline{\beta}_{L_r=4} \approx 2.6$ times smaller than obtained for the prototype. Finally, the prototype with d = 80 mm as reference, will have $\widetilde{\beta_r}_{(L_r=1)} \approx 1$.

- As a consequence of the values of the median value of the distinct scales $\widetilde{\beta_r}_{(L_r=j)}$ still being high, specifically for the length scale L_r = 2 with d = 40 mm, a value of $\widetilde{\beta_r}_{(L_r=2)} \approx 2.6$ was obtained.

  As confirmed in Figure 4.23, a lower plateau region by the right side of the figure (due to low values of $\widetilde{\beta_r}_{(L_r=j)}$) was not found, and as a consequence a modelling criterion cannot be established unless the diameter of nozzle be increased and the Reynolds number *Re* as well.

- In general it can be concluded that the Froude number F_r criterion establishes similitude for forces attributable to fluid inertia and gravity, but it may be insufficient for prescribing similitude of air entrainment. However, the findings presented here can contribute to clarify and understand the variation of the air en-

trainment as the model size is reduced, when ranges of experimentation of hydraulic models (under certain Froude or Reynolds number) can be modeled under low scale effects.

- Finally it is concluded that a generalization regarding scale effects cannot be established yet unless experiments with higher Reynolds number be done ($Re > 1.5 \times 10^5$)), and preferably by considering also enlarging the experimental facilities including testing higher diameters ($d > 80$ mm).

  Likewise in reference to Figure 4.22 for $d = 40$ mm, it would be expected that the path be steeper at $Re \approx 1.5 \times 10^5$ and then with a lower slope until the prototype. It seems that the inflection point would take place in the interval $1.0 \times 10^5 < Re < 2.8 \times 10^5$.

4.5 Air velocity distribution in the surroundings of a free falling water jet

Whenever a moving liquid jet enters a quiescent body of air, it generates an interaction with it by means of the turbulence. Subsequently, it can be transported and even mixed if the kinetic energy of the water jet is high enough. During the fall, the shear stress of the water jet is transmitted to the surrounding mass of air, being dragged with it, as schematized in Figure 4.17.

In a similar way, as is explained in the sketch formulated by Falvey [16] to describe the air-entraining flow regimes in chutes, the air boundary layer grows in the vicinity of the smooth surface (Zone A according to Ervine et al. 1997 [5]) and the rough surface of the jet (Zones B and C). The distribution of the air can be idealized as a mass of air trapped between one moving vertical plate, which is nothing else than the water falling jet, and an imaginary and stationary boundary plate where the air velocity is equal to zero ($u_a = 0$). As a consequence, theoretically it is expected that on the moving boundary the air velocity u_a and the water velocity in contact with the air u_y will move at the same speed ($u_a = u_y$).

4.5.1 Experimental test

The air velocity profile was measured at several distances from the nozzle exit for circular nozzles with diameters of $d = 20$ mm, $d = 40$ mm and $d = 80$ mm with the geometric parameters shown in the Table 4.5. The diameter $d = 10$ mm was not tested due to the low values of the air velocity obtained during the pre-tests.

By convention, the x-axis is the downstream distance along the jet (measured from the nozzle exit) and the y-axis is the cross-jet radial distance from its centerline. The distances where the air velocity was measured for the different nozzle diameters are summarised in Table 4.7.

By using the vane anemometer described in chapter 3, the air velocity was measured at several distances from the nozzle in the surroundings of the water jet. The correct positioning of the meter in the vicinity of the jet was guaranteed by means of a plumb

Distance	d = 20 mm	d = 40 mm	d = 80 mm
x_1	0.965	0.905	0.794
x_2	1.965	1.905	1.294
x_3	2.965	2.905	1.794
x_4	3.965	3.905	2.294
x_5			2.794
x_6			3.294
x_7			3.794

Table 4.7: Distances x where the air velocity was measured. All units are in metres.

bob whose pointed tip was calibrated with the axis head of the vane anemometer which was attached to a suitable mounting. With this support, it had the possibility of sliding in the radial direction to any desired position. Furthermore with a ruler attached to the support, the displacement (in millimeters) of the anemometer in the y-axis could be controlled to obtain the velocity profile at a certain distance from the nozzle exit. The water discharges used are presented in Table 4.8.

Experiment	d = 20 mm		d = 40 mm		d = 80 mm	
	Qw (L/s)	Fr	Qw (L/s)	Fr	Qw (L/s)	Fr
1	0.582	4.2	3.29	4.2	16	3.6
2	0.786	5.6	3.86	4.9	19	4.3
3	0.932	6.7	4.44	5.6		
4	1.09	7.8				
5	1.24	8.9				

Table 4.8: Water discharges Q_w and corresponding Froude number Fr tested.

In Figures 4.24, 4.25 and 4.26 the air velocity u_a profiles obtained in the surroundings of the water jets are plotted against the ratio y/r, where y is the distance from the nozzle axis in the horizontal direction to the point where the air velocity was measured, and r is the radius of the nozzle. By convention, $y = 0$ corresponds to the nozzle axis.

In order to visualize more clearly the air distribution in the proximity of the water jet the y-axis of the plots has been inverted, and the 0-value in the x-axis is the centerline of the nozzle. This means that the abscissae of the plot at (y-values) 10 mm, 20 mm and 40 mm, corresponding to the diameters of 20 mm, 40 mm and 80 mm, are the outer distances of the nozzle. This can be observed in Figure 4.17, as well as the area of influence Ae where the moving air is measured.

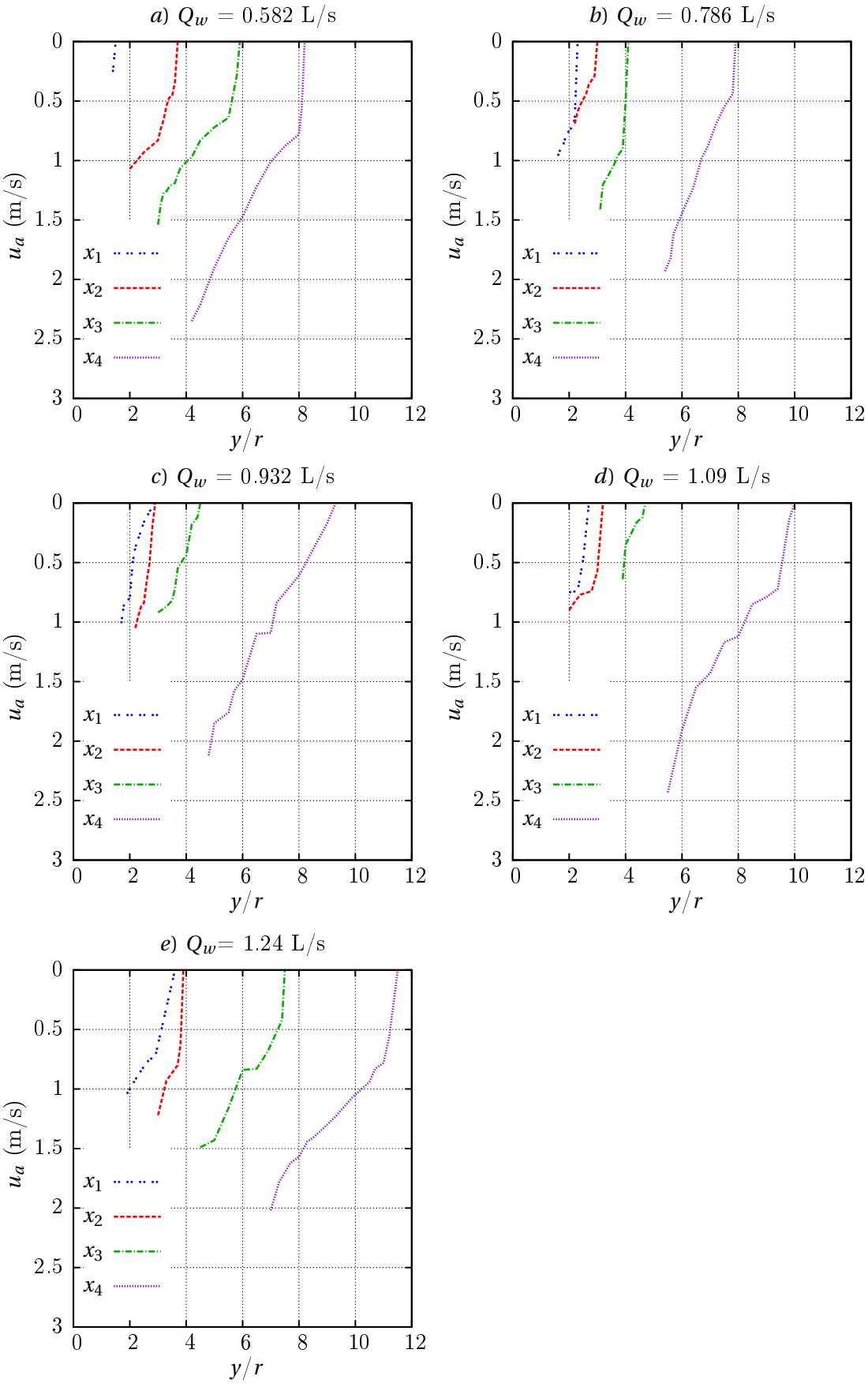

Figure 4.24: Air velocity distribution around a falling water jet for d= 20 mm.

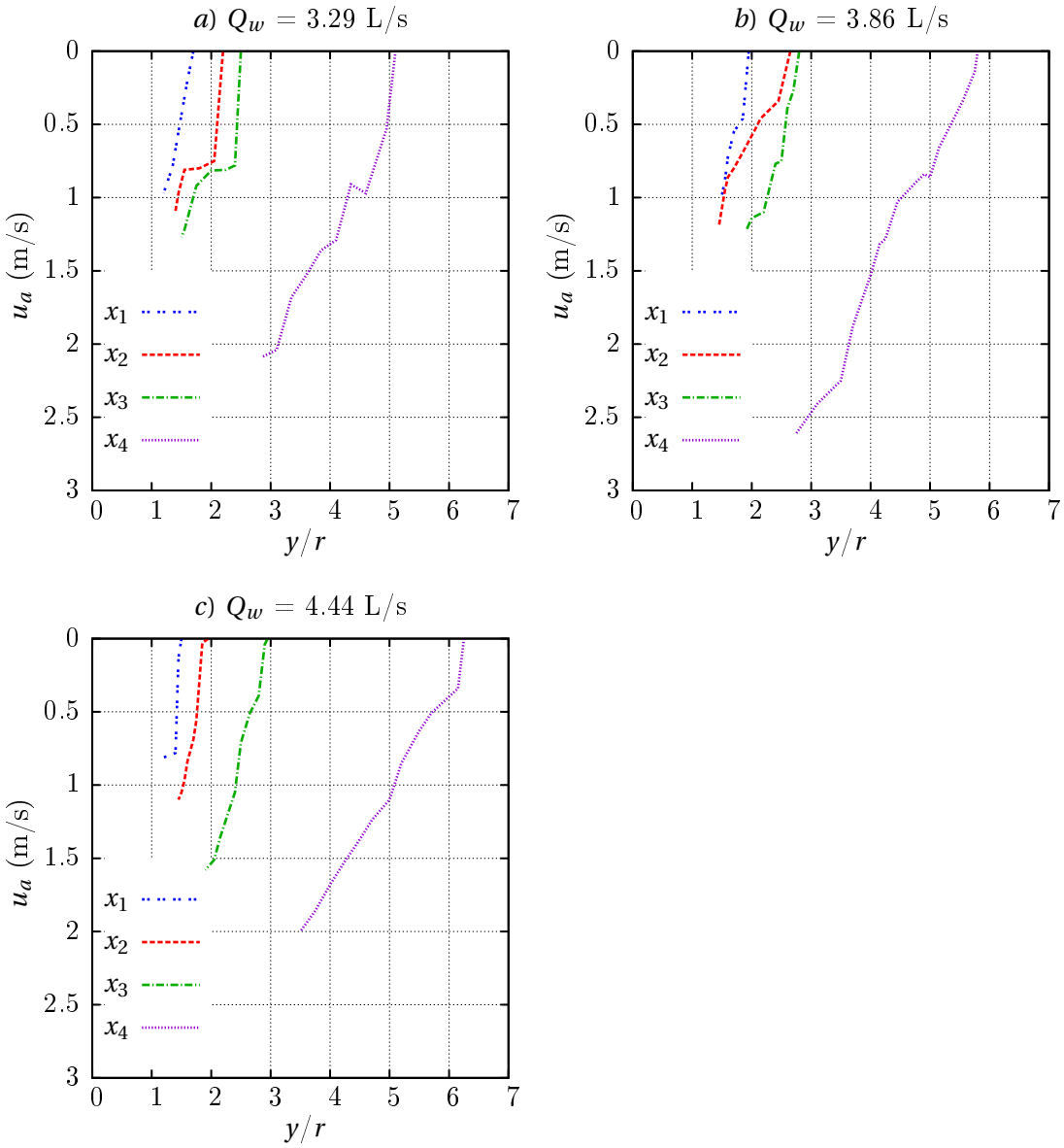

Figure 4.25: Air velocity distribution around a falling water jet for $d = 40$ mm.

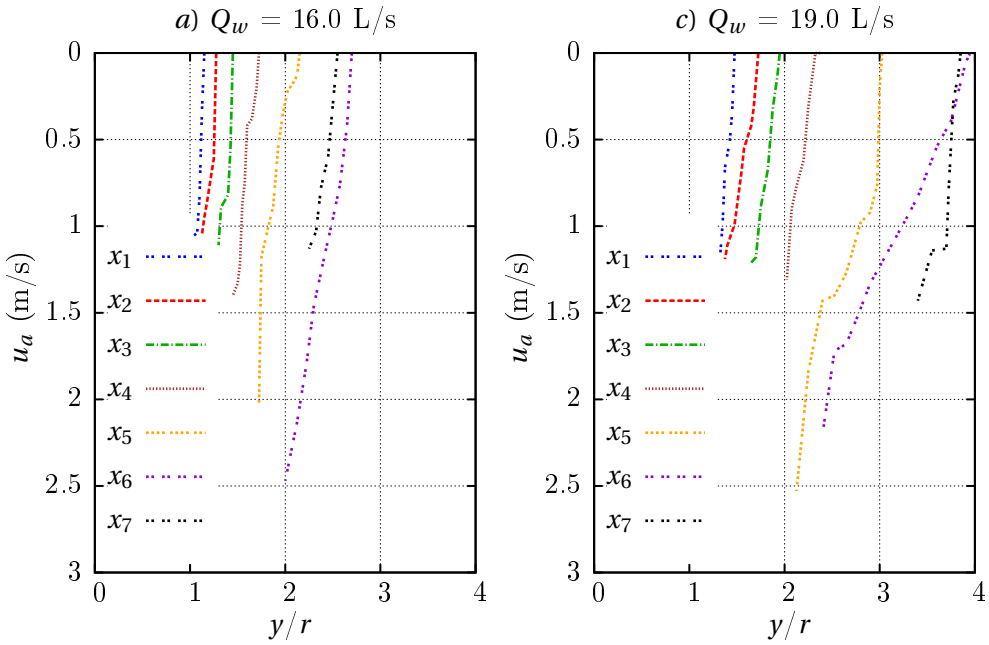

Figure 4.26: Air velocity distribution around a falling water jet for d = 80 mm.

4.5.2 Experimental results

Sikora [99] (reported by [16]) reasoned that the mean air velocity could not exceed the mean water velocity. Experimentally it has been observed in Figures 4.24, 4.25 and 4.26 that at the vicinity of the water jet the air velocity is lower than that of the water jet. This situation may be explained because the closest possible distance reachable for measuring the water jet surface is 2 mm. Recognising this limitation, this was a first attempt to measure and visualize the behavior of the air close to a water jet, as until now experimental measurements of the air velocity close to falling water jets have not been performed. Even Falvey in 1980 [16] claimed that "*unfortunately, data are not presently available that will allow the computation of the shear velocity and boundary layer thickness in the air surrounding a jet for a given jet geometry and flow rate*". Additionally to his previous observations, he suggested that the following equation (2.33) should represent the air velocity profile for any water jet:

$$\frac{U-u_a}{u*} = f\left(\frac{y_a - r_w}{\delta}\right),$$

where U is the water jet velocity, u_a is the air velocity at a point located at distance y_a from the jet centerline, $u*$ is the shear velocity, y_a is the distance from the water surface, r_w is the water jet radius and δ is the thickness of the velocity profile. In Figure 4.27 the experimental tests compared with the formula proposed by Falvey [16] are shown.

According to these results, it can be concluded that equation 2.33 is not appropriate for representing the air velocity profile in the vicinity of free falling water jets. As a consequence, it has been found that a function of the form 4.35 suitably describes the air

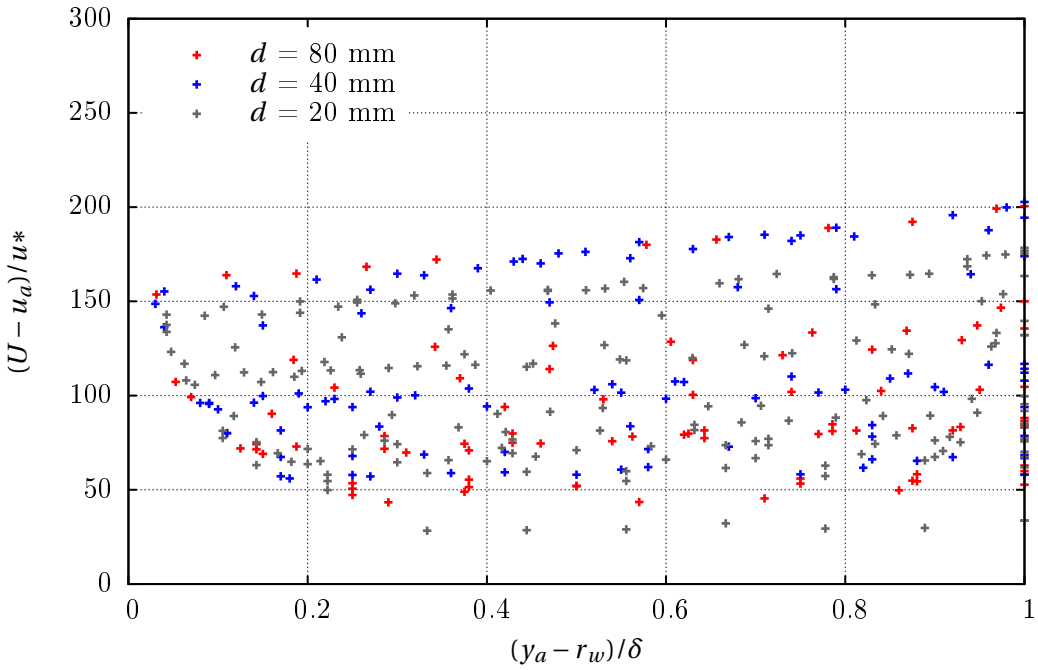

Figure 4.27: Normalized air velocity profiles in free falling water jets based on equation 2.33 suggested by Falvey [16].

velocity profile close to free falling water jets:

$$\frac{u_a}{U} = f\left(\frac{y_a - r_w}{\delta}\right). \tag{4.35}$$

where u_a is the air velocity at a point located at distance y_a from the jet centerline, U is the water jet velocity, y_a is the distance from the water surface, r_w is the water jet radius and δ is the thickness of the air velocity profile. Figure 4.28 shows the experimental set-up which led to the results based on equation 4.35.

In order to represent the physics of the experiments, an approximating cubic spline proposed by Fenton [100] was used. The advantage of such a spline method with respect to others is that this one uses weights for each point in order to constrain the spline at the points $(x_0, y_0) \longrightarrow (0,1)$ and $(x_1, y_1) \longrightarrow (1,0)$. According to the results shown in Figure 4.28, the following can be concluded:

- At a distance of 10% (0.01 in Figure 4.28) of the air velocity profile thickness, measured from the water surface, the air velocity has reached ≈ 0.18 of the water velocity U.
- In general, two distinct linear trends characterize the air velocity profile: a steep slope close to the water jet with high velocities and, a predominant slight slope (m ≈ -0.20) in the remaining ≈ 90% of the distribution of the air velocity profile.
- Equation 4.35 seems to represent with good accuracy the air velocity profile close to free falling water jets.

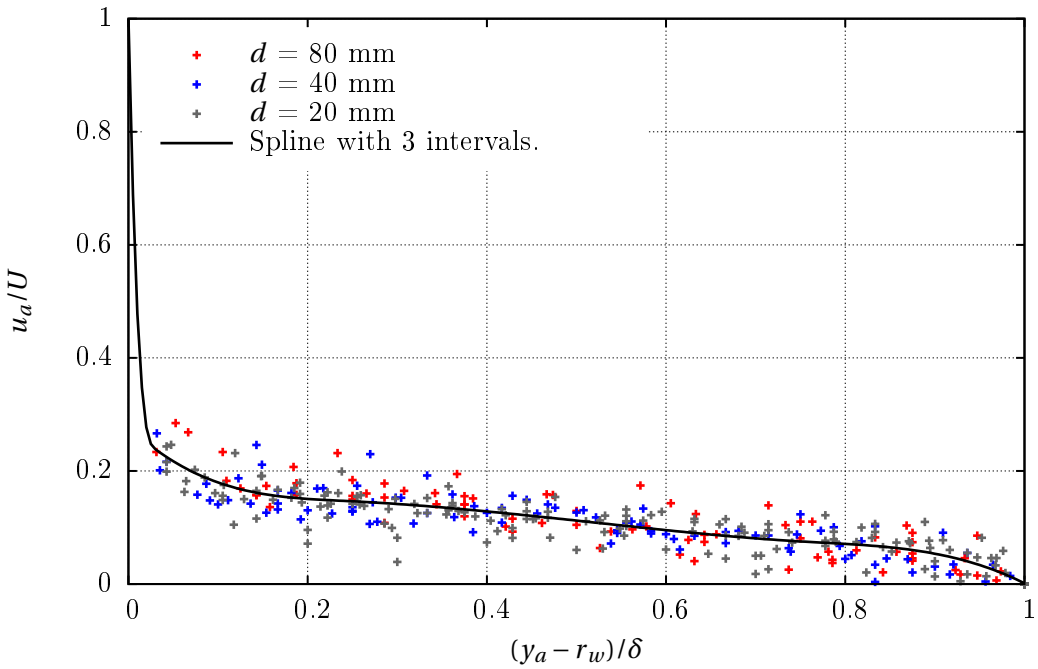

Figure 4.28: Normalized air velocity profile in free falling water jets based on equation 4.35 and approximating cubic spline to data.

4.6 Angle of spread of free jets

Based on the experiments described in Tables 4.7 and 4.8, in Figures 4.29, 4.30 and 4.31 the relative distance from the nozzle exit x/d as a function of the relative lateral spread δ_2/d for diameters of 20 mm, 40 mm and 80 mm are plotted, where x is the distance from the nozzle exit, d is the diameter of the nozzle and, δ_2 is the lateral spread of the liquid jet according to Figure 4.17.

In general, it is worth mentioning that the linearisation approach proposed in the literature of the angle of spread may be appropriate to describe the behavior of water jets [49] just in the flow development region. However, it can be remarked that any linear approximation beyond this region is not adequate at all because as soon as the process of breakup takes place, the angle of spread will increase suddenly and it will be higher than the initial stages.

If all the experiments are re-analysed in terms of $\tan\alpha_d = \delta_2/x$ as a function of the dispersion number $D_0 = Ud^{3/2}(\sigma/\rho)^{1/2}\nu^{-2}$, the results show that the diameter of the nozzle influences the angle of spray as observed in Figure 4.32. For each experiment the angle of spread obtained corresponds to a linearisation of the points measured along the flow development region. As a consequence for the diameters d = 20 mm, d = 40 mm and d = 80 mm, five, three and two angles of spread respectively were computed.

The experimental tests developed in this research for free falling water jets were compared with Dodu's experiment [49] for water jets discharging from injector nozzles (reana-

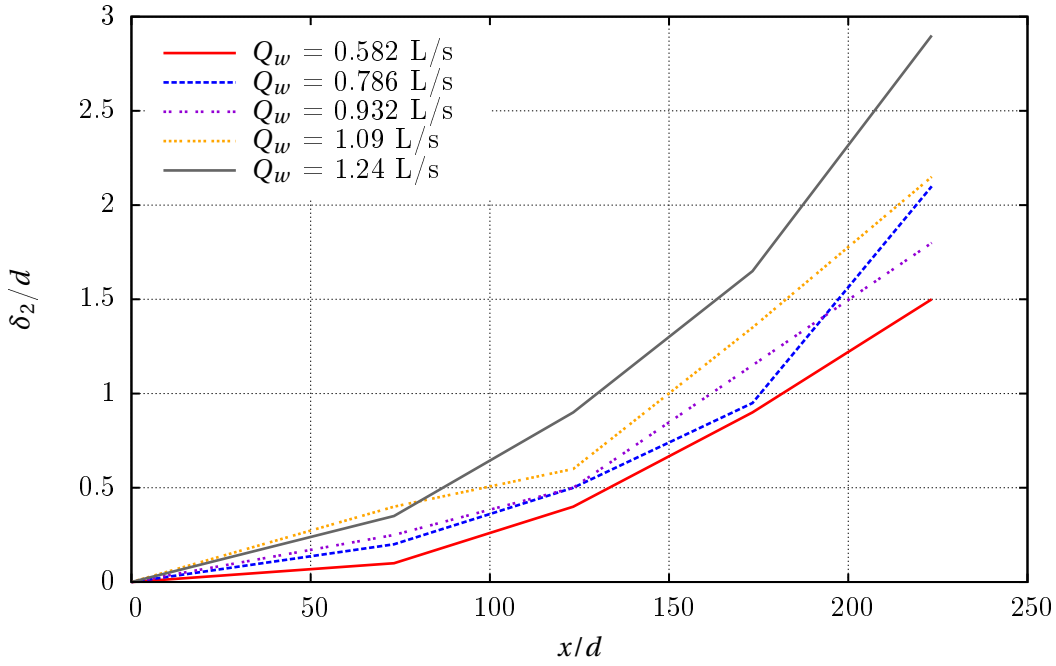

Figure 4.29: Relative distance from the nozzle exit x/d as a function of the relative lateral spread δ_2/d for $d = 20$ mm.

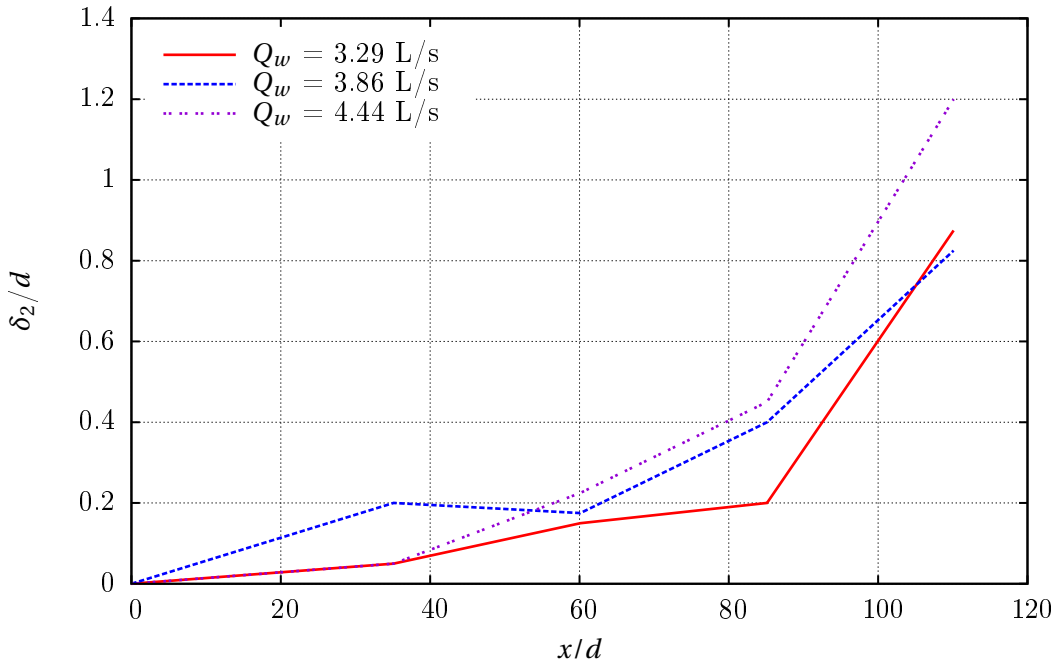

Figure 4.30: Relative distance from the nozzle exit x/d as a function of the relative lateral spread δ_2/d for $d = 40$ mm.

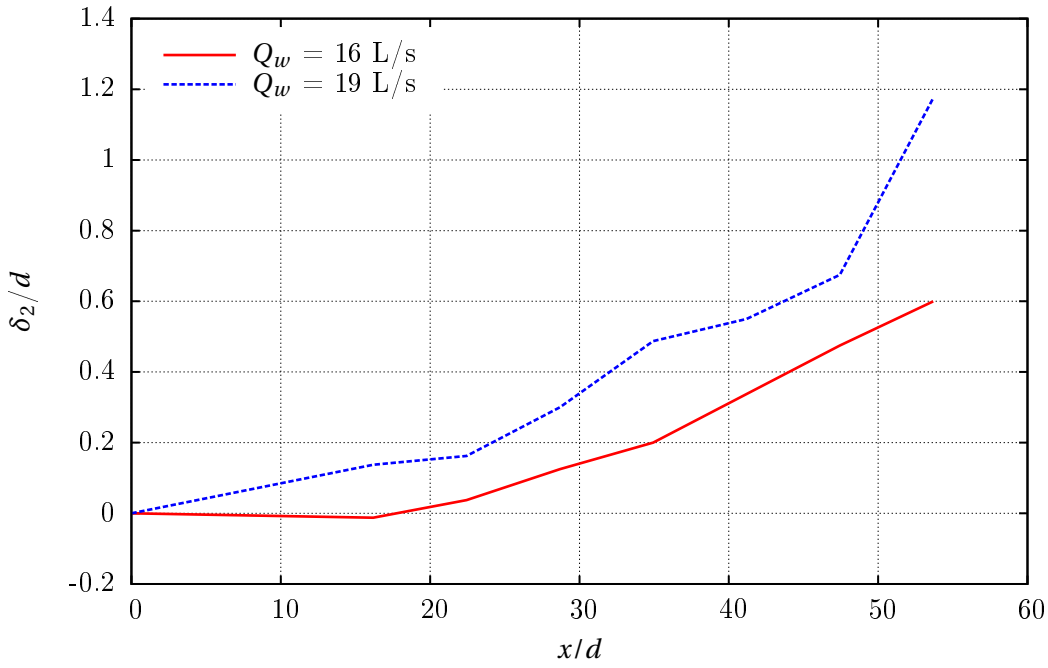

Figure 4.31: Relative distance from the nozzle exit x/d as a function of the relative lateral spread δ_2/d for d = 80 mm.

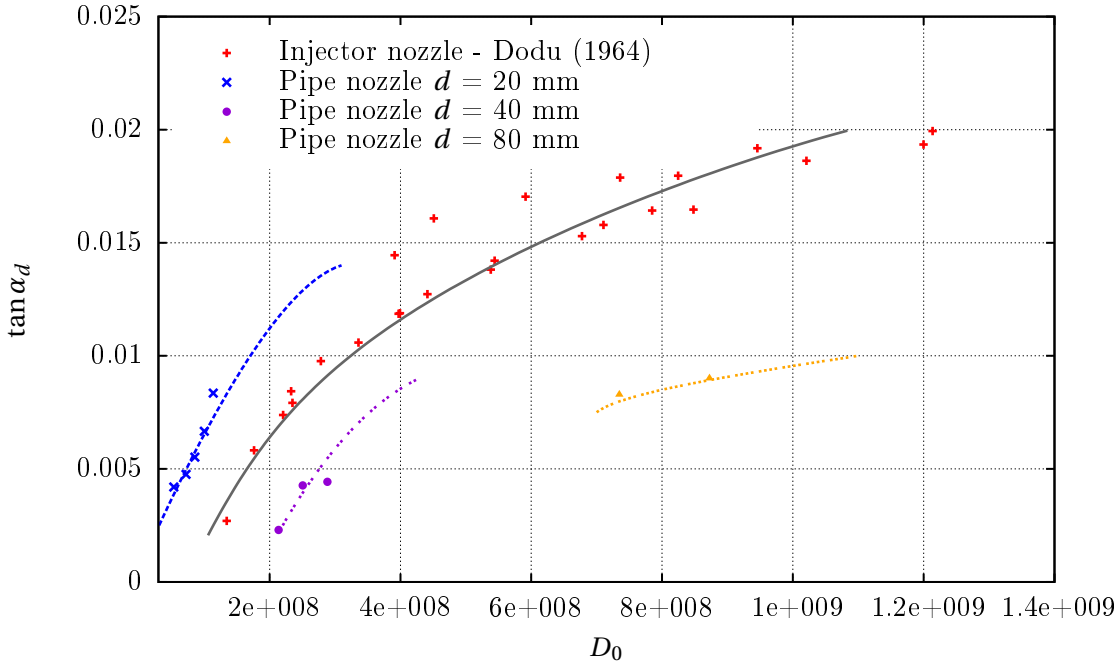

Figure 4.32: Dispersion angle α_d as function of dispersion number D_o.

lyzed by Hager [51]) in order to compare the influence of the dispersion number D_o on the spread angle tan α_d. The observations found are as follow:

- It is worth mentioning that Dodu's experiments [49] used water as a liquid jet. Contrary to the suggestion of Hager [51], the dispersion angle α_d does not vary proportionally with the dispersion number D_0 and is not universally valid for all nozzle jets as can be observed in figure 4.32.

- The impact of the nozzle geometry influences the spread angle as has been already reported by Dodu [49] and Rouse et al. [58]. For the particular case of the model family of nozzles tested with diameters d of 20 mm, 40 mm and 80 mm, the function D_0 vs $\tan\alpha_d$ does not converge and four distinct trends can be observed (including Dodu's experiments). Despite the small range of data tested, the experiments for the diameters of 20 mm and 40 mm only describe a small interval of the plot, which would correspond to the initial stage of the plot D_0 vs $\tan\alpha_d$. However, the experiments for the diameter of 80 mm show an advanced stage of the curve mentioned which is parallel to the experiments done by Dodu.

- With increasing the dispersion number D_0, the dispersion angle tends to reduce its steepness in the curve. The relationship between both parameters seems to be dependent on the nozzle diameter. As a consequence, more experiments are necessary in order to get a generalization.

- Last but not least, it can be remarked that the level of turbulence Tu in the nozzle would impact the angle of spread and it should not be disregarded in future experimental tests.

CHAPTER

5 Air concentration in free falling water jets

In the following chapter the experimental results of measuring the air concentration C of free falling water jets flowing from pipe nozzles with diameters d equal to 10 mm, 20 mm, 40 mm and 80 mm is presented. The air concentration was measured continuously at certain distances from the nozzle exit (x-axis) and transversally (y-axis) in the radial direction from the centerline of the jet in order to determine the air concentration profile at the axis of the jet.

The configuration of the model rig is as described in section 3.2. Likewise, the instrumentation used to measure the air concentration, the sapphire optical probe, is described in section 3.3.3.

Once the model family of nozzles was tested in the laboratory, the scale effects of air-water models were analysed statistically and discussed in terms of the length scale L_r.

5.1 Experimental investigations: measurements and test results

The model rig in which the experiments measuring the air concentration were done is described in section 3.2. Furthermore the geometrical parameters of the different pipe nozzles, consisting of four nozzles in diameters d of 10 mm, 20 mm, 40 mm and 80 mm are presented in Table 3.2.

In Table 5.1 the tested water discharges Q_w for the different nozzles are presented. The range of operation of the experiments was limited between the minimum value of the water discharge of 9 L/s and, a maximum of 27.7 L/s which was the maximum discharge achievable in the model rig for the nozzle diameter d = 80 mm. As a consequence, the rest of the experiments were dependent on this range to test model-prototype pairs according to the Froude similarity law Fr_r = 1.

Experiment	d = 10 mm	d = 20 mm	d = 40 mm	d = 80 mm
1	0.050	0.281	2.56	9.0
2	0.072	0.540	2.82	13.0
3	0.099	1.000	3.09	18.0
4	0.138	1.430	3.35	25.0
5	0.153	2.00	3.62	27.7
6	0.153	2.50	5.00	
7			7.00	
8			9.00	

Table 5.1: Water discharges Q_w tested. All the units are in l/s.

In Table 5.2 the distances x from the nozzle exit where the air concentration C(%) was measured are shown. The selection of the furthest distance from the nozzle exit obeyed the restrictions in the measurement of the air concentration for the diameter 80 mm because of the limited height of the rig and the length of the optic probe on the bottom of the rig. However, a representative range of operations has been obtained as will be later shown in the Ohnesorge diagram.

Distance	d = 10 mm	d = 20 mm	d = 40 mm	d = 80 mm
x_1	0.100	0.05	0.45	1.73
x_2	0.216	0.26	0.95	2.23
x_3	0.279	0.683	1.45	2.73
x_4	0.341	0.78	2.95	3.23
x_5	0.404	1.28	3.95	

Table 5.2: Distances x from the nozzle exit where the air concentration was measured. All the units are in m.

In order to visualize the expected flow characteristics of the free falling water jets tested herein, their location or expected mode of disintegration according to the Ohnesorge diagram is presented in Figure 5.1.

As shown in Figure 5.1, the experiments developed for d = 10 mm were mainly located in regions I and II, which correspond to a mode of disintegration of the jet of axisymmetric surface oscillations and spiral formation. However, for the rest of the experiments tested (d = 20 mm, d = 40 mm and d = 80 mm) the modes of jet breakup were not defined in the original Ohnesorge diagram. However, if the proposed domain is extended beyond that, it would suggest that the mode of the disintegration corresponds to the spiral formation and atomization type. Until now the original Ohnesorge diagram has not been supplemented by additional experiments beyond the original limits proposed by Ohnesorge and there is a lack of research for the mode of jet breakup for higher

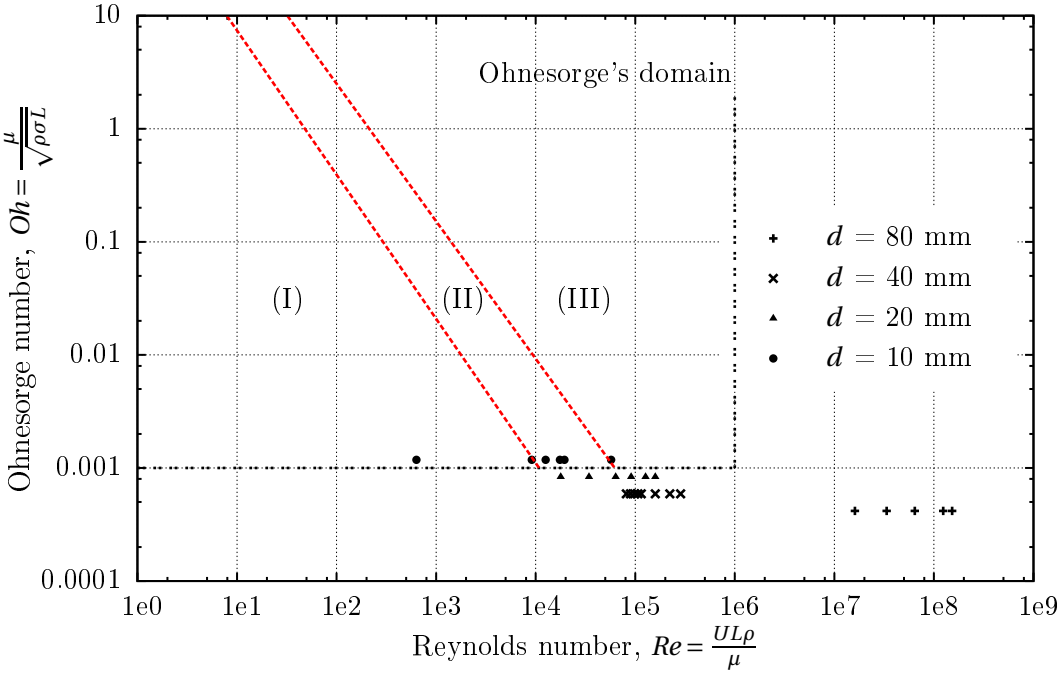

Figure 5.1: Classification of the current experiments in the Ohnesorge diagram.

turbulent flows (beyond $Re > 1 \cdot 10^6$) and diameters bigger than 15 mm, which are the normal situations (greater scales) present in hydraulic engineering.

In Figures 5.2, 5.3, 5.4 and 5.5 the air concentration for diameters of d = 80 mm, d = 40 mm, d = 20 mm and d = 10 mm, measured at several distances from the nozzle exits are shown. In the x-axis of the plot the dimensionless ratio y/r represents the relative distance from the nozzle axes where the air concentration was measured transversally along the centerline of the nozzle, or so-called radial direction. Likewise r is the radius of the nozzle. On the same plot, the y-axis is the air concentration measured with the sapphire optical probe at those positions. In order to simplify the measurements of the air concentration, for a single test their values were measured along the complete cross section in order to verify symmetry in the profile, and then the measurements were done from the outer part of the water jet until 30% beyond the longitudinal axis of the nozzle exit. As a consequence, the experiments presented here will be shown on a half of the cross section of the water jet because the left side is a mirror of the curves obtained. Therefore the value $y/r = 0$ is the longitudinal axis of the nozzle exit.

Once the experiments were performed the following observations can be made:

- In the case of diameter d = 80 mm (see Figure 5.2), the variability of the air concentration is slight because the flow falls into the development region. In spite of the fact that the Ohnesorge diagram would classify the mode of jet breakup as spray, the core of the jet is maintained and there was no breakup even until the last stages of the casting box. Once the flow discharge is increased three times (from 9 L/s to

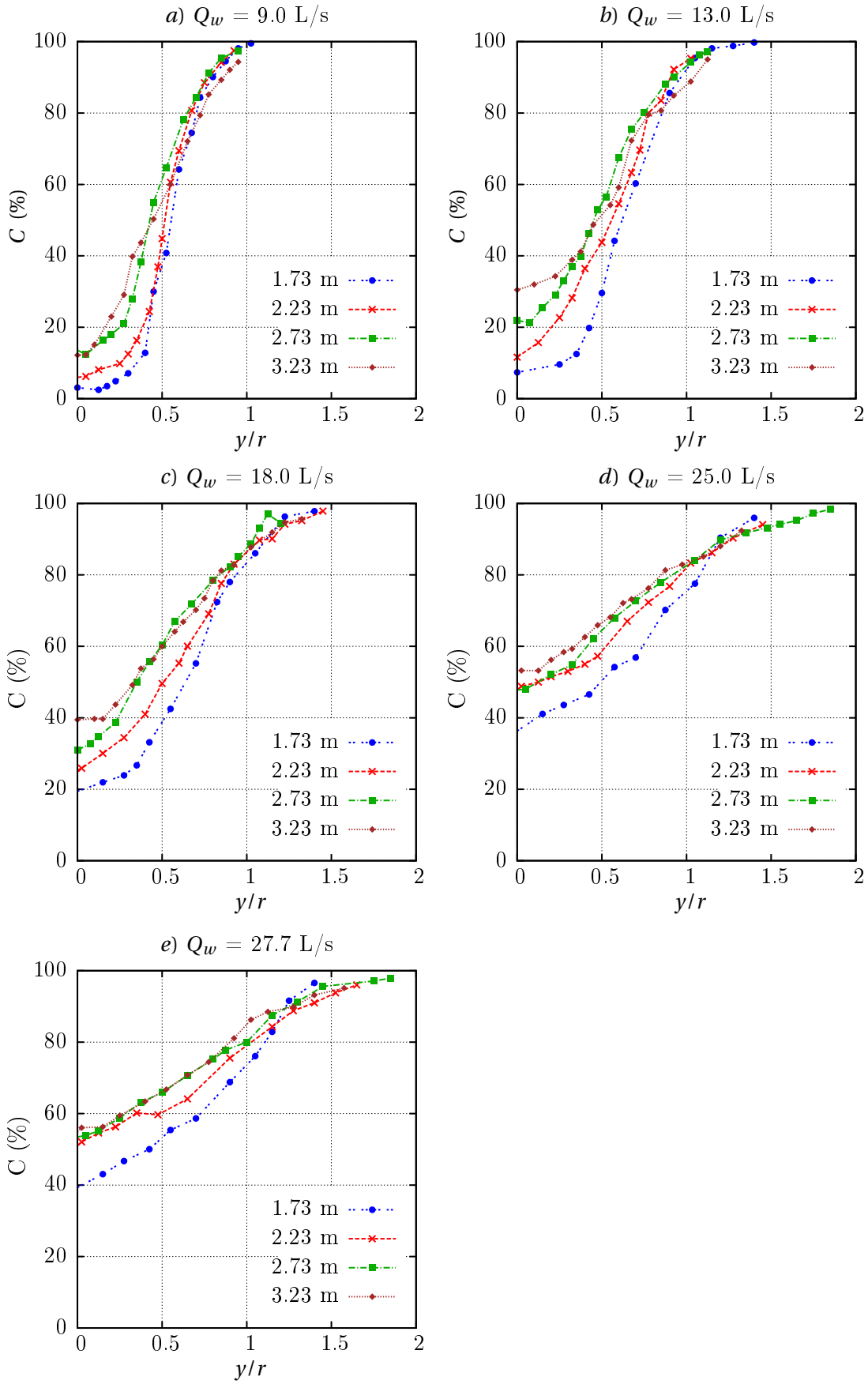

Figure 5.2: Air concentration C(%) versus the relative distance from the nozzle axis y/r at several distances from the nozzle exit for the diameter d = 80 mm.

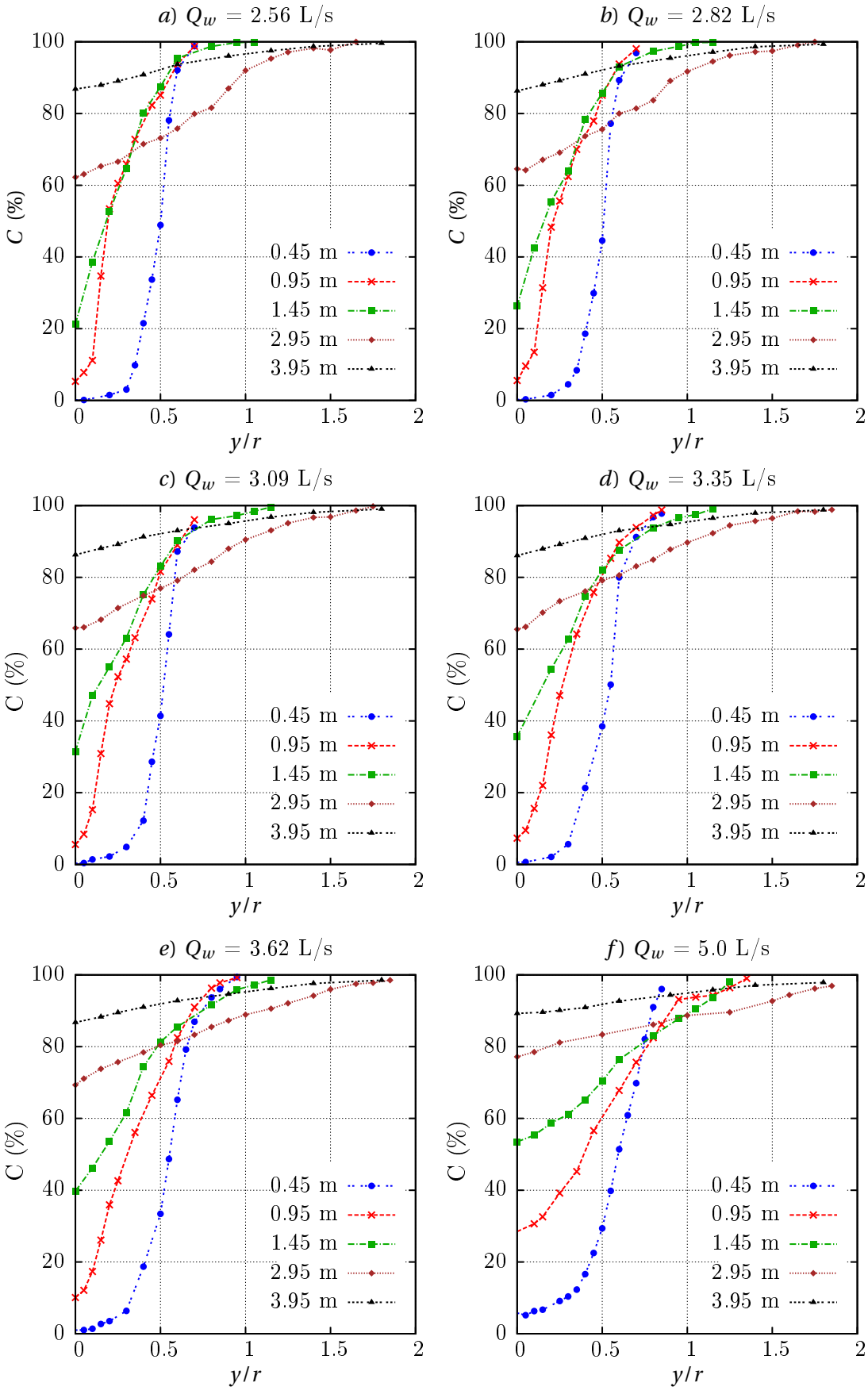

Figure 5.3: Air concentration C(%) versus the relative distance from the nozzle axis y/r at several distances from the nozzle exit for the diameter d = 40 mm (to be continued)

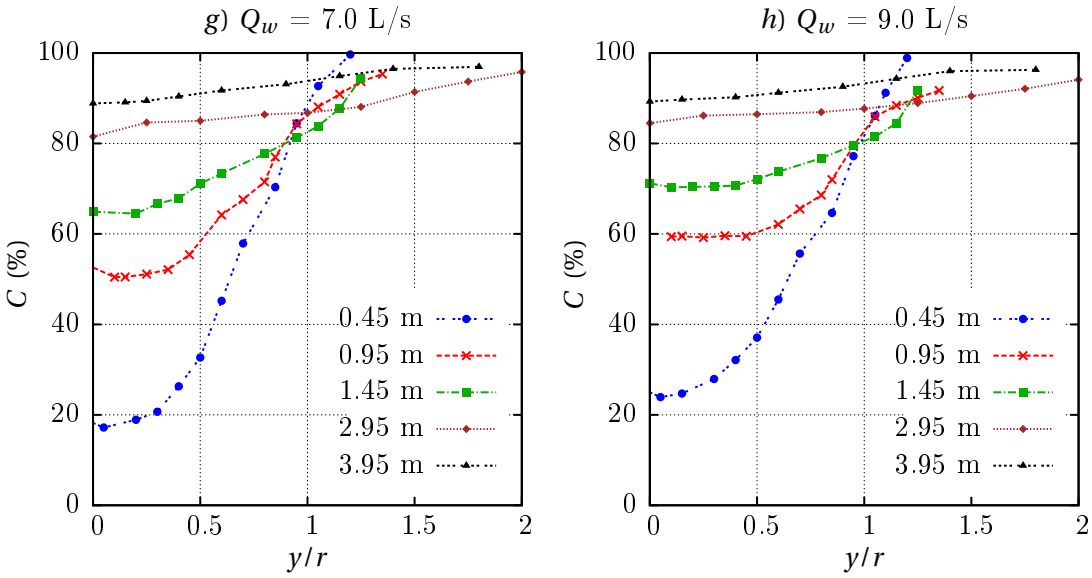

Figure 5.3: Air concentration $C(\%)$ versus the relative distance from the nozzle axis y/r at several distances from the nozzle exit for the diameter d = 40 mm.

27.7 L/s), the value of the air concentration in the axis of the jet varies from ~ 4 % to ~ 40 % for the maximum distance measured.

- A considerable variability in the results was obtained for diameters d = 20 and d = 40 mm. Although it might be thought that the mechanism of entrainment would be as it has been described by Falvey [101], the experimental tests show that the axi-symmetrical movement of the jet induces the false air entrainment in the jet. This ensures that the air concentration has a certain value which is not correlated with the entrance of air bubbles into the water although it has been obtained due to the sinuous movement of the water around its axes.

- In the case of diameter d = 10 mm, the water jet core remained unbroken until a distance of 0.40 m and the proof of this evidence is that the air concentration remains equal or almost zero for all the experiments as can be observed in Figure 5.5.

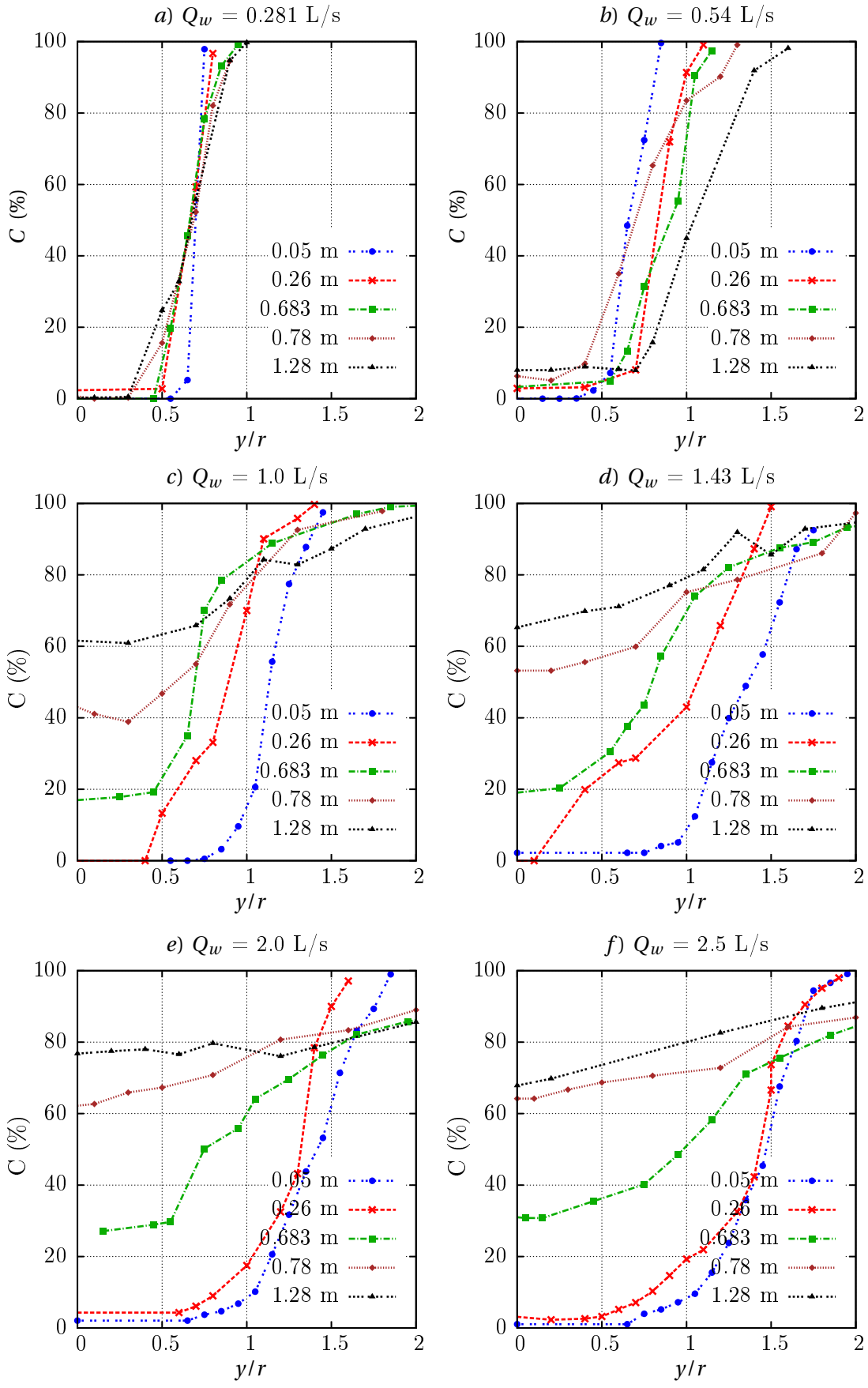

Figure 5.4: Air concentration C(%) versus the relative distance from the nozzle axis y/r at several distances from the nozzle exit for the diameter d = 20 mm.

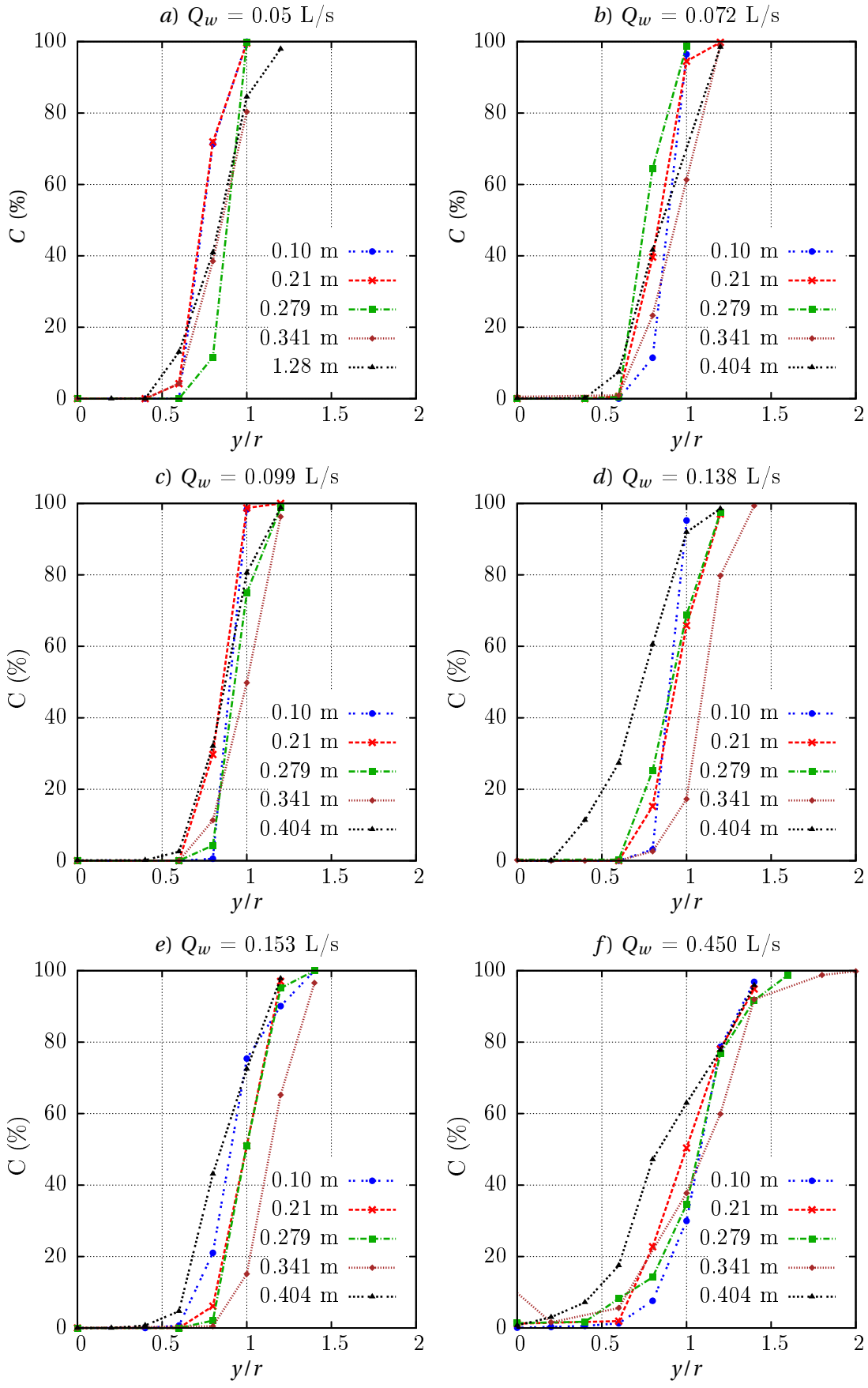

Figure 5.5: Air concentration C(%) versus the relative distance from the nozzle axis y/r at several distances from the nozzle exit for the diameter d = 10 mm.

5.2 Comparison of the model family using Froude similarity law Fr_r

The results of studying a model family of water jets discharging into the atmosphere is presented here. By applying the Froude similarity law, the scale effects are analyzed and discussed in terms of the air concentration measured for the distinct diameters with the specifications shown in Table 5.3. Where *Experiment* is the type of experiment, d is the diameter of the nozzle, L_n is the exit length of the nozzle, $C.R.$ is the contraction ratio defined as d/D, $A.R.$ is the aspect ratio and L_r is the length scale. Based on this, a prototype was considered (for the diameter d = 80 mm) and the rest of the diameters have be defined as models. As a consequence, three length scales ratio will be tested L_r = 2, 4 and 8.

Experiment	d (mm)	L_n (m)	$C.R.$	$A.R.$	L_r
Prototype	80	1.40	0.53	17.5	1
Model 1	40	0.70	0.266	17.5	2
Model 2	20	0.35	0.133	17.5	4
Model 3	10	0.175	0.33	17.5	8

Table 5.3: Circular nozzle experiments.

Certainly, based on the equations of the scales of velocity U_r (equation 4.9) and water discharge Qw_r (equation 4.10) the values shown in Tables 5.4 and 5.5 could be computed. In Table 5.4 the first column with the name *prototype* shows the velocity (units in m/s) in the nozzle exit, the successive three columns (L_r = 2, L_r = 4 and L_r = 8) their corresponding values of velocity, and the last column *Code* is an identifier of the experiment.

Similar to Table 5.4, in Table 5.5 the first field *prototype* corresponds to the water discharge in L/s from the nozzle exit in the prototype, then the water discharges are presented for the length scales L_r = 2 (d = 40 mm), L_r = 4 (d = 20 mm) and L_r = 8 (d = 10 mm) and, finally the *Code* is the name of the experiment or pairs model-prototype build for comparison.

Likewise, the corresponding distances x from the nozzle exit where the measurements of the air concentration were done are shown in Table 5.6. Here five positions (distances from the nozzle exit, x) were defined in order to compare the different values of the air concentration obtained for the set of experiments according to the Froude similarity law. That means that in the case of the distance 1 (see column 1 of Table 5.6), the air concentration for the prototype (d = 80 mm) at a distance of 1.73 m would be equivalent or comparable at those measurements done at a distance of 0.865 m, 0.433 m and 0.216 m for the model nozzles with diameters of 40 mm (L_r = 2), 20 mm (L_r = 4) and 10 mm (L_r = 8), respectively.

Prototype (80 mm)	Nozzle exit velocity U_0 in the models $L_r = 2$ (40 mm)	L_r=4 (20 mm)	$L_r = 8$ (10 mm)	Code	Fr
1.790	1.266	0.895	0.633	*ex*1	2.0
2.586	1.829	1.293	0.914	*ex*2	2.9
3.581	2.532	1.790	1.266	*ex*3	4.0
4.974	3.517	2.487	1.758	*ex*4	5.6
5.511	3.897	2.755	1.948	*ex*5	6.2

Table 5.4: Required outlet velocity U_0 according to the Froude similarity law. All the units are in $m\ s^{-1}$.

Prototype (80 mm)	Discharge Q_w in the models $L_r = 2$ (40 mm)	L_r=4 (20 mm)	$L_r = 8$ (10 mm)	Code
9.0	1.59	0.281	0.050	*ex*1
13.0	2.30	0.406	0.072	*ex*2
18.0	3.18	0.563	0.099	*ex*3
25.0	4.42	0.781	0.138	*ex*4
27.7	4.90	0.866	0.153	*ex*5

Table 5.5: Required discharge Q_w according to the Froude similarity law (all the units are in L/s).

By convention, in order to compare the model family of experiments, the relative distances x/d shown in column 6 of Table 5.6 refers to the distance equivalent models-prototype at the distances 1, 2, 3 and 4.

Distance	Prototype $L_r = 1$ (80 mm)	Distances x in the models $L_r = 2$ (40 mm)	$L_r = 4$ (20 mm)	$L_r = 8$ (10 mm)	x/d
1	1.730	0.865	0.433	0.216	21.6
2	2.230	1.115	0.558	0.279	27.9
3	2.730	1.365	0.683	0.341	34.1
4	3.230	1.615	0.808	0.404	40.4

Table 5.6: Distances from the nozzle exit x where the air concentration was measured. All the units are in meters.

In order to analyse the scale effects due to changes in the geometric scales and the kinematic inlet conditions of the flow, the experimental test results $C(\%) = f(y/r)$ ob-

tained in Tables 5.2, 5.3, 5.4 and 5.5 served as a base for inferring the distribution $C_n = f(y/r)_n$ in those experiments where it may be required. The following procedure was established:

- For each curve, the set of experimental results consisting of pairs of data for air concentration vs relative position y/r were converted into a continuous function by using techniques by *interpolating cubic splines* and *piecewise polynomial form-lineal* [102] [103]. The first method consists of joining the control points (here the experimental tests) with a spline and the second one by a piecewise linear function. The main advantage of such interpolation methods is that the original experimental data remains and they are not subject to changes in case of using fitting techniques where the data are just fitted to a curve type.

  In the specific case of $C(\%) = 0$ the calculation of piecewise linear line segments was applied.

- Between two positions x_i and x_{i+1} where the values $C_i = f(y/r)_i$ and $C_{i+1} = f(y/r)_{i+1}$ were measured, an interpolated function $C_n = f(y/r)_n$ at a distance x_n from the nozzle exit was calculated by determining initially the arc length S_i and S_{i+1}. As a consequence S is defined as:

$$S = \int_a^b \sqrt{1 + [f'(y)]^2}\, dy \tag{5.1}$$

  where $f(y)$ is a real function such that $f(y)$ and its derivative with respect to y, $f'(y)$, are continuous on [a, b].

- The arc lengths S_i and S_{i+1} were discretised in terms of percentages and the positions on the curve $C_i = f(y/r)_i$ and $C_{i+1} = f(y/r)_{i+1}$ were determined. Accordingly the equal positions (obtained for the same percentages) of both curves were joined by lines and in the required distance x as result the desired function $C_n = f(y/r)_n$ can be calculated by using linear interpolation.

The analysis of the scale effects deals with evaluating similarity between experimental curves *model-prototype* and to estimate the effects and variation of a parameter as a function of its scale. The difficulty mainly is about how to assess the accuracies of each implemented model taking into account the variability and the complexity of the results.

In Figures 5.6, 5.7, 5.8, 5.9 and 5.10 the comparison of the air concentration computed for distinct experiments (experiments *ex*1, *ex*1, *ex*2, *ex*3, *ex*4 and *ex*5) and length scales (L_r = 2, 4 and 8) are presented. Each figure shows five subplots (a, b, c, d and e) which correspond to the values of the air concentration profile measured at the distances x_1, x_2, x_3, x_4 and x_5 shown in Table 5.6. Likewise, in each subplot the corresponding comparison of experiments models L_r = 2, 4 and 8 are shown.

The main results obtained are:

- As is expected according to the Ohnesorge diagram, the modes of breakup for all the experiments done for the model (d = 10 mm) consisted in the formation of

slight axisymmetric surface oscillations, and the breakup length $\overline{L}$ would be bigger than 0.404 m if the results shown in Figure 4.16 are considered, which correspond to the distance x_5 shown in Table 5.6. As a consequence, if there was no breakup, for all the experiments, the air concentration in the center and its vicinity of the water jet was $C(\%) = 0$.

- Likewise, for the diameter d = 20 mm there was no breakup of the water jet either, and the axisymmetric surface oscillations were slight. As a result the air concentration was almost zero for the lowest discharge but for the rest of the experiments the air concentrations measured were low but non-zero in the adjacent region of the axis of the water jet. In general the constitution of the air concentration profile was similar to that obtained for the model (d = 10 mm).

- Once the size of the nozzle is increased or, in other terms, when the scales (L_r = 4 and 8) are higher, the air plays a relevant role associated with the mode of disintegration of water jets proposed by Ohnesorge according to the properties of the flow and kinematic conditions of the flow tested herein: spiral formation for d = 40 mm and spray formation for d = 80 mm.

- On the contrary of the curves prototype-model 2 (d = 80 mm - d = 20 mm) and prototype-model 3 (d = 80 mm - d = 10 mm), the air concentration profiles for the diameters d = 80 mm (prototype) and d = 40 mm (Model 1) show a good approximation or similarity between curves at different distances (x/d = 21.6, 27,9, 34.1 and 40.4) and all the experiments (ex_1 to ex_2). As a consequence, the goodness of fit between curves will be evaluated in the next section in order to analyse scale effects.

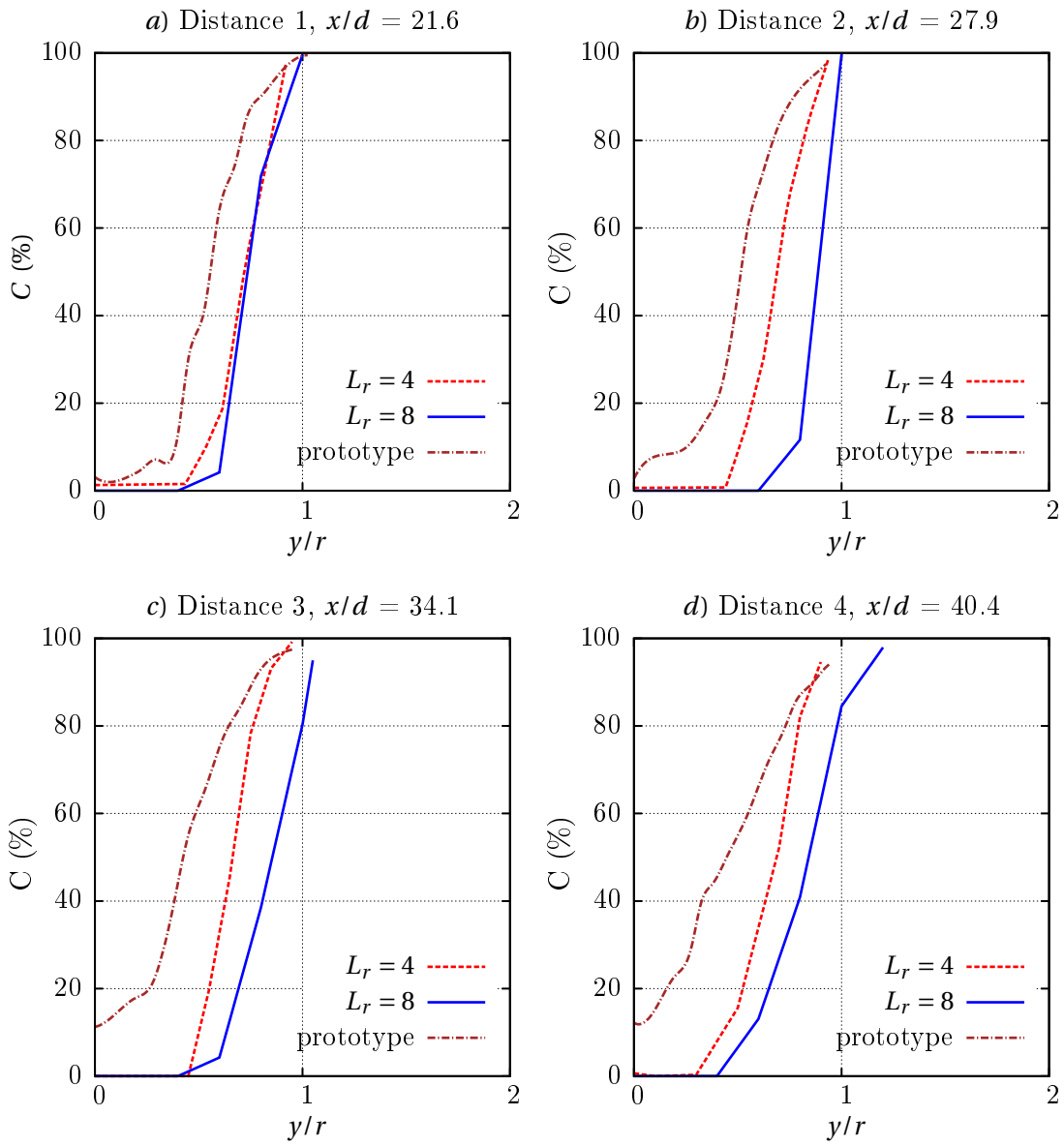

Figure 5.6: Experiment *ex*1: $C(\%) = f(y/r)$ for different distances x and length scales L_r.

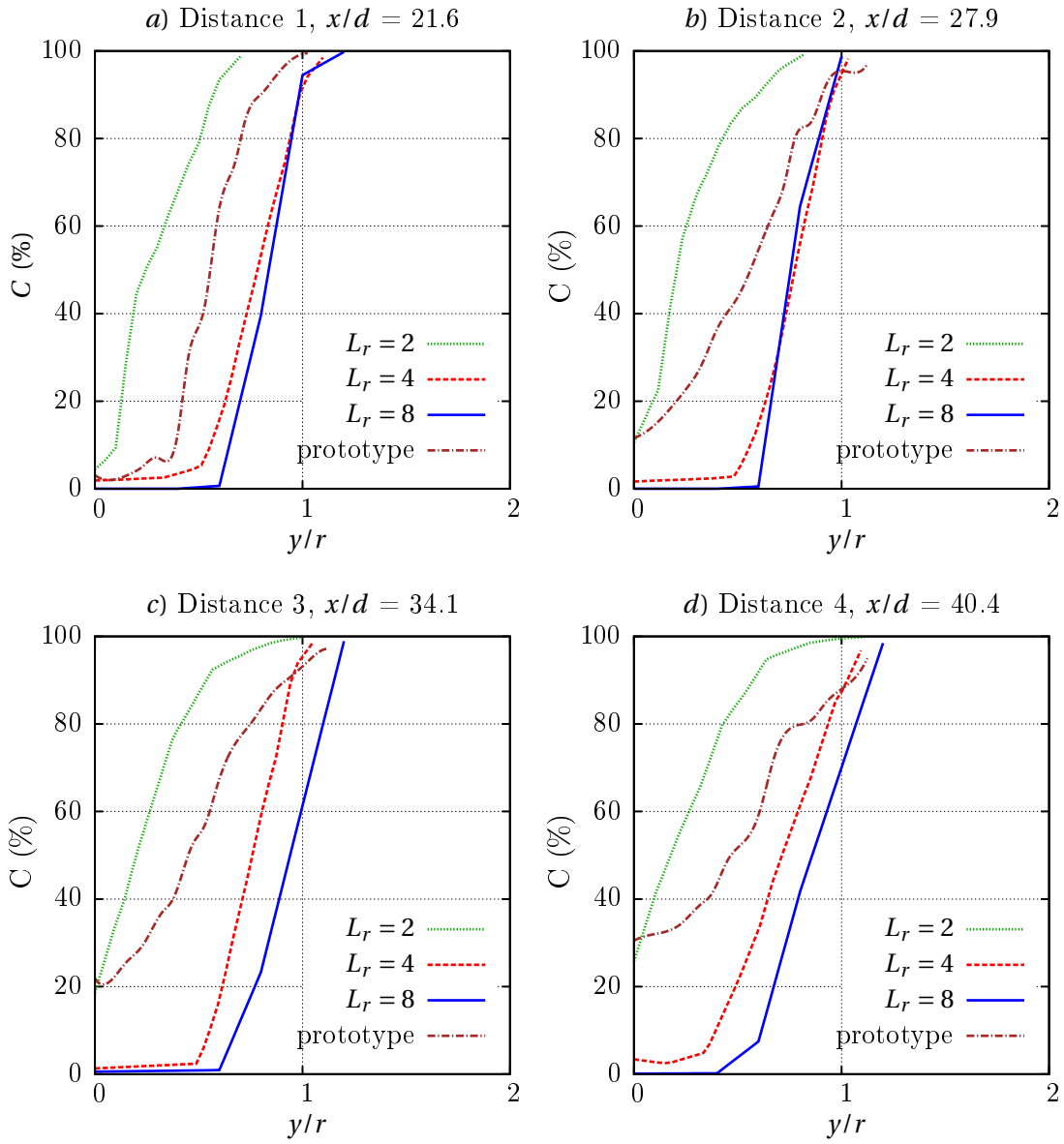

Figure 5.7: Experiment *ex*2: $C(\%) = f(y/r)$ for different distances x and length scales L_r.

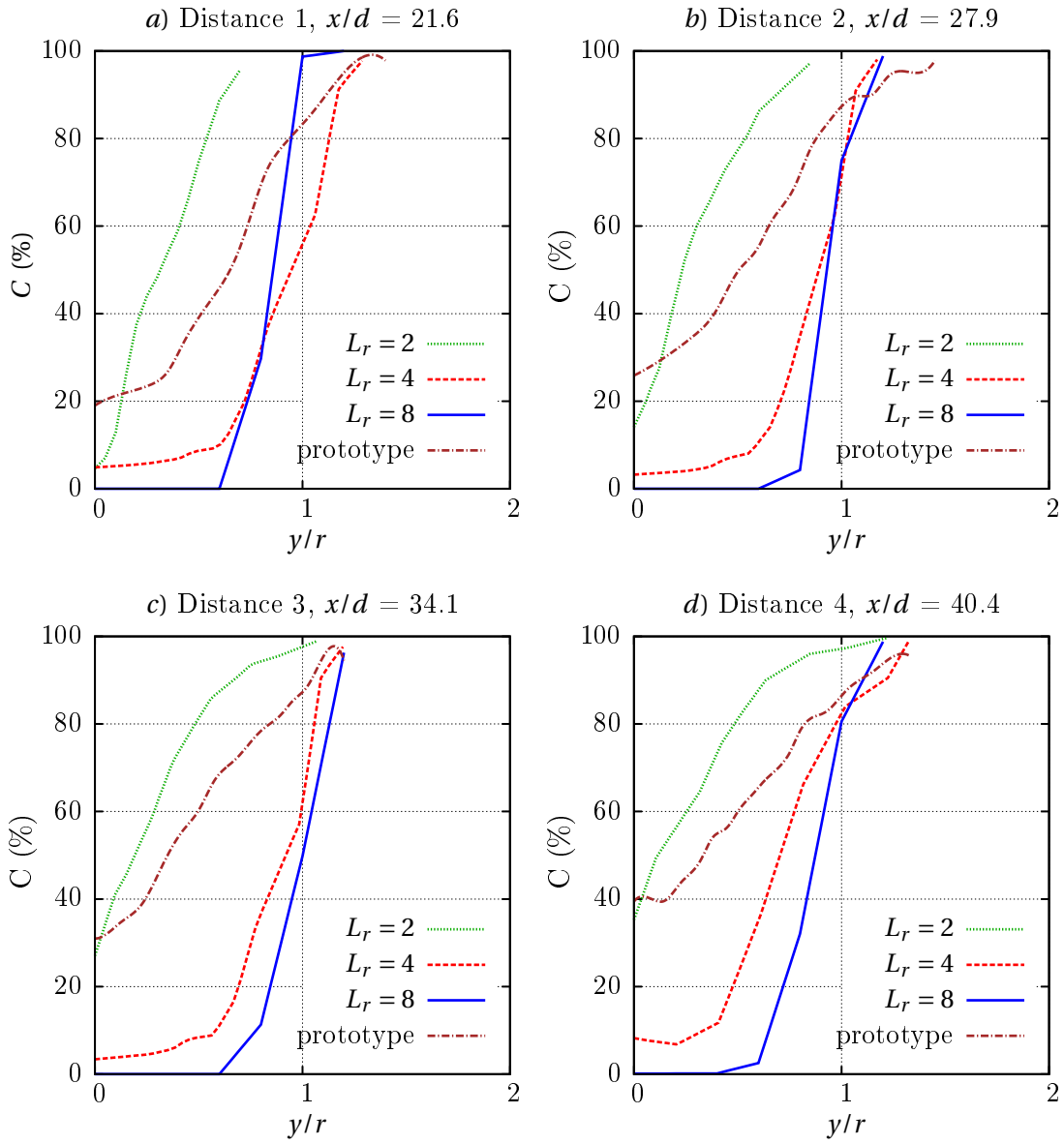

Figure 5.8: Experiment *ex*3: $C(\%) = f(y/r)$ for different distances x and length scales L_r.

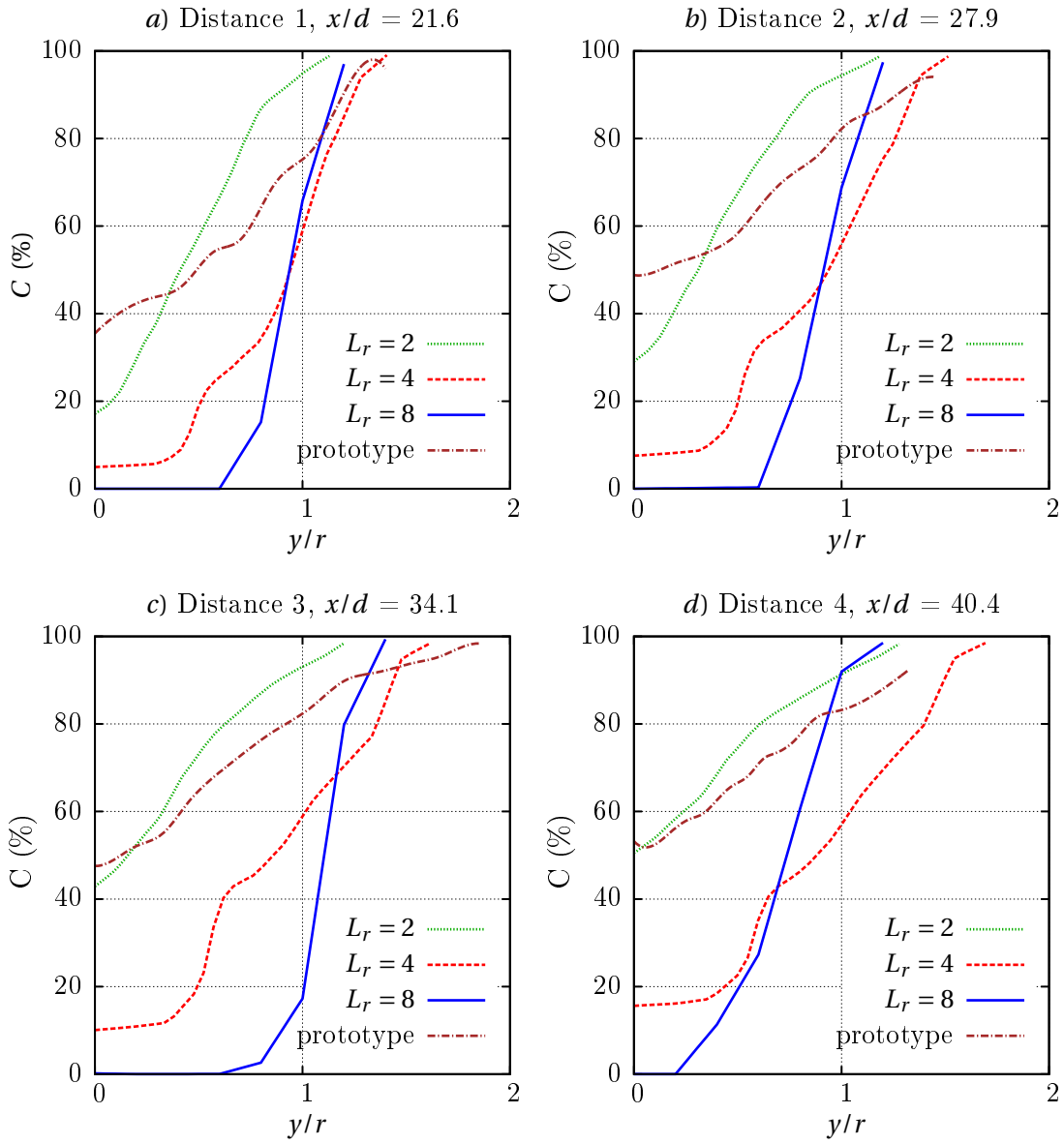

Figure 5.9: Experiment *ex*4: $C(\%) = f(y/r)$ for different distances x and length scales L_r.

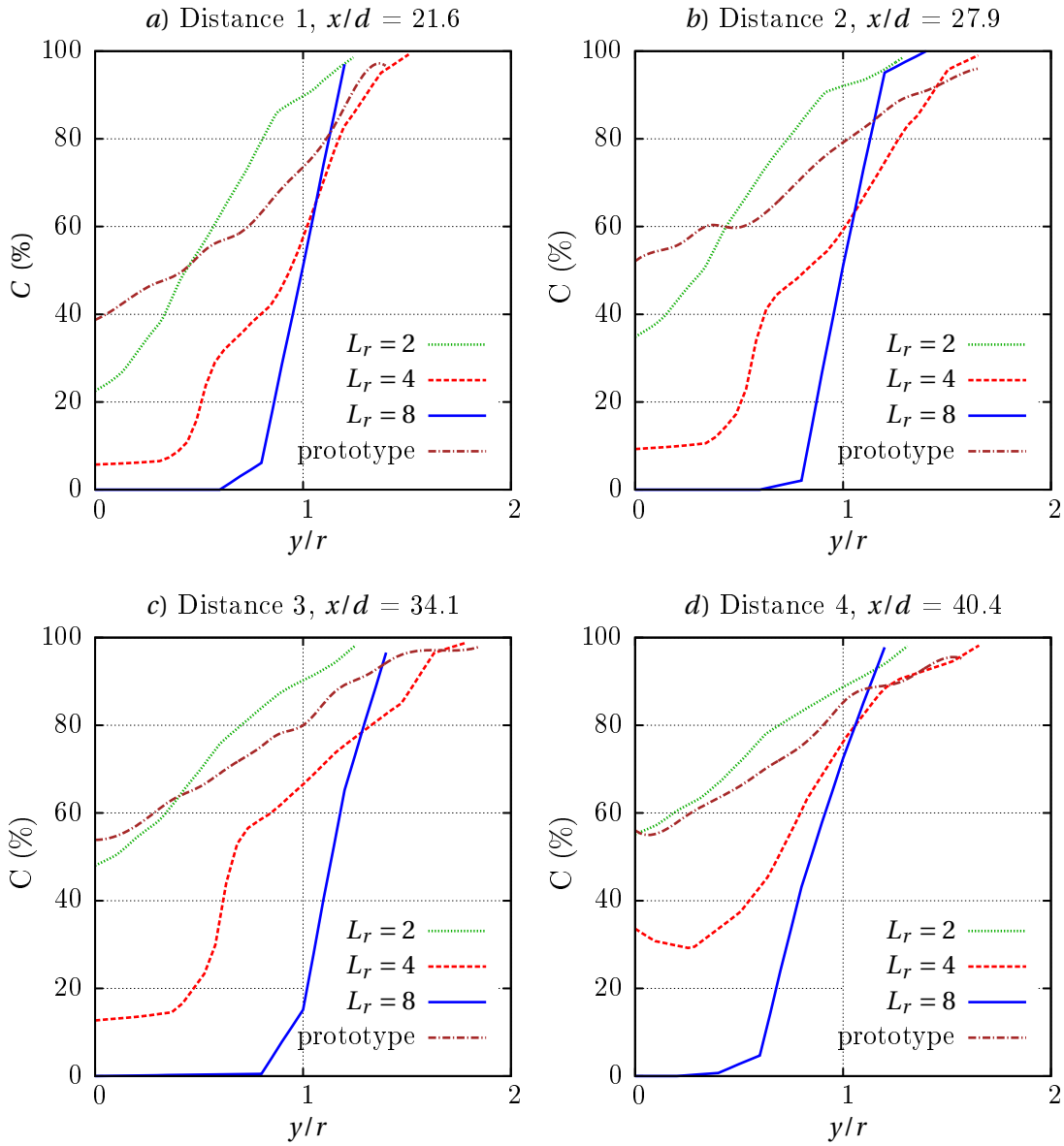

Figure 5.10: Experiment *ex*5: $C(\%) = f(y/r)$ for different distances x and length scales L_r.

5.3 Analysis of scale effects: curves matching evaluation

The main concern in comparing shapes (or polylines) is that of defining a metric that measures the difference between them. Due the discrepancy in the length of the intervals in the y-axis in matching two experimental curves, air concentration versus the relative position ($C(\%) = f(y/r)$), the use of statistical methods for measuring the magnitude of a varying quantity as *root-mean-square difference* (see equation 5.2) is ruled out, even if normalized data are used, because it would contribute to errors in the results,

$$\ell(p,m) = \sqrt{\sum_{i=1}^{n}(p(x_i) - m(x_i))^2}, \tag{5.2}$$

where ℓ is the root-mean-square difference, and $m(x)$ and $p(x)$ are functions that denote *model* and *prototype*.

As a consequence, the necessity arises of implementing a measure of likeness between curves considering the dissimilarity of the y-values and the length of the y-interval that could overcome this difficulty.

5.3.1 Discrete Fréchet distance

A heuristic method that has been implemented in fields such as *image recognition* and *handwritten recognition* is the *Fréchet distance*. This mathematical model is described as the minimum length of a leash that connects dog and its owner, which are constrained to separate paths (α_T and β_T) as they walk along them in the same direction from the beginning until the end of their trajectories. The man and the dog must both walk continuously, their motion is required to be monotonic, and the Fréchet distance between α_T and β_T is the minimum leash length needed. Formally, let $d(m,p)$ denote the *Euclidean distance* between two points m and p in the plane and the Fréchet distance between α and β is:

$$\delta_{dF}(M,P) = \inf_{\alpha_T,\beta_T} \max_{t\in[0,1]} \Big[d\big((M(\alpha_T(t)), P(\beta_T(t))\big)\Big] \tag{5.3}$$

where M and P are continuous nondecreasing functions which are defining the positions of the man and the dog on the curve at every instant, and t is the time parameter which in general terms it obeys to define at time t the position of the dog $P(\alpha_T(t))$ and the dog's owner $M(\beta_T(t))$.

An improvement to the original method [104], called the *coupling distance* or the *discrete Fréchet distance* proposed by Eiter & Mannila [105], consists in a discrete variation of the *Fréchet distance* for polygonal curves, δ_{dF}, which is based on the idea of looking at all possible couplings between the end points of the line segments of the polygonal curves. Given polynomial curves P and M, their *discrete Fréchet distance* is defined to be:

$$\delta_{dF}(M,P) = \min\big\{\|L\| \,|\text{L is a coupling between } M \text{ and } P\big\} \tag{5.4}$$

where the length $\|L\|$ of the coupling L (between M and P) is the length of the longest link in L [105]. As the unit of δ_{dF} is centimetre [cm], for the current studies it will be presented dimensionless $\delta_{dF}/[\text{cm}]$.

Mainly, the goodness of matching between two curves is defined *empirically* and *a posteriori* by establishing a range of acceptability depending on the metric obtained after comparing several curves. Once the discrete Fréchet distance δ_{dF} is calculated, the lower and upper values of the associated intervals are defined and then, some range of confidence will be associated with its correspondent scale effects χ.

On the left side of Figure 5.11 (subplots a, c, e, g and i) the length scale L_r vs the Fréchet distance δ_{dF} for the experiments *ex*1, *ex*1, *ex*2, *ex*3, *ex*4 and *ex*5 is plotted. On each subplot the four distances x/d (see Table 5.6) where the air concentrations was measured is drawn.

Although the discrete Fréchet distance is a tool that gives the possibility of evaluating the matching of two discretised curves, a limitation lies in the necessity of defining (decision making) ranges of acceptability which should be done *a priori* by the modeler and the results may fall and lead to biased results.

Based on the results obtained from the plots mentioned above, in Table 5.7 the ranges of certainty associated with the scale effects are defined.

Range of values δ_{dF}	Scale effects (χ)
$5 <$	negligible
$5 \leq \delta_{dF} < 10$	moderate
≥ 10	high

Table 5.7: Empirical goodness of fit by using the discrete Fréchet distance.

5.3.2 Procrustes analysis

The mathematical model called *procrustes analysis* was applied to establish the goodness-of-fit (similarity) between multivariate observations. This technique is specifically used in *computer vision* and *survey* for determining linear transformations such as translation, reflection, orthogonal rotation and scaling of the points constitutive of the curve m to best conform them to the points constitutive of a curve p. The goodness-of-fit criterion is based on a *Standardized Dissimilarity Measure*, SDM, which is obtained by comparing the sum of squared deviations between the set of points with the sum of squared deviations of the original points from their column means. The equation to obtain the transformed shape, Z, is:

$$Z = bYT + c \tag{5.5}$$

where b is a scaling factor that stretches (b > 1) or shrinks (b < 1) the points, T is the orthogonal rotation and reflection matrix, and c is a matrix with constant values in each column, used to shift the points. The dissimilarity, SDM, gives a number between 0 and

1 describing the difference between the target shape (model) and the transformed shape (prototype). How much SDM approximates to 0, is an indication of how much the expected curves match the reference curve (*prototype*), while values near 1 imply dissimilarity.

In the subplots b, d, f, h and j of Figure 5.11 the scale effects based on the air concentration for the distinct scales at several distances x are evaluated by using procrustes analysis for the experiments $ex1$, $ex1$, $ex2$, $ex3$, $ex4$ and $ex5$. Each subplot shows in the abscissa the length scale L_r and in the ordinate the Standardized Dissimilarity Measure (SDM) obtained for the distinct distances where the air concentration was measured.

In order to visualize the results obtained by both methodologies, on the left side of Figure 5.11 the calculations by using the Discrete Fréchet distance are shown, and beside them (on the right side) have been placed the corresponding results using Procrustes analysis.

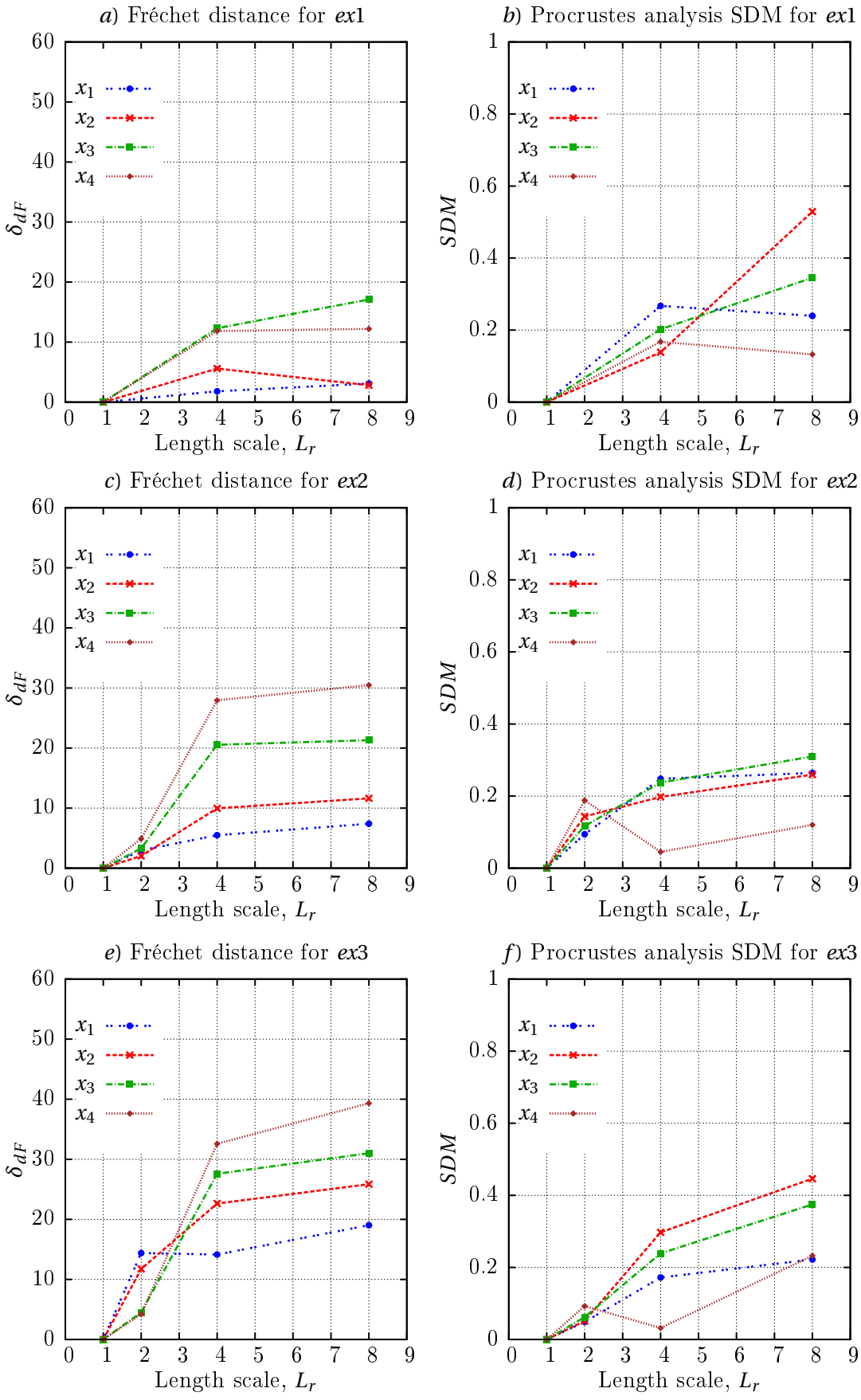

Figure 5.11: Dissimilarity measure by using Discrete Fréchet distance and Procrustes analysis.

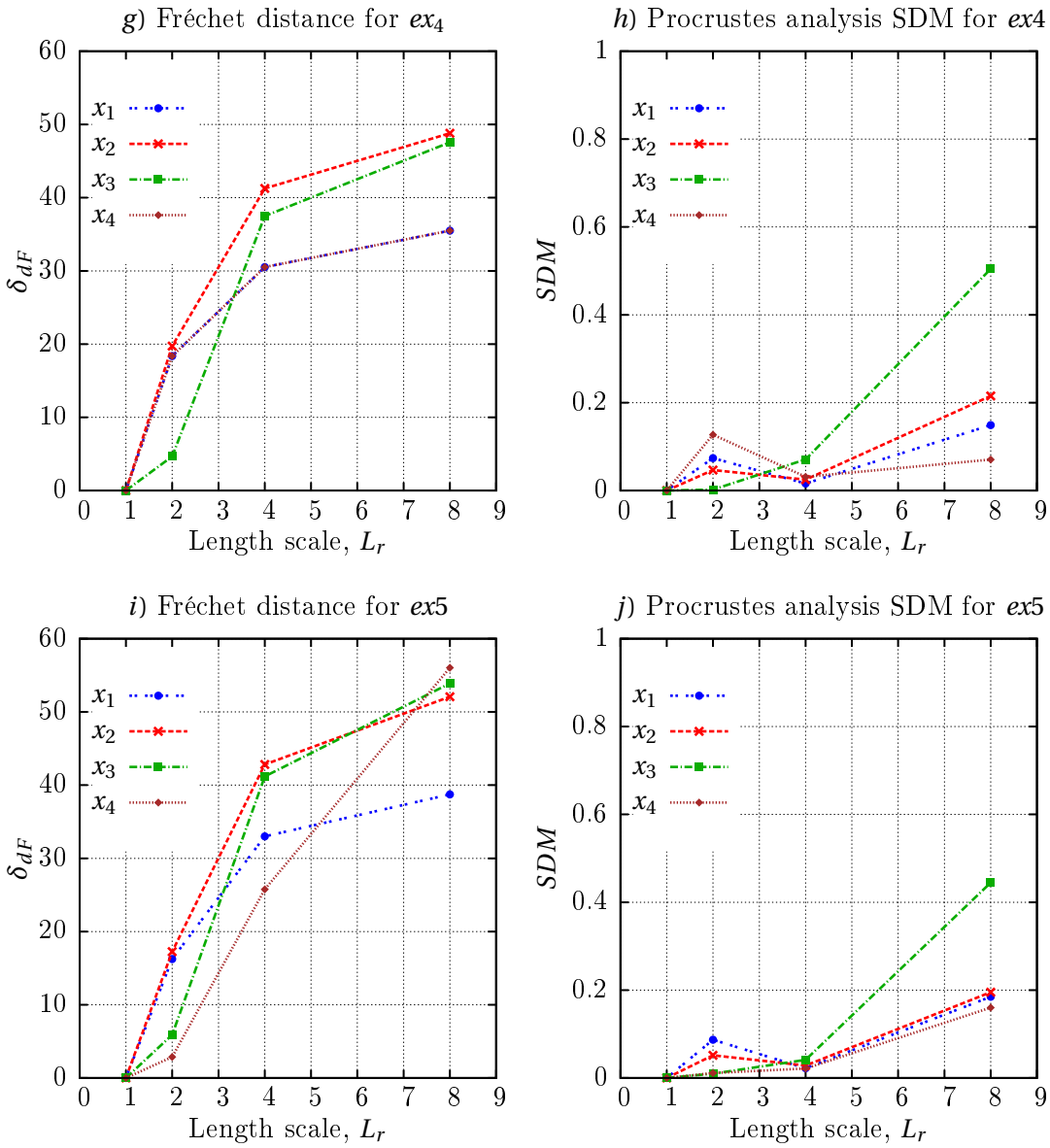

Figure 5.11: Dissimilarity measure by using Discrete Fréchet distance and Procrustes analysis.

5.3.3 Discussion and results

In order to evaluate the impact of the scale effects on the air concentration profile of a model family of circular nozzles in range $2 \leq Fr \leq 6.2$, the resumé of the calculations by using the discrete Fréchet distance method and Procrustes analysis can be observed in Figures 5.12-a and 5.12-b. As a consequence, the following can be concluded:

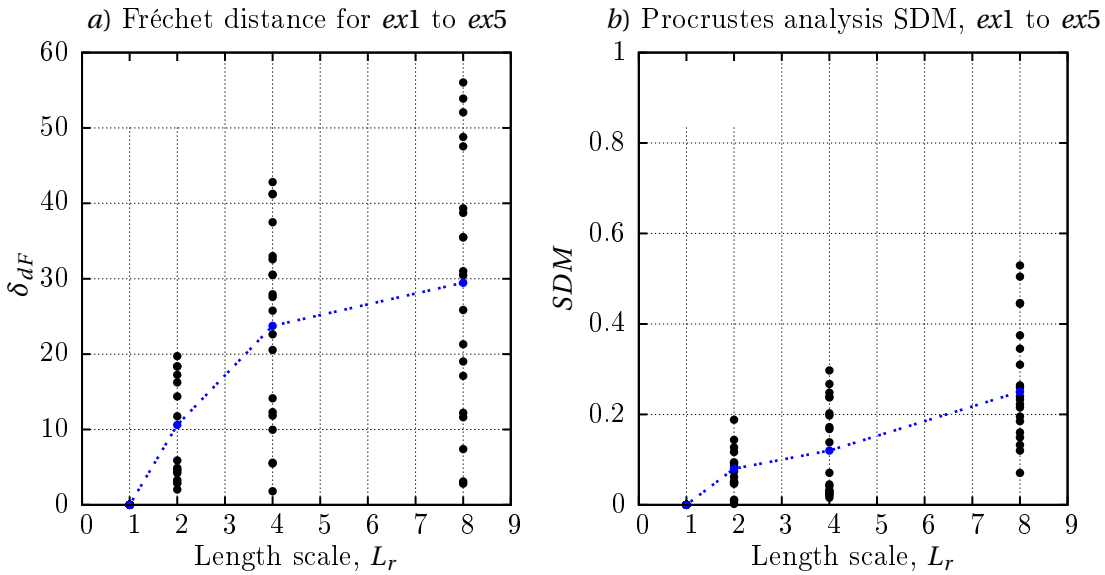

Figure 5.12: Comparison of dissimilarity measure by using Fréchet distance and Procrustes analysis.

- In Figure 5.12-a the results for all the experiments *ex*1 to *ex*5 (column 5 of Table 5.4) by using the discrete Fréchet distance method show that as the length scale increases, the greater the dissimilarity of the air concentration profiles. If the average of the Discrete Fréchet distance $\overline{\delta_{dF}}$ is calculated for the different scales and distances x, it will be observed that its values will increase successively: $\overline{\delta_{dF}} = 10.6$ for $L_r = 2$, $\overline{\delta_{dF}} = 23.7$ for $L_r = 4$ and, $\overline{\delta_{dF}} = 29.4$ for $L_r = 8$, as shown with a dashed line in Figure 5.12-a. As a consequence, based on the empirical goodness of fit proposed in Table 5.7, the scale effects for the length scale $L_r = 2$ may be defined as *moderate* and, for the higher length scales ($L_r = 4$ and $L_r = 8$) will be categorized as with a *high* presence of scale effects.

  Likewise, the results suggest that if the scale is doubled, the dissimilarity model-prototype increases but not as much as for the length scales $L_r = 4$ and 8. This can be justified in terms of the standard deviation (s) because the computed dispersions of the data are 0.05, 0.09 and 0.13 for the length scales $Lr = 2$, $Lr = 4$ and $Lr = 8$, respectively.

  As discussed in the previous chapter concerning the air entrainment in free falling water jets, while reducing the diameter of the nozzle, the values of the air concentration will be lower. For the model family of nozzles it was found that two distinct trends in the variation of the air concentration can be observed for the plots 5.12-a

and 5.12-b: 1) by using the Discrete Fréchet distance, a first interval from $L_r = 1$ (d = 80 mm) to $L_r = 4$ (d = 40 mm) where a linear proportionally can be observed and, from d = 40 mm until d = 80 mm where the rate of change is reduced in comparison with the first interval, and 2) by using Procrustes analysis SMD, where approximately a linear proportionally can be observed along the interval $1 < L_r < 8$.

In terms of the scale effects it may suggest that in applications in hydraulic engineering the model must be under scaled and as a consequence, values with lower concentrations will be found. This is the case for the diameter d = 80 m (prototype) where the measured air concentration always was bigger than zero ($C(\%) > 0$) but in the case of d = 10 mm (Model 3 - $L_r = 8$) the air concentration was equal to zero (see Figures 5.3 and 5.5).

- Procrustes analysis led to evaluate the air concentration profile in terms of a Standard Dissimilarity Measure - SDM (or error) for different scales. Shown with a dash line in Figure 5.12-b, are the errors obtained by averaging all the experiments for a same scale. As a consequence the averaged Standard Dissimilarity Measure $\overline{SDM}$ for $L_r = 2$, $L_r = 4$, and $L_r = 8$ are 0.08 (8%), 0.124 (12.4%) and 0.27 (27%), respectively. In general terms, it can be concluded that when the length scale is doubled, the SDM increases by 12% at L_r, and then for $L_r > 4$ the scale effects are considerable high because the value of the error ≈ 27%.

In Figure 5.13 the boxplot of the Standard Dissimilarity Measure (SDM) for the different diameters is presented.

In a similar way to section 4.4.4 the median value obtained for the SDM for a certain length scale $L_r = j$ is represented as $\widetilde{SDM}_{(L_r=j)}$, where j is the length scale 1, 2, 4 or 8 for the diameters 80 mm, 40 mm, 20 mm and 10 mm, respectively. As mentioned before, the SDM is a metric which indicates how a curve model matches the prototype curve. As a consequence, by definition, the prototype d = 80 mm will have $\widetilde{SDM}_{(L_r=1)} \approx 0$.

The median value of the SDM for d = 10 mm is $\widetilde{SDM}_{(L_r=8)} = 0.23$. Likewise, for model 2 with d = 20 mm, $\widetilde{SDM}_{(L_r=4)} = 10$, and for model 1 with d = 40 mm, $\widetilde{SDM}_{(L_r=2)} = 0.6$. The low values of $\widetilde{SDM}_{(L_r=4)}$ and $\widetilde{SDM}_{(L_r=2)}$ indicate that the scale effects would be low for these experiments. However, the interquartile range (IQR) obtained for d = 40 shows that the variability or data dispersion is almost half that obtained for d = 20 mm, and additionally, the low value computed for the third quartile ($\approx <$ 10) would suggest that the scale effects are low when the length scale $L_r = 2$. Finally, the last-mentioned would confirm that the non-dimensional air concentration profiles at different distances x for the diameters d = 80 mm and 40 mm are similar.

As confirmed in Figure 5.13, a low plateau region by the right side of the plot was found because of the low values of $\widetilde{SDM}_{(L_r=4)} = 0.06$ obtained for the Model 1. In order to obtain a critical non-dimensional threshold, the variation of Reynolds number respect to the Standard Dissimilarity Measure for the distinct experiments *ex1* to *ex5* are shown in Figure 5.14, analogous to calculations presented in Figure 4.22.

Figure 5.13 confirms the suggestions described in section 4.4.4 that in the case of d = 40 mm it would be expected that the scale effects would be low when Re reaches values

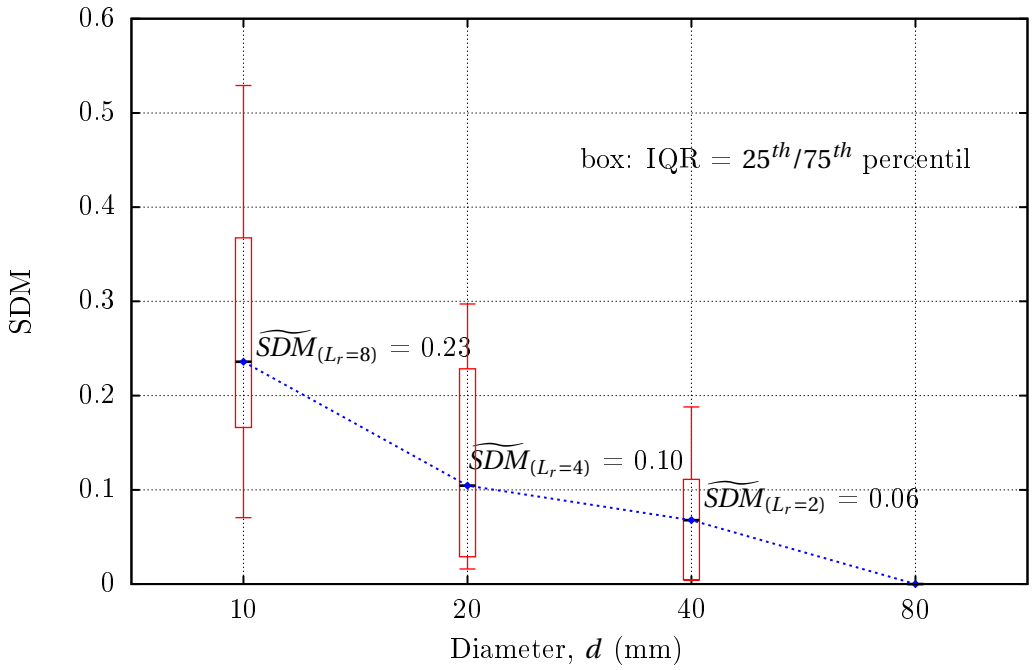

Figure 5.13: Boxplot of SDM for a model family of four nozzle pipes in diameters d of 10 mm (model 3 - $L_r = 8$), 20 mm (model 2 - $L_r = 4$), 40 mm (model 1 - $L_r = 2$) and 80 mm (prototype - $L_r = 1$) in the range $2.0 \leq Fr \leq 6.2$.

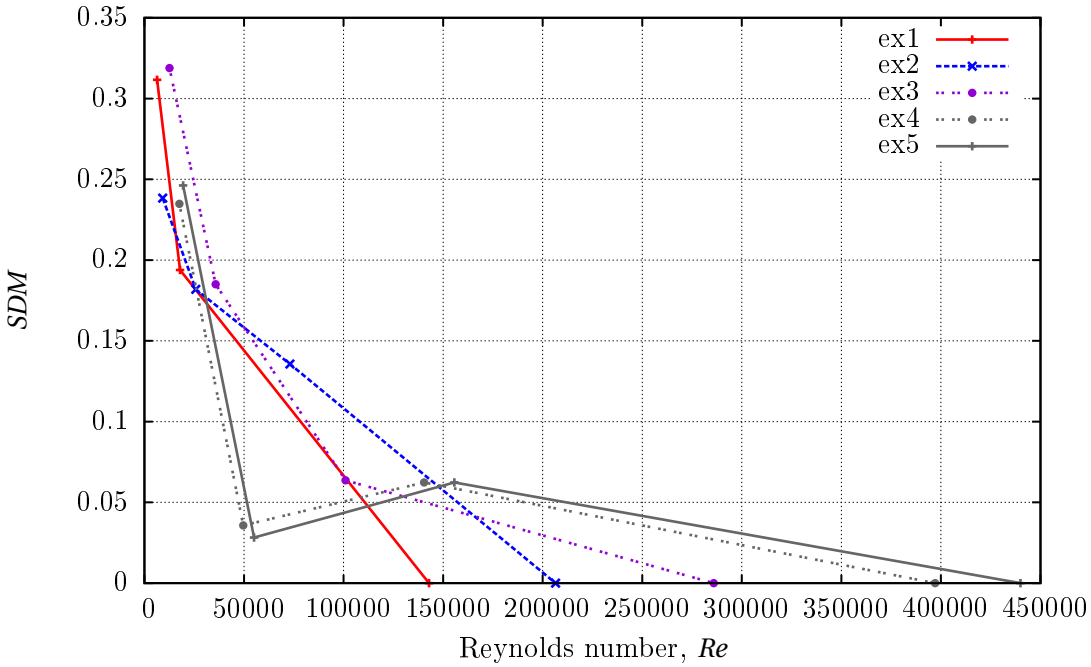

Figure 5.14: SDM vs Reynolds number (*Re*) obtained for circular nozzles in the range of $2.0 \leq Fr \leq 6.2$.

of the order of $\approx 1.5 \times 10^5$. This hypothesis can be verified with experiments *ex4* and *ex5* because their respective models at $L_r = 2$ have values of $Re = 1.4 \times 10^5$ and $Re = 1.6 \times 10^5$, respectively.

Once the model size and Reynolds number reduce, the scale effects are predominant for the lowest diameters and the dispersion in the results are high for d = 20 mm and 10 mm, as can be observed for the experiments in models with values $Re \lesssim 1.5 \times 10^5$ because of the stepped trends found in plots of SDM vs *Re*.

According to the model family of pipe nozzles here analyzed, the scale effects are negligible or low when:

- Diameter of the nozzle pipe $d \geq 40$ mm.
- Reynolds number in the nozzle exit $Re > 1.5 \times 10^5$.
- Weber number $We > 6900$.

CHAPTER

6 Computational Fluid Dynamics (CFD) simulations using the Volume of Fluid (VOF) method

The breakup phenomena of water jets discharging from circular nozzles into quiescent air is characterized as an unsteady flow with the presence of incremental changes in the water surface during its falling. To get reliable results during numerical simulations the use of a suitable method must be considered that allows generation of a dynamic interaction between the air-water phases in order to produce breakup.

Nowadays, a flexible and suitable tool to carry out this problem numerically is the solver for two incompressible, isothermal immiscible fluids using a VoF (Volume of Fluid) phase-fraction method (Hirt & Nichols [77]) based on an interface capturing approach called interFoam implemented in the OpenFOAM library. This tool is an extensive collection of code written in the C++ programming language with independent modules that can be interconnected with other routines because many features are common. Moreover, it has the capability of code customisation, extending library functionality and parallelization [79].

6.1 Challenges of Computational Fluid Dynamics in hydraulic engineering

Any solution of the Navier-Stokes equations applied to free-surface flows is a real challenge for Computational Fluid Dynamics (CFD) tools because of the highly complex hydrodynamic features consisting of the strong interface deformations and air entrainment (Prosperetti & Tryggvason [106], Lubin & Caltagirone [107], Lubin et al. [108]). The current knowledge of aerated flows relies upon laboratory investigations under controlled flow conditions in which the scale effect are predominant and a generalized equation or relationship cannot be applied at all. As a consequence, the developments of numerical models and their validation constitute a challenge in the prediction of air concentration $C(\%)$ in high speed water flows that cannot be achieved in under-scaled models in the laboratory. In spite of Kolev [109] stating that the estimation of the Reynolds stresses in multi-phase flows is in its initial stage, the determination and analysis of breakup mechanism and air entrainment constitutes an exciting challenge for theoreticians and

experimental scientists.

Chanson [110] established that hydraulics of aerated flows can greatly benefit from insights provided by numerical simulations, which may supplement the use of physical models to overcome the limitation of experimental measurements. Beyond the instrumentation it is worth adding that the scale of the model (under-scaled) plays a decisive role in the convection mechanism of the entrainment of air into the water which implies the presence of less air as the scale L_r is increased, just as concluded in the previous chapters.

As has been mentioned before, one of the challenges of the physical simulation of aerated flows is to deal with the scale effects and the restrictions for predicting the air entrainment in prototypes that can be overcome by using computational fluid dynamics techniques with an adequate validation in terms of comparing void fractions, velocity, turbulence intensity and bubble-droplet chord sizes.

In spite of the numerical methods applied to multi-phase flows that could help to improve the simulation of the air-water flow conditions to get reliable results, the main limitation is related to reproduce and to capture its nature because they are mostly turbulent and, the small-scale interactions may have profound effects on large-scale behaviours. As a consequence there is a necessity to reduce the model domains and the grid sizing enough to capture processes at the Kolmogorov scale (10^{-4}-10^{-5}m) which have effects in the small size of the cells required and, as a result a huge number of operations required that can only be overcome by computational resources such as clusters.

6.2 Case setup and numerical procedure

The open source OpenFOAM v. 2.3.1 was selected as the tool to carry out the numerical calculation. Two modes of free falling water jets with a nozzle diameter d = 20 mm were selected to be simulated in order to reproduce spiral and spray mode of breakup in conformity with the experimental tests and the description in the Ohnesorge diagram. Accordingly, the results of the computations were to be validated with the corresponding experiments done in the laboratory in terms of the air concentration C(%) measured at several distances from the nozzle exit and the mode of breakup obtained.

6.2.1 Experimental test used for validation

Two experimental tests with water velocities of U_0 = 0.89 m/s and 7.96 m/s (corresponding to the experiments 1 and 6 shown in Table 5.1 for d = 20 mm) will be used to validate the numerical simulations in terms of the air concentration C(%). The hydraulic parameters and characteristics of the experiments are described in Table 6.1, in which *experiment* is a code or identifier of the experiment, U_0 is the water velocity, Q_w is the water discharge, *Fr* is the Froude number, *Re* is the Reynolds number, *We* is the Weber number and *Oh* is the Ohnesorge number.

On the one hand the lowest nozzle water velocity was identified with the code SIM1 and, on the other hand the highest water velocity tested was identified with the code

Experiment	U_0 (m/s)	Q_w (L/s)	*Fr*	*Re*	*We*	*Oh*
SIM1	0.89	0.281	2.0	0.18×10^5	219	8.2×10^{-4}
SIM2	7.96	2.50	17.9	1.60×10^5	17403	8.2×10^{-4}

Table 6.1: Hydraulic parameters of the experimental tests used for the simulations.

SIM2, which is approximate by ten times the lowest.

The decision for choosing the experimental test for d = 20 mm was based on the following numerical and experimental aspects:

- According to preliminary CFD calculations the number of cells of the volume of control (VC) should be lower than 5×10^6 to get reasonable results in terms of computational time (< 168 h) and a simulation time of at least 1 s.
- In the event that Direct Numerical Simulation (DNS) was considered as a computational method to execute a simulation of a free falling water jet for d = 20 mm and an exit velocity U_0 = 7.96 L/s, the Kolmogorov length microscale (η) (see equation 6.1) would be in the order of 3.3×10^{-5} m:

$$\eta = \left(\frac{\nu^3}{\epsilon} \right)^{1/4} \tag{6.1}$$

  where ϵ is the average rate of dissipation of turbulence kinetic energy, and ν is the kinematic viscosity of the fluid.

  Considering that a length of 0.8 m is going to be simulated numerically, it would be expected that at least 2.1×10^{11} cells have to be used for the computations. As a consequence, due to the limited computational time available and core resources, this method shall not be considered in the analysis due to practical reasons.

- In reference to the experimental observations and the Ohnesorge diagram (see Figure 5.1), the expected mode of disintegration of the water jet for the lowest and highest water velocity would be by spiral formation and by atomization (spray) mode. In Figures 6.1 and 6.2 the experiments mentioned are shown for the first 0.42 m of falling.

  As observed in Figure 6.1, the water jet follows a varicose and oscillating behavior along its falling where the glass-like condition remains without the presence of air in it. According to the Ohnesorge diagram the characteristic of the jet herein presented obeys a behavior related to region II of the diagram mentioned.

  In Figure 6.2, experiment SIM2 consisting of a high velocity turbulent jet is shown. Within the main characteristics are: mode of disintegration by spray mode (according to the Ohnesorge diagram it would be located in region III), high interaction of the water surface with the surroundings, breaking up of the water surface

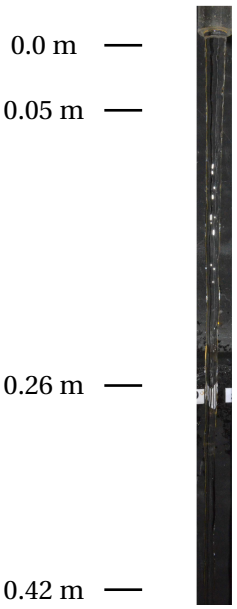

Figure 6.1: Configuration of the water jet for d = 20 mm: U_0 = 0.89 m/s, Q_w = 0.281 L/s.

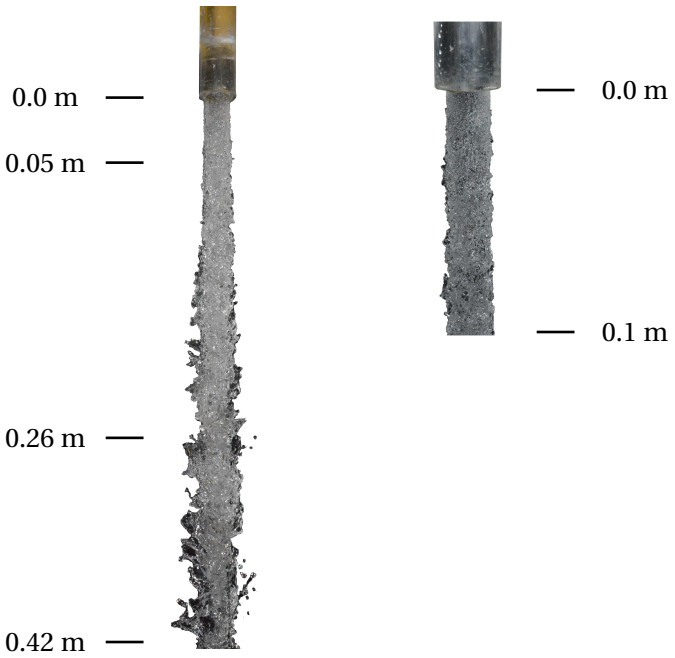

Figure 6.2: Configuration of the water jet for d = 20 mm: U_0 = 7.96 m/s, Q_w = 2.5 L/s.

due to the turbulence effects and the presence of extended filaments and the final occurrence of satellite drops.

Likewise, the distances x_1 to x_4 of the experimental test (see Table 6.2) where the air concentration $C(\%)$ has been measured will be used to validate the values of the air concentration obtained numerically. The distances are summarized in Table 6.2.

Distance	x (m)
x_1	0.05
x_2	0.26
x_3	0.683
x_4	0.78

Table 6.2: Distances from the nozzle exit for d = 20 mm where $C(\%)$ will be computed from numerical calculations.

6.3 Modelling of air-water flows

As has already been mentioned in section 2, the transport equation for the indicator function F (equation 2.39) is

$$\frac{\partial \alpha}{\partial t} + \nabla \cdot (U\alpha) = 0,$$

the mass conservation equation (equation 2.40)

$$\nabla \cdot U = 0,$$

and the momentum equation (see equation 2.51)

$$\frac{\partial (\rho U)}{\partial t} + \nabla \cdot (\rho U U) - \nabla \cdot (\mu \nabla U) - (\nabla U) \cdot \nabla \mu = -\nabla P_d - g \cdot x \nabla \rho + \sigma \kappa \nabla \alpha,$$

represent the dynamics of two phase flows. The implementation of the VOF method in the framework of OpenFOAM is based on the methodology described by Ubbink [111] and Rusche [12], and lately described extensively by Berberovic et al. [78] and Marquez [81]. The VOF equation can be solved numerically by using a Multi-dimensional Limiter for Explicit Solution (MULES) algorithm proposed by Rusche [12] and implemented by OpenCFD to maintain boundedness of the phase fraction, independent of underlying numerical scheme, mesh structure, etc. [79].

Furthermore the spatial discretisation is performed by using a cell centered collocated finite volume method (FVM) for structured and unstructured meshes with arbitrary cell shapes. The pressure-velocity coupling is solved by a Pressure Implicit with Splitting of Operator (PISO) procedure proposed by Issa [112] (summed up in Figure 6.3)

and additionally described by Ferziger & Peric [76], Verteeg & Malalasekera [113] and Villiers [114].

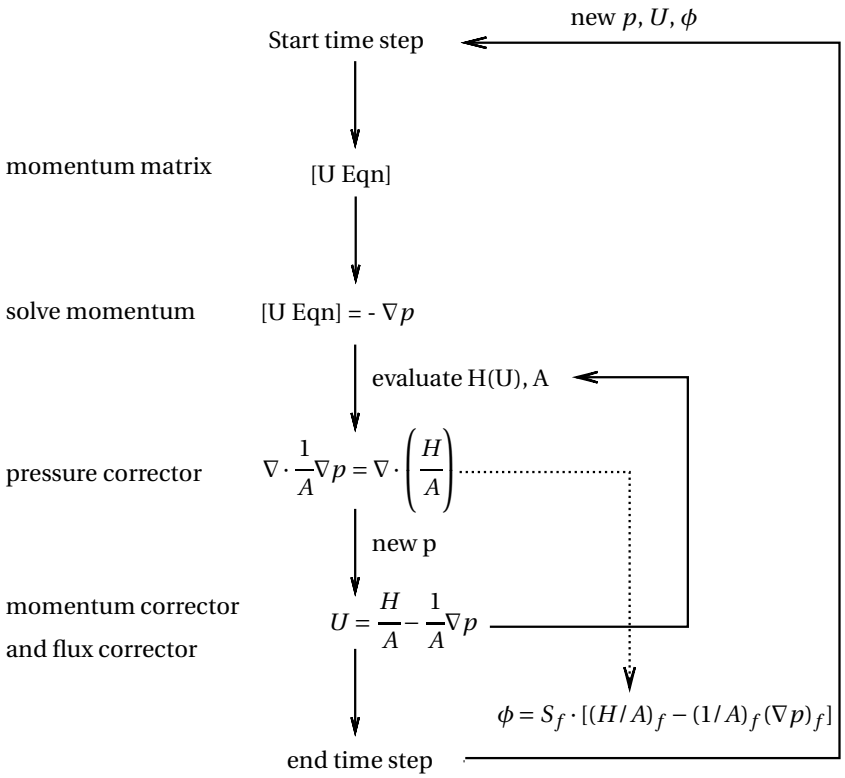

Figure 6.3: PISO algorithm (adap. from [17]).

The PISO algorithm is a predictor-corrector approach for solving transient flow problems. The momentum equation is solved first; however, since the exact pressure gradient source term is not known at this stage, the pressure field from the previous time-step is used instead. This stage is called the momentum predictor and gives an approximation of the new velocity field. Using the predicted velocities, the $H(U)$ operator can be assembled and the pressure equation can be formulated. The solution of the pressure equation gives the first estimate of the new pressure field. This step is called the pressure solution. The overall PISO algorithm can be summarized as follows:

1. Set the initial conditions.
2. Begin the time-marching loop.
3. Assemble and solve the momentum predictor equation with the available face fluxes and pressure field.
4. Solve the equation, and explicitly correct the velocity field. Iterate until the tolerance for the pressure-velocity system is reached. At this stage, pressure and velocity fields for the current time-step are obtained, as well as the new set of conservative fluxes.

5. Using the conservative fluxes, solve all other equations in the system. If the flow is turbulent, calculate the eddy viscosity from the turbulence variables.

6. Go to the next time step, unless the final time has been reached.

6.3.1 Geometry and domain decomposition

The design and construction of the mesh has a relevant effect on the success of the numerical simulations in terms of convergence, solution accuracy and computational time.

To reduce cost of computational time, the domain of the water jet has been set with a nozzle length L_n of 100 mm which discharges into an open cylinder (in contact with the atmosphere in the upper and lower part) of a constant diameter d_2 and a length of 0.80 m. However depending of the grade of dispersion of the water jet simulated, diameters of 60 mm and 100 mm were adopted. In Figure 6.4 the domain of the numerical simulation is shown.

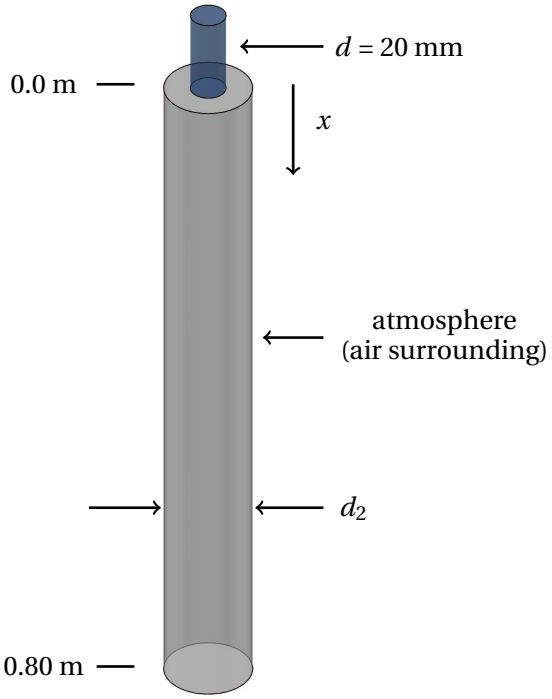

Figure 6.4: Computational fluid dynamic geometry.

The domain was decomposed into a hexahedral block (structured mesh) by using the utility blockMesh of OpenFoam where the edges of the upper cylinder and lower cylinder were built by defining circular arcs. The geometry test consisted of evaluating the aspect ratio of the mesh and the mesh non-orthogonality. As is expected an aspect ratio value of 1.0 is ideal but by complex geometries and skewness of the cells this value

tends to change. Likewise the non-orthogonality is another important characteristic of the meshing which deals with the angle between the line connecting two cell centres and the normal of their common face, where a value equal to zero is the recommended one. The minimum computed size cell during the construction of the mesh are summarized in Table 6.3, where *mesh conf.* refers to a type of mesh configuration, Δz and Δy are the minimum cell size in the radial direction, Δx is the minimum size cell in the longitudinal direction x of the falling water jet (as has been described in the previous chapters) and *No. cells* is the number of cells.

Mesh conf.	Δ z (m)	Δ y (m)	Δ x (m)	No. cells
nozzle	0.65×10^{-3}	0.65×10^{-3}	0.67×10^{-3}	-
mesh0	2×10^{-3}	2×10^{-3}	2×10^{-3}	0.65×10^{6}
mesh1	0.65×10^{-3}	0.65×10^{-3}	1×10^{-3}	1.89×10^{6}
mesh2	0.65×10^{-3}	0.65×10^{-3}	0.5×10^{-3}	4.59×10^{6}
mesh3	0.65×10^{-3}	0.65×10^{-3}	1×10^{-3}	2.31×10^{6}

Table 6.3: Cell size characteristics.

The number of cells shown in Table 6.3 for the mesh configurations 0, 1, 2 and 3 (*mesh0*, *mesh1*, *mesh2* and *mesh3*) include the number of cells computed for the nozzle as well.

6.3.2 Fluid properties

The physical properties for water and air at 20° used for the simulations are given in Table 6.4. The surface tension σ (N/m) between air and water is 7.27×10^{-2}.

Property	Water	Air
Density, ρ (kg/m^3)	999	1.20
Viscosity, μ (Ns/m^2)	9.9×10^{-4}	1.98×10^{-5}

Table 6.4: Physical properties of the fluids used (at 20°C).

6.3.3 Boundary conditions

In general, the initial conditions determine the state of the fluids at time t = 0 s, or at the first step of an iterative scheme. Regardless of the numerical methodology chosen to solve the governing differential equations, suitable initial and boundary conditions have to be specified to reproduce satisfactorily the experimental test. The accuracy of the

solution is strongly dependent on a proper physical and numerical treatment of boundaries where the robustness and convergence speed are considerably influenced by them, otherwise difficulties are encountered in obtaining solutions (Blazec [115], Versteeg & Malalasekera [113]). As a consequence, the correct implementation of boundary conditions is a crucial point of every flow solver.

Since the governing equations are a mixture of elliptic, parabolic and hyperbolic behaviour, boundary conditions must be specified at each cell of the closed solution domain. Boundary conditions can be divided into two types:

- Dirichlet boundary conditions, prescribe the value of the dependent variable ϕ on the boundary and are therefore termed *fixed value*.
- von Neumann boundary conditions, prescribe the gradient of the variable ϕ normal to the boundary and are therefore termed *fixed gradient*.

The most common physical boundary conditions in the discretised equation of the finite volume are:

- Inlet boundary: The most common method is to fix the inlet velocity. Another option is to specify the upstream stagnation pressure and velocity magnitude. A commonly used approach is when the first row of cells next to the boundary is used to construct the velocity distribution (Versteeg & Malalasekera [113]). The boundary velocities are then scaled according to this velocity profile. If the boundary is placed where variation in the flow is small, then a zero gradient condition to the indicator function can be applied.

  For this study, just like all multiphase flow modelling, this implies that the inlet condition of the indicator function needs to be fixed. The domain was specified with a non-uniform initial condition for the phase fraction α_{water}. At the nozzle (upper cylinder in Figure 6.4) α was specified as water phase and for the rest as air phase, according to the following convention:

$$\alpha = \begin{cases} 1 & \text{for the water phase,} \\ 0 & \text{for the air phase.} \end{cases} \tag{6.2}$$

  In the cases of the simulations SIM1 and SIM2 a uniform velocity of 0.89 m/s and 7.96 m/s (a fixed value boundary condition) in the direction x were set up on the top of the domain (nozzle in Figure 6.4). Furthermore, on the walls of the nozzle a non-slip condition was specified as $\vec{U} = 0$.

  The velocity in the upper part of the lower cylinder was specified as an open boundary in contact with the atmosphere.

- Outlet boundary: it is recommended to select that the outlet boundary condition such that it has a weak influence on the upstream flow. It should be placed as far away as possible from the region of interest and should be avoided in regions of strong geometrical changes.

  The velocity in the lowest part of the cylinder (outlet boundary) has been set up as a zero gradient boundary condition.

- Solid wall boundary: The normal velocity is zero; therefore no mass or other convective flux can penetrate the solid body. The other variables at the wall, the tangential velocity and pressure have to be determined by extrapolation from the interior boundary. Accordingly the viscous stress of the velocity component parallel to the boundary is zero.

In the case of the pressure the inlet and walls have been set up as zero gradient boundaries and the boundary fields in contact with the atmosphere have been defined as a boundary condition of total pressure which specifies that while U changes, p is adjusted accordingly. The top boundary is open, with prescribed total pressure consisting of static and dynamic pressure, thus allowing the static pressure to be adjusted according to the calculated velocity field. At the walls a zero gradient is set for the modified pressure.The total pressure p_0 is defined as:

$$p_0 = p + \frac{1}{2}\rho|U| \tag{6.3}$$

where U is the velocity and p is the pressure.

The most common physical condition for internal flows is to fix the outlet of the domain with a static pressure condition and additionally, to set up the outlet velocity field with a zero gradient condition. Subsequently, the scalar field α was defined as a fixed value in the inlet, a zero gradient on the fixed walls and the outlet. Moreover, an *inlet-outlet* condition was established for the patch atmosphere (upper part of the lower cylinder). The *inlet-outlet* boundary condition is defined as a zero gradient boundary condition but it switches to a fixed value if the velocity vector next to the boundary aims towards inside the domain (backward flow).

6.3.4 Time step and output control

The time step during the simulation is adjusted according to the maximum Courant-Friedrichs-Lewy number CFL_{max} prescribed initially. The CFL number is defined as:

$$CFL = \Delta t \sum_{i=1}^{n} \frac{u_{x_i}}{\Delta x_i} \leq CFL_{max} \tag{6.4}$$

where Δt is the time step, n the degree of freedom, u is the magnitude of the velocity, and Δx is the length interval. The setting of the time step is important as it influences the stability of the numerics. In principle, before computing the next approximation of fields of a new time step, the CFL number is calculated from equation 6.4.

In the particular case of the simulation of two phase flows (air-water) mixtures the air cells have a higher CFL number than water cells. In this particular case, Δt has to be set smaller than the simulation of the water volume fraction, and as a consequence prompting an increase of the computational time and numerical errors.

6.4 Turbulence models

The turbulence is a flow regime which is one of the most challenging problems in fluid dynamics whose main property is to be able to mix transport quantities much faster than molecular diffusion. According to Lesieur [116], the main characteristics that define a turbulent flow are: unpredictability, satisfy the increased mixing properties and it must involve coherent vortices or structures.

The most straightforward approach to the solution of turbulence is the implementation of Direct Numerical Simulation (DNS) which directly solves the Navier-Stokes equations without considering any turbulence model. With this method the Navier-Stokes equations are solved numerically to determine $U(x,t)$ for one realization of the flow. However, DNS is computationally expensive because all length scales and time scales have to be resolved, the computational cost increases as Re^3 and, as a consequence this approach is restricted to flows with low-to-moderate Re numbers (Pope [117]). Despite the performance of modern supercomputers, Galambos [118] states that a direct simulation of turbulence by the time-dependent Navier-Stokes equation is applicable only to relatively simple flow problems. Finally, Rodi et al. [119] concluded that DNS is not yet a method suitable for practical calculations.

In order to calculate the flow in other more realistic cases, the complexity of the problem has to be reduced and simplified. This reduction is carried out by applying an averaging operation to the Navier-Stokes equations to determine the mean velocity field $\langle U \rangle$. The classical averaging method is the ensemble average, which produces the Reynolds Averaged Navier-Stokes equations (RANS). As a consequence the Reynolds stresses are obtained from a turbulent viscosity model [117]. Based on the RANS approach, the models $k-\varepsilon$ and $k-\omega$-SST will be tested and their results will be compared with the experiments SIM1 and SIM2 shown in Table 6.1.

Besides RANS, Large-Eddy Simulation (LES) arises as an alternative to the typical viscous models applied to solve RANS models. The difference between both methods lies in the treatment of the turbulence and the equations for LES models are solved for a filtered velocity field $\overline{U}(x,t)$ which is representative of the larger scale turbulent motions. Pope [117] remarks that LES can be expected to be more accurate and reliable than Reynolds stress models for flows in which large unsteadiness is significant.

6.4.1 Standard k-ϵ model

The $k-\epsilon$ model is a two-equation model (proposed by Launder and Spalding, 1974) represented by a transport equation for the length scale ℓ which characterizes the process of transport of energy k containing eddies and the process of dissipation ϵ which destroys the small eddies. An assumption of the model is that the turbulent viscosity is isotropic [113] and also assumes that the production and destruction of the dissipation rate ϵ is proportional to the turbulent kinetic energy: the dissipation rate ϵ is large where production of k is large (Veersteeg & Malalasekera [113]).

The equation that represents the eddy viscosity ν_t is [120] [113]:

$$\nu_t = \rho c_\mu \frac{k^2}{\varepsilon} \tag{6.5}$$

where c_μ is an empirical and dimensionless constant, k is a direct measure of the intensity of the turbulence fluctuations in the three directions, and ϵ is the viscous dissipation. The standard model uses the following transport equations for k and ϵ [113]:

$$\frac{\partial \rho k}{\partial t} + \nabla \cdot (\rho k U) = \nabla \cdot \left[\frac{\mu_t}{\sigma_k} \nabla k \right] + 2\mu_t E_{ij} \cdot E_{ij} - \rho \varepsilon \tag{6.6}$$

$$\frac{\partial \rho \varepsilon}{\partial t} + \nabla \cdot (\rho \varepsilon U) = \nabla \cdot \left[\frac{\mu_t}{\sigma_\varepsilon} \nabla \varepsilon \right] + 2\mu_t c_{1\varepsilon} \frac{\varepsilon}{k} E_{ij} \cdot E_{ij} - c_{2\varepsilon} \rho \frac{\varepsilon^2}{k} \tag{6.7}$$

where the values of the five empirical and adjustable constants (not universals) has been obtained by comprehensive data fitting for a wide range of turbulent flows whose values are summarized in Table 6.5.

Constant	value
c_μ	0.09
$c_{1\epsilon}$	1.44
$c_{2\epsilon}$	1.92
σ_k	1.0
σ_ϵ	1.30

Table 6.5: Values of the constants in the $k-\epsilon$ model.

Nowadays, the most commonly used turbulence model in hydraulic engineering is this standard $k-\epsilon$ model, since it has proven to be quite stable and often produces reasonably realistic and satisfactory results [118]. Many researchers have shown that it often produces a high turbulent viscosity and is not able to capture properly the behaviour of turbulent boundary layers up to separation (Bates et al. [121], ERCOFTAC [122]). The weaknesses of the standard $k-\epsilon$ model can be summarized as follows:

- A source of uncertainly that the incoming turbulence intensity k is unknown and it must be defined as a boundary condition.
- Laminar and transitional regimes of flow cannot be modelled with the standard $k-\epsilon$ model;
- Regions of recirculation in a swirling flow are under-estimated;
- The turbulent kinetic energy is over-predicted in regions of flow impingement and reattachment leading to poor prediction of the development of flow around leading edges;

- Flow separation from surfaces under the action of adverse pressure gradients is poorly predicted;
- Flow recovery following re-attachment is poorly predicted;

In the cases of the simulations SIM1 and SIM2, an initial boundary condition with isotropic turbulence was prescribed ($U_x^2 = U_y^2 = U_x^2$), the characteristic length ℓ scale was 4×10^{-3} m and the initial turbulence was $Tu = 3\%$. As a consequence, the turbulent kinetic energy k equations reduce to:

$$k = \frac{3}{2} U'^2 \tag{6.8}$$

where $U' = Tu\, U_o$. The turbulent dissipation rate ϵ follows the equation:

$$\epsilon = \frac{c_\mu^{0.75}\, k^{1.5}}{\ell} \tag{6.9}$$

The parameters computed for the simulations are summarized in Table 6.6.

Experiment	k	ϵ
SIM1	0.0854	1.026
SIM2	0.00108	0.00146

Table 6.6: Values of the parameters k and ϵ for the $k-\varepsilon$ turbulent model.

6.4.2 k-ω SST model

Considering the pros and cons of different methods, on one hand the k-ϵ models are more accurate in shear type flows and are well behaved in the far field, and in other hand the k-ω turbulence model are more accurate and much more numerically stable in the near wall region [123]. Additional advantages of the k-ω turbulence model are:

- Allows for a more accurate near-wall treatment;
- Demonstrates superior performance for wall-bounded and low Reynolds number flows;
- Shows potential for predicting transition;
- Performs significantly better under adverse pressure gradient;
- Does not employ damping functions which leads to significant advantages in numerical stability.

Menter [124], considering the goodness of both methods, proposed a method, the so-called Menter Shear Stress Transport (SST) turbulence model which has the following form:

$$\frac{\partial k}{\partial t} + U_i \frac{\partial k}{\partial x_i} = \frac{\partial}{\partial x_i}\left[(\nu + \sigma_k \nu_t)\frac{\partial k}{\partial x_i}\right] + P_k - C_\mu \omega k, \tag{6.10}$$

$$\frac{\partial \omega}{\partial t} + U_i \frac{\partial \omega}{\partial x_i} = \frac{\partial}{\partial x_i}\left[(\nu + \sigma_\omega \nu_t)\frac{\partial \omega}{\partial x_i}\right] + \gamma \frac{\omega}{k} P_k - \beta \omega^2 + (1 - F_1)\frac{2\sigma_\omega}{\omega}\frac{\partial k}{\partial x_i}\frac{\partial \omega}{\partial x_i}, \tag{6.11}$$

where the blending function F_1 is defined as:

$$F_1 = \tanh\left[\min\left(\max\left(\frac{\sqrt{k}}{C_\mu \omega y}, \frac{500\nu}{y^2 \omega}\right), \frac{4\rho\sigma_{\omega 2} k}{CD_{k\omega} y^2}\right)\right]^4 \tag{6.12}$$

where k is the turbulent kinetic energy and ω is the specific turbulent dissipation rate.

Equation 6.10 solves for the turbulent kinetic energy k and equation 6.11 for the specific turbulent dissipation rate, ω (or turbulent frequency). The values of the specific turbulent dissipation rate ω calculated for experiments SIM1 and SIM2 in the computational fluid dynamics simulations are shown in Table 6.7.

Experiment	ω
SIM1	133.4
SIM2	15.0

Table 6.7: Values of the parameters ω and ϵ for the $k-\omega$ SAS turbulence model.

6.4.3 Large Eddy Simulation (LES)

This mathematical model for turbulence developed by Smagorinsky [125] was initially proposed for studying the dynamics of the general circulation of the atmosphere. Lately, applications in meteorological science were implemented by Lilly [126] and Deardorff [127].

In Large Eddy Simulations the dynamics of the larger-scale motions or large turbulent structures (which are affected by the flow geometry and are not universal) are computed explicitly, while the effect of the smaller scales (which have, to some extent, a universal character) or sub-grid scales (SGS) are modelled by simple models [117] [79]. In principle, LES were developed to obtain a Direct Numerical Simulation (DNS) equivalent solution for the large scale turbulence on a much coarser grid than required for DNS.

Compared with DNS, the vast computational cost of explicitly representing the small-scale motions is avoided by using LES methods.

According to Pope [117] there are four conceptual steps in LES:

- A filtering operation to decompose the velocity $U(x,t)$ into two components: a filtered component $\overline{U}(x,t)$ and a residual component $u'(x,t)$ called sub-grid scale.

$$U(x,t) = \overline{U}(x,t) + u'(x,t) \tag{6.13}$$

- The equations for the evolution of the filtered velocity field contain the *Residual Stress Tensor* RST (or SGS stress tensor) that arises from the residual motions.
- The closure is obtained by modelling the RST by a eddy-viscosity model.
- $\overline{U}(x,t)$ is computed from the model filtered equations.

In LES a space filter width, normally the grid space, is used as a scale to filter out the small scale eddies (Hinze [128], Shang et al. [129]). The scale is defined by:

$$G(x,x') = \begin{cases} x_{scale} & \text{x' } \in \text{V} \\ 0 & \text{x' } \notin \text{V} \end{cases} \tag{6.14}$$

A filtered variable φ is defined by

$$\bar{\phi}(x) = \int_V \overline{\phi}(x')\, G(x,x')\, dx' \quad \text{x' } \in \text{V}, \tag{6.15}$$

where V is the local computational volume. The Subgrid-Scale (SGS) stress is filtered and can be modeled by using the Boussinesq hypothesis as in RANS models as [128],

$$\tau_{ij} - \frac{1}{3}\tau_{kk}\delta_{ij} = -2\mu_t \overline{S}_{ij}, \tag{6.16}$$

where μ_t is the subgrid-scale (SGS) turbulent viscosity, τ_{kk} is the isotropic part of the subgrid-scale stresses, $\overline{S}_{ij}$ is the rate-of-strain tensor defined as below.

$$\overline{S}_{ij} = \frac{1}{2}\left(\frac{\partial \overline{u_i}}{\partial x_j} + \frac{\partial \overline{u_j}}{\partial x_i}\right). \tag{6.17}$$

In general, LES models are divided into anisochoric and isochoric types, and since the flow in the current research is incompressible it is assumed that an isochoric model is applicable because the volume is kept constant.

There are many LES models for the subgrid-scale turbulent viscosity, but in this specific research the Smagorinsky model, k-equation Eddy-Viscosity model and the $k-\omega$-SST scale adaptative simulation (SAS) model will be implemented to reproduce the experiments compiled in Table 6.1.

6.4.3.1 Smagorinsky model

This model proposed by Smagorinsky (1969) is one of the earliest subgrid scale models (SGS) founded under the assumption that the local equilibrium prevails [79]. Here the local subgrid-scale stresses R_{ij}, are stated to be proportional to the local rate strain of the resolved flow $\overline{S}_{ij}$ and, according to Penttinen [130] the equations describing the model are,

$$R_{ij} = -2\mu_{SGS}\overline{S}_{ij} + \frac{1}{3}R_{ij}\delta_{ij} = -\mu_{SGS}\left(\frac{\partial \overline{u}_i}{\partial x_j} + \frac{\partial \overline{u}_j}{\partial x_i}\right) + \frac{1}{3}R_{ij}\delta_{ij}, \tag{6.18}$$

where the last term ensures that the sum of the SGS stresses is equal to the kinetic energy of the SGS eddies. $\overline{S}_{ij}$ is defined as,

$$\overline{S}_{ij} = \frac{1}{2}\left(\frac{\partial \overline{u}_i}{\partial x_j} + \frac{\partial \overline{u}_j}{\partial x_i}\right). \tag{6.19}$$

Into the source code of OpenFOAM `Smagorinsky.C` the constants in Table 6.8 are prescribed.

Constant	value
ck	0.094
ce	1.048

Table 6.8: Values of the parameters ck and ce of the Smagorinsky (LES) turbulent model.

likewise the source code `Smagorinky.H` states that:

$$B = \frac{2}{3}k\,I - 2\mu_{SGS} * \mathrm{dev}(D) \tag{6.20}$$

$$B_{\mathrm{Eff}} = \frac{2}{3}k\,I - 2\mu_{\mathrm{Eff}} * \mathrm{dev}(D), \tag{6.21}$$

where B is the local subgrid-scale stresses, the operator *dev* is the deviatoric component of D, and furthermore D, k, μ_{SGS} and μ_{Eff} are defined as:

$$D = \mathrm{symm}(\nabla U) \tag{6.22}$$

$$k = \frac{2(ck)}{ce}\Delta^2 \|D\|^2 \tag{6.23}$$

$$\mu_{SGS} = ck\sqrt{k}\Delta \tag{6.24}$$

$$\mu_{\mathrm{Eff}} = \mu_{SGS} + \mu. \tag{6.25}$$

6.4.3.2 k-equation eddy-viscosity model

The k-equation Eddy-Viscosity Model which is applicable to incompressible flows is implemented in OpenFOAM under the routine `OneEqEddy.C`. In this method the subgrid-scale turbulent viscosity μ_t can be modeled mathematically based on some certain hypothesizes. In this method the eddy viscosity is modelled similarly as in the Smagorinsky

model, but here an additional transport equation for the subgrid-scale turbulent kinetic energy is added. In general, the subgrid scale (eddy) viscosity comes into some of the terms in the governing equation. This method use a modeled balance equation for the subgrid-scale turbulent energy to simulate the behavior of k. An extended explanation of this method is given by De Villiers [114]. The equation representing the turbulent dynamics in the source code `oneEqEddy.H` of OpenFoam 2.3 is:

$$\frac{\partial}{\partial t}k + \frac{\partial}{\partial x_i}(U_i k) - \frac{\partial}{\partial x_i}\left(\nu_{\text{Eff}}\frac{\partial}{\partial x_i}k\right) = -BL - \frac{ce\,k^{3/2}}{\Delta}. \tag{6.26}$$

In equation 6.26 the first term describes the change of the turbulent SGS kinetic energy with respect to time, the second term is the convection component, the third term describes the diffusion, the fourth term equal to $-BL$ represents the decay of turbulence from the resolved scales to the sub-grid scales via the energy cascade, and the last term on the right hand corresponds to turbulent dissipation. Extended documentation is presented by Penttinen [130]. The term BL is defined as the double inner product of D and B ($D:B$), which are defined as:

$$D = \text{symm}(\nabla U), \tag{6.27}$$

$$B = \frac{2}{3}k\,I - 2\mu_{\text{SGS}}\text{dev}(D). \tag{6.28}$$

6.4.3.3 $k-\omega$-SST scale adaptative simulation (SAS) model

The LES $k-\omega$-SST scale adaptative simulation (SAS) model for incompressible flows was based on the approach developed by Menter and co-workers in the European founded project DESider between 2004 and 2007. Davidson [131] proposed an additional term in the ω equation which detects the unsteadiness of the flow equations and as a consequence increases the production of ω. In principle this is a RANS-LES hybrid model based on the original $k-\omega$ *SST* model, that mixes two turbulence models: (a) the model in the near wall region, where vorticity is expected and, (b) the model further out. As a consequence with hybrid RANS-LES models, part of the turbulence is resolved and part of the turbulence is modelled [131].

In OpenFOAM 2.3 the source code `kOmegaSSTSAS.H` is built on the studies of Davidson [131] but the first term of the Q_{SAS} expression is corrected following the studies of Menter & Egorov [132].

6.5 Computational Resources

The calculations were executed in the Vienna Scientific Cluster 2 (VSC-2) which is a high-performance computing cluster assembled at Vienna University of Technology [1]. The system contains the following characteristics: 1314 compute nodes, each node has two processors of type AMD Opteron 6132 HE with a clock rate of 2.2 GHz and each time 8 processor cores.

[1] `http://vsc.ac.at/`

To carry out the current research, it was granted with access to 1000 parallel cores and 2×10^6 core-h.

6.6 General elementary rules

The following compendia of recommendations should be considered in order to guarantee accuracy and stability of the simulations according to Ferziger & Peric [76], Versteeg & Malalasekera [113], Guerrero [18] and Lidtke [133]:

- Good initial conditions can improve the stability and convergence rate.
- Explore initially computationally inexpensive solutions on a coarse mesh and then to interpolate it to a fine mesh.
- First order schemes are too diffusive, which mean that the forces could be under predicted and smear the gradients.
- The stability of the solution should be checked during the numerical calculations.
- The mesh quality must be checked.
- Do not push too much the numerical scheme on highly non-orthogonal meshes (60>NO).

6.7 Numerical schemes and solvers

The numerical schemes denote the class of numerical discretisation for solving a determinate partial differential equation. In OpenFOAM a wide range of schemes are available for Time, Convective, Gradient, Laplacian, Surface Normal Gradient and Interpolation. According to Lidtke [133], two aspects should be taken into account:

1. A linear scheme should applied first, and
2. Time and convective scheme affect in more proportion the stability of the simulations.

6.7.1 Time derivative schemes

As is known, the time derivative scheme $\partial/\partial t$ influences the maximum time step. For the simulations two schemes were implemented:

1. *Euler scheme* is first-order accurate which generally gives fastest convergence but in the case of transient simulations reduces the accuracies. In the case of the simulations by using RANS and LES models this scheme will be applied for the simulations.
2. *Crank-Nicolson scheme* is second-order accurate but some researchers have reported instabilities for a range of problems. However Likdte [133] suggests using this scheme as a must for Large Eddy Simulations. As a consequence, in case of instabilities Euler Schemes will be used initially, but in case of problems of convergence the scheme adopted will be of the Crank-Nicolson type.

6.7.2 Gradient schemes, ∇

The way to calculate the gradients is defined through the `gradSchemes` dictionary in OpenFOAM. It can be computed using *Gauss method* or the *least square method -LSM-*. Furthermore, the gradient limiter avoid over and under shoots on the gradients computations. There are two types of limiting: (a) *Cell limiting*, determines the limited gradient along a line connecting adjacent cell center and, (b) *Face limiting*, determines the limited gradient on the face itself. In general, *Cell limiting* should be less dissipative than *Face limiting*.

Standard gradient limiting, i.e. `cellLimited`, clips each component of the gradient equally (it is a vector). Likewise, `cellMDLimited` is a Multi-Dimensional limiter whereby the gradient is clipped in the direction normal the cell faces.

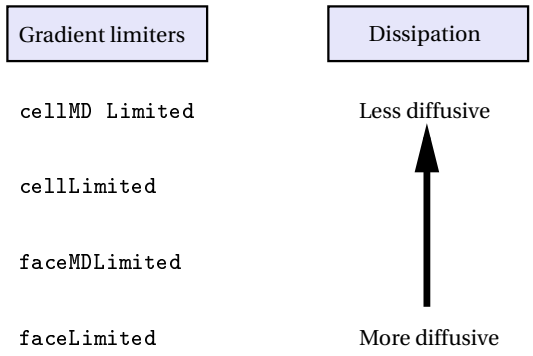

Figure 6.5: Gradient limiters (adap. from [18]).

In the case of the simulations done, the discretisation scheme *Gauss* was selected. This is a second-order scheme which specifies the standard finite volume discretisation of Gaussian integration which requires the interpolation of values from cell centres to face centres. Therefore, the `Gauss` entry must be followed by the choice of interpolation scheme. For this specific case the `linear` scheme was set up which is an effective choice.

6.7.3 Divergence schemes, $\nabla \cdot$

The Gauss scheme is the only choice of discretisation and requires a selection of the interpolation scheme for the dependent field. The interpolation scheme selected was `linear` in which numerical behavior is of second-order and unbounded.

6.7.4 Laplacian schemes, $\nabla \cdot \nabla$

The Laplacian, denoted as Δ, $\nabla \cdot \nabla$ or ∇^2 is a differential operator that represents the divergence of the gradient of a function in Euclidean space. In fluid dynamics the typical Laplacian term found is $\nabla \cdot (\nu \nabla U)$.

In OpenFoam the `Gauss` scheme is the only choice of discretisation and requires a selection of both an interpolation scheme for the diffusion coefficient, i.e. ν in our example, and a surface normal gradient scheme, i.e. ∇U. As a consequence, the `linear`

scheme was the interpolation scheme for the simulations and the normal gradient scheme was `corrected`.

6.7.5 Interpolation schemes

The interpolation schemes in the `interpolationSchemes` sub-dictionary contain terms that are interpolations of values typically from cell centres to face centres. For all the simulations centred schemes of the type Linear interpolation (central differencing) was set up.

6.7.6 Surface normal gradients Schemes

A surface normal gradient is evaluated at a cell face; it is the component, normal to the face, of the gradient of values at the centres of the two cells that the face connects. A surface normal gradient may be specified in its own right and is also required to evaluate a Laplacian term using Gaussian integration. For all the simulations an Explicit non-orthogonal correction scheme was selected.

6.8 Results and discussion

In the following section the numerical results of five turbulent models k-ϵ, k-ω SST, LES Smagorinsky, LES k-equation eddy- viscosity model and $k-\omega$-SST scale adaptative simulation (SAS) model were implemented to simulate the experiments SIM1 and SIM2. In order to compare them, the time evolution has been recorded for the simulation times t = 0.02, 0.04, 0.06, 0.08, 0.10 and 2.0 s and, the phases air and water will be analyzed by means of an air concentration profile in the plane xy (which is also equivalent to the plane xz) along the longitudinal axes of the jet.

Furthermore, at each computational step Δt the phase α at radial distances from the nozzle axis in the positions summarized in Table 6.2 was stored. Considering that the phase α is a value between 0 and 1, it was stated that a value bigger than 0.5 will correspond to a water fraction (α = 1) and below it will be an air fraction value (α = 0). Taking into account that the computational time step $\triangle t$ is not constant because it is strongly dependent on the prescribed *CFL* number and its value varies during the simulations, therefore a value of Δt = 0.0001 s was established in order to build a vector time $t = (t_1, t_2, \ldots, t_n)$, where t_n is the maximal simulation time and n the number of simulation times. As a consequence, for each simulation time, let say vector time, the corresponding value of the phase α is calculated. Consequently, a corresponding vector of the phase ($\alpha = (\alpha_1, \alpha_2, \ldots, \alpha_n)$) will be obtained and finally, the air concentration at certain position x in the radial direction ($y = z$) will be calculated as:

$$C(\%) = \frac{\Sigma \alpha}{n} \tag{6.29}$$

by averaging the data at the same point.

The results of the simulations done for the experiments SIM1 and SIM2 are presented as follows.

6.8.1 Simulations of the experiment SIM1: spiral mode of disintegration

The experimental test SIM1 corresponds to a relatively low water velocity condition and the mode of disintegration obtained was of the type with spiral formation.

In Figures 6.6, 6.7, 6.8, 6.9 and 6.10 the time evolution of the water discharging into the atmosphere for the turbulent models k-ϵ, k-ω SST, LES Smagorinsky, LES k-equation eddy-viscosity model and $k-\omega$-SST scale adaptative simulation (SAS) model are presented. In order to visualize the position of the water along its fall a lateral tick has been added to each plot which indicates the distance from the nozzle exit (reference 0.0 m) until the end of the domain, located at 0.80 m away from it.

The simulations started by considering that the nozzle is full of water until the nozzle exit and the initial velocity direction U_0 = 0.89 m/s is straight in the x-direction. The remain of the domain is fulfill of air (α = 0).

Based on the time evolution plots, the following conclusions can be drawn:

- The RANS turbulent model k-ϵ shows a homogeneous behavior of the water during its discharge into the atmosphere, demonstrating that in the case of using this turbulent model the surface tension is dominating the fluid and the convection of the fluid prevails downward.

  Moreover, the forefront of the water jet shows a compact fluid without the presence of filaments or visible protuberances on the water surface. On the contrary, the numerical results show a permanent glass like condition along the falling jet where the cross section (xy-plane)of the water jet tends to be reduced as it falls by the effect of the acceleration of the flow due to gravity.

  The main characteristic of using the turbulent k-ϵ model is that the water jet is unbroken. Even if the turbulent intensity and the number of cells is increased, numerically this does not influence the water surface and always the constitution of the jet will be stretched as it falls and the water surface will be smooth. It is worth mentioning that in pre-tests done by using this turbulence model, even for longer distances (until 4.0 m) and mesh configurations, there was never water jet break up and it did not show threads or even satellite drops at all.

  For carrying on this simulation a parallelization on 128 cores was done, by using the mesh configuration *mesh2* (see Table 6.3) which required an execution time of 74.2 h for a simulation time of 2.0 s.

- Particularly at the first 0.10 s by using the RANS turbulent k-ω SST model, unlike the k-ϵ results, does not reveal a sharp end. After the water jet goes through the casing pipe until the end of the domain (at the position 0.80 m) the flow is stabilized (0.3 s) and the water jet has the same behavior as obtained for the k-ϵ model described above.

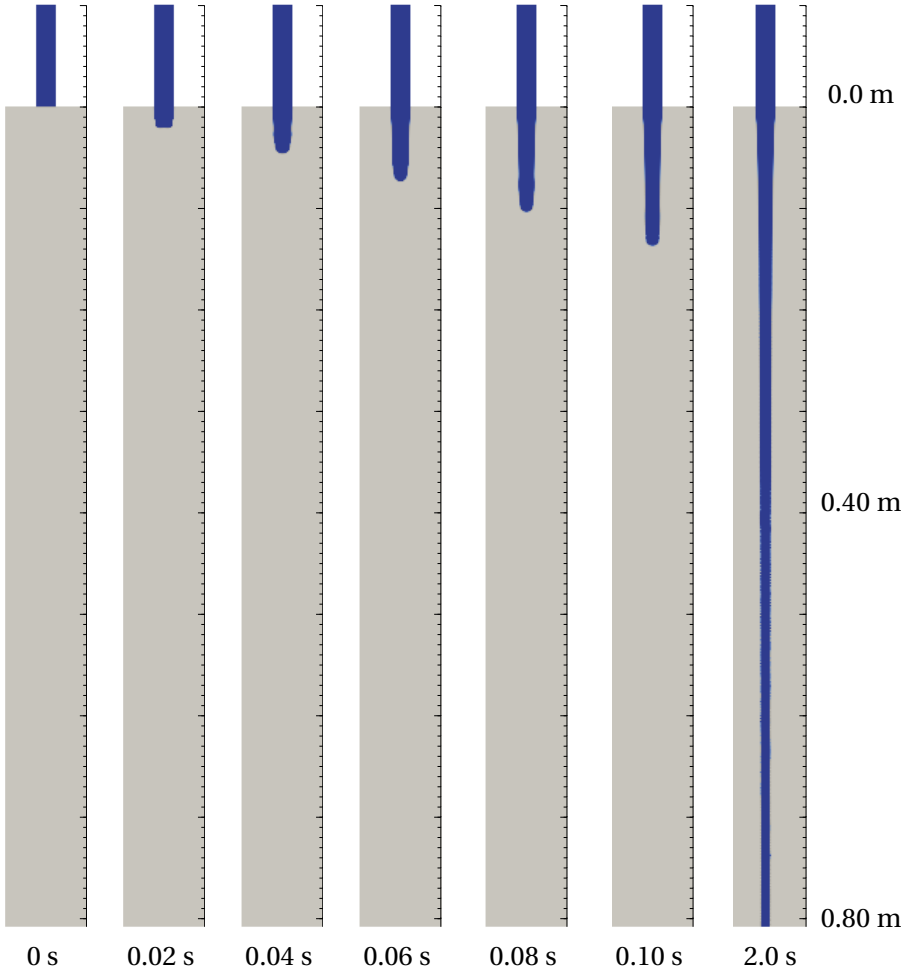

Figure 6.6: Time evolution of a free falling water jet by using the turbulent model k-ϵ for d = 20 mm and U_0 = 0.89 m/s.

It is worth mentioning that the results obtained for the RANS models, in spite of the expectation that the numerical simulations reproduce partially the behavior of the experiments, in neither case breakup was reproduced, even for much longer lengths.

To get a simulation time of 2.0 an execution time of 69.7 h was required. Additionally the parallelization was done in 128 cores and the mesh configuration *mesh2* was set up.

- In Figure 6.8 the results obtained for the turbulent model LES Smagorinsky are presented. In spite of a premature breakup which took place at 0.70 m (at 2.0 s), this turbulence model was able to generate irregularities on the water surface and the air-water interaction took place from an earlier distance (0.40 m) than in the experimental test.

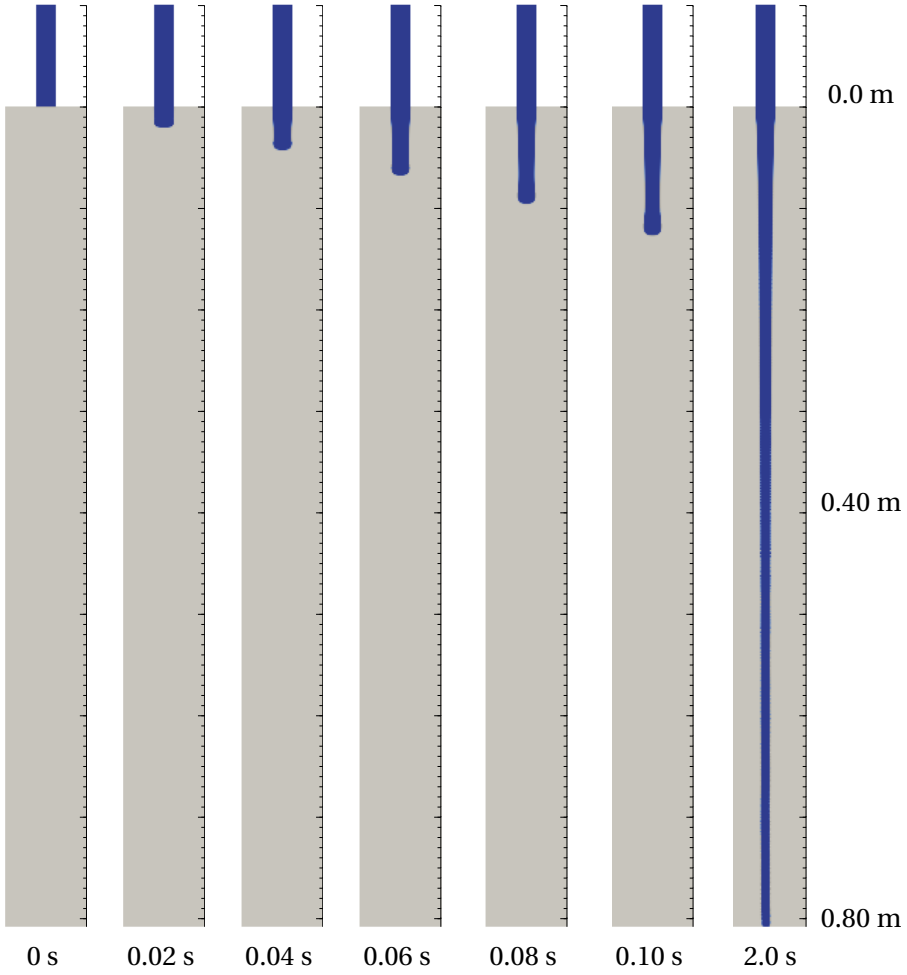

Figure 6.7: Time evolution of a free falling water jet by using the turbulent model k-ω SST for d = 20 mm and U_0 = 0.89 m/s.

Unlike the RANS models, the LES turbulence models demonstrated a valuable capability of inducing an active interaction between both phases during the falling, characterized by the occurrence of breakup at approximately 0.70 m from the nozzle exit. However, the LES Smagorinsky method was characterized by a high instability of the simulations depending on the mesh configuration. Moreover, in pre-tests it was found that LES turbulence models are quite sensitive to the mesh geometry configuration and as a consequence, the lower cylinder of the domain (which is in contact with the atmosphere) was modified in the transverse section (plane yz) from circular to rectangular in order to reduce the non-orthogonality of the mesh. The computational time for 2.0 s was 145.7 h by using 128 cores in parallel with the mesh configuration *mesh3* (see Table 6.3).

- The results of using an LES k-equation eddy viscosity model shown in Figure 6.9

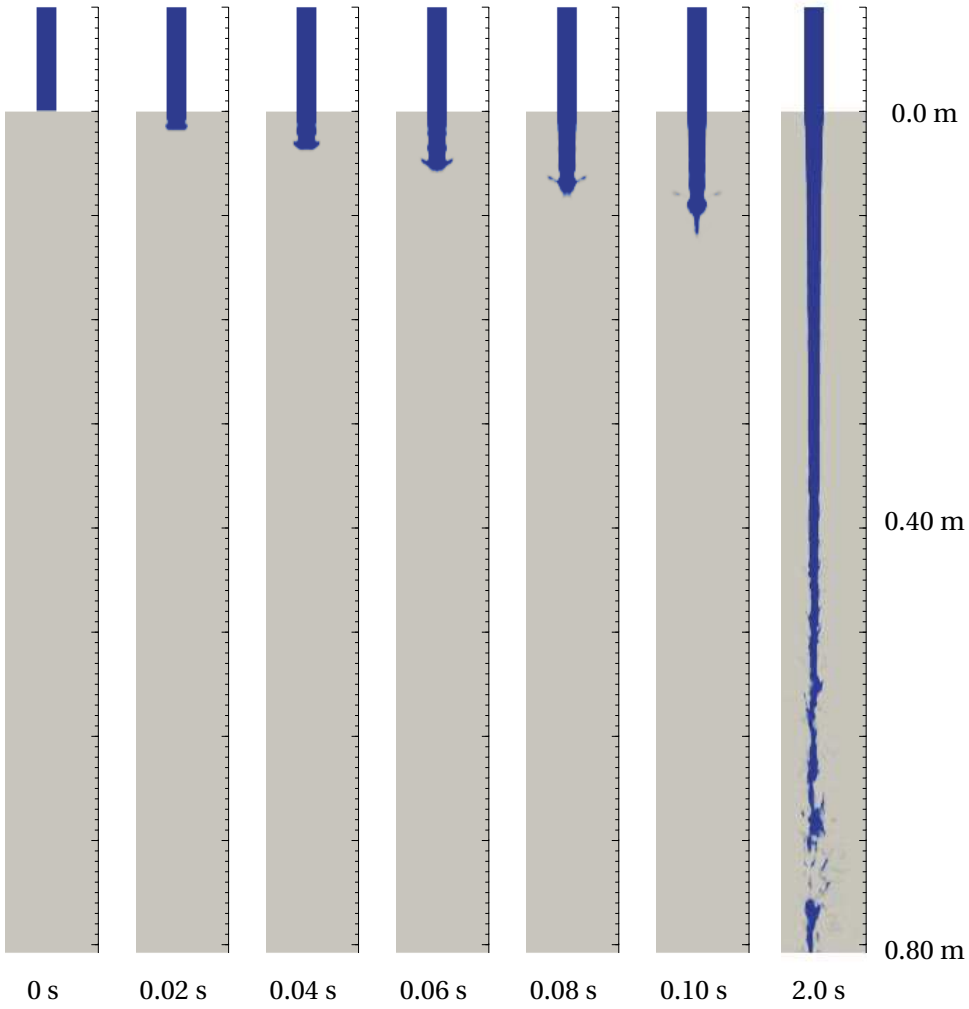

Figure 6.8: Time evolution of a free falling water jet by using the turbulent model LES Smagorinsky for d = 20 mm and U_0 = 0.89 m/s.

gave similar results to those obtained by using the LES Smagorinsky model. This turbulence model led to the induction of an active diffusion of the air into the mass of water by a mechanism of water separation from a distance of 0.50 m. Furthermore the dynamics of the flow contributed to the formation of breakup at 0.63 m. By using the mesh configuration *mesh3* and 128 cores in parallel the computational time for 2.0 s was 148.3 h.

- The time evolution using the $k-\omega$-SST scale adaptative simulation (SAS) model (see Figure 6.10) was quite similar as obtained for the those obtained with the k-ϵ model. There was no breakup and the water surface was not altered at all by using this turbulence model. The computational time for 2.0 s was 301.3 h by using 32 cores in parallel

Based on the computational fluid dynamics (CFD) calculations done with five differ-

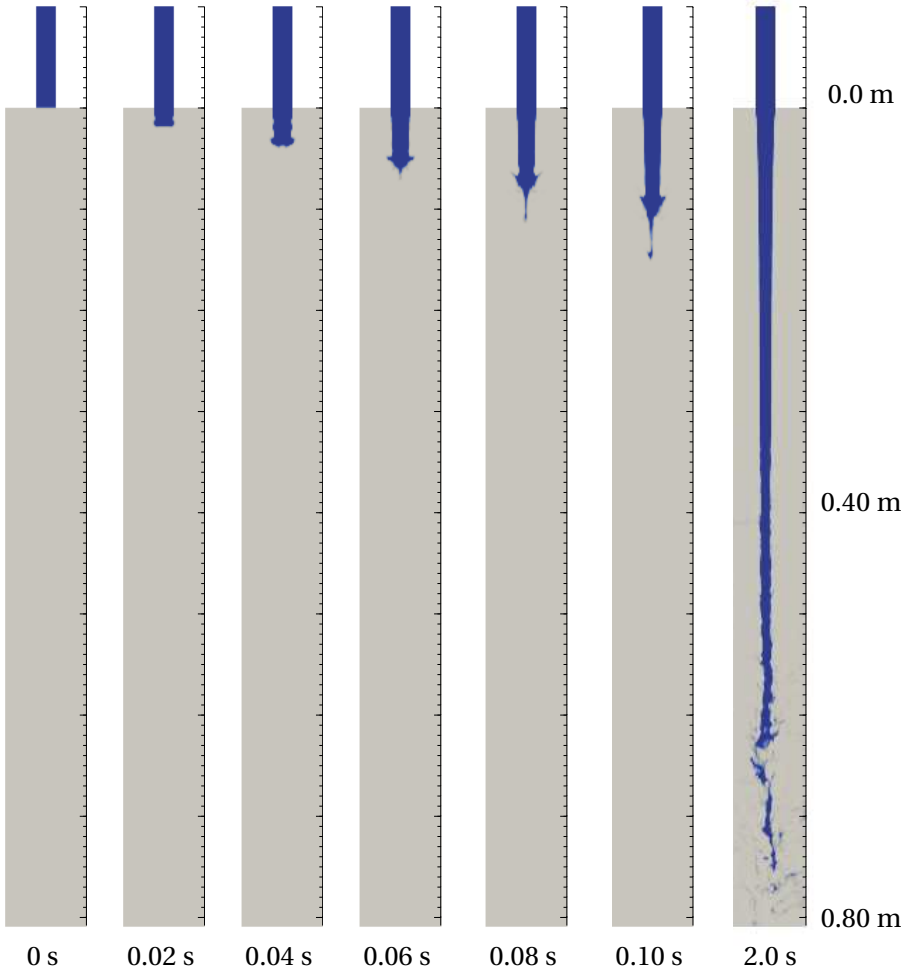

Figure 6.9: Time evolution of a free falling water jet by using the turbulent model LES - k equation eddy viscosity model for d = 20 mm and U_0 = 0.89 m/s.

ent turbulent models for a nozzle pipe with a diameter of d = 20 mm (or radius, r = 10 mm), the values of the air concentration $C(\%)$ versus the relative position y/r was calculated at the distances x = 0.05 m, 0.26 m, 0.683 m and 0.78 m as it can be observed in Figure 6.11. As follows, the convention for the legend is resumed: (1) `exp`, is the experimental test, (2) k-ϵ, corresponds to the numerical simulation by using the turbulence model mentioned, (3) k-ω `SST`, corresponds to the numerical simulation by using the mentioned turbulence model, (4) LES Smag., corresponds to the numerical simulation by using Large Eddy Simulation - Smagorinsky turbulence model, (5) LES k-Eq., corresponds to the numerical simulation by using Large Eddy Simulation - k-equation eddy-viscosity model, and (6) LES Hyb, is the calculation obtained for the $k-\omega$-SST scale adaptative simulation (SAS) model. Below there is a summary that arises out of Figure 6.11 corresponding to the computation of the air concentration at several distances:

- The experimental tests (with the legend `exp`) showed that for the range analyzed

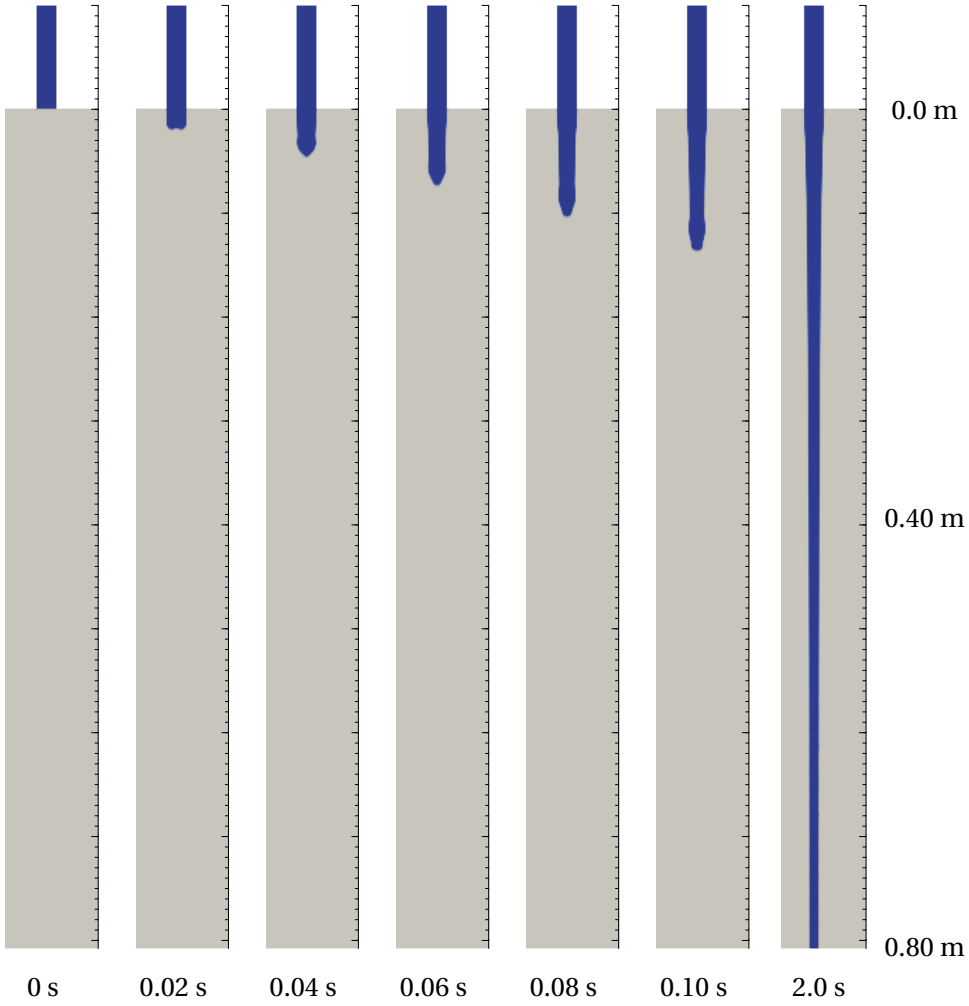

Figure 6.10: Time evolution of a free falling water jet by using the turbulent model $k-\omega$-SST scale adaptative simulation (SAS) model for d = 20 mm and U_0 = 0.89 m/s.

(until 0.80 m) there is no breakup and the water jet cross section gets narrower as the velocity increases due the falling. As a consequence, the angle of spread θ becomes negative. In general, always a massive core jet was observed and towards the center of the jet the air concentration reached a value of 0%.

- The results obtained by using the turbulence models k-ϵ, k-ω SST and $k-\omega$-SST scale adaptative simulation (SAS) are similar. Always a massive core was obtained from the numerical simulations and there was no presence of drops or threads in the water surface.

  It is worth mentioning that the use of Reynolds-averaged Navier-Stokes (RANS) turbulence models as k-ϵ and k-ω SST did not reproduce the breakup phenomena or even protuberances in the water surface.

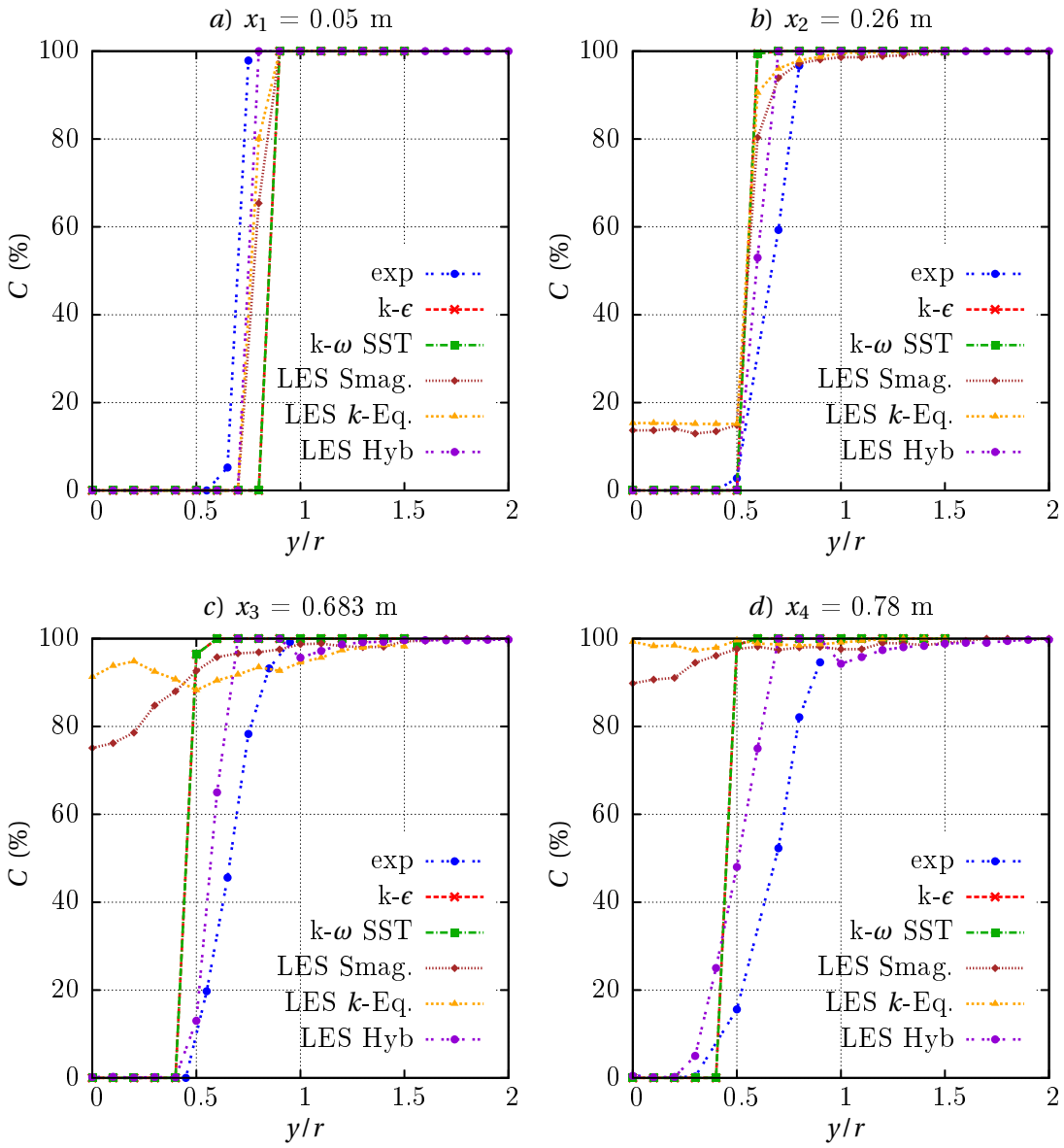

Figure 6.11: Air concentration at several locations - for $d = 20$ mm and $U_0 = 0.89$ m/s.

- Although the air concentration profile obtained by LES - Smagorinsky turbulence model and LES - k-equation eddy-viscosity model were different for longer distances (x_2 = 0.683 m and x_4 = 0.78 m) from those measured experimentally, it is worth mentioning that these methods were able to generate the turbulence necessary in the water jet in order to reproduce breakup.

  For both turbulence models, in spite of the water jet breakup taking place at an earlier stage, they follow the expected behaviour in nature, unlike the RANS models. As a consequence of this, the air concentration profiles shown in Figure 6.11-c and 6.11-d are flattened.

  In general, it may be concluded that LES methods (Smagorinsky and k-equation eddy-viscosity model) are able to reproduce the phenomena of air entrainment, the high interaction of the water surface with the air at high velocities and finally reproduce breakup in water jets.

- Furthermore, it should be mentioned that in general terms the computational time for LES Smagorinsky and LES k-equation eddy-viscosity model is twice as long as that using RANS models. Likewise, the $k-\omega$-SST scale adaptative simulation (SAS) model required a computational time sixteen times that of RANS turbulence models when the efficiency is evaluated in terms of time/processor.

- In conclusion, at comparing the results of the numerical simulations at low Reynolds number, the LES turbulence model $k-\omega$-SST scale adaptative simulation (SAS) reproduced suitable the air concentration profiles obtained experimentally.

6.8.2 Simulation of the experiment SIM2: atomization

These numerical calculations are an attempt to simulate and reproduce the experimental test shown in Figure 6.2. The water jet ejected into quiescent air from a nozzle of diameter d = 20 mm has an initial velocity U_0 = 7.96 m/s and the mode of disintegration was of spray type or atomization.

In Figures 6.12, 6.13, 6.14, 6.15 and 6.16 the time evolution of the water discharging into the atmosphere for different turbulent models k-ϵ, k-ω SST, LES Smagorinsky, LES k-equation eddy-viscosity model and $k-\omega$-SST scale adaptative simulation (SAS) model are shown. In the same way as mentioned before, the simulations at the beginning (time t = 0 s) considered that the nozzle was full of water until the nozzle exit and the initial velocity direction U_0 = 7.96 m/s was downward. The rest of the domain was full of air (α = 0).

Based on the time evolution Figures for high turbulent water jets shown in Figures 6.12 - 6.16, the following conclusions can be drawn:

- In the case of using the k-ϵ turbulence model the mesh configuration *mesh0* (see Table 6.3) was used, which required an execution time of 13.4 h for a simulation time of 2.0 s. The parallelization was set up on 128 cores.

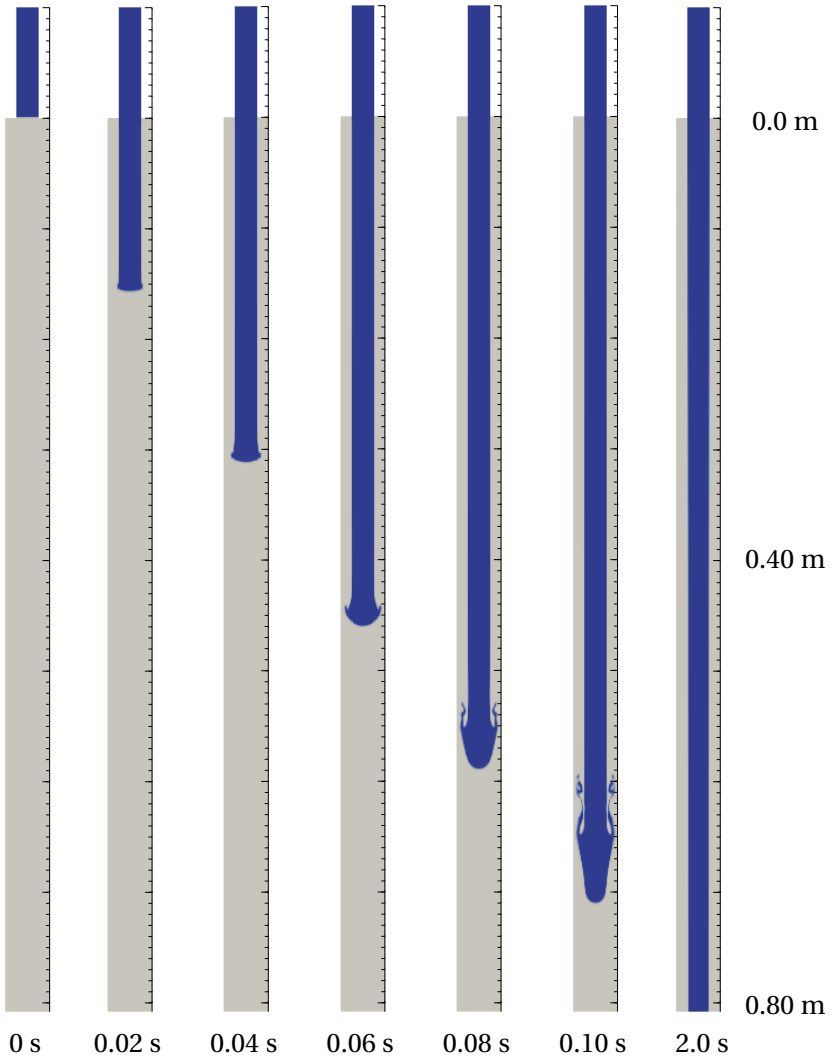

Figure 6.12: Time evolution of a free falling water jet by using the turbulent model k-ϵ for d = 20 mm and U_0 = 7.96 m/s.

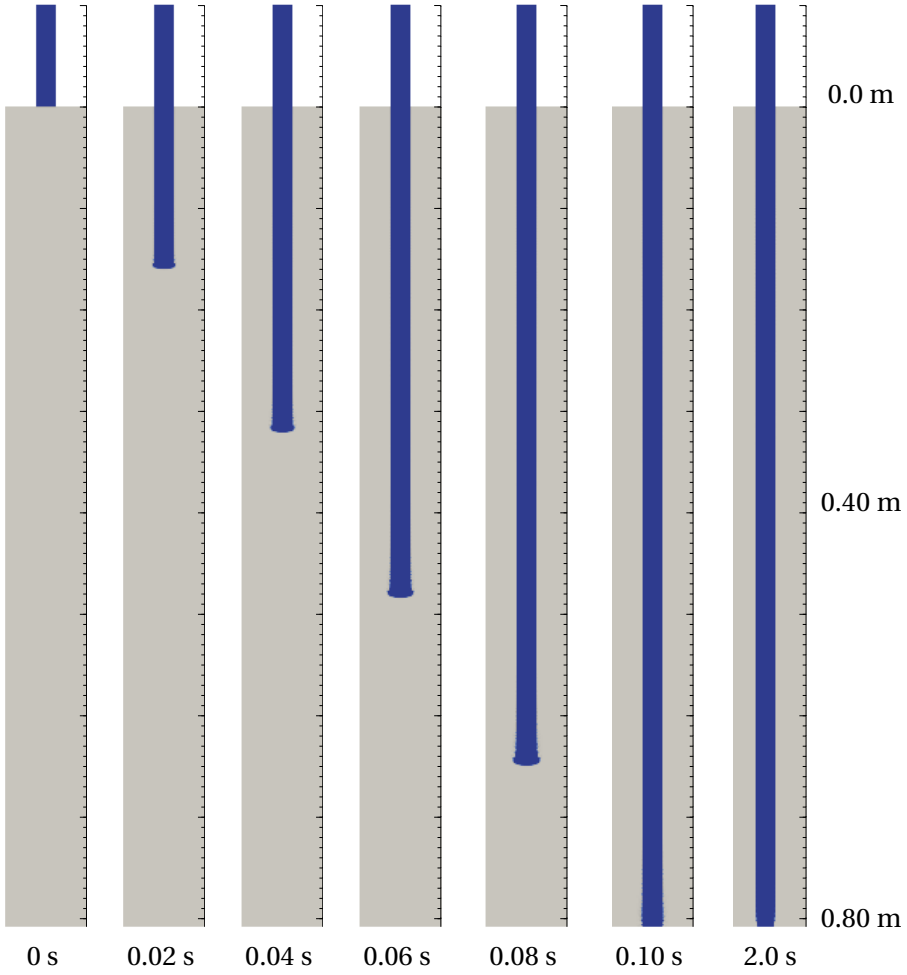

Figure 6.13: Time evolution of a free falling water jet by using the turbulent model k-ω SST for d = 20 mm and U_0 = 7.96 m/s.

In Figure 6.12 the time evolution of the water jet falling into air can be visualized. At 0.02, 0.04 and 0.06 s a massive front formed and at the sides a sheet of water formed which started to separate from the whole fluid after 0.08 s at 0.65 m from the nozzle exit. As a consequence, a thin filament of water at 0.10 s separated from the water but after the fluid stabilized the water jet behaved as a whole mass of fluid without the presence of atomization or satellite drops emerging from it. The results obtained with this turbulent model were the same as obtained for low water velocity and under neither circumstance did the breakup take place.

- In Figure 6.13 the time evolution for the k-ω SST turbulent model is shown. This simulation was done with the mesh configuration *mesh1*. Moreover a computational time of 68.1 h was invested for a simulation time of 2 s in 128 cores.

Unlike the k-ϵ model at initial times (until 0.10 s), the k-ω SST turbulent model re-

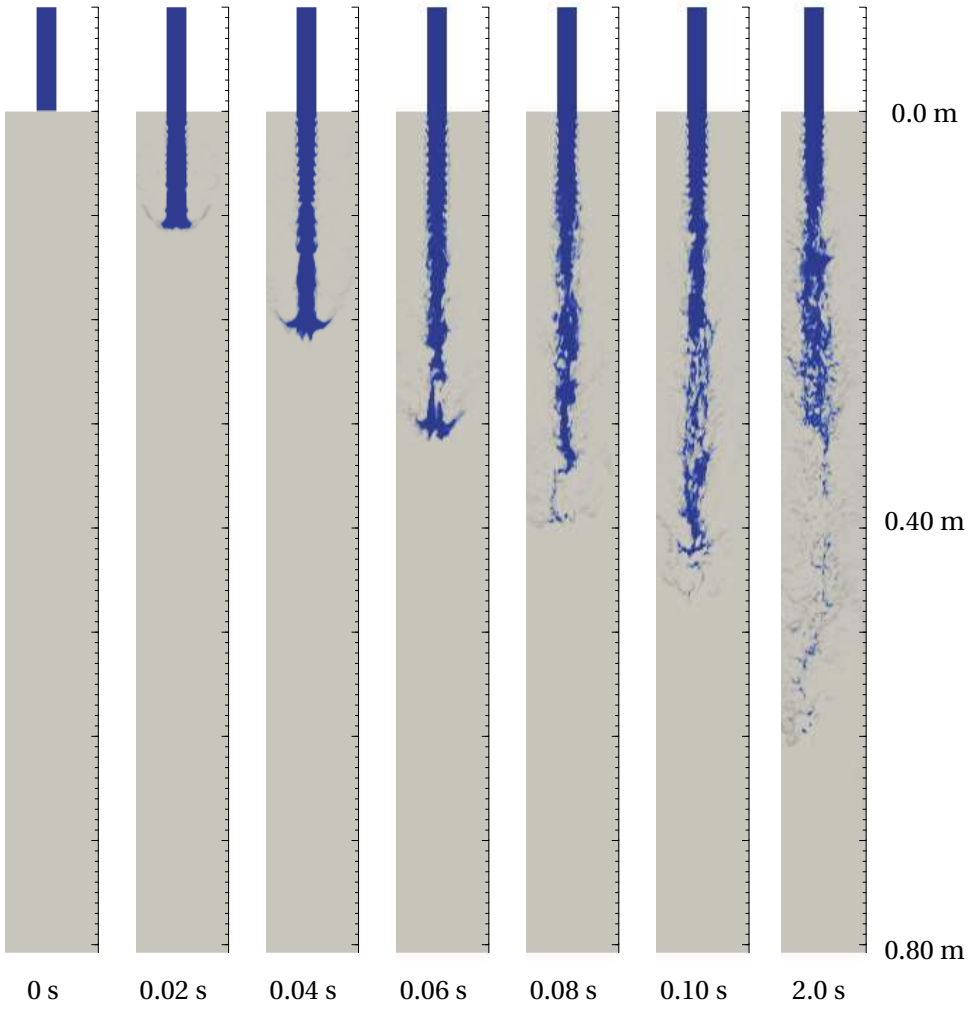

Figure 6.14: Time evolution of a free falling water jet by using the turbulent model LES Smagorinsky for d = 20 mm and U_0 = 7.96 m/s.

produced the same behavior as that obtained for low water velocity. Additionally, in neither case did this method reproduce or generate breakup of the water jet.

- The Large Eddy Simulation - Smagorinsky method reveals the spray formation in the simulations. To perform the simulations the following characteristics were set up and obtained: the mesh configuration *mesh3*, 128 cores in parallel computing and an execution time of 203.4 h. In Figure 6.14 the behavior of the water jet is presented at several time steps. Of great interest is the observation that the method is able to reproduce not just break up, but atomization too at 0.3 m from the nozzle exit.
- In Figure 6.15 the results from Large Eddy Simulation - k-equation eddy-viscosity model are presented. Although this method is less diffusive than the Smagorinsky

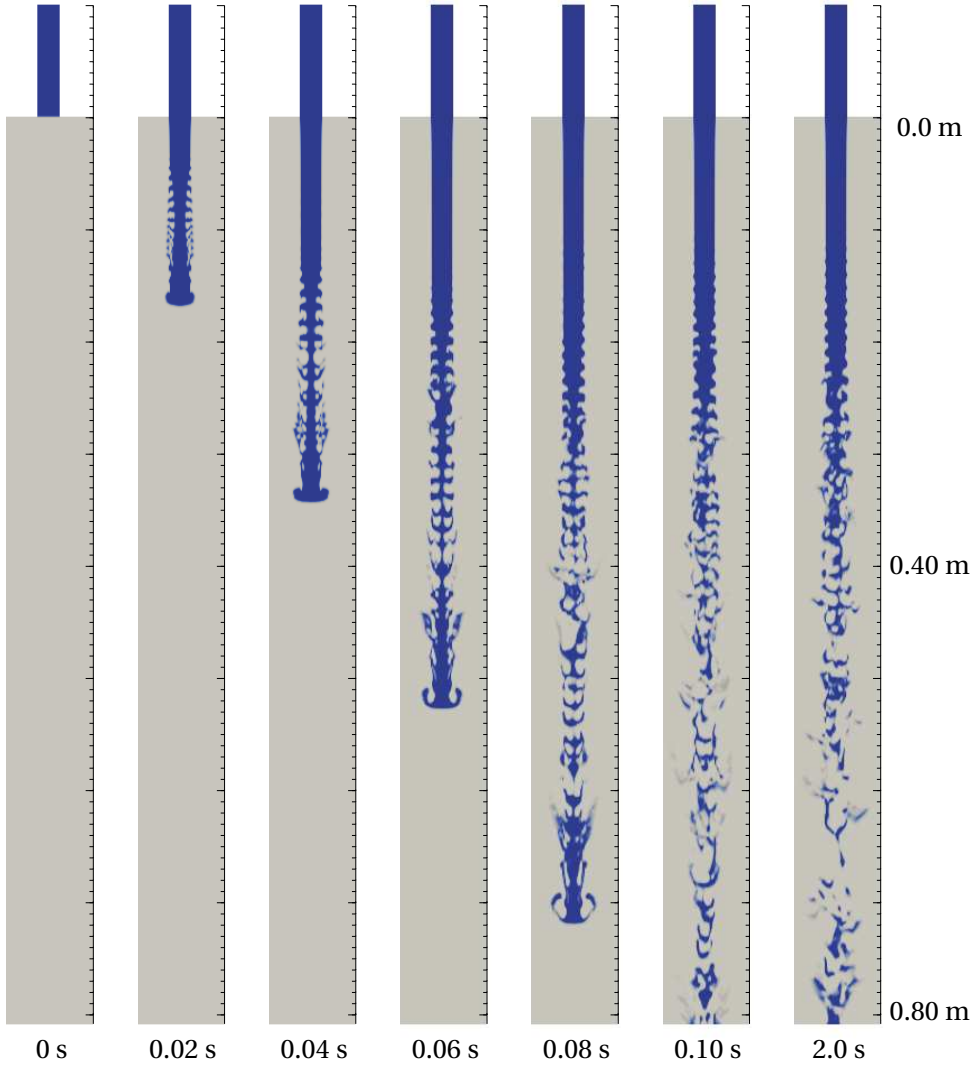

Figure 6.15: Time evolution of a free falling water jet by using the turbulent model LES - k-equation eddy-viscosity model for d = 20 mm and U_0 = 7.96 m/s.

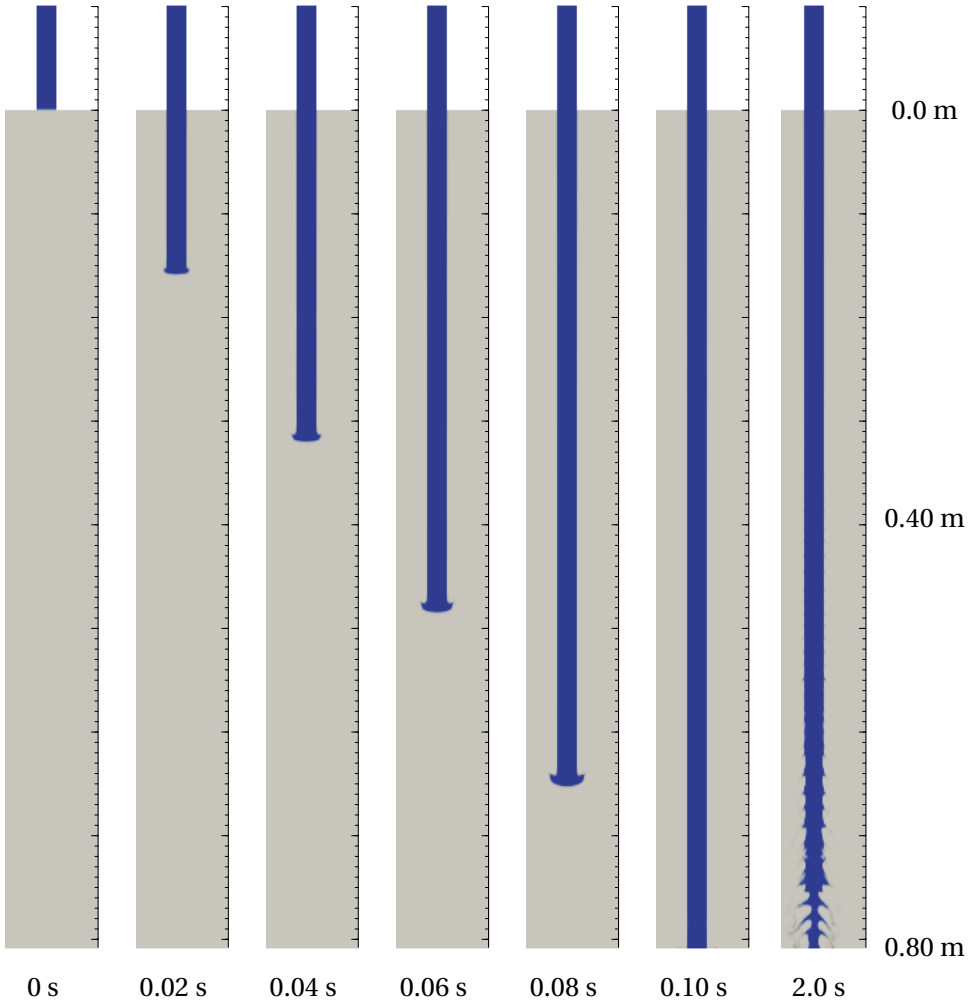

Figure 6.16: Time evolution of a free falling water jet by using the turbulent model $k-\omega$-SST scale adaptative simulation (SAS) model for d = 20 mm and U_0 = 7.96 m/s.

model, its behavior (qualitatively), approximates the experimental test more. Unlike the Smagorinsky model, the mass of fluid still remains in the falling water jet and a combination of primary breakup and secondary breakup mechanism took place over a longer scale.

To carry out this simulation the mesh configuration *mesh3* was used, it was in 128 cores parallelized and required an execution time of 216.9 h.

- In Figure 6.16 the time evolution of the $k-\omega$-SST scale adaptative simulation (SAS) model is drawn. For the first 0.10 s the water jet shows a water configuration similar to that obtained for RANS turbulence models. However, after this time the water jet stabilized and followed a stable behavior during its falling, consisting of the break of the water surface from the distance 0.60 m, being more critical at 0.76 m where

the mass of flow start to break up. This method required an execution time of 381.4 h for a simulation time of 2.0 s. The parallelization was set up on 32 cores.

For the distinct LES done, although this turbulent model was less diffusive than the Smagorinsky model and the k-equation eddy-viscosity model, it was able to reproduce breakup afterwards.

Based on the results of the numerical simulations mentioned above, the air concentration was computed for the different turbulent models following the convention mentioned in the previous section. In Figure 6.17 the air concentration distribution of the experimental test (exp) and the numerical simulations by using the turbulence models k-ϵ, k-ω SST, LES Smagorinsky (LES Smag.), LES k-equation eddy-viscosity model (LES k-Eqn), and the $k-\omega$-SST scale adaptative simulation (SAS) model (LES Hyb) are presented.

Based on Figure 6.17 the following statements can be made:

- The results obtained with the fiber optical probe showed that in the experimental test, (with the legend, exp), the water achieved a positive angle of spray θ from the beginning of the nozzle exit. At the beginning (until x = 2.5 d) the spray angle θ became θ = 1/13, however as the the water jet left the nozzle exit at x, $\sim$ 40 $d \longrightarrow \theta$ $\sim$ 1/8.

  Other alternatives to evaluate the evolution of the air concentration as the water jet left the nozzle is considering the value of the air concentration at the jet core at y/r = 0 at several distances. Based on this the water jet reached an air concentration (C(%)) of 65% at $x \sim 40d$. It is worth mentioning that until $x \sim 25d$ the air concentration in the jet core was still $\sim$ 0%.

- The RANS turbulent models k-ϵ and k-ω SST showed the same results as obtained for low water velocities. In both simulations, there was no water separation, no breakup and the angle of spray θ was negative ($y/s < 1$) due to constriction of the cross section far away from the nozzle exit due to the acceleration of gravity.

  A consequence of the analysis described above is that the air concentration along the cross section was zero (C(%) = 0).

- Although the LES Smagorinsky model at x_1 = 0.05 m shows an air concentration profile similar to those obtained experimentally, the later premature breakup has an impact on the values of C(%) at successive distances. Such is the case at x_2 = 0.26 m where the computed values of C(%) $\sim$ 40 % but experimentally is almost zero ($C(\%) \sim 0$). For the successive distances the air concentration approximated to C(%) $\sim$ 100 % because the water jets transformed into spray.

- In the case of Large Eddy Simulation - k-equation eddy-viscosity model the results are similar to those obtained from the Smagorinsky model at x_1 = 0.05, x_3 = 0.683 and x_4 = 0.78 m. However, the LES - k-equation eddy-viscosity model is less diffusive than the LES - Smagorinsky model and still some mass of water remained during the falling.

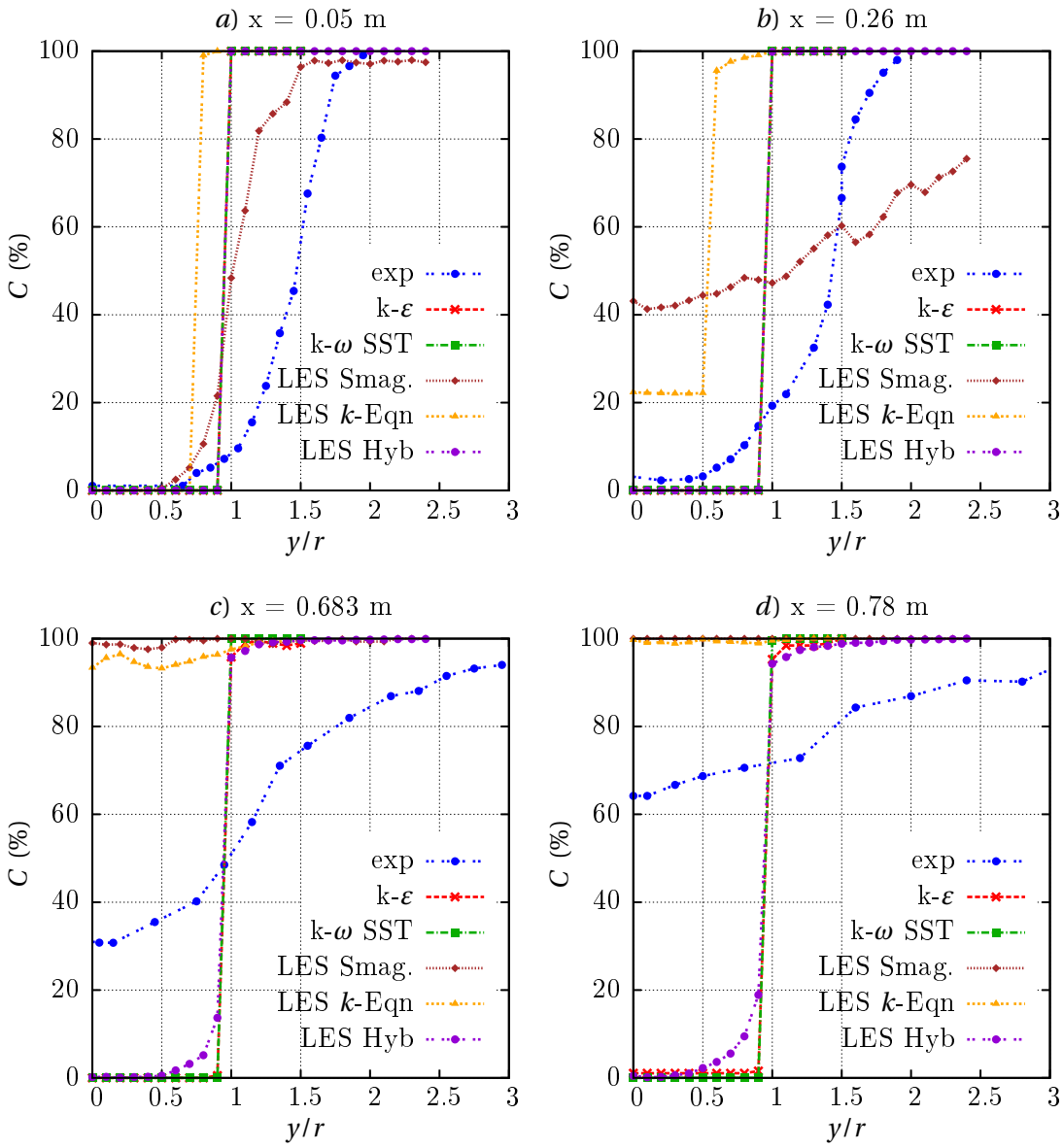

Figure 6.17: Air concentration at several locations - d = 20 mm and U_0 = 7.96 m/s.

- The air concentration profile for the the $k-\omega$-SST scale adaptative simulation (SAS) model delivered similar curves to those obtained for the RANS model. The impact of the mechanism of breakup on the water surface is visible at x_3 = 0.683 and 0.78 m because the smooth transition of the curve in the change from air concentration from $C(\%)$ = 0 to 100%.

CHAPTER

7 Conclusions and further research

The main accomplishments of this work consist of the following:

- The failure of any theory for describing the phenomena of water jet breakup is due to the strong interaction among independent variables as oscillating pressure, nozzle geometry, ambient properties, liquid properties and the level of turbulence that influence the flow characteristics. To mention just an example, parameters such as the nozzle geometry (generally omitted in descriptions) and the intensity of the turbulence in the nozzle have been generally disregarded in classic literature, even nowadays, contributing to misunderstanding, a lack of consistent information, a scattered variety of empirical formulae and dissimilar results of experiments when they has been reproduced in different laboratory facilities. Likewise, it has been revealed that the experimental results are strongly dependent on the type of nozzle and inlet conditions employed.

- To start with, the *jet stability curve* (see Figure 2.3) is an empirical and useful concept that describes the length breakup of a liquid jet $\overline{L}$ as function of the outlet velocity U_0 in the nozzle. Despite the wide empirical data found in the literature for distinct liquid jets, its existence and general behavior in the turbulent regime (where hysteresis and super-cavitation may take place) remain practically unknown.

  As a consequence, in the scientific literature most of the approaches are applied to the turbulent regime (without hysteresis behavior) on which the model type one-term power fit represents the experimental behavior under different turbulence levels Tu when the liquid discharge Q_w is plotted against the breakup length $\overline{L}$. Since these experimental findings were obtained by Ervine et al. [11] in 1980, a mathematical generalization has not been proposed yet and the theories and models developed by Ervine et al. [5] and Phinney [32] [2] are valid for specific conditions. Their lack of universality has been analysed in this research.

In general, in the mechanism of jet breakup, under a given set of conditions, some factors may have a dominant influence and overshadow others. As a consequence, it can be concluded that the nozzle geometry, the inlet velocity components and the turbulence level Tu in the nozzle are dominant factors that put conditions on the stability of a water jet. Furthermore, attention should be given to the lower envelope found in the curve of breakup length vs discharge (see Figure 4.15), which would indicate an early breakup length common to distinct liquid jets under high turbulence levels.

- When a model family of circular jets of diameter d = 10 mm , 20 mm, 40 mm and 80 mm is analysed in terms of the Froude similarity law, it has been found that as the size of the model reduces, the lower the air entrainment transported in its vicinity. Although this is not something new, as it has been reported by several authors, the construction of the model family in this research led to determining the scale effects on air entrainment for three under-scaled models L_r = 2, 4 and 8 in the experimental rig 1.

  It has been found that if the model size is a half (L_r = 2), the averaged air entrainment ratio $\overline{\beta}$ reduces by 60%. Likewise, for the second interval ($2 < L_r < 4$), the averaged air entrainment ratio $\overline{\beta}$ reduces by 70%. Afterwards, when the length scale increases from L_r = 4 to L_r = 8, the air entrainment coefficient reduces by 45%.

  Moreover it was found that the air entrainment coefficient scale β_r varies linearly with the length scale L_r. An empirical equation (4.33) has been proposed.

  As a consequence of the fact that the median values for the distinct scales $\widetilde{\beta_r}_{(L_r=j)}$ are still high, a lower plateau region by the right side of Figure 4.23 (due to low values of $\widetilde{\beta_r}_{(L_r=j)}$) was not found, and as a result a modelling criteria cannot be established for this model family unless additional experiments were done with bigger diameters and higher Reynolds numbers $Re > 1.5 \times 10^5$ (see Figure 4.22).

- It has been found that the function $u_a/U = f((y_a - r_w)/\delta)$ suitably describes the air velocity profile close to free-falling water jets. However, more research should be done in order to quantify the turbulence effects over the air velocity profile because more interaction between the air and water phases is expected as the turbulence level Tu increases.

  Likewise, it was found experimentally that the dispersion angle α_d does not vary proportionally with the dispersion number D_0 and there is not a universally-valid equation for all nozzles. Even for the same type of nozzle, different trends were found. Moreover, it is worth mentioning that the level of turbulence Tu in the nozzle would impact the angle of spread and it should not be disregarded in future experimental tests.

- The scale effects were determined by measuring the air concentration C profile at several distances from the nozzle exit of a model family of free falling water jets flowing from pipe nozzles with diameters d equal to 10 mm, 20 mm, 40 mm and 80 mm in the experimental rig 2. Experimentally, the scale effects, in the case of the air concentration, are evident as the length scale L_r increases. This is the case tested for the larger diameter d = 80 m where the air concentration at the axis was always greater than zero ($C(\%) > 0$) for the longer distance x_4 but in the case of d = 10 mm the air concentration was always equal to zero.

  Based on the Froude similarity law $Fr_r = 1$, experimental model-prototype curves were plotted and the similarities between them were evaluated by mean of: 1) Discrete Fréchet distance ($\overline{\delta_{dF}}$), through an empirical goodness of fit, and 2) Procrustes analysis, based on a Standardized Dissimilarity Measure SDM.

  When using the Discrete Fréchet distance $\overline{\delta_{dF}}$ it was found that the scale effects for L_r = 2 were moderate, and for $L_r > 4$ were high. The conclusion that scale effects were high follows from the results that the air concentration profiles were underpredicted for under-scaled models and their results disagreed with the expected values. In order to quantify the quality of the results in the laboratory, the Standardized Dissimilarity Measure led to the result that the averaged error increased from ~ 8% to ~ 12% when the length scale increased from $L_r = 2$ to $L_r = 4$. Likewise, when the scale was $L_r = 8$ the error was of the order of ~ 27%.

  As confirmed in Figure 5.13, a lower plateau region by the right side of the plot was found because the relative high Reynolds number in the prototype led to low values of $\widetilde{SDM}_{(L_r=4)}$ = 0.06 for model 1 (d = 40 mm). As a consequence of the experimental test of free falling water jets from pipe nozzles, the scale effects are negligible or low when: the diameter of the nozzle pipe $d \geq 40$ mm, the Reynolds number in the nozzle exit $Re > 1.5 \times 10^5$ and the Weber number $We > 6900$.

- The computational simulation of inertia-dominated flows with large density ratios is nowadays still a challenge in fluid mechanics in order to reproduce the nature of breakup. Two experiments on free falling water jets with a nozzle diameter d = 20 mm have been simulated in order to reproduce the spiral and spray modes of breakup in conformity with the experimental tests and the description shown in the Ohnesorge diagram. Furthermore, the computed air concentration profiles at several distances from the nozzle exit were validated with those obtained experimentally.

  In order to perform the simulations, two groups of turbulence models were used: Reynolds averaged Navier-Stokes equations (RANS) and Large Eddy Simulation (LES). On the one hand, in the case of the RANS approach, the standard $k-\epsilon$ model and the $k-\omega$-SST were implemented. On the other hand, in the case of LES, each of the Smagorinsky model, the k-equation eddy-viscosity model and the $k-\omega$-SST scale adaptative simulation (SAS) model were used to validate the experiments.

In general, it can be concluded that the Reynolds Averaged Navier-Stokes equations (RANS) in neither case would generate water separation from the surface and no breakup will take place. Moreover, the angle of spray θ will be always negative ($y/s < 1$) due to the constriction of the cross section far from the nozzle exit due to the acceleration of gravity.

In the case of LES, despite the turbulence models generating an early breakup in the case of the Smagorinsky model and the k-equation eddy-viscosity model, they were able to reproduce the physics of the phenomena in nature consisting of the dynamic interaction between the air-water phases and the breakup processes. The LES $k-\omega$-SST scale adaptative simulation (SAS) model is less diffusive than the other LES models and the results constituted an intermediate solution with the RANS models. Likewise this hybrid model was able to simulate a dynamic interaction in the surface and may generate breakup too but unfortunately requires more computational resources than the other LES models tested.

In general, despite the LES turbulence models requiring a computational time twice that of RANS models, they were able to simulate the high dynamic interaction between the air and water, as well as breakup. Furthermore, nowadays with the accelerated performance of processors, their use is suggested in hydraulic engineering consulting for studying problems in which the air is of concern.

Bibliography

[1] W. Ohnesorge, "Die Bildung von Tropfen an Düsen und die Auflösung flussiger Strahlen," *Zeittschrift für Angewandte Mathematik und Mechanik*, vol. 16 (6), pp. 355–358, 1936.

[2] R. Phinney, "The breakup of a turbulent liquid jet in a gaseous atmosphere," *Journal of Fluid Mechanics*, vol. 60, pp. 689–701, 1973.

[3] W. Kraatz, "Flow characteristics of a free circular water jet," in *11th IAHR Congress*, 1965.

[4] G. D. Silvio, "Indagine sperimentale sulle condizioni di similitudine di grossi getti liquidi liberamente effluenti," *L'energia elettrica*, 1970.

[5] D. Ervine, H. Falvey, and W. Withers, "Pressure fluctuations on plunge pool floors," *Journal of hydraulic research*, vol. 35, pp. 257–279, 1997.

[6] R. Grant and S. Middleman, "Newtonian jet stability," *American Industrial Chemical Engineering Journal*, vol. 12, pp. 669–678, 1966.

[7] F. White, *Fluid Mechanics*. McGraw Hill, 4 ed. ed., 2003.

[8] D. Ervine and H. Falvey, "Behavior of turbulent water jets in the atmosphere and in plunge pools," *Proceedings of the Institution of Civil Enginneers*, vol. 83, no. Part 2, pp. 295–314, 1987.

[9] H. Chanson, "Turbulent airŰwater flows in hydraulic structures: dynamic similarity and scale effects," *Environmental Fluid Mechanics*, vol. 9, pp. 125–142, 2009.

[10] M. Birouk and N. Lekic, "Liquid jet breaup in quiescent atmos," *Atomization and sprays*, vol. 19, no. 6, pp. 501–528, 2009.

[11] D. Ervine, E. McKeogh, and E. M. Elsawy, "Effect of turbulence intensity on the rate of air entrainment by plunging water jets," *Proc. Instn. Civ. Engrs.*, vol. 69, pp. 425–445, 1980.

[12] H. Rusche, *Computational Fluid Dynamics of Dispersed Two-Phase Flows at High Phase Fractions*. PhD thesis, Department of Mechanical Engineering - Imperial College of Science, Technology & Medicine, January 2002.

[13] T. Menard, S. Tanguy, and A. Berlemont, "Coupling level set/VOF/ghost fluid methods: Validation and application to 3d simulation of the primary break-up of a liquid jet," *International Journal of Multiphase Flow*, vol. 33, no. 5, pp. 510 – 524, 2007.

[14] J. Shinjo and A. Umemura, "Simulation of liquid jet primary breakup: Dynamics of ligament and droplet formation," *International Journal of Multiphase Flow*, no. 36, pp. 513–532, 2010.

[15] RBI Instrumentation et Mesure, Chemin du Vieux Chene -F-38240 Meylan France, *Two-Phase Flow equipment with ATL unit - User's guide*, 2013.

[16] H. Falvey, "Air-water flow in hydraulic structures - engineering monograph no. 41," tech. rep., United State Department of the Interior - Water and Power Resources Services, 1980.

[17] OpenCFD, *OpenFOAM The open source CFD toolbox. Version 2.0.1. Foundation and Advanced course.*, November 2011.

[18] J. Guerrero, "Tips and tricks," in *Introductory OpenFOAM Course*, 2014.

[19] H. E. Kobus, "An introduction to air-water flows in hydraulics." Institut für Wasserbau der Universität Stuttgart, Oktober 1985.

[20] M. Wickenhäuser, "Zweiphasenströmung in Entlüftungssystemen von Druckstollen." VAW Mitteilung 205, ETH Zürich, 2008.

[21] L. Rayleigh, "On the instability of jets," *Proceedings of the London Mathematical Society*, vol. 10, pp. 4–13, 1878.

[22] J. A. F. Plateau, *Statique expérimentale et théorique des liquides soumis aux seules forces moléculaires*, vol. 2. Gauthier-Villars, 1873.

[23] C. Weber, "Zum Zerfall eines Flüssigkeitsstrahles," *Zeittschrift für angewandte Mathematik und Mechanik*, vol. 11, pp. 136–154, April 1931.

[24] A. Haenlein, "Über den Zerfall eines Flüssigkeitsstrahles," *Forschung auf dem Gebiete des Ingenieurwesen*, vol. 2, no. 4, pp. 139–149, 1931.

[25] N. Tamaki, M. Shimizu, K. Nishida, and H. Hiroyasu, "Effects of cavitation and internal ftow on atomization of a liquid jet," *Atomization and Sprays*, vol. 8, pp. 179–197, 1998.

[26] N. Tamaki, M. Shimizu, and H. Hiroyasu, "Enhancement of the atomization of a liquid jet by cavitation in a nozzle hole," *Atomization and Sprays*, vol. 11, pp. 125–137, 2001.

[27] G. H. McKinley and M. Renardy, "Wolfgang von Ohnesorge," *Physics of fluids*, vol. 23, 2011.

[28] C. Miesse, "Correlation of experimental data on the disintegration of liquid jets," *Industrial & Engineering Chemistry*, vol. 47, no. 9, pp. 1690–1701, 1955.

[29] S. Smith and H. Moos, "Experiments with mercury jets," *Proceedings of the Royal Society of London*, vol. 93, pp. 373–393, july 1917.

[30] E. Giffen and A. Muraszew, *The atomization of liquid fuels*. Chapman & Hall Ltd., 1953.

[31] J. Skripalle, "Zwangsbelüftung von Hochgeschwindigkeitströmungen an zurückspringenden Stufen im Wasserbau (Mitteilung nr. 124), Institut für Wasserbau und Wasserwirtschaft, Technische Universität Berlin." Technische Universität Berlin, Berlin, April 1994.

[32] R. Phinney, "Stability of a laminar viscous jet: the influence of the initial disturbance level," *A.I.Ch.E. J.*, no. 18, 1972.

[33] M. J. McCarthy and N. A. Molloy, "Review of stability of liquid jets and the influence of nozzle design," *Chemical engineering journal*, vol. 7, pp. 1–20, 1974.

[34] P. H. Schweitzer, "Mechanism of disintegration of liquid jets," *Journal of applied physics*, vol. 8, pp. 513–521, 1937.

[35] H. Hiroyasu, M. Shimizu, and M. Arai, "The breakup of high speed jet in a high pressure gaseous atmosphere," *ICLASS-82*, pp. 69–74, 1982.

[36] H. Hiroyasu, "Spray breakup mechanism from the hole-type nozzle and its applications," *Atomization and Sprays*, vol. 10, pp. 511–527, 2000.

[37] H. Hiroyasu, M. Arai, and M. Shimizu, "Break-up length of a liquid jet and internal ftow in a nozzle," *ICLASS-91*, pp. 275–282, 1991.

[38] M. Arai, M. Shimizu, and H. Hiroyasu, "Break-up length and spray angle of high speed jet," *ICLASS-85*, 1985.

[39] M. Arai, M. Shimizu, and H. Hiroyasu, "Break-up length and spray formation mechanism of a high speed liquid jet," *ICLASS-88*, pp. 177–183, 1988.

[40] M. Arai, M. Shimizu, and H. Hiroyasu, "Similarity between the break-up lengths of a high speed liquid jet in atmospheric and pressurized conditions," *ICLASS-91*, pp. 563–570, 1991.

[41] G. Batchelor, *An introduction to fluid dynamics*. Cambridge University Press, 2002.

[42] D. Heraud, *Dispersion des jets liquides: Influence des rugosités de paroi*. PhD thesis, Faculte des Sciences de l'Universite de Grenoble, 1966.

[43] J. Dodu, "Étude de la couche limite d'air autour d'un jet d'eau a grande vitesse," *Seventh Congress of the International Association of Hydraulic Research, Lisbon, Portugal*, 1957.

[44] P. Oguey and M. Mamin, "Etude théorique et expérimentale de la dispersion du jet dans la turbine pelton," *Bulletin technique de la Suisse romande*, vol. 70, pp. 281–291, October 1944.

[45] P. Oguey, M. Mamin, and F. Baatard, "Etude théorique et expérimentale de la dispersion du jet dans la turbine pelton," *Bulletin Technique de la Suize Romande*, 1951.

[46] J. Kozeny, *Hydraulik: ihre Grundlagen und praktische Anwendung*. Springer-Verlag Wien, 1953.

[47] J. Farmer . *Proc. Roy. Soc. Canada, II. Bd.*, 1986.

[48] P. Horeni, "Desintegration of a free jet of water in air." Byzkumny ustav vodohospadarsky prace a studie, Sesit 93, Praha, Pokbaba, 1956.

[49] J. Dodu, "Contribution a l'etude de la dispersion des jets liquides a grande vitese." Publications Cientifiques et Techniques du Ministere de L'air, 1964. No. 407.

[50] T. Chen and J. Davis, "Disintegration of a turbulent water jet," *Journal of the Hydraulics Division (ASCE)*, vol. 90, pp. 175–206, January 1964.

[51] W. Hager, *Energy dissipation: Trajectory basins*, ch. 7, pp. 111–149. No. 9 in Hydraulic structures design manual, IAHR: International Association for Hydraulic Research, Balkema, Rotterdam, 1995.

[52] N. B. Isachenko and A. G. Chanishvili, "Distortion of a jet diverted by a flip bucket," *Hydrotechnical construction*, vol. 2, pp. 253–262, 1968.

[53] J. Weisbach, *Lehrbuch der Ingenieur- und Maschinen-Mechanik*. Braunschweig, 1845.

[54] J. Weisbach, *Die Experimental-Hydraulik*. Freiberg: Engelhardt-Verlag, 1855.

[55] J. R. Freeman, *Hydraulic Laboratory Practice*. American Society of Mechanical Engineers, 1929.

[56] P. Neményi, *Wasserbauliches Strömungslehre*. J. A. Bartth, 1933.

[57] J. Schuster, "Hydraulic model studies of the eucumbene-tumut tunnel junction shaft," tech. rep., Bureau of Reclamation - Hydraulics Laboratory Report HYD-392, Denver, Colorado, August 1954.

[58] H. Rouse, J. W. Howe, and D. Metzler, "Experimental investigations of fire monitors and nozzles," *Proceedings of American Society of Civil Engineers*, vol. 77, pp. 1147–1175, October 1951.

[59] R. Fenn and S. Middleman, "Newtonian jet stability: The role of air resistance," *AIChE Journal*, vol. 15, no. 3, pp. 379–383, 1969.

[60] A. Lefebvre, *Atomization and sprays*. Taylor and Francis, 1989.

[61] T. Baron, "Technical report," Tech. Rep. 4, University of Illinois, 1949.

[62] E. McKeogh, *A Study of Air Entrainment using Plunging Water Jets*. PhD thesis, Queens University, Belfast, Ireland, October 1978.

[63] W. Withers, *Pressure Fluctuations in the Plunge Pool of an Impinging Jet Spillway*. PhD thesis, University of Glasgow, February 1991.

[64] J. W. Hoyt and J. Taylor, "Waves on water jets," *Journal of Fluid Mech.*, vol. 83, part 1, pp. 119–127, 1977.

[65] S. Spangelo, N. Lekic, S. Fabbro, and M. Birouk, "Effects of nozzle geometry on the near-field characteristics of a liquid jet," in *ICLASS 2009, 11th Triennial International Annual Conference on Liquid Atomization and Spray Systems*, 2009.

[66] J.-P. Franc and L.-M. Michel, *Fundamentals of Cavitation*. Kluwer Academic Publishers, 2005.

[67] S. Dabiri, W. A. Sirignano, and D. D. Joseph, "Cavitation in an orifice flow," *Physics of Fluids*, vol. 19, 2007.

[68] N. Chigier and R. D. Reitz, *Recent Advances in Spray Combustion: Spray Atomization and Drop Burning Phenomena*, vol. 166, ch. 4: Regimes of jet breakup and breakup mechanisms (physical aspects), pp. 109–135. AIAA, 1996.

[69] V. Heller, "Scale effects in physical hydraulic engineering models," *Journal of hydraulic research*, vol. 49, pp. 293–306, 2011.

[70] R. Ettema, *Hydraulic modeling concepts and practice*. American Society of Civil Engineers, 2000.

[71] P. Novak, V. Guinot, A. Jeffrey, and D. Reeve, eds., *Hydraulic Modeling - an introduction: principles, methods and applications*. Spon Press, 2010.

[72] A. M. Proudovsky, "General principles of approximate hydraulic modelling," in *Symposium on Scale Effects in Modelling. Hydraulic Structures* (H. Kobus, ed.), International Association for Hydraulic Research, september 1984.

[73] H. Kobus and G. Abraham, *Hydraulic modelling*. Band 7 von German Association for Water Resources and Land Improvement, Bulletin., 1980.

[74] H. Chanson, *Air Bubble Entrainment in Free-Surface Turbulent Shear Flows*, vol. 9999. NOSE, 1997.

[75] P. Wisner, "Sur le role du critere de Froude dans l'etude de l'entrainement de l'air par les courants a grande vitesse," in *International Association for Hydraulic Research, 11th congress*, vol. Paper 1.15, (Leningrad USSR), 1965.

[76] J. Ferziger and M. Peric, *Computational methods for fluid dynamics*. Springer, 2002.

[77] C. W. Hirt and B. D. Nichols, "Volume of fluid (VOF) method for the dynamics of free boundaries," *Journal of Computational Physics*, vol. 39, pp. 201–225, 1981.

[78] E. Berberović, N. P. van Hinsberg, S. Jakirlić, I. V. Roisman, and C. Tropea, "Drop impact onto a liquid layer of finite thickness: Dynamics of the cavity evolution," *Physical Review E.*, vol. 79, 2009.

[79] OpenFOAM-Foundation, "The open source CFD toolbox, User Guide v. 2.3.0." http://www.openfoam.org/index.php, February 2014.

[80] H. Jasak, *Error analysis and estimation for the finite volume method with applications to fluid Flows*. PhD thesis, University of London, 1996.

[81] S. Márquez-Damián, *An extended mixture model for the simultaneous treatment of short and long scale interfaces*. PhD thesis, Universidad Nacional del Litoral, 2013.

[82] H. Vahedi and B. Pourdeyhimi, "The effects of nozzle geometry on waterjet breakup at high reynolds numbers," *Experiments in fluids*, vol. 35, pp. 364–371, 2003.

[83] V. Srinivasan, A. J. Salazar, and K. Saito, "Modeling the disintegration of modulated liquid jets using volume-of-fluid (VOF) methodology," *Applied Mathematical Modelling*, vol. 35, pp. 3710–3730, 2011.

[84] S. Velkova, "Das hydraulische Verhalten eines HW-Schachtüberfalls," Master's thesis, Institut für Wasserbau und Ingenieurhydrologie - Technische Universität Wien, 2008.

[85] M. Reis, "Lufteinzug in vertikalen Fallschächten," Master's thesis, Institut für Wasserbau und Ingenieurhydrologie - Technische Universität Wien, 2009.

[86] M. Nagy, "Lufteintrag in vertikalen Fallstrahlen," Master's thesis, Institut für Wasserbau und Ingenieurhydrologie - Technische Universität Wien, 2012.

[87] E. Tabova, "Velocity measurements in free falling water jets," Master's thesis, Institut für Wasserbau und Ingenieurhydrologie - Technische Universität Wien, 2012.

[88] R. Boes and W. Hager, "Fiber optical experimentation in two-phase cascade flow," *Proc. Intl. RCC Dams Seminar*, 1998.

[89] R. Boes, "Fiberoptische Messung von lokalen Luftkonzentrationen und Fliegeschwindigkeiten in Zweiphasenströmungen," in *Wasserbauliche Mitteilungen Heft 13*, pp. 205–214, Institut für Wasserbau und Technische Hydromechanik der TU Dresden, 1998.

[90] R. Boes, *Zweiphasenströmung und Energieumsetzung an Grosskaskaden*. PhD thesis, Eidgenössischen Technischen Hochschule Zürich, 2000.

[91] K. Kramer, "Development of aereted chute flow." VAW Mitteilung 183, ETH Zürich, 2004.

[92] M. Pfister, "Schussrinnenbelüfter - lufttransport ausgelöst durch interne Abflussstruktur." VAW Mitteilung 203, ETH Zürich, 2008.

[93] RBI Instrumentation et Mesure, Chemin du Vieux Chene -F- 38240 Meylan France, *Iso Software - User's guide*, 2013.

[94] F. Florez, R. Prenner, and N. Krouzecky, "Measurements of air concentration and velocities in a free falling water jet," *Transactions of Famena*, vol. 40, no. 1, pp. 57–68, 2016.

[95] The MathWorks, Inc, *Image processing toolbox: user's guide*, r2015a ed.

[96] O. Marques, *Practical Image and video processing using Matlab*. Wiley, 2011.

[97] W. Burger and M. Burge, *Digital image processing: an algorithm introduction using Java*. Springer, 2008.

[98] T. Takahashi and Y. Kitamura, "Effect of nozzle length on breakup length of liquid jet," in *Memoirs of the School of Engineering, Okayama University,*, vol. 4, pp. 57–64, 1969.

[99] A. Sikora, "Zavdusnenie sachtovych priepadov," *Viskumny Ustav Vodohospodarsky, Bratislava, Prace a studie 37, p. 112, (Air Entrainment in Shaft Spillways, Czechoslovakia)*, 1965.

[100] J. Fenton, "Splines." http://johndfenton.com/Alternative-Hydraulics.html, August 2015.

[101] H. Falvey and D. A. Ervine, "Aeration in jets and high velocity flows," in *Model prototype correlation* (H. Kobus, ed.), 1987.

[102] A. Davis and P. Samuels, *An introduction to computational geometry for curves and surfaces*. Oxford applied mathematics and computing science series, Oxford University Press, 1996.

[103] C. de Boor, *A practical guide to splines*. Springer, Nov 2001.

[104] H. Alt and M. Godau, "Computing the Fréchet distance between two polygonal curves," *International Journal of Computational Geometry & Applications*, vol. 5, no. 1 & 2, pp. 75–91, 1995.

[105] T. Eiter and H. Mannila, "Computing discrete Fréchet distance." Christian Doppler Labor für Expertensyteme - Technische Universität Wien, 1994.

[106] A. Prosperetti and G. Tryggvason, eds., *Computational Methods for Multiphase Flow*. Cambridge University Press, 2009.

[107] P. Lubin and J.-P. Caltagirone, "Large eddy simulation of the hydrodynamics generated by breaking waves," *Advances in numerical simulation of nonlinear water waves*, vol. 11, pp. 575–604., 2010.

[108] P. Lubin, S. Glockner, O. Kimmoun, and H. Branger, "numerical simulations of spilling breaking waves," in *Conference on coastal engineering, Jun 2010, Shangai, China. Coastal Engineering Research Council, 32 (wave.11)*, pp. 1–9, 2010.

[109] N. Kolev, *Multiphase Flow Dynamics 1 Fundamentals*. Springer-Verlag, 2005.

[110] H. Chanson, "Hydraulics of aerated flows: qui pro quo?," *Journal of Hydraulic Research*, vol. 51, no. 3, pp. 223–243, 2013.

[111] O. Ubbink, *Numerical prediction of two fluid systems with sharp interfaces*. PhD thesis, Imperal Collegue of Science, Technology and Medicine, London, 1997.

[112] R. Issa, "Solution of the implicitly discretised fluid flow equations by operator-splitting," *Journal of Computational Physics*, vol. 62, pp. 40–65, January 1986.

[113] H. Versteeg and W. Malalasekera, *An introduction to computational fluid dynamics the finite volume method*. Longman Scientific & Technical, 1995.

[114] E. de Villiers, *The Potential of Large Eddy Simulation for the Modeling of Wall Bounded Flows*. PhD thesis, Department of Mechanical Engineering Imperial College of Science, Technology and Medicine, July 2006.

[115] J. Blazec, *Computational fluid dynamics: principles and applications*. Elsevier, 2001.

[116] M. Lesieur, *Turbulence in fluids*. Kluwer Academic Publishers, 1995.

[117] S. Pope, *Turbulent Flows*. Cambridge University Press, 2000.

[118] I. Galambos, *Improved understanding of performance of local controls linking the above and below ground components of urban flood flows*. PhD thesis, University of Exeter, 2012.

[119] W. Rodi, G. Constantinescu, and T. Stoesser, *Large-Eddy simulations in hydraulics*. Taylor & Francis Group, 2013.

[120] W. Rodi, *Turbulence models and their application in hydraulics A state-of-the-art review*. A.A. Balkelma, 1993.

[121] P. Bates, S. Lanes, and R. Fergunson, *Computational Fluid Dynamics - Applications in Environmental Hydraulics*. John Wiley & Sons, 2005.

[122] ERCOFTAC, *Best Practice Guidlines for Industrial Computational Fluid Dynamics of Single-Phase Flows*. Lausanne, 2000.

[123] R. H. Nichols, "Turbulence models and their application to complex flows." University of Alabama at Birmingham. Revision 4.01.

[124] F. Menter, "Zonal two equation k-ω turbulence models for aerodynamic flows," *AIAA*, vol. 93, July 1993.

[125] J. Smagorinsky, "General circulation experiments with the primitive equations," *Monthly Weather Review*, vol. 91, no. 3, pp. 99–164, 1963.

[126] D. K. Lilly, "The representation of small-scale turbulence in numerical simulation experiments," *In H. H. Goldstine (Ed.), Proc. IBM Scientific Computing Symp. on Environmental Sciences*, 1967.

[127] J. W. Deardorff, "A numerical study of three-dimensional turbulent channel flow at large reynolds numbers," *Journal of Fluid Mechanics*, vol. 41, pp. 453–480, April 1970.

[128] J. Hinze, *Turbulence*. Mc Graw-Hill Publishing Co., 1975.

[129] Z. Shang, D. R. Emerson, and X. Gu, "Numerical investigations of cavitation around a high speed submarine using openfoam with les," *International Journal of Computational Methods*, vol. 9, no. 3, p. 1250040 (14 pages), 2012.

[130] O. Penttinen, "A pimplefoam tutorial for channel flow, with respect to different LES models," tech. rep., Chalmers University of Technology, 2011.

[131] L. Davidson, "Evaluation of the sst-sas model: channel flow, asymmetric diffuser and axi-symmetric hill," *European Conference on Computational Fluid Dynamics ECCOMAS CFD 2006.*, 2006.

[132] F. R. Menter and Y. Egorov., *DESider A European Effort on Hybrid RANS-LES Modelling: Results of the European-Union Funded Project, 2004 - 2007 (Notes on Numerical Fluid Mechanics and Multidisciplinary Design)*, ch. 2, section 8 Formulation of the Scale-Adaptive Simulation (SAS). Springer-Verlag Berlin Heidelberg, 2009.

[133] A. Lidtke, "Solution techniques in OpenFOAM." University of Southampton, November 2014.